

LOUGHBOROUGH UNIVERSITY

**Mathematical Modelling of Nonlinear  
Waves in Layered Waveguides with  
Delamination**

by

Matthew Tranter

A thesis submitted in partial fulfillment for the  
degree of Doctor of Philosophy

in the

School of Science

Department of Mathematical Sciences

June 2018



*“Mathematics should be studied if only for that it puts the mind in order.”*

Mikhail Lomonosov

LOUGHBOROUGH UNIVERSITY

# *Abstract*

School of Science

Department of Mathematical Sciences

Doctor of Philosophy

by Matthew Tranter

The propagation of nonlinear bulk strain waves in layered elastic waveguides has many applications, particularly its potential use for non-destructive testing, where a small defect in the bonding between the layers of a waveguide can lead to a catastrophic failure of the structure. Experiments have shown that strain solitons can propagate for significantly longer distances than the waves used in current methods, and therefore they are of great interest.

This thesis considers two problems. Firstly, we consider the scattering of nonlinear bulk strain waves in two types of waveguides: a perfectly bonded layered waveguide, and a layered waveguide with a soft bond between the layers, when the materials in the layers have similar properties. In each case we assume that there is a region where the bond is absent - a delamination. This behaviour is described by a system of uncoupled or coupled Boussinesq equations, with conditions on the interface between the sections of the bar. This is a complicated system of equations, and we develop a direct numerical method to solve these equations numerically.

A weakly nonlinear solution is then constructed for the system of equations, describing the leading order reflected and transmitted strain waves. In the case of a layered elastic bar with a perfect bond we obtain Korteweg-de Vries equations, and in the case of a soft bond between the layers, where the properties of the layers are close, we obtain coupled Ostrovsky equations describing the propagation of the reflected and transmitted waves in each layer of the waveguide. In the delaminated regions of the bar, Korteweg-de Vries equations are derived in every case and therefore we make use of the Inverse Scattering Transform to provide theoretical predictions in this region.

The modelling in each case is extended to the case of a finite delamination in the waveguide, and we study the effect of re-entering a bonded region on a strain wave. In each case considered we develop a measure of the delamination length in terms of the change in amplitude of the incident wave, and furthermore the structure of the wave provides

further insight about the structure of the waveguide. Numerical simulations are developed using finite-difference techniques and pseudospectral methods, and these are detailed in the appendices.

Finally, we consider the initial value problem for the Boussinesq equation with an Ostrovsky term, on a periodic domain. The initial condition for this equation does not necessarily have zero mean on the interval. The mean value is subtracted from the function so that a weakly nonlinear solution to the problem can be constructed where all functions in this expansion have zero mean. This is necessary as the derived Ostrovsky equations have zero mean. The expansion is constructed in increasing powers of  $\sqrt{\epsilon}$  up to and including  $O(\epsilon)$ , where  $\epsilon$  is a small amplitude parameter in the equation. We compare the results for a wide range of values of  $\gamma$  (the coefficient of the Ostrovsky term) and varying mean values for the initial condition, to confirm that the expansion is valid. A comparison of the errors shows that the constructed expansion is correct and the errors behave as predicted by the expansion. This was further confirmed for non-unity coefficients in the equation.

## *Acknowledgements*

First and foremost, I would like to thank my supervisor, Karima Khusnutdinova, for her guidance and support throughout the course of my studies. She has helped provide inspiration and to shape my research throughout the past few years. She has often gone above and beyond the requirements of a supervisor in her aim of shaping the future researchers in our field. I hope to continue my journey to becoming an established mathematician and to be able to inspire the future generation as well.

I would also like to thank the staff and other research students in my department, as the many discussions with them have been invaluable. Special thanks go to Andrea Savoldi; we met as colleagues and left as great friends.

Last and certainly not least, my deepest and most sincere thanks go to my beautiful wife Kerry. Her support and guidance during my degree and further studies have helped me to do things I never thought possible. You are my best friend, the love of my life, the light of my heart. I will love you forever and always.

# Contents

<b>Abstract</b>	<b>iv</b>
<b>Acknowledgements</b>	<b>vi</b>
<b>List of Figures</b>	<b>x</b>
<b>List of Tables</b>	<b>xv</b>
<b>Abbreviations</b>	<b>xvi</b>
<b>Publications</b>	<b>xxi</b>
<b>1 Introduction</b>	<b>1</b>
<b>2 Modelling Wave Propagation in Solids</b>	<b>5</b>
2.1 Fermi-Pasta-Ulam Model . . . . .	5
2.2 Doubly Dispersive Equation Model . . . . .	9
2.2.1 Derivation . . . . .	10
2.2.2 Comparison of Equations . . . . .	12
2.3 Coupled FPU Chains . . . . .	12
2.4 Weakly Nonlinear Solution of Initial Value Problem . . . . .	14
2.4.1 Initial Value Problem for Coupled Boussinesq Equations . . . . .	14
2.4.2 Initial Value Problem for the Boussinesq and Boussinesq-type Equations . . . . .	16
2.5 Weakly Nonlinear Solution of the Scattering Problem . . . . .	18
<b>3 Modelling of Nonlinear Wave Scattering in a Delaminated Elastic Bar</b>	<b>21</b>
3.1 Introduction . . . . .	21
3.2 Problem Formulation . . . . .	22
3.3 Weakly Nonlinear Solution . . . . .	23
3.4 The Inverse Scattering Transform and Fission of Solitons . . . . .	26
3.5 Results for a Two-Section Bar . . . . .	29
3.5.1 Test Cases . . . . .	32

3.5.2	Predictions . . . . .	34
3.5.3	Predicted Amplitude of Lead Soliton . . . . .	37
3.5.4	Comparison of Schemes . . . . .	37
3.6	Results for a Three-Section Bar . . . . .	40
3.6.1	Weakly Nonlinear Solution . . . . .	40
3.6.2	Prediction of Lead Soliton Amplitude . . . . .	42
3.6.3	Numerical Results . . . . .	43
3.7	Conclusions . . . . .	45
<b>4</b>	<b>Modelling of Nonlinear Wave Scattering In a Bi-Layer with a Soft Bonding Layer</b>	<b>49</b>
4.1	Introduction . . . . .	49
4.2	Problem Formulation . . . . .	52
4.3	Weakly Nonlinear Solution . . . . .	54
4.3.1	Region 1: Two Homogeneous Layers . . . . .	55
4.3.2	Region 2: Bi-Layer with Soft Bonding . . . . .	57
4.3.3	Region 3: Delamination . . . . .	59
4.3.4	Matching at Boundaries: Continuity Conditions . . . . .	61
4.4	Numerical Modelling . . . . .	63
4.4.1	Solitons in the Delaminated Section . . . . .	65
4.4.2	Delamination of Semi-Infinite Length . . . . .	66
4.4.3	Delamination of Finite Length . . . . .	69
4.4.4	Further experiments . . . . .	74
4.5	Concluding Remarks . . . . .	75
<b>5</b>	<b>Initial Value Problem for the Boussinesq-Ostrovsky Equation</b>	<b>79</b>
5.1	Introduction . . . . .	79
5.2	Weakly Nonlinear Solution . . . . .	80
5.2.1	Terms at $O(\sqrt{\epsilon})$ . . . . .	82
5.2.2	Terms at $O(\epsilon)$ . . . . .	83
5.2.3	Terms at $O(\epsilon^{3/2})$ . . . . .	84
5.2.4	Terms at $O(\epsilon^2)$ . . . . .	86
5.3	Results . . . . .	87
5.3.1	Error Analysis . . . . .	87
5.3.2	Results for Unity Coefficients . . . . .	88
5.3.3	Results for Non-Unity Coefficients . . . . .	92
5.4	Conclusions . . . . .	96
<b>6</b>	<b>Conclusions and Future Work</b>	<b>99</b>
<b>Appendix A Finite-difference Techniques for the Boussinesq and Boussinesq-type Equations</b>		<b>103</b>
A.1	Finite-Difference Method for the Boussinesq Equation . . . . .	104
A.2	Direct Numerical Method for a System of Two Boussinesq-type Equations	106
A.2.1	Derivation for Boussinesq Equation . . . . .	106
A.2.2	Extension to Coupled Regularised Boussinesq Equations . . . . .	110

A.3 Direct Numerical Method for a System of $M$ Boussinesq Equations . . . .	113
<b>Appendix B SSPRK(5,4) Scheme for KdV Equations</b>	<b>121</b>
<b>Appendix C Pseudospectral Methods</b>	<b>125</b>
C.1 Pseudospectral Scheme for the KdV Equation . . . . .	128
C.2 Pseudospectral Scheme for the Ostrovsky and Coupled Ostrovsky Equations	129
C.2.1 Ostrovsky Equation . . . . .	129
C.2.2 Linearised Ostrovsky Equation on Non-Zero Background . . . . .	131
C.2.3 Pseudospectral Scheme for the Coupled Ostrovsky Equations . . .	133
C.3 Pseudospectral Scheme for the Boussinesq-Ostrovsky Equation . . . . .	135
 <b>Bibliography</b>	 <b>139</b>



# List of Figures

2.1	The FPU model for a series of equidistant particles connected by weakly nonlinear springs. . . . .	6
2.2	The solution to the KdV equation (2.16) where $\delta = 0.022$ , where we have the initial condition (black, dashed), the solution at $t = t_b$ (red, dash-dot) and the solution at $t = 3.6t_b$ (blue, solid). We clearly see eight solitons generated from this initial condition. . . . .	9
2.3	Model of an elastic bar with rectangular cross section. . . . .	9
2.4	The coupled FPU model for a series of equidistant particles connected by weakly nonlinear springs. . . . .	12
3.1	Two-layered symmetric bar with delamination at $x > 0$ . . . . .	22
3.2	The initial condition and solution at $t = 1000$ in the second section of the bar, for the direct numerical scheme (blue, solid) and semi-analytical method (red, dashed) with exact initial conditions, $\alpha = \beta = c = 1$ and initial position $x = -50$ . . . . .	33
3.3	The reflected and transmitted waves in each section of the bar, for the direct numerical scheme (blue, solid) and semi-analytical method (red, dashed) with exact initial conditions, $\alpha = \beta = 1$ , $c = 3/4$ and initial position $x = -50$ . . . . .	35
3.4	The reflected and transmitted waves in each section of the bar, for the direct numerical scheme (blue, solid) and semi-analytical method (red, dashed) with exact initial conditions, $\alpha = \beta = 1$ , $c = 2$ and initial position $x = -50$ . . . . .	36
3.5	The waves in the transmitted wave field for various configurations of the bar, corresponding to different values of $n$ and $k$ . Each of the results is presented at the same time moment, for the direct numerical scheme (blue, solid) and semi-analytical method (red, dashed) with exact initial conditions and initial position $x = -50$ . . . . .	38
3.6	Two-layered symmetric bar with a finite delamination at $0 < x < x_a$ . . . . .	40
3.7	The solution in each section of the bar for the direct numerical scheme (blue, solid) and semi-analytical method (red, dashed) with $\beta = 2/5$ , corresponding to $n = 2$ and $k = 2$ , and initial position $x = -50$ . . . . .	44
3.8	Graphs of the change in amplitude of the transmitted soliton in comparison to the incident soliton, as measured by $\sigma$ . Graph (a) corresponds to changing values of $\epsilon$ , while graph (b) corresponds to changing values of $\beta$ (changing the geometry of the waveguide). . . . .	46

4.1	Typical generation of radiating solitary waves in system (4.1), from pure solitary wave initial conditions, for $f$ (solid line) and $g$ (dashed line). Here $c = 1.05$ , $\alpha = \beta = 1.05$ . (a) Initial condition at $t = 0$ : pure solitary wave solution with $\delta = \gamma = 0$ and $v = 1.3$ . (b) Radiating solitary wave solution with $\delta = \gamma = 0.01$ at $t = 400$ . . . . .	51
4.2	Two branches of the linear dispersion curve of system (4.1) for $c = 1.05$ , $\alpha = \beta = 1.05$ , $\delta = \gamma = 0.01$ and a resonance for $p = 1.3$ (horizontal, dashed line). . . . .	51
4.3	Bi-layer with two homogeneous layers for $x < x_a$ , a bonded two-layered section for $x_a < x < x_b$ and a delaminated section for $x > x_b$ . . . . .	52
4.4	The waves $f$ (upper layer) and $g$ (lower layer) in the various sections of the bi-layer, for $\alpha = \beta = 1.05$ , $c = 1.025$ , $\delta = \gamma = 1$ , $v_1 = 1.025$ , $\sigma = 1$ and $\epsilon = 0.05$ : direct numerical simulations (blue, solid line) and semi-analytical method (red, dashed line). For the direct numerical method, the full computational domain is $[-1000, 1000]$ . In the pseudospectral method, $N = 16384$ . . . . .	67
4.5	The waves $f$ (upper layer) and $g$ (lower layer) in the various sections of the bi-layer, for $\alpha = \beta = 1.05$ , $c = 1.025$ , $\delta = \gamma = 1$ , $v = 1.025$ , $\sigma = 0$ and $\epsilon = 0.05$ : direct numerical simulations (blue, solid line) and semi-analytical method (red, dashed line). For the direct numerical method, the full computational domain is $[-1000, 1000]$ . In the pseudospectral method, $N = 16384$ . . . . .	68
4.6	Bi-layer with two homogeneous layers for $x < x_a$ , a bonded two-layered section for $x_a < x < 0$ , a delaminated section for $0 < x < x_b$ and another bonded two-layered section for $x > x_b$ . . . . .	70
4.7	The waves $f$ (upper layer) and $g$ (lower layer) in the various sections of the bi-layer, for $\alpha = \beta = 1.05$ , $c = 1.025$ , $\delta = \gamma = 1$ , $v = 1.025$ , $\sigma = 0$ and $\epsilon = 0.05$ : direct numerical simulations (solid line) and weakly nonlinear solution (dashed line). Two homogeneous layers, of the same material as the upper layer, are on the left, and the waves propagate to the right. For the direct numerical method, the full computational domain is $[-600, 1000]$ . In the semi-analytical method, $N = 8192$ . . . . .	71
4.8	A comparison between the case without delamination (blue) and with delamination (red) of differing lengths, measured in FWHM of the incident soliton. The model is the same as that used in Figure 4.7 with the same parameters, and all images are for $t = 1200$ . . . . .	72
4.9	The percentage decrease in amplitude for various delamination lengths, measured in FWHM, at (a) $\epsilon = 0.05$ , and (b) various values of $\epsilon$ . . . . .	73
4.10	The waves $f$ (upper layer) and $g$ (lower layer) in the various sections of the bi-layer, for $\alpha = \beta = 1.05$ , $c = 1.025$ , $\delta = \gamma = 1$ , $v_1 = 1.025$ , $\sigma = 0$ and $\epsilon = 0.05$ : direct numerical simulations (blue, solid line) and semi-analytical method (red, dashed line). Two homogeneous layers, of the same material as the upper layer, are on the right, and the waves propagate to the left. For the direct numerical method, the full computational domain is $[-400, 1200]$ . In the semi-analytical method, $N = 8192$ . . . . .	76

5.1 A comparison of the original Boussinesq-Ostrovsky equation (5.1) (solid, blue) at  $t = 1/\epsilon$ , for the weakly nonlinear solution including leading order (dashed, red),  $O(\sqrt{\epsilon})$  (dash-dot, black) and  $O(\epsilon)$  (dotted, green) corrections, for (a)  $d = 1$  and (b)  $d = 7$ . Parameters are  $L = 40$ ,  $N = 800$ ,  $k = 1/\sqrt{3}$ ,  $\alpha = \beta = c = 1$ ,  $\gamma = 0.1$ ,  $\epsilon = 0.001$ ,  $\Delta t = 0.01$  and  $\Delta T = \epsilon \Delta t$ . We see that the solution agrees well to leading order and this agreement is improved with the addition of higher order corrections. . . . . 89

5.2 A comparison of the original Boussinesq-Ostrovsky equation (5.1) (solid, blue) at  $t = 1/\epsilon$ , for the weakly nonlinear solution including leading order (dashed, red),  $O(\sqrt{\epsilon})$  (dash-dot, black) and  $O(\epsilon)$  (dotted, green) corrections, for (a)  $d = 1$  and (b)  $d = 7$ . Parameters are  $L = 40$ ,  $N = 800$ ,  $k = 1/\sqrt{3}$ ,  $\alpha = \beta = c = 1$ ,  $\gamma = 0.5$ ,  $\epsilon = 0.001$ ,  $\Delta t = 0.01$  and  $\Delta T = \epsilon \Delta t$ . We see that the solution agrees well to leading order and this agreement is improved with the addition of higher order corrections. . . . . 89

5.3 A comparison of error curves for varying values of  $\epsilon$ , at  $t = 1/\epsilon$ , for the weakly nonlinear solution including leading order (upper, blue),  $O(\sqrt{\epsilon})$  (middle, red) and  $O(\epsilon)$  (lower, black) corrections, for (a)  $d = 1$  and (b)  $d = 7$ . Parameters are  $L = 40$ ,  $N = 800$ ,  $k = 1/\sqrt{3}$ ,  $\alpha = \beta = c = 1$ ,  $\gamma = 0.1$ ,  $\Delta t = 0.01$  and  $\Delta T = \epsilon \Delta t$ . We see that the inclusion of more terms in the expansion increases the accuracy, and that the errors increase for larger values of  $d$ . . . . . 90

5.4 A comparison of error curves for varying values of  $\epsilon$ , at  $t = 1/\epsilon$ , for the weakly nonlinear solution including leading order (upper, blue),  $O(\sqrt{\epsilon})$  (middle, red) and  $O(\epsilon)$  (lower, black) corrections, for (a)  $d = 1$  and (b)  $d = 7$ . Parameters are  $L = 40$ ,  $N = 800$ ,  $k = 1/\sqrt{3}$ ,  $\alpha = \beta = c = 1$ ,  $\gamma = 0.5$ ,  $\Delta t = 0.01$  and  $\Delta T = \epsilon \Delta t$ . We see that the inclusion of more terms in the expansion increases the accuracy, and that the errors increase for larger values of  $d$ . The upper and lower curves are steeper for smaller values of  $d$ , and tend to their theoretical values as  $d$  increases. . . . . 90

5.5 A comparison of the original Boussinesq-Ostrovsky equation (5.1) (solid, blue) at  $t = 1/\epsilon$ , for the weakly nonlinear solution including leading order (dashed, red),  $O(\sqrt{\epsilon})$  (dash-dot, black) and  $O(\epsilon)$  (dotted, green) corrections, for (a)  $d = 1$  and (b)  $d = 7$ . Parameters are  $L = 40$ ,  $N = 800$ ,  $k = 1/\sqrt{3}$ ,  $\alpha = \beta = c = 2$ ,  $\gamma = 0.1$ ,  $\epsilon = 0.001$ ,  $\Delta t = 0.01$  and  $\Delta T = \epsilon \Delta t$ . We see that the solution agrees well to leading order and this agreement is improved with the addition of higher order corrections. . . . . 93

5.6 A comparison of the original Boussinesq-Ostrovsky equation (5.1) (solid, blue) at  $t = 1/\epsilon$ , for the weakly nonlinear solution including leading order (dashed, red),  $O(\sqrt{\epsilon})$  (dash-dot, black) and  $O(\epsilon)$  (dotted, green) corrections, for (a)  $d = 1$  and (b)  $d = 7$ . Parameters are  $L = 40$ ,  $N = 800$ ,  $k = 1/\sqrt{3}$ ,  $\alpha = \beta = c = 2$ ,  $\gamma = 0.5$ ,  $\epsilon = 0.001$ ,  $\Delta t = 0.01$  and  $\Delta T = \epsilon \Delta t$ . We see that the solution agrees well to leading order and this agreement is improved with the addition of higher order corrections. . . . . 93

5.7 A comparison of error curves for varying values of  $\epsilon$ , at  $t = 1/\epsilon$ , for the weakly nonlinear solution including leading order (upper, blue),  $O(\sqrt{\epsilon})$  (middle, red) and  $O(\epsilon)$  (lower, black) corrections, for (a)  $d = 1$  and (b)  $d = 7$ . Parameters are  $L = 40$ ,  $N = 800$ ,  $k = 1/\sqrt{3}$ ,  $\alpha = \beta = c = 2$ ,  $\gamma = 0.1$ ,  $\Delta t = 0.01$  and  $\Delta T = \epsilon \Delta t$ . We see that the inclusion of more terms in the expansion increases the accuracy, and that the errors increase for larger values of  $d$ . . . . . 94

- 5.8 A comparison of error curves for varying values of  $\epsilon$ , at  $t = 1/\epsilon$ , for the weakly nonlinear solution including leading order (upper, blue),  $O(\sqrt{\epsilon})$  (middle, red) and  $O(\epsilon)$  (lower, black) corrections, for (a)  $d = 1$  and (b)  $d = 7$ . Parameters are  $L = 40$ ,  $N = 800$ ,  $k = 1/\sqrt{3}$ ,  $\alpha = \beta = c = 2$ ,  $\gamma = 0.5$ ,  $\Delta t = 0.01$  and  $\Delta T = \epsilon \Delta t$ . We see that the inclusion of more terms in the expansion increases the accuracy, and that the errors increase for larger values of  $d$ . The upper and lower curves are steeper for smaller values of  $d$ , and tend to their theoretical values as  $d$  increases. . . . . 94

# List of Tables

3.1	Predictions on the number of solitons present in the transmitted wave field in the delaminated section of the bar, for various choices of $n$ and $k$ .	37
3.2	Comparison of lead soliton amplitude as predicted from the IST with the numerically calculated values from both numerical schemes, for various choices of $n$ and $k$ .	39
4.1	Comparison of numerically calculated soliton amplitudes in the delaminated area for both layers with the predicted value using the IST, for zero mean ( $\sigma = 1$ ) and non-zero mean ( $\sigma = 0$ ) initial conditions.	69
5.1	Maximum absolute error scaling parameters for the leading order weakly nonlinear solution for the initial condition in (5.46). The domain lengths and parameters are $\alpha = \beta = c = 1$ , $L = 40$ and $k = 1/\sqrt{3}$ .	91
5.2	Maximum absolute error scaling parameters for the weakly nonlinear solution up to $O(\sqrt{\epsilon})$ for the initial condition in (5.46). The domain lengths and parameters are $\alpha = \beta = c = 1$ , $L = 40$ and $k = 1/\sqrt{3}$ .	91
5.3	Maximum absolute error scaling parameters for the weakly nonlinear solution up to $O(\epsilon)$ for the initial condition in (5.46). The domain lengths and parameters are $\alpha = \beta = c = 1$ , $L = 40$ and $k = 1/\sqrt{3}$ .	91
5.4	Intercept point of error curves, in terms of $\epsilon$ , representing the maximum value of $\epsilon$ at which the inclusion of $O(\sqrt{\epsilon})$ or $O(\epsilon)$ terms will decrease the error.	92
5.5	Maximum absolute error scaling parameters for the leading order weakly nonlinear solution for the initial condition in (5.46). The domain lengths and parameters are $\alpha = \beta = c = 2$ , $L = 40$ and $k = 1/\sqrt{3}$ .	95
5.6	Maximum absolute error scaling parameters for the weakly nonlinear solution up to $O(\sqrt{\epsilon})$ for the initial condition in (5.46). The domain lengths and parameters are $\alpha = \beta = c = 2$ , $L = 40$ and $k = 1/\sqrt{3}$ .	95
5.7	Maximum absolute error scaling parameters for the weakly nonlinear solution up to $O(\epsilon)$ for the initial condition in (5.46). The domain lengths and parameters are $\alpha = \beta = c = 2$ , $L = 40$ and $k = 1/\sqrt{3}$ .	95
5.8	Intercept point of error curves in Figures 5.7 and 5.8, in terms of $\epsilon$ , representing the maximum value of $\epsilon$ at which the inclusion of $O(\sqrt{\epsilon})$ or $O(\epsilon)$ terms will decrease the error.	96



# Abbreviations

<b>cRB</b>	Coupled Regularised Boussinesq
<b>DDE</b>	Doubly Dispersive Equation
<b>FFT</b>	Fast Fourier Transform
<b>FPU</b>	Fermi-Pasta-Ulam
<b>FWHM</b>	Full Width at Half Magnitude
<b>IST</b>	Inverse Scattering Transform
<b>KdV</b>	Korteweg-de Vries
<b>NLS</b>	Nonlinear Schrödinger
<b>ODE</b>	Ordinary Differential Equation
<b>PCP</b>	Polychloroprene
<b>PMMA</b>	Polymethylmethacrylate
<b>PS</b>	Polystyrene
<b>SSPRK</b>	Strong Stability Preserving Runge-Kutta



*For my wife, Kerry, the love of my life. Without her support and guidance this would not have been possible.*



## *Publications*

The results of this thesis are partially summarised in the following papers:

- (i) K. R. Khusnutdinova and M. R. Tranter, *Modelling of nonlinear wave scattering in a delaminated elastic bar*, P. Roy. Soc. A **471** (2183), 20150584 (2015).
- (ii) K. R. Khusnutdinova and M. R. Tranter, *On radiating solitary waves in bi-layers with delamination and coupled Ostrovsky equations*, Chaos **27**, 013112 (2017).
- (iii) K. R. Khusnutdinova and M. R. Tranter, *Scattering of bulk strain solitary waves in bi-layers with delamination*, Procedia Eng. **199**, 1533-1538 (2017).



# Chapter 1

## Introduction

The study of nonlinear waves is an actively growing field in modern mathematics. Studies of nonlinear waves and their effects have taken place in nonlinear optics, mathematical biology, fluid and solid mechanics (see, for example, [1–8] and references therein). For fluids and elastic solids we often consider the cases with weak nonlinearity and dispersion, in particular if there is a balance between these two quantities then stable localised solutions can exist, such as solitons and wave packet solutions of the Ostrovsky equation [9], studied in [10–12]. In what follows we will refer to these solutions as Ostrovsky wave packets, for brevity.

The first observation of solitons dates back to 1834, when John Scott Russell observed “the great wave of translation” along the Edinburgh-Glasgow canal and followed the wave on horseback for several miles, noting that the shape of the wave did not change. He reported this observation to the British Association for the Advancement of Science in 1844 [13]. It was not until several years later that the first mathematical models of this phenomena were derived, initially by Boussinesq in 1872 [14] and 1877 [15], Lord Rayleigh in 1876 [16] and the famous work of Korteweg & de Vries in 1895 [17].

Much work was completed using these equations in the context of fluids, but they appeared once more in the context of the Fermi-Pasta-Ulam problem in the studies of solids. In 1955 they considered a chain of identical equidistant particles connected by weakly nonlinear springs, known as the Fermi-Pasta-Ulam (FPU) lattice model, and showed that there was an absence of equipartition of energy among the modes of the harmonic approximation [18]. This observation motivated Zabusky and Kruskal to consider the long-wave approximation to the problem in their groundbreaking work in 1965 [19]. They showed that Boussinesq and Korteweg-de Vries (KdV) equations arise in this new setting and numerical studies of solutions of the KdV equation followed [19]. These

numerical studies showed that localised stable travelling waves of permanent form exist in these equations; they were described as ‘solitons’.

The discovery of solitons as travelling waves of permanent form is intrinsically linked with a second fundamental discovery – the Inverse Scattering Transform (IST) for the KdV equation. The IST is a method for solving a large class of initial-value problems on the infinite line, as found by Gardner, Greene, Kruskal and Miura [20]. A further work by the same authors showed that solitons, when present, constitute the main part of the long-time asymptotics of initial-value problems for localised initial data [21]. Solitons have therefore proven to be of importance in physical settings, across all scales [22–25]. Furthermore, it has been shown that the IST can be used to help develop efficient numerical approaches to solving the KdV equation [26], as well as another equation that is integrable by the IST – the Nonlinear Schrödinger (NLS) equation [27–29].

Recently, the IST has been used in studies of the scattering of long longitudinal bulk strain solitons in a symmetric perfectly bonded layered bar with delamination [30]. Long longitudinal bulk strain solitary waves were experimentally observed in various elastic waveguides, including rods, bars, plates and shells, and modelled using Boussinesq-type equations [25, 31–33]. The exceptional stability of bulk strain solitons [34, 35] makes them an attractive candidate for the introscopy of layered structures, in addition to existing methods [36, 37].

The modelling of longitudinal wave propagation can be extended to layered bars with a soft bonding between the layers, instead of a perfect bond. The governing equation is no longer a single Boussinesq equation; it is replaced by coupled regularised Boussinesq (cRB) equations [38]. In this case, it has been shown that if the layers have similar properties and the bonding is sufficiently soft, bulk strain solitons do not exist in this case – instead they are replaced by radiating solitary waves, that is a solitary wave with a co-propagating one-sided oscillatory tail [38]. Such waves have also been observed experimentally [36]. If the layers have distinctly different properties, then the radiating solitary wave is replaced by an Ostrovsky wave packet [39]. These nonlinear waves originally arose in the context of oceanic waves, when the effect of background rotation is taken into account [9] and many studies have taken place to describe their effects, both in the context of the single Ostrovsky equation [10–12] and for the cRB equations derived in the context of an inviscid, incompressible, density stratified fluid with oceanic boundary conditions, with no background shear [40] and with background shear included [41]. The description of the weakly nonlinear solution to such a scattering problem is yet to be fully understood, but we will provide some results for an initial value problem.

This thesis will discuss the modelling of longitudinal wave scattering in layered waveguides and the development of an efficient semi-analytical numerical technique for solving the scattering problem using the derived KdV and Ostrovsky equations [42, 43]. In Chapter 2 we overview the existing literature for models describing longitudinal wave propagation in layered structures. Firstly we discuss the nonlinear elasticity model used to describe the propagation of longitudinal waves in a layered elastic bar with a perfect bond [30]. This system is governed by Boussinesq equations in each section. We introduce an FPU chain model and discuss how this can be extended to a system of coupled FPU chains. This can be compared to the layered lattice model used in [38], which describes the propagation of longitudinal waves in a layered waveguide with a soft bond between the layers. Finally we review the existing results for scattering problems, including experimental results for layered bars [31, 33, 44]. We also discuss the initial value problem for the Boussinesq, Boussinesq-type equation with an Ostrovsky term, and coupled Boussinesq equations, with an overview of existing results for these equations [39, 45, 46].

Next we discuss the modelling of long longitudinal bulk strain waves in a perfectly bonded layered elastic waveguide in Chapter 3. This uses the nonlinear elasticity model introduced in Chapter 2. We review a weakly nonlinear solution to the problem constructed in [30] and show that the derived equations for leading order transmitted and reflected strain waves are governed by KdV equations, with reflection and transmission coefficients defined by the conditions on the boundary between the sections of the bar. This weakly nonlinear solution is used to develop a semi-analytical numerical technique, which is compared to direct numerical modelling of the original problem formulation, and to theoretical predictions based upon the weakly nonlinear solution. These numerical simulations show that the semi-analytical method has a very good agreement with the direct numerical simulations, and can be computed significantly faster [42]. We extend this to the case of finite delamination and show that, given the relevant parameters of the problem, we can predict the length of the delamination from the resulting wave in the second bonded section of the bar.

In Chapter 4 we consider the case of a layered bar with a soft bond between the layers, using an extension of the coupled FPU chain model introduced in Chapter 2, derived in [38]. We assume that the materials in the layers have similar elastic properties, so that their characteristic speeds are close. The weakly nonlinear solution of the initial-value problem has been constructed in [39, 47], however here we study the scattering problem. The model in this case leads to cRB equations in the bonded sections of the bar and uncoupled Boussinesq equations in the delaminated sections of the bar. As with the previous work for a perfectly bonded bar, we seek a weakly nonlinear solution to the problem and derive coupled Ostrovsky equations to describe the leading order

strain waves in the bonded sections of the bar, and KdV equations in the delaminated sections of the bar. We again compare the semi-analytical method to the direct numerical simulations and show that the agreement between the regimes is very good. This is extended to the case of finite delamination and we show that the shape and structure of the resulting wave in the second bonded region can be used to determine the length of the delamination region and an approximation of its position.

In Chapter 5 we consider a Boussinesq-type equation with the Ostrovsky term, an extension of the Boussinesq equation derived in Chapter 2. If we derive a weakly nonlinear solution to this equation using the same technique as Chapter 3 or Chapter 4 we can describe the leading order right- and left-propagating waves using the Ostrovsky equation. This model can arise naturally for long waves in shallow water when the Coriolis effect is taken into account. It can be shown that the classical solutions of the Ostrovsky equation have zero mean, therefore the initial condition for this equation must have zero mean. This suggests we need to use a different approach. It can be shown that the mean value of this equation oscillates in time [46, 48]. We therefore subtract this mean value from the Boussinesq-type equation and construct a weakly nonlinear solution in increasing powers of  $\sqrt{\epsilon}$ , where  $\epsilon$  is the small amplitude parameter, in contrast to the Boussinesq equation where the solution was for increasing powers of  $\epsilon$ . The solution of the Boussinesq-type equation is compared to the weakly nonlinear solution with an increasing number of terms included from the weakly nonlinear solution, in increasing powers of  $\sqrt{\epsilon}$  and we show that the error agrees with the next order of the expansion as expected. Furthermore, we can estimate the value of  $\epsilon$  required to ensure the solution is sufficiently “weakly nonlinear” i.e. that the value of  $\epsilon$  is small enough so that the inclusion of more terms in the expansion results in a more accurate solution. This result is tested for non-unity coefficients in the equation and we find that the same results hold, with better adherence to the theoretical estimates than the previous case with unity coefficients.

The final chapter is dedicated to a summary of the results of the previous chapters and a discussion of future work that could be performed in this field.

In Appendices A - C we present the numerical techniques used to solve the direct numerical problem in two sections, then three or more sections, and finally the semi-analytical techniques using the SSPRK(5,4) scheme for KdV equations and pseudospectral techniques for KdV and Ostrovsky equations, respectively.

## Chapter 2

# Modelling Wave Propagation in Solids

In this chapter we present the models used for describing the propagation of longitudinal bulk strain waves in layered waveguides, with either a perfect bond between the layers or a sufficiently soft bond. We start from the viewpoint of the Fermi-Pasta-Ulam (FPU) model and discuss how the Boussinesq equation can be derived from such a model. This model is compared to the model derived using nonlinear elasticity theory, showing that the equations derived in these methods are of the same type. This modelling is then extended to a system of coupled FPU chains as an example of a system for a layered waveguide, following [47]. A more complicated lattice model taking into account all degrees of freedom of a realistic waveguide was derived in [38], and the coupled FPU model is an idealisation of this complicated model.

### 2.1 Fermi-Pasta-Ulam Model

The first model we consider is the FPU chain model in its original formulation [18]. Let us consider a chain of equidistant particles connected by weakly nonlinear springs to their nearest neighbours, where the displacement of the  $n$ -th particle from the equilibrium is denoted by  $u_n$ . Refer to the diagram in Figure 2.1 for a graphical representation of this problem. We assume that both sides of the chain are clamped at equilibrium. If we have a chain of  $N + 1$  particles we have  $u_0 = u_N = 0$ . It is assumed that the equilibrium distance between particles is  $a$ .

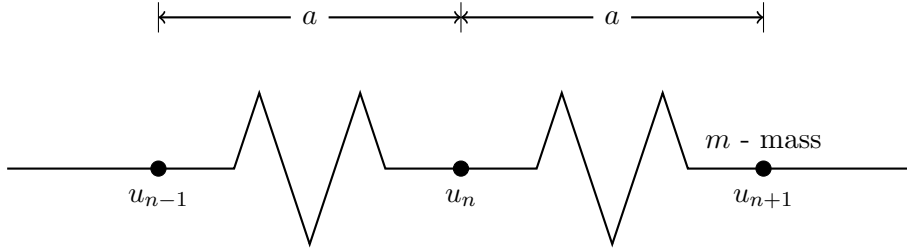


FIGURE 2.1: The FPU model for a series of equidistant particles connected by weakly nonlinear springs.

Our aim is to describe the displacement of these particles from their rest state. The kinetic energy of the chain,  $T$ , and the potential energy of the chain,  $U$ , are given by

$$T = \sum_n \frac{m \dot{u}_n^2}{2}, \quad U = \sum_n \left( \frac{k}{2} (u_{n+1} - u_n)^2 + \frac{\alpha}{3} (u_{n+1} - u_n)^3 \right), \quad (2.1)$$

respectively, where  $k$  is the linear spring constant and  $\alpha$  can be thought of as a nonlinear spring constant. As usual, the Lagrangian of the system is  $L = T - U$ , therefore the equations of motion are given by the Euler-Lagrange equations

$$\frac{d}{dt} \left( \frac{\partial L}{\partial \dot{u}_n} \right) - \frac{\partial L}{\partial u_n} = 0, \quad (2.2)$$

leading to the system

$$m \ddot{u}_n = (u_{n+1} - 2u_n + u_{n-1}) [k + \alpha (u_{n+1} - u_{n-1})]. \quad (2.3)$$

This is a discrete system of equations describing the motion of the particles in the chain. This model was extended by Zabusky and Kruskal to derive a continuous model for the displacements, rather than a discrete model [19]. Following their work we consider the continuum approximation, assuming that

$$u_n(t) = u(x_n, t) = u(na, t), \quad u_{n\pm 1} = u(x_n \pm a, t), \quad (2.4)$$

where the displacement field  $u$  varies slowly. This justifies the use of the Taylor expansion for the terms in (2.3) and therefore allows us to convert this discrete model to a continuous model. If we use the Taylor expansion

$$u_{n\pm 1}(t) = u(x_n, t) \pm a u'(x_n, t) + \frac{a^2}{2} u''(x_n, t) \pm \frac{a^3}{6} u'''(x_n, t) + \frac{a^4}{24} u''''(x_n, t) + \dots, \quad (2.5)$$

and substitute (2.5) into (2.3), we obtain the following differential equation (truncating the series to exclude higher-order terms)

$$mu_{tt} = ka^2u_{xx} + 2\alpha a^3u_xu_{xx} + \frac{ka^4}{12}u_{xxxx}. \quad (2.6)$$

This is a Boussinesq equation and can be used to describe the propagation of long waves in this chain model. We rescale the equation to the form

$$u_{tt} - c^2u_{xx} = \epsilon c^2(u_xu_{xx} + \delta^2u_{xxxx}), \quad (2.7)$$

where

$$c^2 = \frac{ka^2}{m}, \quad \epsilon = \frac{2\alpha a}{k}, \quad \delta^2 = \frac{a^2}{12\epsilon}.$$

We can regularise (2.7) using the asymptotic relation  $u_{ttxx} = c^2u_{xxxx} + O(\epsilon)$  to obtain

$$u_{tt} - c^2u_{xx} = \epsilon c^2\left(u_xu_{xx} + \frac{\delta^2}{c^2}u_{ttxx}\right). \quad (2.8)$$

This form of the equation is easier to solve numerically and will be used in our later work. An asymptotic multiple-scales expansion can be constructed to obtain the leading order left- and right-propagating waves to the Boussinesq equation (2.8). Following the work of Zabusky and Kruskal, we consider the right-propagating wave and construct an asymptotic multiple-scales expansion of the form

$$u = f(\xi, T) + \epsilon u^{(1)}(\xi, \eta, T) + \dots, \quad (2.9)$$

where  $\xi = x - ct$ ,  $\eta = x + ct$  and  $T = ct$  is the slow time. Substituting (2.9) into (2.8), we obtain

$$-4c^2u_{\xi\eta}^{(1)} = 2cf_{\xi T} + c^2f_{\xi}f_{\xi\xi} + c^2\delta^2f_{\xi\xi\xi\xi} = F(\xi, T), \quad (2.10)$$

where we note that  $F$  is a function of  $\xi$  and  $T$  only. Therefore  $u^{(1)}$  will grow linearly in  $\eta = x + ct$  unless  $F \equiv 0$ , leading to the equation

$$2cf_{\xi T} + c^2f_{\xi}f_{\xi\xi} + c^2\delta^2f_{\xi\xi\xi\xi} = 0. \quad (2.11)$$

We introduce  $g = f_{\xi}$  and the rescaling  $\tilde{q} = \alpha g$ ,  $\tilde{\xi} = \beta\xi$  and  $\tilde{T} = \gamma T$ , so we have

$$\gamma\tilde{q}_{\tilde{T}} + \frac{c\beta}{2\alpha}\tilde{q}\tilde{q}_{\tilde{\xi}} + \frac{c\delta^2}{2}\beta^3\tilde{q}_{\tilde{\xi}\tilde{\xi}\tilde{\xi}} = 0. \quad (2.12)$$

To obtain the KdV equation in the form presented in [19] (replacing  $\delta^2$  with  $\lambda^2$ ), we must solve the system

$$\frac{c\beta}{2\alpha\gamma} = 1, \quad \frac{c\delta^2\beta^3}{2\gamma} = \lambda^2. \quad (2.13)$$

We equate the coefficients of (2.12) with those in [19] to obtain the solution for  $\alpha$ ,  $\beta$  and  $\gamma$ , so we have

$$\alpha = \frac{c}{2\gamma}, \quad \beta = 1, \quad \gamma = \frac{c\delta^2}{2\lambda^2}. \quad (2.14)$$

This corresponds to the scaling

$$\tilde{q} = \frac{c}{2\gamma}q, \quad \tilde{\xi} = \xi, \quad \text{and} \quad \tilde{T} = \frac{c\delta^2}{2\lambda^2}T. \quad (2.15)$$

In [19] Zabusky and Kruskal showed that solitons are generated from a cosine initial condition, where a number of solitons are produced for a given value of  $\delta^2$ . The interaction of the solitons was shown to be elastic i.e. there was no discernible change in amplitude after interaction of two solitons, the only evidence of their interaction was a phase shift. This led to the phenomenon they refer to as “recurrence”, where the solitons converge at a common point and the initial condition is almost reconstructed. They showed that at subsequent recurrence times the reconstruction is not as good as the first recurrence. Explicitly they solved the equation

$$u_t + uu_x + \delta^2 u_{xxx} = 0, \quad (2.16)$$

where  $\delta = 0.022$ . The initial condition was taken as  $u(x, 0) = \cos(\pi x)$ . Initially the dispersive term is small and therefore the behaviour is governed by the nonlinear term. Zabusky and Kruskal showed that this leads to the formation of a discontinuity at the time  $t = t_b = 1/\pi$  [19]. We reproduce the figure from [19] in Figure 2.2, which shows the initial condition (dashed, black), the solution at the breaking time (dashed, red) and the solution at  $t = 3.6t_b$  (solid, blue), where we can clearly see eight solitons. The small perturbations present at  $t = t_b$  are due to the dispersive term becoming larger and therefore balancing the nonlinearity. This solution was found using the pseudospectral technique described in Appendix C.1.

It was later shown in the works of Gardner, Greene, Kruskal and Miura that the number of solitons generated from a localised initial condition is determined by the parameters of the equation and the amplitude of the initial pulse [20, 21]. For a periodic initial condition, instead of a localised initial condition, some recent results have shown that the number of solitons generated by the initial condition can be approximated using the Wentzel-Kramers-Brillouin method [49] and these results have been compared to physical experiments in shallow water with good agreement, as well as confirming the results observed by Zabusky and Kruskal [50].

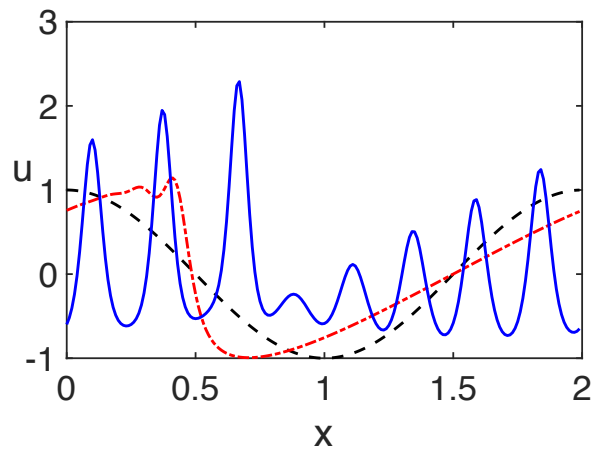


FIGURE 2.2: The solution to the KdV equation (2.16) where  $\delta = 0.022$ , where we have the initial condition (black, dashed), the solution at  $t = t_b$  (red, dash-dot) and the solution at  $t = 3.6t_b$  (blue, solid). We clearly see eight solitons generated from this initial condition.

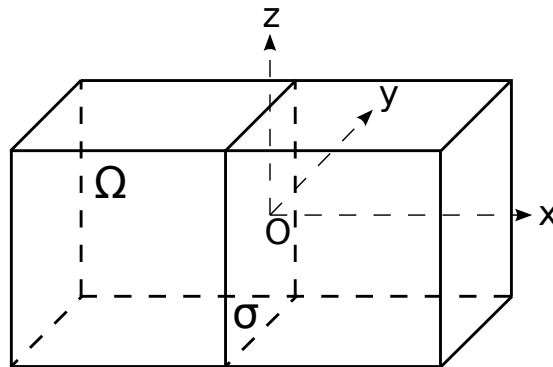


FIGURE 2.3: Model of an elastic bar with rectangular cross section.

## 2.2 Doubly Dispersive Equation Model

We now consider another model for describing the propagation of a long longitudinal bulk wave in a symmetric elastic layered bar, using nonlinear elasticity theory [30]. We briefly outline the method here. We introduce the coordinate frame and structure of the bar in Figure 2.3.

We describe the model using nonlinear dynamic elasticity theory and, once the model is derived, we compare the model to the FPU model to obtain lattice parameters in terms of the material parameters.

### 2.2.1 Derivation

Let us consider an isotropic elastic bar of rectangular cross section  $\sigma$ , where we have  $\sigma = \{-a \leq y \leq a; -b \leq z \leq b\}$ . Let us assume that the bar is initially in an equilibrium state. We introduce the Lagrangian coordinates  $(x, y, z)$ , where  $Ox$  is directed along the bar in the centre of the cross section. We consider the problem in the framework of nonlinear dynamic elasticity with action functional

$$S = \int_{t_0}^{t_1} \int_{\Omega} \mathcal{L}(U, U_t, U_x, \dots, x, t) \, d\Omega \, dt, \quad (2.17)$$

where  $\mathcal{L}$  is the Lagrangian density per unit volume,  $t$  is time,  $\Omega$  is the space domain occupied by the waveguide and  $U = \{u, v, w\}$  is the displacement vector in coordinates  $(x, y, z)$  [31]. The Lagrangian density in material variables is the difference of kinetic energy density  $K$  and potential energy density  $\Pi$ , namely

$$\mathcal{L} = K - \Pi = \frac{\rho}{2} \left( \frac{\partial U}{\partial t} \right)^2 - \rho \Pi(I_k), \quad (2.18)$$

where  $\rho$  is the density and  $I_k = I_k(C)$  are the invariants of the Cauchy-Green deformation tensor

$$C = \left[ \nabla U + (\nabla U)^T + \nabla U \cdot (\nabla U)^T \right]. \quad (2.19)$$

Explicitly the invariants are given by

$$I_1 = \text{tr } C, \quad I_2 = \frac{1}{2} \left[ (\text{tr } C)^2 - \text{tr } C^2 \right], \quad I_3 = \det C. \quad (2.20)$$

We use Murnaghan's model for  $\Pi$  and take the energy expansion up to the 5-constant approximation i.e.

$$\Pi = (\lambda + 2\mu) \frac{I_1^2}{2} - 2\mu I_2 + (l + 2m) \frac{I_1^3}{3} - 2m I_1 I_2 + n I_3 + \dots, \quad (2.21)$$

where  $\lambda$  and  $\mu$  are Lamé's coefficients and  $l, m, n$  are Murnaghan's moduli.

We want to simplify the problem to the case where the only nonlinear equation is for the longitudinal displacements. We use the planar cross-section hypothesis and apply approximate relations for transverse displacements in terms of the longitudinal strain components as

$$u \approx u(x, t), \quad v \approx -y\nu u_x, \quad w \approx -z\nu u_x, \quad (2.22)$$

where

$$\nu = \frac{\lambda}{2(\lambda + \mu)} \quad (2.23)$$

is Poisson's ratio [51, 52]. Similar relations exist in the case of a cylindrical bar of circular cross section in [53–55].

Using relations (2.22) we obtain approximate expressions for the invariants, valid for small amplitude long longitudinal elastic waves, and therefore we have simplified expressions for  $K$  and  $\Pi$  as

$$K = \frac{1}{2}\rho(u_t^2 + v_t^2 + w_t^2) = \frac{\rho}{2}[u_t^2 + (y^2 + z^2)\nu^2 u_{xt}^2] + \dots, \quad (2.24)$$

$$\Pi = \frac{1}{2}\left(Eu_x^2 + \frac{\beta}{3}u_x^3 + \mu\nu^2(y^2 + z^2)u_{xx}^2\right). \quad (2.25)$$

Here the nonlinearity coefficient  $\beta$  depends on the Murnaghan's moduli  $l, m, n$ , Young's modulus  $E = \mu(3\lambda + 2\mu)/(\lambda + \mu)$  and Poisson's ratio  $\nu$ . This expression is given by

$$\beta = 3E + 2l(1 - 2\nu)^3 + 4m(1 + \nu)^2(1 - 2\nu) + 6n\nu^2. \quad (2.26)$$

With expressions (2.17) and (2.18), we can obtain the Euler-Lagrange equation

$$\frac{\partial \mathcal{L}_\sigma}{\partial u} - \left(\frac{\partial}{\partial t} \frac{\partial \mathcal{L}_\sigma}{\partial u_t} + \frac{\partial}{\partial x} \frac{\partial \mathcal{L}_\sigma}{\partial u_x}\right) + \frac{\partial^2}{\partial x^2} \frac{\partial \mathcal{L}_\sigma}{\partial u_{xx}} + \frac{\partial^2}{\partial x \partial t} \frac{\partial \mathcal{L}_\sigma}{\partial u_{xt}} + \dots = 0, \quad (2.27)$$

where  $L_\sigma = \int_\sigma L \, d\sigma$  is the Lagrangian density per unit length. Substituting (2.24) and (2.25) into (2.18) and then substituting this into (2.27), we obtain the so-called doubly dispersive equation (DDE) for long nonlinear longitudinal displacement waves in a bar of rectangular cross section

$$u_{tt} - c^2 u_{xx} = \frac{\beta}{\rho} u_x u_{xx} + \frac{J\nu^2}{\sigma} (u_{tt} - c_1^2 u_{xx})_{xx}. \quad (2.28)$$

Here we have linear longitudinal wave velocity  $c = \sqrt{E/\rho}$ , linear shear wave velocity  $c_1 = c/\sqrt{2(1+\nu)}$ , and the polar moment of inertia of the rectangular cross section  $\sigma$ ,

$$J = \int_\sigma (y^2 + z^2) \, d\sigma = \frac{4ab(a^2 + b^2)}{3}.$$

Applying the change of variables

$$\tilde{t} = \frac{t}{T}, \quad \tilde{x} = \frac{x}{X}, \quad \tilde{u} = \frac{u}{U}, \quad (2.29)$$

where

$$cT = X, \quad U = \frac{-12\epsilon EX}{\beta}, \quad X = \sqrt{\frac{J\nu^2}{2\epsilon\sigma} \left(1 - \frac{c_1^2}{c^2}\right)}, \quad (2.30)$$

we can rewrite the equation as a regularised Boussinesq equation

$$u_{tt} - u_{xx} = \epsilon [-12u_x u_{xx} + u_{ttxx}], \quad (2.31)$$

where we have used the asymptotic relation  $u_{ttxx} = u_{xxxx} + O(\epsilon)$ .

### 2.2.2 Comparison of Equations

We now compare equations (2.8) and (2.31) to show that there is a formal correspondence between the derived equations. This allows for the lattice parameters to be expressed in terms of the material parameters.

Therefore, we compare the coefficients to uniquely find the relations

$$a^2 = \frac{12J\nu^2 (c^2 - c_1^2)}{\sigma c^2}, \quad k = \frac{c^2}{a^2}, \quad \alpha = \frac{\beta}{2\rho a^3}. \quad (2.32)$$

## 2.3 Coupled FPU Chains

We now consider an extension of the FPU model in Section 2.1 in the case where we have two FPU chains that are weakly coupled, as discussed in [47]. This model can be considered as a simplified version of the model for a layered waveguide, in contrast to the single chain considered earlier. We present a representation of this in Figure 2.4.

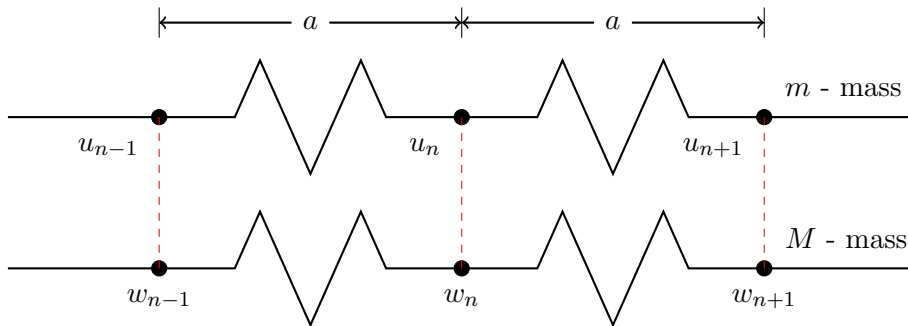


FIGURE 2.4: The coupled FPU model for a series of equidistant particles connected by weakly nonlinear springs.

The derivation can be followed in the same way as Section 2.1, that is we calculate the kinetic energy and potential energy in the system. The expression for the kinetic energy is the same as for the single chain, that is we add together the expressions for  $K$  in each chain to obtain the expression for the system. The expression for  $\Pi$  is found in the same

way, but with the addition of a coupling term. Explicitly we have

$$U = \sum_n = \left[ \frac{\alpha}{2} (u_{n+1} - u_n)^2 + \frac{\beta}{3} (u_{n+1} - u_n)^3 + \frac{\tilde{\alpha}}{2} (w_{n+1} - w_n)^2 + \frac{\tilde{\beta}}{3} (w_{n+1} - w_n)^3 + \frac{\gamma}{2} (u_n - w_n)^2 \right], \quad (2.33)$$

where  $\alpha, \tilde{\alpha}$  can be thought of as spring constants in each chain and  $\beta, \tilde{\beta}$  are nonlinearity coefficients for each chain, while  $\gamma$  is a coupling coefficient. The Lagrangian is calculated in the same way as before, that is  $L = T - U$ , and this Lagrangian is substituted into the Euler-Lagrange relations

$$\frac{d}{dt} \left( \frac{\partial L}{\partial \dot{u}_n} \right) - \frac{\partial L}{\partial u_n} = 0, \quad \frac{d}{dt} \left( \frac{\partial L}{\partial \dot{w}_n} \right) - \frac{\partial L}{\partial w_n} = 0, \quad (2.34)$$

to obtain a system of difference-differential equations taking the form

$$\begin{aligned} m\ddot{u}_n &= (u_{n+1} - 2u_n + u_{n-1}) (\alpha + \beta (u_{n+1} - u_{n-1})) - \gamma (u_n - w_n), \\ M\ddot{w}_n &= (w_{n+1} - 2w_n + w_{n-1}) (\tilde{\alpha} + \tilde{\beta} (w_{n+1} - w_{n-1})) + \gamma (u_n - w_n). \end{aligned} \quad (2.35)$$

As before, we can use a Taylor expansion for the derived difference-differential equations in each chain, about the equilibrium point, to obtain differential equations in terms of  $u$  and  $w$  as continuous functions. Following [47], we take the Taylor expansion (2.5) and a similar expansion for  $w_n$ , and truncate the expansion so that we obtain the coupled Boussinesq equations in the form

$$\begin{aligned} u_{tt} - c_0^2 u_{xx} &= E_1 u_x u_{xx} + E_2 u_{ttxx} - E_3 (u - w), \\ w_{tt} - \tilde{c}_0^2 w_{xx} &= \tilde{E}_1 w_x w_{xx} + \tilde{E}_2 w_{ttxx} + \tilde{E}_3 (u - w), \end{aligned} \quad (2.36)$$

where the coefficients are

$$\begin{aligned} c_0^2 &= \frac{\alpha a^2}{m}, & E_1 &= \frac{2\beta a^3}{m}, & E_2 &= \frac{a^2}{12}, & E_3 &= \frac{\gamma}{m}, \\ \tilde{c}_0^2 &= \frac{\tilde{\alpha} a^2}{M}, & \tilde{E}_1 &= \frac{2\tilde{\beta} a^3}{M}, & \tilde{E}_2 &= \frac{a^2}{12}, & \tilde{E}_3 &= \frac{\gamma}{M}. \end{aligned} \quad (2.37)$$

This is a simple model for the displacements in a coupled system of equations and can be thought of as a toy model for wave propagation in a layered waveguide. In our subsequent results, we use the more complex layered lattice model described in [38].

## 2.4 Weakly Nonlinear Solution of Initial Value Problem

The initial value problem for the Boussinesq and Boussinesq-type equation has appeared in many recent works. The validity of regularised models and proofs of local well-posedness and existence, in the context of water waves, has been studied in many works, for example [56–59] and references therein. Previous works showed the emergence of two KdV equations as a leading order approximation to the solution of Boussinesq-type equations, as well as some approximations for the higher-order corrections [6, 60–67].

In the following subsections we overview the initial value problem for the Boussinesq, Boussinesq-type equation with an Ostrovsky term, and coupled Boussinesq equations and discuss the results derived in the existing literature.

### 2.4.1 Initial Value Problem for Coupled Boussinesq Equations

Recent works relevant to the problems discussed in this thesis have been dedicated to constructing a weakly nonlinear solution to the initial value problem for a system of coupled Boussinesq equations on the infinite line [39], where it was assumed that the initial data is localised or sufficiently rapidly decaying. Explicitly they considered the problem

$$\begin{aligned} f_{tt} - f_{xx} &= \epsilon \left[ \frac{1}{2} (f^2)_{xx} + f_{ttxx} - \delta (f - g) \right], \\ g_{tt} - c^2 g_{xx} &= \epsilon \left[ \frac{\alpha}{2} (g^2)_{xx} + \beta g_{ttxx} + \gamma (f - g) \right], \end{aligned} \quad (2.38)$$

with initial data

$$\begin{aligned} f|_{t=0} &= F(x), & g|_{t=0} &= G(x), \\ f_t|_{t=0} &= V(x), & g_t|_{t=0} &= W(x). \end{aligned} \quad (2.39)$$

This form of the system (2.38) (with a mixed 4<sup>th</sup> order derivative instead of a 4<sup>th</sup> order spatial derivative) is preferable for numerical simulations as the short wave instability is suppressed [56, 68]. A further point to note is that, for the Boussinesq equation (i.e. setting  $\delta = \gamma = 0$ ), the form of the equation with the 4<sup>th</sup> order spatial derivative is integrable by the IST but the form with a mixed 4<sup>th</sup> order derivative is not integrable by the IST [1, 69]. There are two cases considered in [39], where the weakly nonlinear solution takes a different form dependent upon the value of  $c$ .

In the first case, when  $c - 1 = O(\epsilon)$ , it can be shown that the left- and right-propagating waves at leading order are described by coupled Ostrovsky equations (see [40, 41] for

their derivation in the context of water waves and [38] in the context of layered elastic waveguides). Introducing the fast characteristic variables  $\xi = x - t$  and  $\eta = x + t$ , and the slow time variable  $T = \epsilon t$ , the leading order right-propagating waves are described by

$$\begin{aligned} \left(2f_T^- + f^- f_\xi^- + f_{\xi\xi\xi}^-\right)_\xi &= \delta(f^- - g^-), \\ \left(2g_T^- + \frac{c^2 - 1}{\epsilon} g_\xi^- + \alpha g^- g_\xi^- + \beta g_{\xi\xi\xi}^-\right)_\xi &= \gamma(g^- - f^-), \end{aligned} \quad (2.40)$$

where  $f^-$  describes the right-propagating wave for the first equation and  $g^-$  for the second equation. Similarly, the leading order left-propagating waves are described by

$$\begin{aligned} (-2f_T^+ + f^+ f_\eta^+ + f_{\eta\eta\eta}^+)_\eta &= \delta(f^+ - g^+), \\ \left(-2g_T^+ + \frac{c^2 - 1}{\epsilon} g_\eta^+ + \alpha g^+ g_\eta^+ + \beta g_{\eta\eta\eta}^+\right)_\eta &= \gamma(g^+ - f^+), \end{aligned} \quad (2.41)$$

where  $f^+$  describes the left-propagating wave for the first equation and  $g^+$  for the second equation. As done in [39], higher-order corrections can be found in terms of the leading order solution.

In the second case, when  $c - 1 = O(1)$ , the left- and right-propagating waves at leading order are described by single Ostrovsky equations, which arise in the context of oceanic waves when the Coriolis effect is taken into account [9]. In this case the solitary wave solutions of the KdV equation cannot exist, and are instead replaced by a localised wave packet [70–73]. In contrast to the previous case, we introduce two sets of characteristic variables, one set for the first equation and another set for the second equation. Introducing  $\xi_1 = x - t$ ,  $\xi_2 = x - ct$ ,  $\eta_1 = x + t$ ,  $\eta_2 = x + ct$  and  $T = \epsilon T$ , the equations take the form [39]

$$\begin{aligned} \left(2f_T^- + f^- f_{\xi_1}^- + f_{\xi_1\xi_1\xi_1}^-\right)_{\xi_1} &= \delta f^-, & \left(2cg_T^- + \alpha g^- g_{\xi_2}^- + \beta c^2 g_{\xi_2\xi_2\xi_2}^-\right)_{\xi_2} &= \gamma g^-, \\ (-2f_T^+ + f^+ f_{\eta_1}^+ + f_{\eta_1\eta_1\eta_1}^+)_\eta &= \delta f^+, & (-2cg_T^+ + \alpha g^+ g_{\eta_2}^+ + \beta c^2 g_{\eta_2\eta_2\eta_2}^+)_\eta &= \gamma g^+, \end{aligned} \quad (2.42)$$

where the meaning of  $f^\pm$  and  $g^\pm$  is the same as the previous case. Following the method outlined in [39], higher order corrections can again be found in terms of the leading order. The weakly nonlinear expansion is substituted into the initial conditions (2.39) to obtain initial conditions for the functions  $f^\pm$  and  $g^\pm$ , which take the form of d'Alembert's solution,

$$f^\pm|_{T=0} = \frac{1}{2} \left( F(x \pm t) \pm \int_{-\infty}^{x \pm t} V(x) dx \right),$$

$$g^\pm|_{T=0} = \frac{1}{2} \left( G(x \pm ct) \pm \frac{1}{c} \int_{-\infty}^{x \pm ct} W(x) dx \right). \quad (2.43)$$

### 2.4.2 Initial Value Problem for the Boussinesq and Boussinesq-type Equations

Referring to (2.39), we note that the initial condition does not explicitly contain terms in  $O(1)$  and  $O(\epsilon)$ . The extension of this model, to accommodate explicit terms in the initial condition at  $O(1)$  and  $O(\epsilon)$ , was considered in [45] by setting the coupling terms to zero ( $\gamma = \delta = 0$ ) i.e. the Boussinesq equation

$$f_{tt} - f_{xx} = \epsilon \left[ \frac{1}{2} (f^2)_{xx} + f_{ttxx} \right]. \quad (2.44)$$

The initial condition is written with explicit powers of  $\epsilon$ , of the form

$$f|_{t=0} = F^0(x) + \epsilon F^1(x) + O(\epsilon^2), \quad f_t|_{t=0} = V^0(x) + \epsilon V^1(x) + O(\epsilon^2). \quad (2.45)$$

In [45] a weakly nonlinear solution is constructed of the form

$$f = f^-(\xi, T) + f^+(\eta, T) + \epsilon f^1(\xi, \eta, T) + O(\epsilon^2), \quad (2.46)$$

where  $\xi = x - t$ ,  $\eta = x + t$  and  $T = ct$ . Substituting (2.46) into (2.44) and comparing at  $O(\epsilon)$  we obtain

$$\begin{aligned} -4f_{\xi\eta}^1 &= \left( 2f_T^- + f^- f_\xi^- + f_{\xi\xi\xi}^- \right)_\xi + \left( -2f_T^+ + f^+ f_\eta^+ + f_{\eta\eta\eta}^+ \right)_\eta \\ &\quad + 2f_\xi^- f_\eta^+ + f^+ f_{\xi\xi}^- + f^- f_{\eta\eta}^+. \end{aligned} \quad (2.47)$$

Equations for  $f^-$  and  $f^+$  can be derived by either integrating (2.47) and requiring that  $f^1$  is non-secular i.e. [60], or by averaging with respect to  $t$  [39, 45, 65]. Averaging at constant  $\xi$  or  $\eta$  leads to a KdV equation describing the leading order left- and right-propagating waves, of the form

$$2f_T^- + f^- f_\xi^- + f_{\xi\xi\xi}^- = 0, \quad -2f_T^+ + f^+ f_\eta^+ + f_{\eta\eta\eta}^+ = 0. \quad (2.48)$$

Substituting (2.48) back into (2.47) and integrating with respect to the characteristic variables yields [45]

$$f^1 = -\frac{1}{4} \left( 2f^- f^+ + f_\xi^- \int f^+ d\eta + f_\eta^+ \int f^- d\xi \right) + \phi(\xi, T) + \psi(\eta, T). \quad (2.49)$$

The initial conditions for each term in (2.46) are found by substituting (2.46) into (2.45) and solving the derived system. As shown in [45], the initial conditions for the leading order functions are

$$f^\pm|_{T=0} = \frac{1}{2} \left( F^0(x \pm t) \pm \int_{-\infty}^{x \pm t} V^0(x) dx \right), \quad (2.50)$$

while at  $O(\epsilon)$  the initial conditions for  $\phi$  and  $\psi$  take the form

$$\begin{aligned} \phi(\xi, T) &= \frac{1}{2} \left[ R_1(\xi, T) + \int_{-\infty}^{\xi} R_2(x, T) dx \right], \\ \psi(\eta, T) &= \frac{1}{2} \left[ R_1(\eta, T) - \int_{-\infty}^{\eta} R_2(x, T) dx \right], \end{aligned} \quad (2.51)$$

where

$$\begin{aligned} R_1(x, T) &= \frac{1}{4} \left[ 2f^- f^+ + f_\xi^- \int f^+ d\eta + f_\eta^+ \int f^- d\xi \right]_{T=0} + F^1(x), \\ R_2(x, T) &= \left[ f_T^- + f_T^+ + \frac{1}{4} \left( f^+ f_\xi^- - f^- f_\eta^+ + f_{\xi\xi}^- \int f^+ d\eta - f_{\eta\eta}^+ \int f^- d\xi \right) \right]_{T=0} - V^1(x). \end{aligned} \quad (2.52)$$

A further study of the Boussinesq equation and also the Boussinesq equation with the addition of an Ostrovsky term is performed in [46]. The Boussinesq equation with an Ostrovsky term was derived in the context of water waves in [74]. In [46] a systematic and rigorous approach was developed, using Fourier series, for the derivation and justification of the weakly nonlinear solution for the Boussinesq and Boussinesq-type equations, and the effect of a non-zero mean initial condition was considered. This approach also found expressions for the error terms and these estimates were confirmed in numerical simulations.

The discussion of the mean value is important when we consider the Boussinesq equation with an Ostrovsky term, as the equations derived when constructing the weakly nonlinear solution are Ostrovsky equations, which necessarily require zero mean [9, 46]. Indeed, for the typical Ostrovsky equation

$$(f_t + ff_x + f_{xxx})_x = \gamma f, \quad (2.53)$$

where  $f$  is periodic on the domain  $[-L, L]$ , we can clearly see the conservation law for smooth functions of the form

$$\int_{-L}^L f dx = 0. \quad (2.54)$$

Therefore the initial condition for  $f$  should satisfy (2.54). As was shown in [46], this

requirement of zero mean initial condition can be accommodated in Boussinesq-type equations by considering the behaviour of the mean value of the equation in time. Let us consider the Boussinesq-type equation on the domain  $x \in [-L, L]$ , of the form

$$u_{tt} - u_{xx} = \epsilon \left[ \frac{1}{2} (u^2)_{xx} + u_{ttxx} - \gamma u \right], \quad (2.55)$$

where  $\gamma > 0$ . Integrating (2.55) in  $x$  over the period  $2L$ , we obtain an evolution equation for the mean value, which can be solved to find

$$\langle u \rangle := \frac{1}{2L} \int_{-L}^L u \, dx = F_0 \cos(\sqrt{\epsilon\gamma}t) + V_0 \frac{\sin(\sqrt{\epsilon\gamma}t)}{\sqrt{\epsilon\gamma}}, \quad (2.56)$$

where we have

$$F_0 = \frac{1}{2L} \int_{-L}^L u(x, 0) \, dx \quad \text{and} \quad V_0 = \frac{1}{2L} \int_{-L}^L u_t(x, 0) \, dx. \quad (2.57)$$

To accommodate this mean value we introduce  $\tilde{u} = u - \langle u \rangle$ , where the initial condition for  $\tilde{u}$  will now have zero mean. The construction of the weakly nonlinear solution is detailed in [46] and we will discuss another type of derivation for the Boussinesq equation with an Ostrovsky term in Chapter 5.

## 2.5 Weakly Nonlinear Solution of the Scattering Problem

An important theme of recent research in physics has been the study of longitudinal bulk strain solitary waves in nonlinearly elastic waveguides (e.g. [31, 32] and references therein). The earliest model derived for long waves in the context of the solid waveguides was the KdV equation [75–77], however it was shown in [78] that the KdV model has limitations and, indeed in this paper, the long longitudinal bulk strain solitary waves in an elastic rod are shown to be governed by the DDE.

Previous studies have shown that nonlinear waves are sensitive to delamination regions, and much of the recent work has been dedicated to constructing models to describe the scattering of a longitudinal solitary wave in rods, plates and bars, and these were observed in experiments [25, 30, 33, 38, 44, 79–83]. This modelling has important physical implications, as it can potentially be used to detect delamination. Current methods of non-destructive testing are based upon ultrasonic waves [84, 85] but recent experiments have suggested that strain solitary waves can propagate for longer distances in solid waveguides [34], making them an attractive candidate for introscopy.

To model the scattering of longitudinal bulk strain solitary waves in elastic layered waveguides, the approach outlined in [30] can be followed. As discussed in Section 2.2, the longitudinal displacements in an elastic waveguide can be governed by the DDE with different coefficients in each domain. This is completed with continuity conditions on the interface between sections; continuity of longitudinal displacements and continuity of normal stress. Assuming the displacement for  $x < 0$  is denoted by  $u^-$  and for  $x > 0$  is denoted by  $u^+$ , with the delamination present for  $x > 0$ , the displacements are described by two DDEs (in dimensionless form)

$$u_{tt}^{\pm} - c_{\pm}^2 u_{xx}^{\pm} = \frac{\beta_{\pm} c_{\pm}^2}{E_{\pm}} u_x^{\pm} u_{xx}^{\pm} + \frac{J_{\pm} \nu^2}{\sigma_{\pm}} (u_{tt}^{\pm} - c_{1\pm}^2 u_{xx}^{\pm})_{xx}, \quad (2.58)$$

where the values of the coefficients are as defined in [30] and repeated above in Section 2.2, where the minus indices are the coefficients for the bonded section of the waveguide (which can be treated as a single thick bar), and the positive indices are for the delaminated section of the waveguide (which can be treated as a thin bar). The continuity conditions are written as

$$u^-|_{x=0} = u^+|_{x=0}, \quad (2.59)$$

for continuity of longitudinal displacement, and

$$c_-^2 u_x^- + \left[ \frac{\beta_- c_-^2}{2E_-} (u_x^-)^2 + \frac{J_- \nu^2}{\sigma_-} (u_{tt}^- - c_{1-}^2 u_{xx}^-)_x \right] \Big|_{x=0} = c_+^2 u_x^+ + \left[ \frac{\beta_+ c_+^2}{2E_+} (u_x^+)^2 + \frac{J_+ \nu^2}{\sigma_+} (u_{tt}^+ - c_{1+}^2 u_{xx}^+)_x \right] \Big|_{x=0}, \quad (2.60)$$

for continuity of normal stress.

The question of constructing a weakly nonlinear solution to such a system was addressed in [30] and we overview this in Chapter 3 when developing a semi-analytical method to this problem. The modelling of longitudinal strain wave propagation in such a structure is similar to calculating the reflected and transmitted waves when a surface or internal soliton passes through an area of rapid depth variation [86–90]. A similar effect can also be seen for internal waves [89–91].



## Chapter 3

# Modelling of Nonlinear Wave Scattering in a Delaminated Elastic Bar

### 3.1 Introduction

In this chapter, we consider the case of a perfectly bonded elastic bar with a delamination area. The results have been partially published in [42]. The aim of our work is to develop an efficient semi-analytical approach, based on the weakly nonlinear analysis of the problem developed in [30], which could be used to model the scattering of nonlinear waves across the delaminated sections of the bar. A semi-analytical approach involves numerically solving the weakly nonlinear solution to the original problem rather than solving the full problem numerically. Such an approach can be applied to more complex structures, and in the final part of this chapter we will consider the case when the delamination is finite or the case where the materials are different in each section of the bar.

The structure of the chapter is as follows. Firstly, we will overview the problem formulation for the scattering of an incident strain soliton in a symmetric layered bar with delamination, assuming that the material in each section of the bar can be different. We look for a weakly nonlinear solution of the problem to obtain equations that are simpler to solve. The approach gives rise to three KdV equations describing the behaviour of the leading order incident, transmitted and reflected waves, and terms for the higher order corrections. We describe fission of the transmitted and reflected strain solitary waves and establish predictions for the number of solitary waves present in each section of the bar. Two numerical schemes are utilised, the first for the direct problem and the

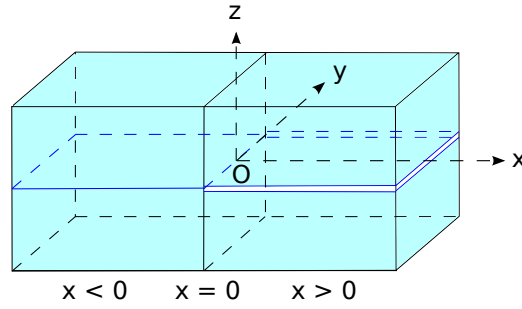


FIGURE 3.1: Two-layered symmetric bar with delamination at  $x > 0$ .

second for the equations derived via the weakly nonlinear approach. The results obtained via these numerical schemes are compared against each other and the theoretical predications, and the agreement is checked for various configurations of the delaminated bar.

## 3.2 Problem Formulation

The graphical representation of the structure we are considering is shown in Figure 3.1. We can see that there are two layers in the bar, with a ‘perfect’ bond between the layers for  $x < 0$  and delamination for  $x > 0$ . The material of the layers is assumed to be the same (a symmetric bar), while the material to the left and to the right of the  $x = 0$  cross-section can be different. We assume that the height of the bonding region is negligible compared to the layers of the structure, therefore we do not expect any scattering in the bonding region to affect the longitudinal waves in the main structure.

Let us consider the propagation of a long longitudinal bulk wave in such a structure. Assuming that the cross-section at  $x = 0$  is a perfect interface as well, and that the layers have width  $2a$  and height  $b$ , we can apply the model described in Section 2.2 and describe the behaviour of long longitudinal waves in this medium. Assuming that the longitudinal displacements for  $x < 0$  are given by  $u^-$  and similarly longitudinal displacements for  $x > 0$  are given by  $u^+$ , we obtain the non-dimensional equations

$$\begin{aligned} u_{tt}^- - u_{xx}^- &= \epsilon \left[ -12u_x^- u_{xx}^- + 2u_{ttxx}^- \right], & x < 0, \\ u_{tt}^+ - c^2 u_{xx}^+ &= \epsilon \left[ -12\alpha u_x^+ u_{xx}^+ + 2\frac{\beta}{c^2} u_{ttxx}^+ \right], & x > 0, \end{aligned} \quad (3.1)$$

with appropriate initial conditions

$$u^\pm(x, 0) = F^\pm(x), \quad (3.2)$$

and associated continuity conditions

$$u^-|_{x=0} = u^+|_{x=0}, \quad (3.3)$$

$$u_x^- + \epsilon \left[ -6(u_x^-)^2 + 2u_{ttx}^- \right] \Big|_{x=0} = c^2 u_x^+ + \epsilon \left[ -6\alpha (u_x^+)^2 + 2\frac{\beta}{c^2} u_{ttx}^+ \right] \Big|_{x=0}, \quad (3.4)$$

where  $c$ ,  $\alpha$  and  $\beta$  are constants defined by the geometrical and physical parameters of the structure and  $\epsilon$  is the small wave amplitude parameter. Condition (3.3) describes the continuity of longitudinal displacement, while condition (3.4) describes the continuity of normal stress.

To reduce the number of parameters in the numerical experiments, we will use the values presented in [30], namely that  $\alpha = 1$  and

$$\beta = \frac{n^2 + k^2}{n^2(1 + k^2)}, \quad (3.5)$$

where  $n$  represents the number of layers in the structure and  $k$  is defined by the geometry of the waveguide. These can be seen in Figure 3.1 as follows: the cross-section  $x = 0$  has width  $2a$  and the height of each layer is  $b$ . In terms of these values,  $k = b/a$  and, as there are two layers in this example,  $n = 2$ .

### 3.3 Weakly Nonlinear Solution

The system (3.1) - (3.4) is complicated and therefore, in order to obtain a simpler system that is asymptotically equivalent to the original system, we follow the approach developed in [30] and consider a weakly nonlinear solution to (3.1) of the form

$$\begin{aligned} u^- &= I(\xi_-, X) + R(\eta_-, X) + \epsilon P(\xi_-, \eta_-, X) + O(\epsilon^2), \\ u^+ &= T(\xi_+, X) + \epsilon Q(\xi_+, \eta_+, X) + O(\epsilon^2), \end{aligned} \quad (3.6)$$

where the characteristic variables are given by

$$\xi_- = x - t, \quad \xi_+ = x - ct, \quad \eta_- = x + t, \quad \eta_+ = x + ct, \quad X = \epsilon x.$$

The functions  $I$ ,  $R$ ,  $T$  describe the leading order incident, reflected and transmitted waves respectively, while the functions  $P$  and  $Q$  describe the higher-order corrections. Substituting (3.6) into (3.1) the system is satisfied at leading order, while at  $O(\epsilon)$  we

have

$$\begin{aligned} -2P_{\xi_-\eta_-} &= \left( I_X - 3I_{\xi_-}^2 + I_{\xi_-\xi_-\xi_-} \right)_{\xi_-} + \left( R_X - 3R_{\eta_-}^2 + R_{\eta_-\eta_-\eta_-} \right)_{\eta_-} \\ &\quad - 6(RI_{\xi_-} + IR_{\eta_-})_{\xi_-\eta_-}. \end{aligned} \quad (3.7)$$

To leading order the right-propagating incident wave,

$$I = \int \tilde{I} d\xi_-, \quad (3.8)$$

is defined by the solution of the KdV equation

$$\tilde{I}_X - 6\tilde{I}\tilde{I}_{\xi_-} + \tilde{I}_{\xi_-\xi_-\xi_-} = 0. \quad (3.9)$$

Similarly the reflected wave

$$R = \int \tilde{R} d\eta_-, \quad (3.10)$$

satisfies the KdV equation

$$\tilde{R}_X - 6\tilde{R}\tilde{R}_{\eta_-} + \tilde{R}_{\eta_-\eta_-\eta_-} = 0. \quad (3.11)$$

Substituting these conditions into (3.7) and integrating with respect to both characteristic variables, we obtain an expression for higher-order terms satisfying

$$P = 3(RI_{\xi_-} + IR_{\eta_-}) + \phi(\xi_-, X) + \psi(\eta_-, X), \quad (3.12)$$

where  $\phi$  and  $\psi$  are arbitrary functions. The first radiation condition requires that the solution to the problem should not change the incident wave (there should be no corrections to the given incident wave in the disturbance caused by it) [30]. In our problem the incident wave is the solitary wave solution of the KdV equation (3.9), with corrections at  $O(\epsilon^2)$ . Therefore, the radiation condition implies that  $\phi = 0$ . We find  $\psi$  from conditions (3.3) and (3.4) later.

We can apply the same methodology to the second equation in (3.1) to obtain

$$-2c^2Q_{\xi_+\eta_+} = \left( c^2T_X - 3T_{\xi_+}^2 + \beta T_{\xi_+\xi_+\xi_+} \right)_{\xi_+}. \quad (3.13)$$

Looking for the leading order transmitted wave satisfying

$$T = \int \tilde{T} d\xi_+, \quad (3.14)$$

where

$$\tilde{T}_X - \frac{6}{c^2} \tilde{T} \tilde{T}_{\xi_+} + \frac{\beta}{c^2} \tilde{T}_{\xi_+ \xi_+ \xi_+} = 0, \quad (3.15)$$

higher order corrections are given by

$$Q = q(\xi_+, X) + r(\eta_+, X), \quad (3.16)$$

where  $q$  and  $r$  are arbitrary functions. The second radiation condition states that if the incident wave is right-propagating, then there should be no left-propagating waves in the transmitted wave field [30]. Thus,  $r = 0$ .

We have derived equations describing the leading order incident, reflected and transmitted waves. However, we still have to take account of the continuity conditions. We are seeking ‘initial conditions’ for the strain waves and therefore we differentiate (3.3) with respect to  $t$  to obtain

$$u_t^-|_{x=0} = u_t^+|_{x=0}.$$

Substituting the weakly nonlinear solution (3.6) into this expression, to leading order we obtain

$$I_{\xi_-}|_{X=0} - R_{\eta_-}|_{X=0} = cT_{\xi_+}|_{X=0}, \quad (3.17)$$

and at  $O(\epsilon)$  we have

$$\psi_{\eta_-}|_{X=0} + cq_{\xi_+}|_{X=0} = 3(I_{\xi_- \xi_-} R - IR_{\eta_- \eta_-})|_{X=0} = f(t, X)|_{X=0}. \quad (3.18)$$

Following the same approach for condition (3.4), at leading order we obtain

$$I_{\xi_-}|_{X=0} + R_{\eta_-}|_{X=0} = c^2 T_{\xi_+}|_{X=0}, \quad (3.19)$$

and at  $O(\epsilon)$  we have

$$\begin{aligned} \psi_{\eta_-}|_{X=0} - c^2 q_{\xi_+}|_{X=0} &= \left[ - \left( I_X - 6I_{\xi_-}^2 + 2I_{\xi_- \xi_- \xi_-} \right) - \left( R_X - 6R_{\eta_-}^2 + 2R_{\eta_- \eta_- \eta_-} \right) \right. \\ &\quad \left. + c^2 T_X - 6T_{\xi_+}^2 + 2\beta T_{\xi_+ \xi_+ \xi_+} - 3(IR_{\eta_- \eta_-} + I_{\xi_- \xi_-} R) \right] |_{X=0} \\ &= g(t, X)|_{X=0}. \end{aligned} \quad (3.20)$$

The equations (3.17) and (3.19) allow us to express the leading order reflected and transmitted waves in terms of the incident wave, at the boundary  $x = 0$ . Therefore, we obtain ‘initial conditions’ for the previously derived KdV equations (3.11) and (3.15) of the form

$$\tilde{R}|_{X=0} = C_R \tilde{I}|_{X=0}, \quad \tilde{T}|_{X=0} = C_T \tilde{I}|_{X=0}, \quad (3.21)$$

where we have the leading order reflection coefficient

$$C_R = \frac{c-1}{c+1}, \quad (3.22)$$

and the leading order transmission coefficient

$$C_T = \frac{2}{c(c+1)}. \quad (3.23)$$

If we have the same material for  $x < 0$  and  $x > 0$  then  $c = 1$  and, from (3.22) and (3.23), we find that we have full transmission of the incident wave (to leading order) across the interface between the regions and, to leading order, there is no reflected wave.

The expressions for  $f$  and  $g$  in (3.18) and (3.20) respectively can now be reduced using the relations (3.21) and the KdV equations (3.9), (3.11) and (3.15). The simplified form is as follows:

$$f(t, X)|_{X=0} = [3(R + C_R I) I_{\xi_- \xi_-}]|_{X=0}, \quad (3.24)$$

$$g(t, X)|_{X=0} = \left[ 3(1 + C_R^2 - C_T^2) I_{\xi_-}^2 - \left( 1 + C_R - \frac{\beta}{c^2} C_T \right) I_{\xi_- \xi_- \xi_-} - 3(R - C_R I) I_{\xi_- \xi_-} \right] |_{X=0}. \quad (3.25)$$

Finally, we can solve (3.18) and (3.20) for  $\psi_{\eta_-}$  and  $q_{\xi_+}$ . Restoring the dependence of  $f$  and  $g$  on their respective characteristic variables, we obtain

$$\psi(\eta_-, X) = \frac{1}{1+c} \int [cf(\eta_-, X) + g(\eta_-, X)] d\eta_-, \quad (3.26)$$

$$q(\xi_+, X) = \frac{1}{c(1+c)} \int \left[ f\left(-\frac{\xi_+}{c}, X\right) - g\left(-\frac{\xi_+}{c}, X\right) \right] d\xi_+. \quad (3.27)$$

In order to find the constants of integration in the leading order equations and (3.26) - (3.27), additional physical conditions should be used, such as the known value of the solution at the boundaries.

### 3.4 The Inverse Scattering Transform and Fission of Solitons

It is well known that the KdV equation is integrable by the Inverse Scattering Transform (IST) (see [20] for the original paper and [3] for a more detailed treatment). In particular if the initial condition is taken in the form of  $V \operatorname{sech}^2(x)$ , where  $V$  is a constant, it has been shown (e.g. [3]) that, in long time, the initial condition evolves into a number of

solitons (defined by the value of  $V$ ) and dispersive radiation. Crucially, it is possible for multiple solitons to be generated from a single initial pulse.

Let us recall the form of the transmitted wave equation, (3.15). We can rewrite this in the canonical form

$$U_\tau - 6UU_\chi + U_{\chi\chi\chi} = 0, \quad (3.28)$$

via the change of variables

$$U = \frac{1}{\beta} \tilde{T}, \quad \tau = \frac{\beta}{c^2} X, \quad \chi = \xi_+. \quad (3.29)$$

The IST can be used to determine the solution for the KdV equation. We make a similar approximation to what was done in [88], for a soliton moving into a region with different properties, neglecting some short waves as the soliton moves over the  $x = 0$  cross-section. We can define the transmitted wave field by the spectrum of the linear Schrödinger equation,

$$\Psi_{\chi\chi} + [\lambda - U(\chi)] \Psi = 0, \quad (3.30)$$

where the potential is given by

$$U(\chi) = -A \operatorname{sech}^2\left(\frac{\chi}{l}\right), \quad A = \frac{v}{\beta c(1+c)}, \quad l = \frac{2c}{\sqrt{v}}. \quad (3.31)$$

Note that the expressions in (3.31) make use of the constants introduced in (3.29) and also (3.23). Following the method of the IST, we see that the sign of  $A$  will determine if any solitary waves are present in the transmitted wave field (see previous references for details). If  $A < 0$ , the transmitted wave field will not contain any solitons and the initial pulse will degenerate into a dispersive wave train. However when  $A > 0$ , there will always be at least one discrete eigenvalue, corresponding to at least one solitary wave in the transmitted wave field, and accompanying radiation determined by the continuous spectrum.

In some cases more than one secondary soliton can be produced from the single initial soliton, referred to as fission of a soliton [86–88]. The discrete eigenvalues of (3.30) are given by (for example, [92])

$$\lambda = -\kappa_n^2, \quad \text{where} \quad \kappa_n = \frac{1}{2l} \left[ (1 + 4Al^2)^{1/2} - (2n - 1) \right], \quad n = 1, 2, \dots, N. \quad (3.32)$$

Furthermore the number of solitons in the delaminated area,  $N$ , is given by the largest integer satisfying the inequality

$$N < \frac{1}{2} \left( \sqrt{1 + \frac{4\delta^2}{\pi^2}} + 1 \right), \quad (3.33)$$

where

$$\delta = \pi\sqrt{A}l = 2\pi\sqrt{\frac{c}{\beta(1+c)}}. \quad (3.34)$$

The parameters  $\beta$  and  $c$  depend on the properties of the material and the geometry of the waveguide, and so  $\delta$ , and therefore  $N$ , depend on these properties. We can see from (3.33) that, for small  $\delta$ , there will always be one soliton while, as  $\delta$  increases, more solitons will emerge. As  $\tau \rightarrow +\infty$ , the solution will evolve into a train of solitary waves, ordered by their heights, propagating to the right and some dispersive radiation propagating to the left (in the moving reference frame) i.e.

$$U \sim -\sum_{n=1}^N 2\kappa_n^2 \operatorname{sech}^2(\kappa_n(\chi - 4\kappa_n^2\tau - \chi_n)) + \text{radiation}, \quad (3.35)$$

where  $\chi_n$  is the phase shift.

The above results allow us to determine if an incident soliton fissions in the delaminated section of the bar, and we can see from (3.33) and (3.34) that these are dependent upon the parameters  $c$  and  $\beta$ . Therefore, following [30], we ask the following question: is soliton fission possible if the waveguide is made of one and the same material? If the material is the same in both sections then we have  $c = 1$ . However, the value of  $\beta$  is determined by the number of layers in the bar and the geometry of the waveguide. Recalling the expression (3.5), where  $n$  is the number of layers and  $k = b/a$ , the number of solitary waves produced is the largest integer satisfying

$$N < \frac{1}{2} \left( \sqrt{1 + 8n^2 \frac{1+k^2}{n^2+k^2}} + 1 \right).$$

Therefore, given the values of  $n$  and  $k$ , we can create a series of predictions for the number of solitary waves present in the delaminated section of the bar, based upon the value of  $\beta$ . We will check these predictions in Section 3.5.

A similar approach can be followed for the reflected wave field. We note that the KdV equation describing reflected waves, (3.11), is already written in canonical form. We make use of the ‘‘initial condition’’ and reflection coefficient as presented in (3.21) and (3.22) respectively. The wave field is defined by the spectrum of the Schrödinger equation (3.30), where the potential  $U$  is given by

$$U(\chi) = -B \operatorname{sech}^2\left(\frac{\chi}{m}\right), \quad B = \frac{v}{2}C_R = \frac{v(c-1)}{2(c+1)}, \quad m = \frac{2}{\sqrt{v}}.$$

It is clear that the sign of  $B$  is dependent upon the sign of the reflection coefficient  $C_R$ , as  $v > 0$  for all considerations. If  $c < 1$ , then  $B$  is negative and the reflected wave field does not contain any solitary waves. The initial pulse will degenerate into a dispersive

wave train. For  $c > 1$ ,  $B$  is positive and there will be at least one solitary wave present in the reflected wave field, accompanied by radiation. To describe these solitary waves, one can use (3.32) and (3.33) by making the change  $A \rightarrow B$ , and  $l \rightarrow m$ . Explicitly, we have

$$\lambda = -\kappa_n^2, \quad \text{where} \quad \kappa_n = \frac{1}{2l} \left[ (1 + 4Bm^2)^{1/2} - (2n - 1) \right], \quad n = 1, 2, \dots, N, \quad (3.36)$$

and the number of solitary waves produced in the bonded section,  $N_R$ , is given by the largest integer satisfying the inequality

$$N_R < \frac{1}{2} \left( \sqrt{1 + \frac{4\mu^2}{\pi^2}} + 1 \right), \quad (3.37)$$

where

$$\mu = \pi\sqrt{B} m = \pi\sqrt{2 \frac{c-1}{c+1}}. \quad (3.38)$$

If  $c = 1$  (the structure is of one and the same material) then  $C_R = 0$  and there is no leading order reflected wave.

### 3.5 Results for a Two-Section Bar

In the previous sections of this chapter we have detailed a model for the scattering of long longitudinal waves in a delaminated bar. We then used a weakly nonlinear approach to derive a leading order model for the scattering of the incident wave in this structure. In this section we will compare the derived weakly nonlinear solution to the solution of the original model to determine if the weakly nonlinear solution is a good approximation to the solution of the full problem. We will then consider different configurations of the bar to determine if delamination can be detected within the structure.

The full problem as defined by (3.1) - (3.4) is solved using a finite-difference scheme, as detailed in [42]. We discuss the scheme in Appendix A.2. For the semi-analytical approach using the weakly nonlinear solution, we make use of an SSPRK(5,4) scheme to solve the KdV equations, as we also did in [42]. This is detailed in Appendix B.

In what follows, let  $\epsilon = 0.05$ ,  $v = 0.4$  and take a step size of  $\Delta x = \Delta t = 0.01$  in the direct numerical method and a step size of  $\Delta \xi = 0.1$ ,  $\Delta X = 0.00025$  in the semi-analytical method. The value of  $\Delta \xi$  and  $\Delta X$  chosen for the SSPRK(5,4) scheme was chosen to be similar to the step size taken for the hybrid Runge-Kutta scheme in [93]. The domain size in the semi-analytical method is chosen so that, for the times and spatial positions of interest, the value  $\xi = x - t$  exists. As shown in [39], the finite-difference method for the

Boussinesq equation is linearly stable (using a von Neumann linear stability analysis) for values of  $\kappa$  satisfying

$$\kappa < \kappa_c = \sqrt{\frac{h^2 + 4\beta c^{-2}}{c^2 + f_0}}, \quad (3.39)$$

where  $f_0$  is the constant used in the linearised scheme. In practice the stricter condition of

$$\kappa < \frac{1}{2}\kappa_c \quad (3.40)$$

is imposed, to help accommodate for nonlinear effects. The values of  $\Delta x$  and  $\Delta t$  chosen above satisfy this relation.

In all of our calculations we are taking an incident strain solitary wave and we are interested in the resulting strain waves in the transmitted (and reflected) wave field. Therefore, we solve for the displacements in the direct numerical scheme and differentiate the results with respect to  $x$  to obtain the strain wave. In the semi-analytical method, the KdV equations that we solve are for strain waves, so these do not need to be modified. Therefore we denote  $e^- = u_x^-$  and  $e^+ = u_x^+$  in the results.

To determine the initial condition, we differentiate (3.1) and denote  $e^\pm(x, t) = u_x^\pm(x, t)$ . The initial condition is then taken as the exact solitary wave solution of the equation for  $e^-(x, t)$ , and therefore the exact ‘‘kink’’ solution for  $u^-(x, t)$ . If we choose the position of this exact solitary wave solution to be sufficiently far from the interface at  $x = 0$  then, as the solitary wave is rapidly decaying to zero, we can assume that  $e^+(x, 0) = 0$ . Explicitly we have the Boussinesq equation for  $e^-(x, t)$  given as

$$e_{tt}^- - e_{xx}^- = 2\epsilon \left[ -3 \left( e^- \right)_{xx} + e_{ttxx}^- \right]. \quad (3.41)$$

Looking for a travelling wave solution of the form  $e^-(x, t) = e^-(x - v_1 t)$ , where  $v_1$  is the velocity of the wave, we obtain the exact solitary wave solution

$$e^-(x, t) = A \operatorname{sech}^2 \left( \frac{x - v_1 t}{\Lambda} \right), \quad (3.42)$$

where we have

$$A = \frac{v_1^2 - 1}{4\epsilon} \quad \text{and} \quad \Lambda = \frac{2\sqrt{2\epsilon}v_1}{\sqrt{v_1^2 - 1}}.$$

We evaluate (3.41) at  $t = 0$  to find the initial condition. To obtain the initial condition for  $u^\pm(x, t)$  we integrate (3.42) with respect to  $x$ . We assumed  $e^+(x, 0) = 0$  and therefore  $u^+(x, 0) = \text{constant}$ . We further assume that the strain wave propagates into an unperturbed medium (this is consistent with the choice of position for the strain wave as stated above) and therefore  $u^+(x, 0) = 0$ . Similarly, the constant of integration present in the expression for  $u^-(x, 0)$  is chosen such that, for  $x$  close to 0, we have  $u^-(x, 0) =$

0. Explicitly for  $u^-(x, 0)$  we have

$$u(x, 0)^\pm = -\frac{v_1 \sqrt{v_1^2 - 1}}{\sqrt{2\epsilon}} \left[ \tanh \left( \frac{\sqrt{v_1^2 - 1}}{2v_1 \sqrt{2\epsilon}} x \right) - 1 \right]. \quad (3.43)$$

As we have a second order time derivative, we require two initial conditions for this equation. We have taken the exact travelling wave solution of the equation and therefore the second initial condition takes the form

$$u_t(x, 0) = -v_1 u_x(x, 0), \quad (3.44)$$

where we have already calculated  $u_x(x, 0)$  in (3.42). Taking a forward difference approximation in time allows us to formulate the solution at  $u(x, \Delta t)$ , as required by the numerical scheme outlined in Appendix A.2.

For the weakly nonlinear solution, we take the exact solitary wave solution of the KdV equation governing the leading order incident wave (3.9). As this is the leading order approximation of the Boussinesq equation, these initial conditions will be consistent at leading order with corrections at  $O(\epsilon^2)$ . Therefore we have initial condition

$$I(\xi_-, \epsilon x_a) = -\frac{v}{2} \operatorname{sech}^2 \left( \frac{\sqrt{v}}{2} \xi_- \right), \quad (3.45)$$

where  $x_a$  is the initial position of the soliton,  $v$  is the velocity of the soliton and, recalling the speed of the solution (3.43) is  $v_1$ , satisfies the approximate relation  $v_1 = 1 + \epsilon v + O(\epsilon^2)$ . Note that we do not require a second initial condition here, as we only have a first order time derivative in the KdV equation (3.9). For the equations governing leading order reflected and transmitted waves, we can use relation (3.21), with the reflection and transmission coefficients (3.22) and (3.23) respectively to obtain initial conditions for equations (3.11) and (3.15) in terms of the initial condition (3.45). Therefore we have

$$T(\xi_+, 0) = -\frac{v}{c(c+1)} \operatorname{sech}^2 \left( \frac{\sqrt{v}}{2} \xi_+ \right), \quad (3.46)$$

for the transmitted waves and, for the reflected waves, we have

$$R(\eta_-, 0) = -\frac{v(c-1)}{2(c+1)} \operatorname{sech}^2 \left( \frac{\sqrt{v}}{2} \eta_- \right). \quad (3.47)$$

We note here that, while we have explicitly stated the initial conditions for transmitted and reflected waves here, if the initial condition was not taken as the exact solitary wave solution of the leading order incident wave equation then the theory would still be valid, however we would replace (3.46) and (3.47) with the solution of the leading order

incident wave equation (3.9) at the boundary point  $x = 0$  multiplied by the appropriate transmission or reflection coefficient.

### 3.5.1 Test Cases

Firstly we consider the case where  $\beta = c = 1$ . In this case, we would be modelling the bar without a delaminated region i.e. we have a perfect bond for  $x < 0$  and  $x > 0$ . This makes an ideal test case for the numerical schemes, as we would expect full transmission of the incident strain solitary wave across the interface at  $x = 0$ . The initial condition for the system of Boussinesq equations (3.1) is given by (3.43) and the initial condition for the leading order incident wave (and subsequently the leading order reflected and transmitted wave equations) is given by (3.45). We solve system (3.1) for the displacements  $u^\pm(x, t)$  and plot the strains  $u_x^\pm(x, t)$ , denoted  $e^\pm(x, t)$ .

Viewing the solution of the first scheme as exact, the solution of the second scheme will be accurate to leading order, with a small correction to the wave at  $O(\epsilon^2)$  in this case (in the general case the corrections would be at  $O(\epsilon)$  but we are taking the exact solitary wave solution here). The solution for  $e^-$  at the initial time and for  $e^+$  at a sufficiently large time should describe the same right-propagating solitary wave. The result of the calculation for this case, for both numerical schemes, is presented in Figure 3.2. As  $c = 1$ , there is no leading order reflected wave because the reflection coefficient is zero. Figure 3.2 shows a good agreement between the solutions, with a small phase shift between the results in the transmitted wave field. This can be remedied by including higher order terms in the semi-analytical scheme.

Another test case is for a value of  $c$  such that  $c < 1$ . Considering the expressions for  $C_R$  and  $C_T$ , that is

$$C_R = \frac{c-1}{c+1}, \quad C_T = \frac{2}{c(1+c)},$$

and noting that  $c > 0$  (a physical requirement), we observe that  $C_T > 0$  for all  $c$ , while  $C_R < 0$  for  $c < 1$  and  $C_R > 0$  for  $c > 1$ . Recalling our observations from Section 3.3 we expect that, for a value of  $c < 1$ , a dispersive wave train will be present in the reflected wave field. For  $c = 3/4$ , we have  $C_R = -1/7$  and  $C_T = 32/21$ . The waves in each section of the bar are presented in Figure 3.3. It can be seen that a dispersive wave train is present in the first section of the bar, after the initial wave is incident on the boundary between the two sections. This dispersive wave train is of a small amplitude, but it is clear that the solution does not contain solitons, as predicted. The agreement between the numerical schemes is very good in this case. It is worth noting that this solution looks like the Airy function solution of the linearised KdV equation, which is the small

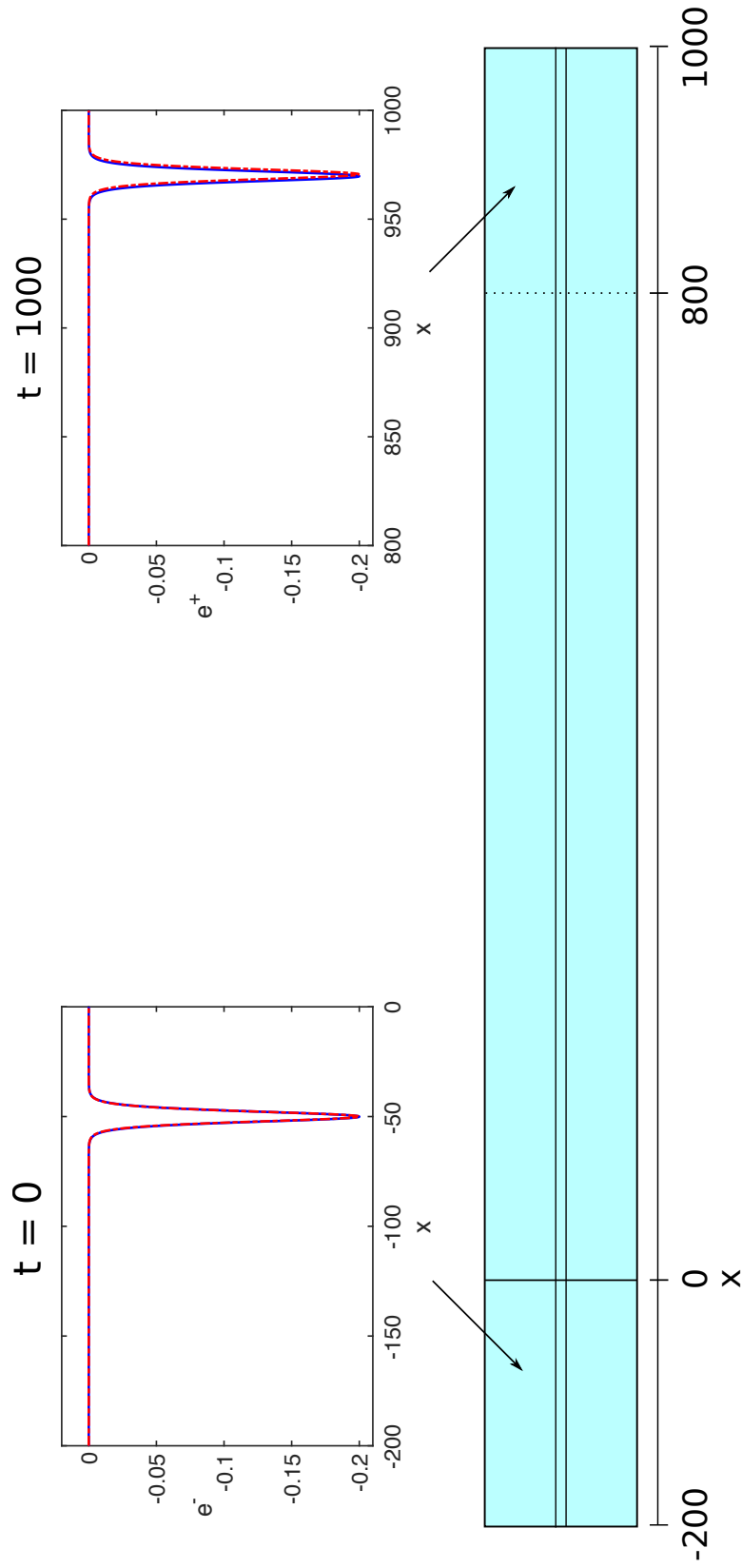


FIGURE 3.2: The initial condition and solution at  $t = 1000$  in the second section of the bar, for the direct numerical scheme (blue, solid) and semi-analytical method (red, dashed) with exact initial conditions,  $\alpha = \beta = c = 1$  and initial position  $x = -50$ .

amplitude limit of the similarity solution of the KdV equation related to the Painleve II equation (see [1, 2] and references therein for more details).

In the second section of the bar, we see that the incident soliton fissions into two solitons and dispersive radiation. The agreement between the solutions on the small amplitude secondary soliton is very good, however there is a larger discrepancy for the larger amplitude lead soliton. This can be understood from the transmission coefficient, as this will amplify the wave and therefore the errors. This would again be improved by the inclusion of higher order corrections, as the error amplification would be present at  $O(\epsilon^2)$  rather than at  $O(\epsilon)$ . We could equally reduce the value of epsilon to reduce the errors.

The next case to consider is for large values of  $c$ . Using the results of Section 3.3, specifically (3.22) and (3.23), we would expect the leading order reflected wave to be closer in amplitude to the initial wave and the transmitted wave to be of a much smaller amplitude. An example is presented in Figure 3.4 for  $c = 2$ , where we have

$$C_R = \frac{1}{3}, \quad C_T = \frac{1}{3},$$

and we can see from the coefficients that we would expect the reflected and transmitted waves to be of approximately equal amplitude. We can see in Figure 3.4 that the waves are indeed of the same amplitude. In each section of the bar, the agreement is very good between the two schemes and we see one soliton in each wave field, with some dispersive radiation present in each case.

### 3.5.2 Predictions

Following the scheme outlined in Section 3.3, we define  $c = 1$  and recall that

$$\beta = \beta(n, k) = \frac{n^2 + k^2}{n^2(1 + k^2)}. \quad (3.48)$$

We now consider the behaviour in our problem formulation using these parameters. The initial condition remains the same and we change the value of  $n$  and  $k$  to obtain different cases. Table 1 in [30] presents results for 9 different configurations and all of these configurations have been checked and are presented in Figure 3.5. The expected number of solitary waves in the transmitted wave field in these cases are summarised in Table 3.1. In each of the following cases we note that, as we have taken  $c = 1$ , there is no leading order reflected wave and therefore only the transmitted wave field is presented. The figures are all presented at the same value of  $t = 1000$  for comparison. We observe that the number of predicted solitons is in agreement with the numerics in most of the

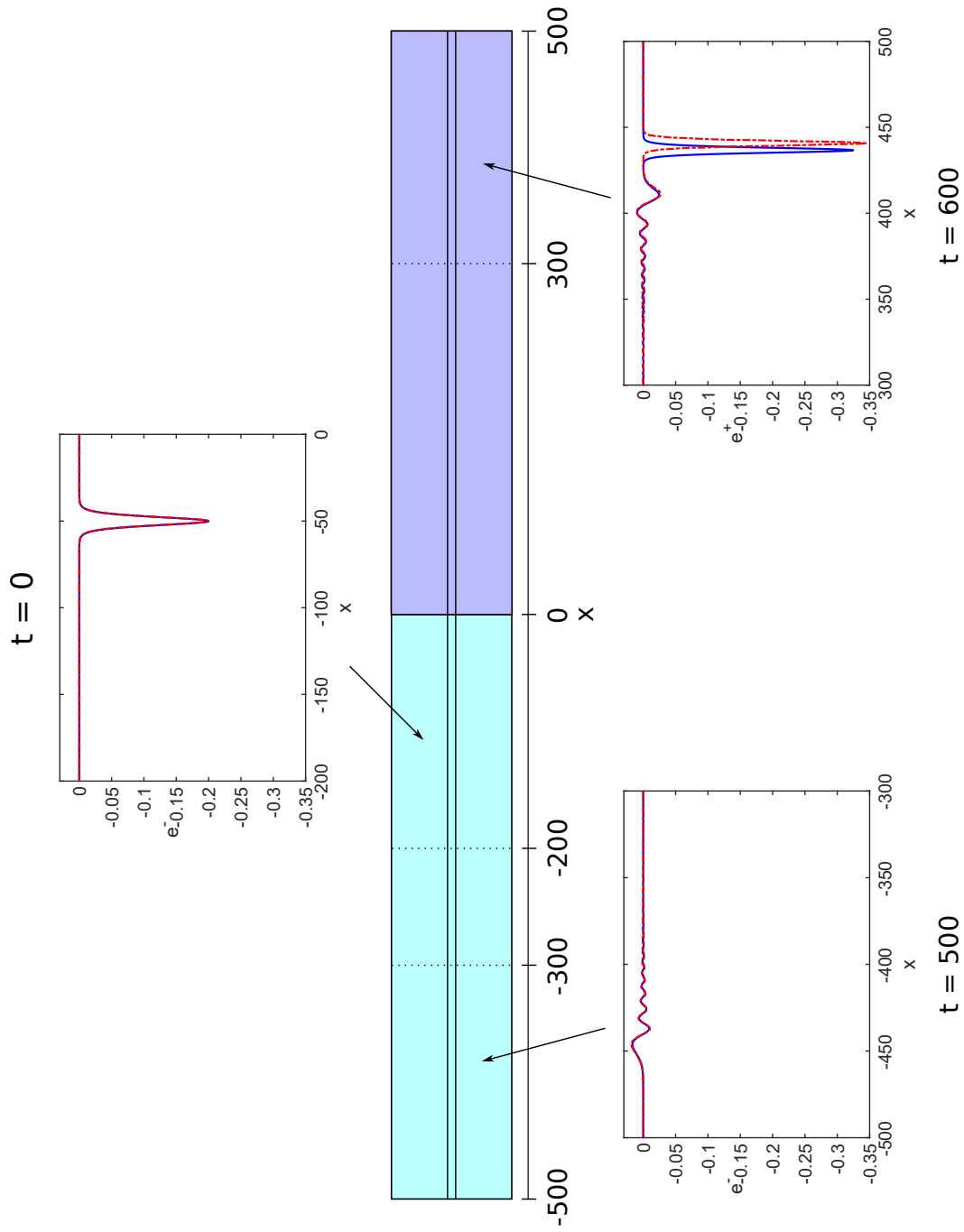


FIGURE 3.3: The reflected and transmitted waves in each section of the bar, for the direct numerical scheme (blue, solid) and semi-analytical method (red, dashed) with exact initial conditions,  $\alpha = \beta = 1$ ,  $c = 3/4$  and initial position  $x = -50$ .

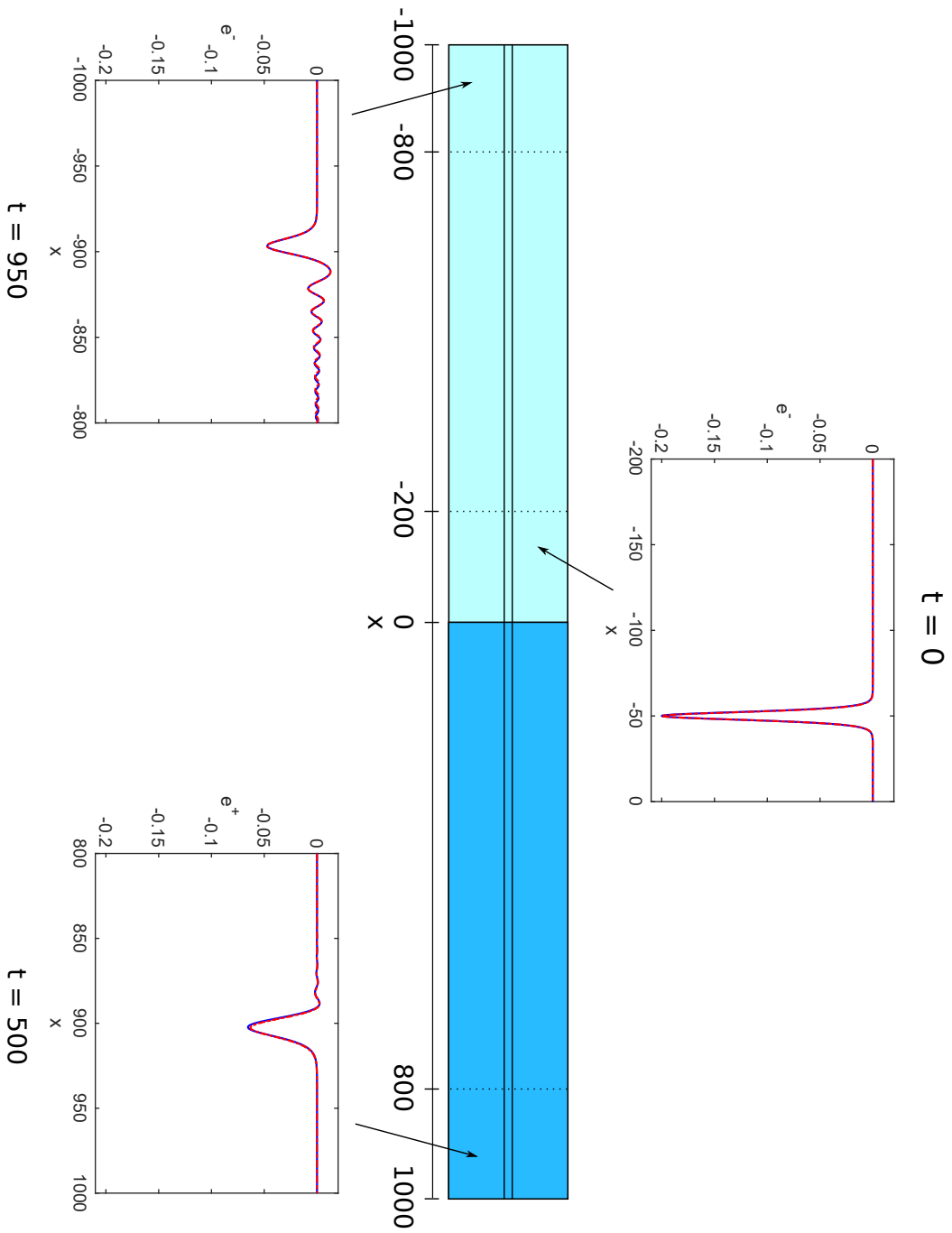


FIGURE 3.4: The reflected and transmitted waves in each section of the bar, for the direct numerical scheme (blue, solid) and semi-analytical method (red, dashed) with exact initial conditions,  $\alpha = \beta = 1$ ,  $c = 2$  and initial position  $x = -50$ .

	$k = 1$			$k = 2$			$k = 3$		
n	2	3	4	2	3	4	2	3	4
N	2	2	2	2	3	3	3	3	4

TABLE 3.1: Predictions on the number of solitons present in the transmitted wave field in the delaminated section of the bar, for various choices of  $n$  and  $k$ .

cases, however in the case of  $n = 2$  and  $k = 3$ , the predicted amplitude of the third soliton is  $-6.079 \times 10^{-5}$  and similarly in the case when  $n = 4$  and  $k = 3$  the predicted amplitude of the fourth soliton is  $-3.954 \times 10^{-4}$ . Therefore, these solitons are buried inside the radiation and numerical experiments up to  $t = 10,000$  show that they have still not separated from the radiation.

### 3.5.3 Predicted Amplitude of Lead Soliton

A prediction for the amplitude of the lead soliton is provided in [30], namely that the ratio of its amplitude to that of the incident soliton is

$$C_a = \frac{\beta}{4} \left( \sqrt{1 + \frac{8}{\beta}} - 1 \right)^2. \quad (3.49)$$

This estimate is found using the IST for an incident solitary wave and we calculate the eigenvalues for the transmitted wave field. In the long-time asymptotics, these eigenvalues correspond to solitary waves, ordered by their heights.

We consider the combination of values  $k = 1, 2, 3$  and  $n = 2, 3, 4$  and compare the amplitude of the lead soliton calculated numerically to the theoretical prediction. Taking step sizes of  $\Delta x = \Delta t = 0.01$  in the direct numerical scheme and step sizes of  $\Delta \xi = 0.1$ ,  $\Delta X = 0.00025$  in the SSPRK(5,4) scheme we compare the errors in Table 3.2. We can see from these results that the maximum error in the amplitude for the direct numerical method is  $4.911 \times 10^{-3}$  and for the semi-analytical method was  $3.398 \times 10^{-4}$ . Therefore we see good agreement between the schemes and the theoretical predictions.

### 3.5.4 Comparison of Schemes

Reviewing the results presented here, it can be seen that the semi-analytical approach produces results comparable to the direct numerical scheme for many cases, particularly for long waves. As the model is a long-wave model, this is the desirable behaviour for the schemes. Crucially, the semi-analytical approach requires the solving of, at most, two equations in each section of a bar (reflected and transmitted) while the direct finite-difference method requires the solution of multiple tridiagonal equations systems, and

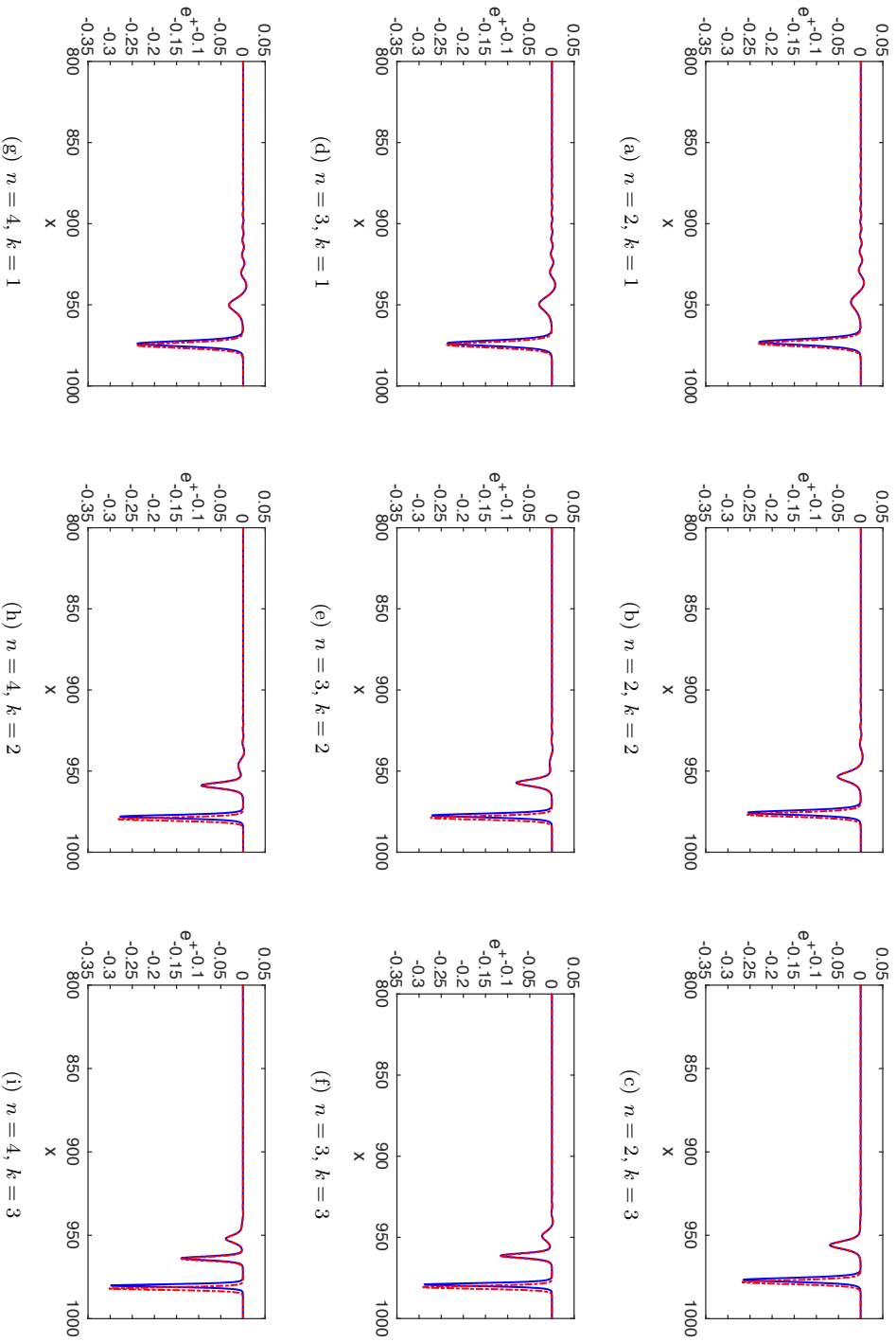


FIGURE 3.5: The waves in the transmitted wave field for various configurations of the bar, corresponding to different values of  $n$  and  $k$ . Each of the results is presented at the same time moment, for the direct numerical scheme (blue, solid) and semi-analytical method (red, dashed) with exact initial conditions and initial position  $x = -50$ .

Number of layers, $n$	Ratio of height and half width, $k$	Error for direct numerical method	Error for semi-analytical method
2	1	$1.253 \times 10^{-3}$	$2.280 \times 10^{-5}$
2	2	$2.396 \times 10^{-3}$	$9.697 \times 10^{-5}$
2	3	$2.992 \times 10^{-3}$	$1.216 \times 10^{-5}$
3	1	$1.661 \times 10^{-3}$	$3.398 \times 10^{-4}$
3	2	$3.391 \times 10^{-3}$	$4.497 \times 10^{-5}$
3	3	$4.083 \times 10^{-3}$	$2.375 \times 10^{-4}$
4	1	$1.701 \times 10^{-3}$	$3.473 \times 10^{-5}$
4	2	$3.799 \times 10^{-3}$	$1.407 \times 10^{-5}$
4	3	$4.911 \times 10^{-3}$	$2.351 \times 10^{-4}$

TABLE 3.2: Comparison of lead soliton amplitude as predicted from the IST with the numerically calculated values from both numerical schemes, for various choices of  $n$  and  $k$ .

the solution of the nonlinear equation derived for  $x = 0$  has to be substituted into the implicit solution at all other points. Therefore, the semi-analytical approach is more desirable as additional sections are included in the bar. In addition, an analysis of the time required to calculate a solution by each scheme shows that the semi-analytical approach is faster. Indeed, both methods were programmed in C and compiled using the Intel compiler. The spatial domain for the semi-analytical method used 75,000 points, while the spatial domain for the direct numerical method used 400,000 points. When run on a 2.66 GHz Intel Core i5 processor, the approximate CPU time for the direct numerical scheme was 12 hours, compared to 4 hours for the semi-analytical method.

Further attempts to improve the calculation time, by reducing the domain size, showed further improvement. Reducing the spatial domain for the direct numerical method to 150,000 points and 15,000 points for the spatial domain in the semi-analytical method the calculation time was reduced to approximately 20 minutes for the direct numerical scheme and 15 minutes for the semi-analytical scheme. This was taken further by increasing the step size and comparing the results for a larger step size to the current results. For the direct numerical scheme we found that it is highly sensitive to increases in step sizes, and therefore we cannot improve the speed of the calculation without allowing significant numerical errors. For the semi-analytical scheme, we found it is not sensitive to considerable increases in the step sizes, and therefore we can take step sizes of  $h = 0.25$  and  $\kappa = 0.01$  without sacrificing significant accuracy. The same calculation as before resulted in a calculation time of 34 seconds. Therefore the resulting calculation in the semi-analytical scheme was 35 times faster than the finite-difference scheme.

The accuracy of the semi-analytical method can be improved further by including higher-order terms [45, 46]. It must be noted that, in these papers, a semi-analytical numerical

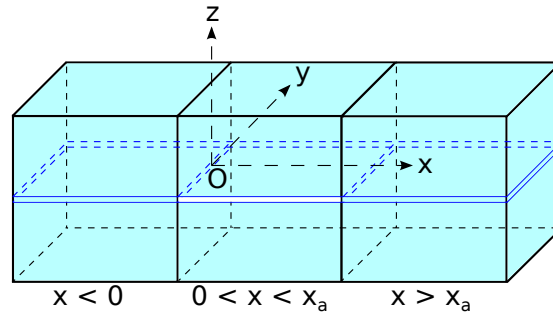


FIGURE 3.6: Two-layered symmetric bar with a finite delamination at  $0 < x < x_a$ .

approach to the solution of the initial value problem for Boussinesq-type equations was derived, however the advantages of the semi-analytical method compared to the standard methods were not obvious in this case, and the increase in computation time was not significant. This improvement was identified in our work in [42] as the complexity of the problem was increased.

### 3.6 Results for a Three-Section Bar

A further extension of this problem is to include another section in the bar, thereby creating a delamination of finite length, in comparison to the semi-infinite delamination that was studied numerically in Section 3.5. We graphically represent this scenario, for two layers, in Figure 3.6. The previous example would be detectable in a physical setting, as the delamination is semi-infinite and therefore would be visible at the end of the structure. Extending this to a delamination of finite length is of more interest from a physical standpoint, as this delamination would not be visible to an observer. To detect such a defect, methods such as ultrasonic or x-rays would have to be used. Assuming that strain solitary waves can be generated and detected in such a structure (as was done for PMMA and PS in [25, 44, 82, 83]) then our aim is to infer the delamination length and position from our studies.

#### 3.6.1 Weakly Nonlinear Solution

We formulate the problem as an extension of our previous study. Let us reduce the problem to the case when the material in all sections of the bar is one and the same, as the extension to this case is trivial and does not introduce any new behaviour. Therefore

we have the equation system

$$\begin{aligned}
u_{tt}^{(1)} - u_{xx}^{(1)} &= \epsilon \left[ -12u_x^{(1)}u_{xx}^{(1)} + 2u_{ttxx}^{(1)} \right], & x < 0, \\
u_{tt}^{(2)} - u_{xx}^{(2)} &= \epsilon \left[ -12u_x^{(2)}u_{xx}^{(2)} + 2\beta u_{ttxx}^{(2)} \right], & 0 < x < x_a, \\
u_{tt}^{(3)} - u_{xx}^{(3)} &= \epsilon \left[ -12u_x^{(3)}u_{xx}^{(3)} + 2u_{ttxx}^{(3)} \right], & x > x_a,
\end{aligned} \tag{3.50}$$

with the same initial condition as before and associated continuity conditions

$$\begin{aligned}
u^{(1)}|_{x=0} &= u^{(2)}|_{x=0}, \\
u^{(2)}|_{x=0} &= u^{(3)}|_{x=0}, \\
u_x^{(1)} + \epsilon \left[ -6 \left( u_x^{(1)} \right)^2 + 2u_{ttx}^{(1)} \right] \Big|_{x=0} &= u_x^{(2)} + \epsilon \left[ -6 \left( u_x^{(2)} \right)^2 + 2\beta u_{ttx}^{(2)} \right] \Big|_{x=0}, \\
u_x^{(2)} + \epsilon \left[ -6 \left( u_x^{(2)} \right)^2 + 2\beta u_{ttx}^{(2)} \right] \Big|_{x=0} &= u_x^{(3)} + \epsilon \left[ -6 \left( u_x^{(3)} \right)^2 + 2u_{ttx}^{(3)} \right] \Big|_{x=0},
\end{aligned} \tag{3.51}$$

$$\tag{3.52}$$

where  $\beta$  is as defined in (3.5) in terms of the geometry of the waveguide and  $\epsilon$  is the small wave amplitude parameter.

We look for a weakly nonlinear solution, as we did in Section 3.3, of the form

$$\begin{aligned}
u^{(1)} &= I(\xi, X) + R^{(1)}(\eta, X) + \epsilon P^{(1)}(\xi, \eta, X) + O(\epsilon^2), \\
u^{(2)} &= T^{(2)}(\xi, X) + R^{(2)}(\eta, X) + \epsilon P^{(2)}(\xi, \eta, X) + O(\epsilon^2), \\
u^{(3)} &= T^{(3)}(\xi, X) + \epsilon P^{(3)}(\xi, \eta, X) + O(\epsilon^2),
\end{aligned} \tag{3.53}$$

where we have the same characteristic variables in each section, specifically  $\xi = x - t$ ,  $\eta = x + t$  and  $X = \epsilon x$ . As before,  $R^{(i)}$  indicate reflected waves in section  $i$  and  $T^{(i)}$  represents transmitted waves in section  $i$  of the bar. As before,  $P^{(i)}$  represents higher order corrections in each section.

We can follow the same derivation as before. From (3.22) and (3.23), we can see that if the material in each section is the same then the reflection coefficient is zero and the transmission coefficient is one. Therefore the leading order reflected wave will be zero and we do not need to derive the governing equation. In the following equations, variables with a tilde have been differentiated with respect to their appropriate characteristic variable. The incident wave is governed by

$$\tilde{I}_X - 6\tilde{I}\tilde{I}_\xi + \tilde{I}_{\xi\xi\xi} = 0, \tag{3.54}$$

the transmitted waves in the second section of the bar satisfy the equation

$$\tilde{T}_X^{(2)} - 6\tilde{T}^{(2)}\tilde{T}_\xi^{(2)} + \beta\tilde{T}_{\xi\xi\xi}^{(2)} = 0, \quad (3.55)$$

and finally the transmitted waves in the third section of the bar are governed by

$$\tilde{T}_X^{(3)} - 6\tilde{T}^{(3)}\tilde{T}_\xi^{(3)} + \tilde{T}_{\xi\xi\xi}^{(3)} = 0. \quad (3.56)$$

### 3.6.2 Prediction of Lead Soliton Amplitude

As we are considering an incident soliton, we can use the IST to find the eigenvalues in the delaminated section of the bar. If we then assume that the solitons are well separated when they enter the third section of the bar, we can apply the same methodology on each soliton and predict the amplitude of the solitons generated in the third section of the bar.

As was seen in (3.49), we can find the ratio of the lead soliton to the incident soliton in the delaminated region. If we assume an incident soliton of the form (3.45), then we note that this soliton has amplitude  $A = -v/2$ . When this soliton enters the second section of the bar, we use the IST to predict the amplitude of the lead soliton as

$$A = -\frac{v}{2}\kappa_1^2\beta, \quad \text{where} \quad \kappa_1 = \frac{1}{2}\left(\sqrt{1 + \frac{8}{\beta}} - 1\right). \quad (3.57)$$

If this soliton is well-separated from the trailing solitons, we can model (3.57) entering the third section of the bar and, following the same steps in the IST, we obtain a prediction for the amplitude of the lead soliton in the third section of the bar as

$$A = -\frac{v}{2}\kappa_1^2\kappa_2^2, \quad \text{where} \quad \kappa_2 = \frac{1}{2}\left(\sqrt{1 + 8\beta} - 1\right), \quad (3.58)$$

and  $\kappa_1^2$  is as defined in (3.57). The same methodology can be applied to all solitons generated in the delaminated section, however we are only interested in the lead soliton as this will be the easiest to detect in a physical setting.

If the solitons do not properly separate then the amplitude of the lead soliton will be closer to the initial amplitude than that predicted in (3.58). If the length of the delaminated region is sufficiently long, then the amplitude of the lead soliton in the third section of the bar will be given by (3.58). As the length of the delaminated region is reduced, the amplitude of the lead soliton in the third region will tend towards the initial amplitude.

We can use the above result to predict the length of the delaminated region. Let us measure the delamination in terms of the Full Width at Half Magnitude (FWHM) of the incident soliton. We introduce a measure of the amplitude of the lead soliton in the third section of the bar in comparison to the incident soliton as

$$\sigma = \frac{\text{Numerical} - \text{Incident}}{\text{Predicted} - \text{Incident}} \times 100. \quad (3.59)$$

These results are discussed in the next section.

### 3.6.3 Numerical Results

We use the same parameters as before, so we have  $v = 0.4$  and we take  $\epsilon = 0.05$  initially. In order to solve the direct problem numerically using the method in Appendix A.2, we have to compute the solution in two regions at a time. Referring to Figure 3.6, we would compute the solution for the regions  $x < 0$  and  $0 < x < x_a$  first, with two constraints: that the wave has not yet reached the boundary  $x = x_a$ , and that the waves reflected from  $x = 0$  have not yet reached the left-hand boundary and reflected back to the  $x = 0$  boundary again. The speed of the solitary wave is known (and is close to the characteristic speed) and therefore we can choose an appropriate time interval for the calculation. We then calculate for the regions  $0 < x < x_a$  and  $x > x_a$  to obtain the final solution.

However we can extend the method in Appendix A.2 to the case of a multi-section bar, where the solution is computed in all sections simultaneously. This extension of the method is described in Appendix A.3 and we use this method to solve the equations described here.

For the semi-analytical method, we use the pseudospectral scheme outlined in Appendix C.1 and we take  $\Delta\xi = 0.3$  and  $\Delta X = 0.001$ . The domain size is chosen in the same way as before, that is we choose a domain length such that, for all values of  $x$  and  $t$  that we are interested in, the value  $\xi = x - t$  is contained within this domain.

Firstly we present the result for the case of two layers with a rectangular cross-section, that is  $n = 2$  and  $k = 2$ . The result is shown in Figure 3.7. We can see that the incident soliton fissions into two solitons in the delaminated section, as predicted from the IST. When these solitons enter a bonded section again, they change amplitude and become wider. The lead soliton is close to the amplitude of the incident soliton, however its amplitude is smaller.

We now model the three-section bar for different lengths of delamination, measured in FWHM of the incident soliton. We use the measure defined in (3.59) to determine the

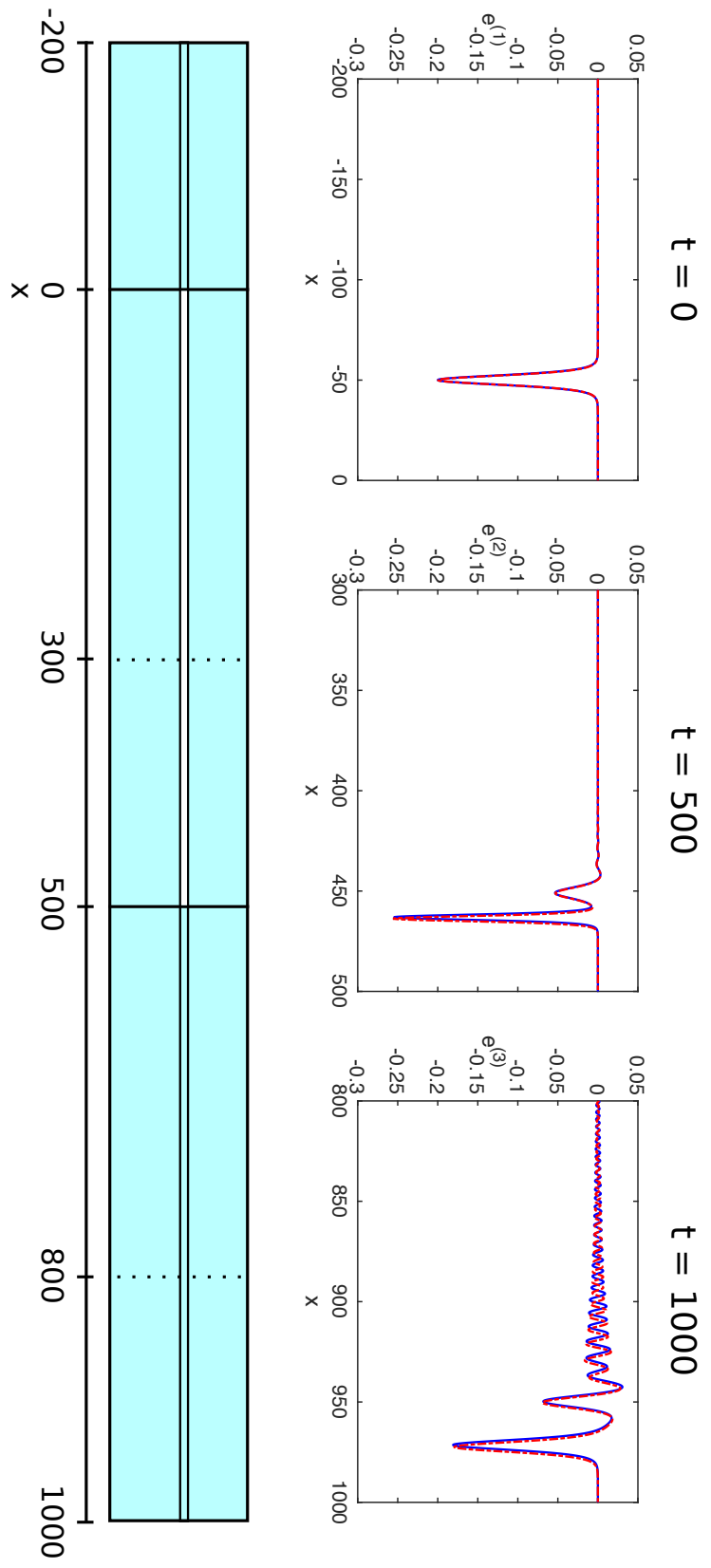


Figure 3.7: The solution in each section of the bar for the direct numerical scheme (blue, solid) and semi-analytical method (red, dashed) with  $\beta = 2/5$ , corresponding to  $n = 2$  and  $k = 2$ , and initial position  $x = -50$ .

change in the amplitude from the incident soliton to the lead soliton in the transmitted region, in comparison to the theoretical prediction. We use the numerical results for the semi-analytical method as the theoretical estimates are based upon the solutions to the KdV equations and therefore they will be the most instructive results.

Let us model for different values of  $\epsilon$ , as seen in Figure 3.8a. From this image we see a reduction in  $\epsilon$  by a factor of two, at a fixed value of  $\sigma$ , results in an increase of the corresponding FWHM by a factor of two. This is expected as the value of  $X$  is linearly dependent upon  $\epsilon$  and therefore the calculation range for  $X$  in the delaminated region is reduced by a factor of two. We perform a similar calculation for different values of  $n$  and  $k$ , representing differing values of  $\beta$ . The results are presented in Figure 3.8b. We can see that, as  $\beta$  decreases, for a fixed value of  $\sigma$  the corresponding value of FWHM increases. This corresponds to the behaviour we observe for decreasing values of  $\epsilon$ , however the relation is not linear in this case.

### 3.7 Conclusions

In this chapter we considered two numerical schemes for solving two, or three, boundary-value problems matched at the interface between the sections of the bar. This problem represents the propagation of a strain wave in a bar with a perfect bonding between the layers for the first boundary-value problem, and a bar with complete delamination in the second boundary-value problem. We then extended this to a system where the delamination is of finite length and we have another perfectly bonded section of the bar.

The problem was modelled within the scope of Boussinesq equations in each section of the bar, with matching conditions across the interface between the sections, as was done in [30]. This complicated problem was solved using a direct numerical scheme based upon finite-difference approximations. However, such methods are expensive as they require the solving of multiple Boussinesq equations and substitution into a nonlinear equation at the interface between each section.

To simplify the numerical problem, we found a weakly nonlinear solution by taking a multiple-scales expansion in terms of the appropriate set of fast and slow variables. This produced KdV equations satisfying initial-value problems, describing the leading order incident, reflected and transmitted waves. The initial values in these equations are fully described in terms of the leading order incident wave, with reflection and transmission coefficients being derived to describe these initial conditions. The KdV equations were solved using a SSPRK(5,4) scheme, with the finite-differenced form of the spatial derivatives used as the function in the scheme [94].

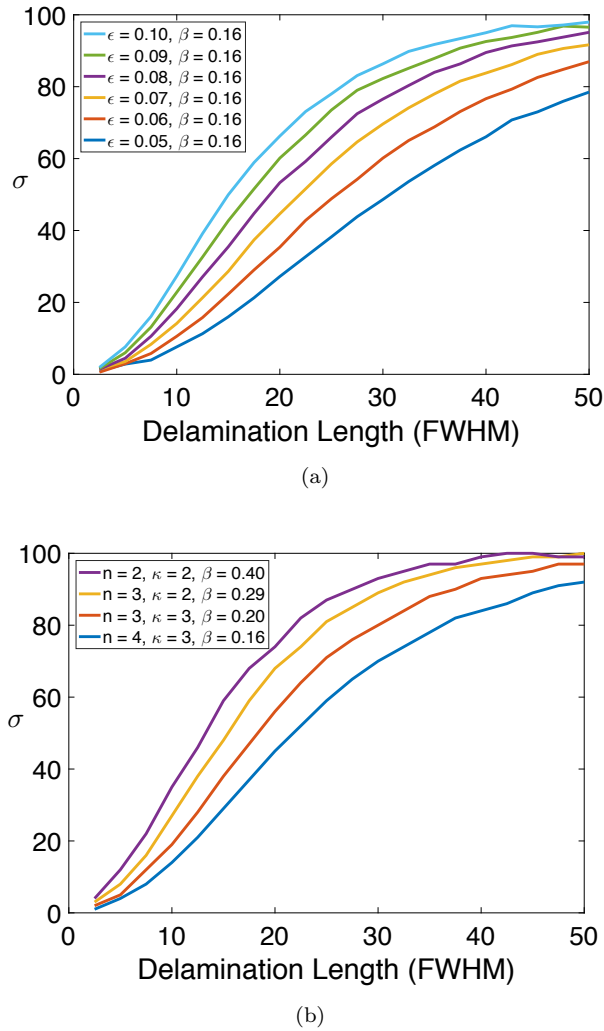


FIGURE 3.8: Graphs of the change in amplitude of the transmitted soliton in comparison to the incident soliton, as measured by  $\sigma$ . Graph (a) corresponds to changing values of  $\epsilon$ , while graph (b) corresponds to changing values of  $\beta$  (changing the geometry of the waveguide).

We predicted the number of solitons in each section of the bar and the eigenvalues that describe the solitons, using the results in [30]. We showed that the predictions can be obtained in each section of the bar, even for a bar of three or possibly more sections. This allowed us to predict the length of the delamination in terms of the FWHM of the incident soliton, and this was shown for multiple configurations of the bar. In addition, we showed that there is very good agreement between the two numerical schemes, with a slight phase shift between the two solutions representing the  $O(\epsilon^2)$  difference between their propagation speeds. They also agreed with theoretical predictions, however it is worth noting that the semi-analytical scheme is significantly faster to compute, and this improvement will become more dramatic as the complexity of the structures increases.

The next extension of this problem would be for a softer bond between the layers, rather than a perfect bond. This will be discussed in the next chapter.



## Chapter 4

# Modelling of Nonlinear Wave Scattering In a Bi-Layer with a Soft Bonding Layer

### 4.1 Introduction

In Chapter 3 we discussed the propagation of waves in a layered bar, from the perspective of nonlinear elasticity theory. We assumed that the bond between the layers was a perfect bond which, for example, is a good model for cyanoacrylate (commercially known as superglue). We now consider the case when the bond is more of a rubber-type glue e.g. polychloroprene (PCP). Such bi-layers have been modelled in [38], as discussed in the Introduction. The results discussed in this chapter have been partially published in [43].

The introduction of a soft bonding layer influences the behaviour of the waves as they propagate through the bar, introducing a new layer of complexity to the problem. If the materials of the layers have similar properties and the bonding between the layers is sufficiently soft ('imperfect bonding'), then the bulk strain soliton that we observed in Chapter 3 does not survive in its usual form, instead it evolves into a *radiating solitary wave*, that is a solitary wave with a co-propagating oscillatory tail [38, 95]. The radiating strain solitary wave has recently been observed in laboratory experiments [36]. Experimental studies of the excitation of resonant radiation by localised waves have arose in many physical settings, such as nonlinear optics. The reviews [96, 97] and the references therein provide an overview of these settings.

Using the layered lattice model as described in [38], we see that the longitudinal strain waves in a bi-layer with a sufficiently soft bonding layer are governed by coupled regularised Boussinesq (cRB) equations (in non-dimensional and scaled form):

$$\begin{aligned} f_{tt} - f_{xx} &= \frac{1}{2}(f^2)_{xx} + f_{ttxx} - \delta(f - g), \\ g_{tt} - c^2 g_{xx} &= \frac{1}{2}\alpha(g^2)_{xx} + \beta g_{ttxx} + \gamma(f - g). \end{aligned} \quad (4.1)$$

In this system  $f$  and  $g$  denote the longitudinal strains in the layers, while the coefficients  $c, \alpha, \beta, \delta, \gamma$  are defined by the physical and geometrical parameters of the problem [38].

In the symmetric case ( $c = \alpha = \beta = 1$ ) system (4.1) can be simplified, via the reduction  $g = f$ , where  $f$  satisfies the equation

$$f_{tt} - f_{xx} = \frac{1}{2}(f^2)_{xx} + f_{ttxx}. \quad (4.2)$$

The Boussinesq equation (4.2) has particular solitary wave solutions

$$f = A \operatorname{sech}^2\left(\frac{x - vt}{\Lambda}\right), \quad A = 3(v^2 - 1), \quad \Lambda = \frac{2v}{\sqrt{v^2 - 1}},$$

where  $v$  is the speed of the wave. In system (4.1), when the characteristic speeds of the linear waves in the layers are close, that is  $c$  is close to 1, these pure solitary wave solutions are replaced with radiating solitary waves, that is solitary waves radiating a co-propagating one-sided oscillatory tail [38, 39, 95] (see also [98–100] for studies of radiating solitary waves in other equations). We show the evolution of this pure solitary wave of system (4.1) with  $\delta = \gamma = 0$  (for a fixed value of  $v$ ) into a radiating solitary wave in Figure 4.1. Radiating solitary waves have been extensively studied in the context of perturbed KdV equations, coupled KdV systems, perturbed NLS equations, and coupled NLS systems [101–107]. Approximate analytical solutions for radiating solitary waves in cRB equations have been constructed in [47, 95]. The relevant linear dispersion relation for the system (4.1) has been analysed in [38]. It is assumed that the coefficients are perturbed compared to the symmetric case, but remain positive. The dispersion relation has the form

$$[k^2(1 - p^2) - k^4 p^2 + \delta][k^2(c^2 - p^2) - \beta k^4 p^2 + \gamma] = \gamma\delta, \quad (4.3)$$

where  $k$  is the wavenumber and  $p$  is the phase speed. A typical plot of (4.3) is shown in Figure 4.2. A significant difference with the linear dispersion curve of the reduction (4.2) is the appearance of the second branch, remaining above the first branch for all  $k$ , going to infinity as  $k \rightarrow 0$ , while approaching zero as  $k \rightarrow \infty$ .

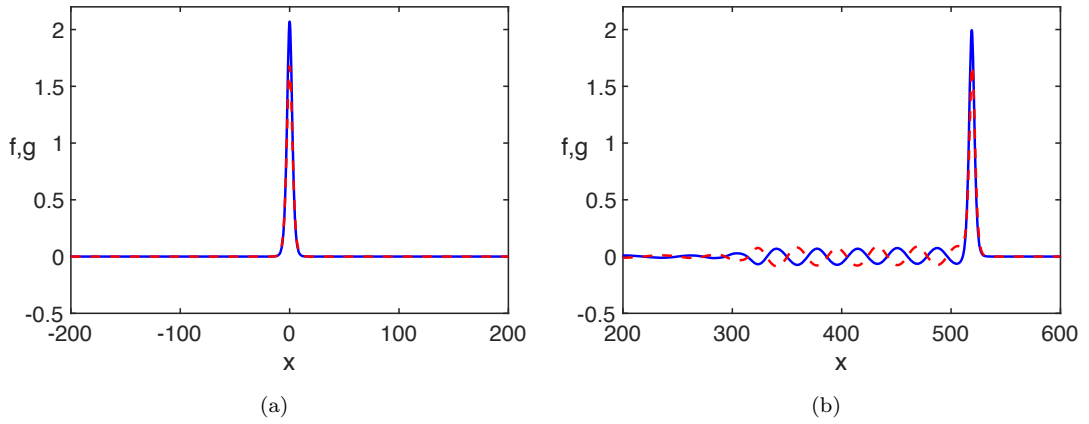


FIGURE 4.1: Typical generation of radiating solitary waves in system (4.1), from pure solitary wave initial conditions, for  $f$  (solid line) and  $g$  (dashed line). Here  $c = 1.05$ ,  $\alpha = \beta = 1.05$ . (a) Initial condition at  $t = 0$ : pure solitary wave solution with  $\delta = \gamma = 0$  and  $v = 1.3$ . (b) Radiating solitary wave solution with  $\delta = \gamma = 0.01$  at  $t = 400$ .

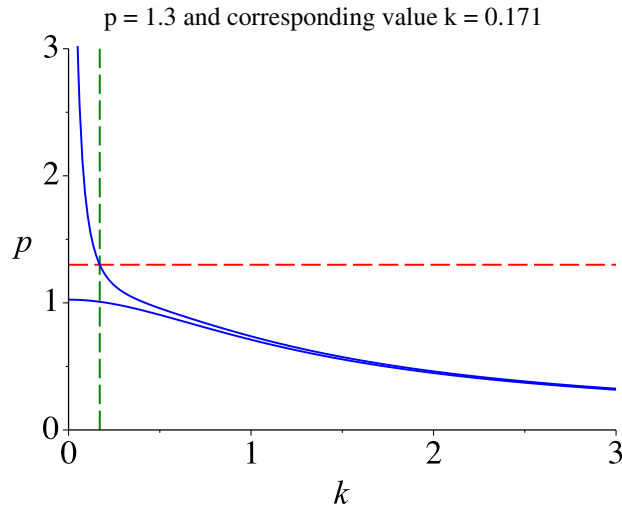


FIGURE 4.2: Two branches of the linear dispersion curve of system (4.1) for  $c = 1.05$ ,  $\alpha = \beta = 1.05$ ,  $\delta = \gamma = 0.01$  and a resonance for  $p = 1.3$  (horizontal, dashed line).

The pure solitary waves of the single Boussinesq equation (4.2) arise as a bifurcation from wavenumber  $k = 0$  of the linear wave spectrum, when there is no possible resonance between the speed  $v$  of the solitary wave and the phase speed  $p$  of some linear wave. In contrast to this, radiating solitary waves arise in the case when there is a possible resonance for some finite non-zero value of  $k$ . In Figure 4.2 we show a possible resonance for  $v = p = 1.3$ .

In this chapter, we will consider the scattering of radiating solitary waves in delaminated areas of imperfectly bonded layered structures (see Figure 4.3). As was done in Chapter 3, we develop a semi-analytical approach to the original model to simplify the equations that need to be solved. We will show that, in the soft bonded regions of the structure,

coupled Ostrovsky equations describe the behaviour of the transmitted and reflected waves in a bi-layer, and uncoupled Korteweg-de Vries equations describe the behaviour in the delaminated area. The Ostrovsky equation was originally derived to describe long surface and internal waves in a rotating ocean [9, 108], but recently it transpired that the equation, as well as the coupled Ostrovsky equations, can also describe nonlinear strain waves in layered elastic waveguides with soft interfaces [39]. Once we have derived the equations describing leading order transmitted and reflected waves, we develop a pseudospectral method for solving KdV and Ostrovsky equations and therefore a semi-analytical method for solving the original problem. These results are compared to the direct numerical method for solving the original problem and theoretical predictions. As in the previous chapter direct numerical simulations are expensive, therefore we then use our semi-analytical method to study the scattering of radiating solitary waves in a wide range of complex imperfectly bonded bi-layers with delamination, giving an elaborate description of the possible dynamical effects.

## 4.2 Problem Formulation

We consider the generation and scattering of a long radiating solitary wave in a two-layered imperfectly bonded bi-layer with delamination, shown in Figure 4.3. The addition of a homogeneous region on the left-hand side of the structure is inspired by the experimental setup [36] to ensure that the same wave propagates in both layers at the initial moment of time. These homogeneous layers are ‘glued’ to a two-layered structure with soft bonding between its layers (in the middle), followed with a delaminated section (on the right). The materials in the bi-layer are assumed to have close properties, leading to the generation of a radiating solitary wave in the bonded section [38]. Our aim is to understand the scattering of this wave by the subsequent delaminated region.

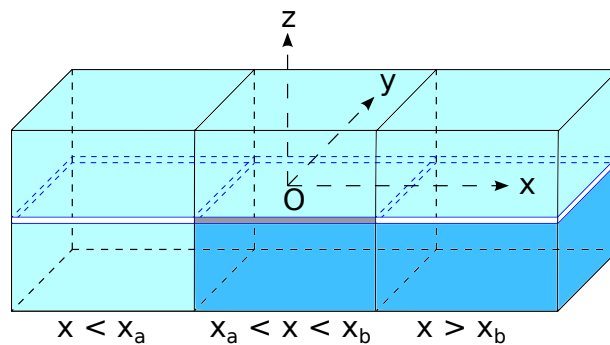


FIGURE 4.3: Bi-layer with two homogeneous layers for  $x < x_a$ , a bonded two-layered section for  $x_a < x < x_b$  and a delaminated section for  $x > x_b$ .

The mathematical problem formulation consists of scaled regularised non-dimensional equations in the respective sections of the complex waveguide [30, 38, 42, 43]. We have

$$\begin{aligned} u_{tt}^{(1)} - u_{xx}^{(1)} &= \epsilon \left[ -12u_x^{(1)}u_{xx}^{(1)} + 2u_{ttxx}^{(1)} \right], \\ w_{tt}^{(1)} - w_{xx}^{(1)} &= \epsilon \left[ -12w_x^{(1)}w_{xx}^{(1)} + 2w_{ttxx}^{(1)} \right] \end{aligned} \quad (4.4)$$

for  $x < x_a$ ,

$$\begin{aligned} u_{tt}^{(2)} - u_{xx}^{(2)} &= \epsilon \left[ -12u_x^{(2)}u_{xx}^{(2)} + 2u_{ttxx}^{(2)} - \delta \left( u^{(2)} - w^{(2)} \right) \right], \\ w_{tt}^{(2)} - c^2w_{xx}^{(2)} &= \epsilon \left[ -12\alpha w_x^{(2)}w_{xx}^{(2)} + 2\beta w_{ttxx}^{(2)} + \gamma \left( u^{(2)} - w^{(2)} \right) \right] \end{aligned} \quad (4.5)$$

for  $x_a < x < x_b$  and

$$\begin{aligned} u_{tt}^{(3)} - u_{xx}^{(3)} &= \epsilon \left[ -12u_x^{(3)}u_{xx}^{(3)} + 2u_{ttxx}^{(3)} \right], \\ w_{tt}^{(3)} - c^2w_{xx}^{(3)} &= \epsilon \left[ -12\alpha w_x^{(3)}w_{xx}^{(3)} + 2\beta w_{ttxx}^{(3)} \right] \end{aligned} \quad (4.6)$$

for  $x > x_b$ . The functions  $u^{(i)}(x, t)$  and  $w^{(i)}(x, t)$  describe longitudinal displacements in the upper and lower layers of the three sections of the waveguide, respectively. The values of the constants  $\alpha$ ,  $\beta$  and  $c$  depend on the physical and geometrical properties of the waveguide, while  $\delta$  and  $\gamma$  depend on the properties of the soft bonding layer, and  $\epsilon$  is a small amplitude parameter [38, 43].

These equations are complemented with continuity conditions at the interfaces between the sections. We have continuity of longitudinal displacement

$$u^{(1)}|_{x=x_a} = u^{(2)}|_{x=x_a}, \quad w^{(1)}|_{x=x_a} = w^{(2)}|_{x=x_a}; \quad (4.7)$$

$$u^{(2)}|_{x=x_b} = u^{(3)}|_{x=x_b}, \quad w^{(2)}|_{x=x_b} = w^{(3)}|_{x=x_b}; \quad (4.8)$$

and continuity of normal stress

$$\begin{aligned} u_x^{(1)} + \epsilon \left[ -6 \left( u_x^{(1)} \right)^2 + 2u_{ttx}^{(1)} \right] \Big|_{x=x_a} &= u_x^{(2)} + \epsilon \left[ -6 \left( u_x^{(2)} \right)^2 + 2u_{ttx}^{(2)} \right] \Big|_{x=x_a}, \\ w_x^{(1)} + \epsilon \left[ -6 \left( w_x^{(1)} \right)^2 + 2w_{ttx}^{(1)} \right] \Big|_{x=x_a} &= c^2w_x^{(2)} + \epsilon \left[ -6\alpha \left( w_x^{(2)} \right)^2 + 2\beta w_{ttx}^{(2)} \right] \Big|_{x=x_a}, \end{aligned} \quad (4.9)$$

and

$$u_x^{(2)} + \epsilon \left[ -6 \left( u_x^{(2)} \right)^2 + 2u_{ttx}^{(2)} \right] \Big|_{x=x_b} = u_x^{(3)} + \epsilon \left[ -6 \left( u_x^{(3)} \right)^2 + 2u_{ttx}^{(3)} \right] \Big|_{x=x_b},$$

$$c^2 w_x^{(2)} + \epsilon \left[ -6\alpha \left( w_x^{(2)} \right)^2 + 2\beta w_{tt}^{(2)} \right] \Big|_{x=x_b} = c^2 w_x^{(3)} + \epsilon \left[ -6\alpha \left( w_x^{(3)} \right)^2 + 2\beta w_{tt}^{(3)} \right] \Big|_{x=x_b}, \quad (4.10)$$

as well as some natural initial and boundary conditions.

### 4.3 Weakly Nonlinear Solution

Differentiating system (4.4) - (4.6) with respect to  $x$  and denoting  $f^{(i)} = u_x^{(i)}$  and  $g^{(i)} = w_x^{(i)}$ , we obtain the equations ‘in strains’ as

$$\begin{aligned} f_{tt}^{(1)} - f_{xx}^{(1)} &= \epsilon \left[ -6 \left( f^{(1)} \right)^2 + 2f_{tt}^{(1)} \right]_{xx}, \\ g_{tt}^{(1)} - g_{xx}^{(1)} &= \epsilon \left[ -6 \left( g^{(1)} \right)^2 + 2g_{tt}^{(1)} \right]_{xx} \end{aligned} \quad (4.11)$$

for  $x < x_a$ ,

$$\begin{aligned} f_{tt}^{(2)} - f_{xx}^{(2)} &= \epsilon \left[ -6 \left( f^{(2)} \right)^2 + 2f_{tt}^{(2)} \right]_{xx} - \epsilon \delta \left( f^{(2)} - g^{(2)} \right), \\ g_{tt}^{(2)} - c^2 g_{xx}^{(2)} &= \epsilon \left[ -6\alpha \left( g^{(2)} \right)^2 + 2\beta g_{tt}^{(2)} \right]_{xx} + \epsilon \gamma \left( f^{(2)} - g^{(2)} \right) \end{aligned} \quad (4.12)$$

for  $x_a < x < x_b$ , and

$$\begin{aligned} f_{tt}^{(3)} - f_{xx}^{(3)} &= \epsilon \left[ -6 \left( f^{(3)} \right)^2 + 2f_{tt}^{(3)} \right]_{xx}, \\ g_{tt}^{(3)} - c^2 g_{xx}^{(3)} &= \epsilon \left[ -6\alpha \left( g^{(3)} \right)^2 + 2\beta g_{tt}^{(3)} \right]_{xx}, \end{aligned} \quad (4.13)$$

for  $x > x_b$ . We are considering localised waves and apply the continuity condition (4.7) for displacements for the time interval when the waves have not yet reached the third region i.e. the waves are contained in regions one and two, which yields, by differentiating with respect to  $t$ , (4.14). Next, we consider the continuity condition for displacements for the time interval when the waves are contained within regions two and three, and similarly obtain the condition (4.15). Thus, the conditions take the form

$$\int_{-\infty}^{x_a} f_t^{(1)} dx = - \int_{x_a}^{x_b} f_t^{(2)} dx, \quad \int_{-\infty}^{x_a} g_t^{(1)} dx = - \int_{x_a}^{x_b} g_t^{(2)} dx, \quad (4.14)$$

$$\int_{x_a}^{x_b} f_t^{(2)} dx = - \int_{x_b}^{\infty} f_t^{(3)} dx, \quad \int_{x_a}^{x_b} g_t^{(2)} dx = - \int_{x_b}^{\infty} g_t^{(3)} dx. \quad (4.15)$$

From continuity of normal stress we have

$$\begin{aligned} f^{(1)} + \epsilon \left[ -6 \left( f^{(1)} \right)^2 + 2f_{tt}^{(1)} \right] \Big|_{x=x_a} &= f^{(2)} + \epsilon \left[ -6 \left( f^{(2)} \right)^2 + 2f_{tt}^{(2)} \right] \Big|_{x=x_a}, \\ g^{(1)} + \epsilon \left[ -6 \left( g^{(1)} \right)^2 + 2g_{tt}^{(1)} \right] \Big|_{x=x_a} &= c^2 g^{(2)} + \epsilon \left[ -6\alpha \left( g^{(2)} \right)^2 + 2\beta g_{tt}^{(2)} \right] \Big|_{x=x_a}, \end{aligned} \quad (4.16)$$

and

$$\begin{aligned} f^{(2)} + \epsilon \left[ -6 \left( f^{(2)} \right)^2 + 2f_{tt}^{(2)} \right] \Big|_{x=x_b} &= f^{(3)} + \epsilon \left[ -6 \left( f^{(3)} \right)^2 + 2f_{tt}^{(3)} \right] \Big|_{x=x_b}, \\ c^2 g^{(2)} + \epsilon \left[ -6\alpha \left( g^{(2)} \right)^2 + 2\beta g_{tt}^{(2)} \right] \Big|_{x=x_b} &= c^2 g^{(3)} + \epsilon \left[ -6\alpha \left( g^{(3)} \right)^2 + 2\beta g_{tt}^{(3)} \right] \Big|_{x=x_b}. \end{aligned} \quad (4.17)$$

To find the weakly nonlinear solution of the complicated scattering problem we consider the equations (4.11) - (4.13). We use several asymptotic multiple-scale expansions, and develop a space-averaging method instead of the time-averaging method used for the homogeneous initial-value problem [39]. All functions present in our expansions and their derivatives are assumed to be bounded and sufficiently rapidly decaying at infinity (these assumptions agree with our numerical simulations). In the regions where the behaviour is governed by uncoupled regularised Boussinesq equations, the derivations in Chapter 3 show that to leading order the weakly nonlinear solution is described by KdV equations. We will overview the derivation in this case, but the focus of this chapter will be for the coupled regularised Boussinesq equations.

### 4.3.1 Region 1: Two Homogeneous Layers

In the first region the equation is identical in both homogeneous layers and therefore we assume the same incident wave in both, and consider asymptotic multiple-scale expansions of the type

$$\begin{aligned} f^{(1)} &= I(\xi, X) + R^{(1)}(\eta, X) + \epsilon P^{(1)}(\xi, \eta, X) + O(\epsilon^2), \\ g^{(1)} &= I(\xi, X) + G^{(1)}(\eta, X) + \epsilon Q^{(1)}(\xi, \eta, X) + O(\epsilon^2), \end{aligned}$$

where the characteristic variables are given by  $\xi = x - t$ ,  $\eta = x + t$ , and the slow space variable  $X = \epsilon x$ . The functions  $I$  and  $R^{(1)}$ ,  $G^{(1)}$  represent the leading order incident and reflected waves respectively and  $P^{(1)}$ ,  $Q^{(1)}$  are the higher order corrections. Substituting the asymptotic expansion into the first equation in (4.11) the system is satisfied at

leading order, while at  $O(\epsilon)$  we have

$$\begin{aligned} -2P_{\xi\eta}^{(1)} &= (I_X - 6II_\xi + I_{\xi\xi\xi})_\xi + \left( R_X^{(1)} - 6R^{(1)}R_\eta^{(1)} + R_{\eta\eta\eta}^{(1)} \right)_\eta \\ &\quad - 6 \left( 2I_\xi R_\eta^{(1)} + R_{\eta\eta}^{(1)}I + I_{\xi\xi}R^{(1)} \right), \end{aligned} \quad (4.18)$$

and a similar equation can be obtained for the second layer. We average (4.18) with respect to the fast space variable  $x$  using

$$\lim_{\chi \rightarrow -\infty} \frac{1}{x_a - \chi} \int_\chi^{x_a} \dots dx, \quad (4.19)$$

in the reference frame moving with the linear speed of right- and left-propagating waves (that is, at constant  $\xi$  or  $\eta$ ). Assuming that all functions and their derivatives remain bounded (in order to avoid secular terms in asymptotic expansions) and decay sufficiently rapidly at infinity we have, for example at constant  $\xi$ ,

$$\begin{aligned} \lim_{\chi \rightarrow -\infty} \frac{1}{x_a - \chi} \int_\chi^{x_a} P_{\xi\eta}^{(1)} dx &= \lim_{\chi \rightarrow -\infty} \frac{1}{2(x_a - \chi)} \int_{2\chi - \xi}^{2x_a - \xi} P_{\xi\eta}^{(1)} d\eta \\ &= \lim_{\chi \rightarrow -\infty} \frac{1}{2(x_a - \chi)} \left[ P_\xi^{(1)} \right]_{2\chi - \xi}^{2x_a - \xi} = 0. \end{aligned} \quad (4.20)$$

Similarly averaging (4.18) with respect to  $x$  at constant  $\eta$  gives

$$\lim_{\chi \rightarrow -\infty} \frac{1}{x_a - \chi} \int_\chi^{x_a} P_{\xi\eta}^{(1)} dx = \lim_{\chi \rightarrow -\infty} \frac{1}{2(x_a - \chi)} \int_{2\chi - \eta}^{2x_a - \eta} P_{\xi\eta}^{(1)} d\xi = 0. \quad (4.21)$$

Therefore we can average (4.18) at constant  $\xi$  to obtain

$$(I_X - 6II_\xi + I_{\xi\xi\xi})_\xi = 0. \quad (4.22)$$

Similarly, averaging (4.18) with respect to  $x$  at constant  $\eta$  gives

$$\left( R_X^{(1)} - 6R^{(1)}R_\eta^{(1)} + R_{\eta\eta\eta}^{(1)} \right)_\eta = 0. \quad (4.23)$$

In each case, we can integrate with respect to the relevant characteristic variable and, recalling that there are no waves at infinity, we obtain

$$I_X - 6II_\xi + I_{\xi\xi\xi} = 0, \quad (4.24)$$

and

$$R_X^{(1)} - 6R^{(1)}R_\eta^{(1)} + R_{\eta\eta\eta}^{(1)} = 0. \quad (4.25)$$

We can then simplify (4.18) using (4.24) and (4.25) and integrate with respect to the characteristic variables to obtain

$$P^{(1)} = 3 \left( 2IR^{(1)} + R_{\eta}^{(1)} \int I \, d\xi + I_{\xi} \int R^{(1)} \, d\eta \right) + \phi_1^{(1)}(\xi, X) + \psi_1^{(1)}(\eta, X), \quad (4.26)$$

where  $\phi_1^{(1)}$  and  $\psi_1^{(1)}$  are arbitrary functions. For the second layer, we have the same equation for the incident wave, (4.24), and for  $G$  we have

$$G_X^{(1)} - 6G^{(1)}G_{\eta}^{(1)} + G_{\eta\eta\eta}^{(1)} = 0. \quad (4.27)$$

The higher order corrections in this layer are given by

$$Q^{(1)} = 3 \left( 2IG^{(1)} + G_{\eta}^{(1)} \int I \, d\xi + I_{\xi} \int G^{(1)} \, d\eta \right) + \phi_2^{(1)}(\xi, X) + \psi_2^{(1)}(\eta, X). \quad (4.28)$$

The first radiation condition is the same as for the previous case in Chapter 3, that is we require that the solution to the problem should not change the incident wave. For the case of an incident solitary wave this implies that  $\phi_1^{(1)} = 0$  and  $\phi_2^{(1)} = 0$ .

### 4.3.2 Region 2: Bi-Layer with Soft Bonding

We stated earlier that we assume the layers have close properties, so that  $c - 1 = O(\epsilon)$ . In this case, the cRB equations admit solutions in the form of radiating solitary waves, as discussed in the introduction to this chapter. Thus, we note that

$$c - 1 = O(\epsilon) \quad \Rightarrow \quad \frac{c^2 - 1}{\epsilon} = O(1),$$

and, following [39], we rearrange the equation for  $w$  in (4.12) as

$$g_{tt}^{(2)} - g_{xx}^{(2)} = \epsilon \left[ -6\alpha \left( g^{(2)} \right)^2 + 2\beta g_{tt}^{(2)} + \frac{c^2 - 1}{\epsilon} g^{(2)} \right]_{xx} + \epsilon\gamma \left( f^{(2)} - g^{(2)} \right). \quad (4.29)$$

Therefore, we can use one set of characteristic variables for  $f^{(2)}$  and  $g^{(2)}$  and this suggests that the waves in each layer will move at the same speed. Let us assume that there is a weakly nonlinear solution to (4.12) of the form

$$\begin{aligned} f^{(2)} &= T^{(2)}(\xi, X) + R^{(2)}(\eta, X) + \epsilon P^{(2)}(\xi, \eta, X) + O(\epsilon^2), \\ g^{(2)} &= S^{(2)}(\xi, X) + G^{(2)}(\eta, X) + \epsilon Q^{(2)}(\xi, \eta, X) + O(\epsilon^2). \end{aligned}$$

The characteristic variables  $\xi$ ,  $\eta$  and  $X$  are the same as before,  $T^{(2)}$  and  $S^{(2)}$  represent the transmitted waves in the second section of the bar, where  $T$  is for the upper layer

and  $S$  is for the lower layer. Similarly  $R^{(2)}$  and  $G^{(2)}$  are the reflected waves, and the higher order corrections in this section are given by  $P^{(2)}$  and  $Q^{(2)}$ , for the upper and lower layers respectively.

The solution is considered from the time when the waves enter the region at  $x = x_a$ , until the waves reflected from the boundary  $x = x_b$ , between the second and the third region, reach the boundary  $x = x_a$ , between the first and the second region. Moreover, the boundary  $x = x_b$  is assumed to be sufficiently far away from the boundary  $x = x_a$ , allowing us to use the averaging

$$\lim_{x_b \rightarrow \infty} \frac{1}{x_b - x_a} \int_{x_a}^{x_b} \dots dx. \quad (4.30)$$

Substituting the asymptotic expansion into the equation for  $f^{(2)}$  in (4.12) the equation is satisfied at leading order, while at  $O(\epsilon)$  we have

$$\begin{aligned} -2P_{\xi\eta}^{(2)} &= \left( T_X^{(2)} - 6T^{(2)}T_\xi^{(2)} + T_{\xi\xi\xi}^{(2)} \right)_\xi - 6 \left( 2T_\xi^{(2)}R_\eta^{(2)} + T^{(2)}R_{\eta\eta}^{(2)} + T_{\xi\xi}^{(2)}R^{(2)} \right) \\ &\quad + \left( R_X^{(2)} - 6R^{(2)}R_\eta^{(2)} + R_{\eta\eta\eta}^{(2)} \right)_\eta - \frac{\delta}{2} \left( T^{(2)} - S^{(2)} + R^{(2)} - G^{(2)} \right). \end{aligned} \quad (4.31)$$

For the equation governing  $g^{(2)}$  we have

$$\begin{aligned} 2Q_{\xi\eta}^{(2)} &= \left( S_X^{(2)} + \frac{c^2 - 1}{2\epsilon} S_\xi^{(2)} - 6\alpha S^{(2)} S_\xi^{(2)} + \beta S_{\xi\xi\xi}^{(2)} \right)_\xi + \frac{\gamma}{2} \left( T^{(2)} - S^{(2)} + R^{(2)} - G^{(2)} \right) \\ &\quad + \left( G_X^{(2)} + \frac{c^2 - 1}{2\epsilon} G_\eta^{(2)} - 6\alpha G^{(2)} G_\eta^{(2)} + \beta G_{\eta\eta\eta}^{(2)} \right)_\eta \\ &\quad - 6\alpha \left( 2S_\xi^{(2)} G_\eta^{(2)} + S^{(2)} G_{\eta\eta}^{(2)} + S_{\xi\xi}^{(2)} G^{(2)} \right). \end{aligned} \quad (4.32)$$

We average equations (4.31) and (4.32) with respect to the fast space variable  $x$  as defined in (4.30). In each case, we average at constant  $\xi$  or  $\eta$ . The same argument for averaging  $P^{(1)}$  and  $Q^{(1)}$  used in the previous section, in (4.20) and (4.21), applies in this case as  $P^{(2)}$  and  $Q^{(2)}$  are also assumed to be bounded and sufficiently rapidly decaying at infinity. Therefore  $P^{(2)}$  and  $Q^{(2)}$  are both zero when averaged at either constant  $\xi$  or constant  $\eta$ . Averaging (4.31) and (4.32) at constant  $\xi$  gives

$$\left( T_X^{(2)} - 6T^{(2)}T_\xi^{(2)} + T_{\xi\xi\xi}^{(2)} \right)_\xi = \frac{\delta}{2} \left( T^{(2)} - S^{(2)} \right), \quad (4.33)$$

$$\left( S_X^{(2)} + \frac{c^2 - 1}{2\epsilon} S_\xi^{(2)} - 6\alpha S^{(2)} S_\xi^{(2)} + \beta S_{\xi\xi\xi}^{(2)} \right)_\xi = \frac{\gamma}{2} \left( S^{(2)} - T^{(2)} \right). \quad (4.34)$$

Equations (4.33) and (4.34) form a system of coupled Ostrovsky equations [39]. Coupled Ostrovsky equations appear naturally in the description of nonlinear waves in layered

waveguides, both solid and fluid [41, 43].

Similarly, averaging (4.31) and (4.32) at constant  $\eta$  gives

$$\left( R_X^{(2)} - 6R^{(2)}R_\eta^{(2)} + R_{\eta\eta\eta}^{(2)} \right)_\eta = \frac{\delta}{2} \left( R^{(2)} - G^{(2)} \right), \quad (4.35)$$

$$\left( G_X^{(2)} + \frac{c^2 - 1}{2\epsilon} G_\eta^{(2)} - 6\alpha G^{(2)}G_\eta^{(2)} + \beta G_{\eta\eta\eta}^{(2)} \right)_\eta = \frac{\gamma}{2} \left( G^{(2)} - R^{(2)} \right), \quad (4.36)$$

respectively. Therefore, to leading order, the transmitted and reflected waves are described by two systems of coupled Ostrovsky equations. This result is consistent with the time-averaged derivation [39].

Substituting (4.33) and (4.35) into (4.31) and integrating with respect to the characteristic variables, we obtain

$$P^{(2)} = 3 \left( 2T^{(2)}R^{(2)} + R_\eta^{(2)} \int T^{(2)} d\xi + T_\xi^{(2)} \int R^{(2)} d\eta \right) + \phi_1^{(2)}(\xi, X) + \psi_1^{(2)}(\eta, X), \quad (4.37)$$

where  $\phi_1^{(2)}$ ,  $\psi_1^{(2)}$  are arbitrary functions.

Similarly, substituting (4.34) and (4.36) into (4.32) and integrating with respect to the characteristic variables, we obtain

$$Q^{(2)} = 3\alpha \left( 2S^{(2)}G^{(2)} + G_\eta^{(2)} \int S^{(2)} d\xi + S_\xi^{(2)} \int G^{(2)} d\eta \right) + \phi_2^{(2)}(\xi, X) + \psi_2^{(2)}(\eta, X), \quad (4.38)$$

where  $\phi_2^{(2)}$ ,  $\psi_2^{(2)}$  are arbitrary functions.

### 4.3.3 Region 3: Delamination

We now consider the third region, where the same bi-layered waveguide does not have a bonding layer, modelling delamination. The motion in this region is governed by two uncoupled regularised Boussinesq equations, but with differing coefficients in each layer. We look for a weakly nonlinear solution to (4.13) of the form

$$\begin{aligned} f^{(3)} &= T^{(3)}(\xi, X) + \epsilon P^{(3)}(\xi, \eta, X) + O(\epsilon^2), \\ g^{(3)} &= S^{(3)}(\nu, X) + \epsilon Q^{(3)}(\nu, \zeta, X) + O(\epsilon^2), \end{aligned}$$

where we have  $X = \epsilon x$  and we use two sets of characteristic variables:  $\xi = x - t$ ,  $\eta = x + t$ ; and  $\nu = x - ct$ ,  $\zeta = x + ct$ . Substituting this into system (4.13) the equation is satisfied

at leading order, while at  $O(\epsilon)$  we have

$$-2P_{\xi\eta}^{(3)} = \left( T_X^{(3)} - 6T^{(3)}T_\xi^{(3)} + T_{\xi\xi\xi}^{(3)} \right)_\xi, \quad (4.39)$$

$$-2c^2Q_{\nu\zeta}^{(3)} = \left( S_X^{(3)} - 6\frac{\alpha}{c^2}S^{(3)}S_\nu^{(3)} + \beta S_{\nu\nu\nu}^{(3)} \right)_\nu. \quad (4.40)$$

We define the averaging in this region as

$$\lim_{\chi \rightarrow \infty} \frac{1}{\chi - x_b} \int_{x_b}^{\chi} \dots dx. \quad (4.41)$$

As before, the function  $P^{(3)}$  averaged at constant  $\xi$  and  $\eta$ , or  $Q^{(3)}$  averaged at constant  $\nu$  and  $\zeta$ , will be zero. We note that averaging (4.39) at constant  $\eta$ , or averaging (4.40) at constant  $\zeta$ , will yield no new information as the equation averages to zero. Therefore, averaging (4.39) with respect to constant  $\xi$  and (4.40) with respect to constant  $\nu$ , and integrating with respect to the appropriate characteristic variable, we obtain two KdV equations of the form

$$T_X^{(3)} - 6T^{(3)}T_\xi^{(3)} + T_{\xi\xi\xi}^{(3)} = 0, \quad (4.42)$$

$$S_X^{(3)} - 6\frac{\alpha}{c^2}S^{(3)}S_\nu^{(3)} + \beta S_{\nu\nu\nu}^{(3)} = 0. \quad (4.43)$$

Substituting the results for (4.42) into (4.39) and integrating with respect to the characteristic variables, we obtain

$$P^{(3)} = \phi_1^{(3)}(\xi, X) + \psi_1^{(3)}(\eta, X), \quad (4.44)$$

where  $\phi_1^{(3)}$ ,  $\psi_1^{(3)}$  are arbitrary functions. The second radiation condition, as used in Chapter 3, states that if the incident wave is right-propagating, then there should be no left-propagating waves in the transmitted wave field. Thus  $\psi_1^{(3)} = 0$ .

Similarly, substituting (4.43) into (4.40) and integrating with respect to the characteristic variables, we obtain

$$Q^{(3)} = \phi_2^{(3)}(\nu, X) + \psi_2^{(3)}(\zeta, X), \quad (4.45)$$

where  $\phi_2^{(3)}$ ,  $\psi_2^{(3)}$  are arbitrary functions. By the second radiation condition, as used above, we have  $\psi_2^{(3)} = 0$ .

We note that the functions which remained undefined in the higher order corrections can be found by considering higher order terms in the equations of motion and the continuity conditions, similarly to the solution of the initial-value problems [39, 46]. However, this is beyond the scope of our work.

### 4.3.4 Matching at Boundaries: Continuity Conditions

In order to find ‘initial conditions’ for the equations derived in Sections 4.3.1 - 4.3.3, we collect the expressions for the weakly nonlinear solutions and substitute them into the continuity conditions (4.14) - (4.17).

We first consider the continuity conditions for displacements for the time interval when the waves have not yet reached the third region. The displacement at negative infinity is assumed to be constant. Differentiating the continuity conditions (4.14) with respect to time at  $x = x_a$ , and recalling that  $f^{(i)} = u_x^{(i)}$ ,  $g^{(i)} = w_x^{(i)}$ , we obtain conditions in terms of the strain rates. So we have

$$\int_{-\infty}^{x_a} f_t^{(1)} dx = - \int_{x_a}^{x_b} f_t^{(2)} dx, \quad (4.46)$$

$$\int_{-\infty}^{x_a} g_t^{(1)} dx = - \int_{x_a}^{x_b} g_t^{(2)} dx. \quad (4.47)$$

Substituting the weakly nonlinear solutions obtained in Section 4.3 into (4.46) and noting that the reflected waves  $R^{(2)}$  and  $G^{(2)}$  in the second section are not yet present, we obtain at leading order

$$\int_{-\infty}^{x_a} (I_\xi - R_\eta^{(1)}) dx = - \int_{x_a}^{x_b} T_\xi^{(2)} dx. \quad (4.48)$$

We can integrate to obtain an expression at  $x = x_a$  by noting that integration with respect to  $x$  can be reduced to integration with respect to the characteristic variable, as  $x$  appears linearly in the expressions for the characteristic variables. By the assumption that the strain waves are localised in the first two regions, when evaluated at either  $x = -\infty$  or  $x = x_b$  the expression will be zero. Therefore, from (4.48) we obtain

$$I|_{X=\epsilon x_a} - R^{(1)}|_{X=\epsilon x_a} = T^{(2)}|_{X=\epsilon x_a}. \quad (4.49)$$

Similarly, from (4.47) we obtain

$$I|_{X=\epsilon x_a} - G^{(1)}|_{X=\epsilon x_a} = cS^{(2)}|_{X=\epsilon x_a}. \quad (4.50)$$

Next, we consider the continuity conditions for displacements for the time interval when the localised strain waves are present in all three regions, but the waves reflected from the boundary  $x = x_b$  between the second and the third region have not yet reached the boundary  $x = x_a$  between the first and the second region. The displacement at positive infinity is assumed to be equal to zero (the waves propagate into unperturbed media). Differentiating the continuity conditions (4.15) with respect to time at  $x = x_b$ ,

and recalling that  $f^{(i)} = u_x^{(i)}$ ,  $g^{(i)} = w_x^{(i)}$ , we obtain the relations

$$\int_{x_a}^{x_b} f_t^{(2)} dx = - \int_{x_b}^{\infty} f_t^{(3)} dx, \quad (4.51)$$

$$\int_{x_a}^{x_b} g_t^{(2)} dx = - \int_{x_b}^{\infty} g_t^{(3)} dx. \quad (4.52)$$

Then, in a similar way to the previous considerations, we obtain

$$T^{(2)}|_{X=\epsilon x_b} - R^{(2)}|_{X=\epsilon x_b} = T^{(3)}|_{X=\epsilon x_b}, \quad (4.53)$$

$$cS^{(2)}|_{X=\epsilon x_b} - cG^{(2)}|_{X=\epsilon x_b} = cS^{(3)}|_{X=\epsilon x_b}. \quad (4.54)$$

We now make use of the continuity conditions for normal stress and, substituting the relevant weakly nonlinear solution into (4.16) we obtain to leading order

$$I|_{X=\epsilon x_a} + R^{(1)}|_{X=\epsilon x_a} = T^{(2)}|_{X=\epsilon x_a}, \quad (4.55)$$

$$I|_{X=\epsilon x_a} + G^{(1)}|_{X=\epsilon x_a} = c^2 S^{(2)}|_{X=\epsilon x_a}. \quad (4.56)$$

Similarly, substituting the relevant weakly nonlinear solutions into (4.17) we have, to leading order,

$$T^{(2)}|_{X=\epsilon x_b} + R^{(2)}|_{X=\epsilon x_b} = T^{(3)}|_{X=\epsilon x_b}, \quad (4.57)$$

$$c^2 S^{(2)}|_{X=\epsilon x_b} + c^2 G^{(2)}|_{X=\epsilon x_b} = c^2 S^{(3)}|_{X=\epsilon x_b}. \quad (4.58)$$

We can now find ‘initial conditions’ for the systems describing transmitted and reflected waves in each section of the bar, expressed in terms of the given incident wave. For the upper layer we have

$$R^{(1)}|_{X=\epsilon x_a} = C_R^{(1)} I|_{X=\epsilon x_a}, \quad T^{(2)}|_{X=\epsilon x_a} = C_T^{(1)} I|_{X=\epsilon x_a}, \quad (4.59)$$

$$R^{(2)}|_{X=\epsilon x_b} = C_R^{(2)} T^{(2)}|_{X=\epsilon x_b}, \quad T^{(3)}|_{X=\epsilon x_b} = C_T^{(2)} T^{(2)}|_{X=\epsilon x_b}, \quad (4.60)$$

where  $C_R^{(i)} = 0$  and  $C_T^{(i)} = 1$  for all  $i$ .

Similarly for the lower layer we have

$$G^{(1)}|_{X=\epsilon x_a} = D_R^{(1)} I|_{X=\epsilon x_a}, \quad S^{(2)}|_{X=\epsilon x_a} = D_T^{(1)} I|_{X=\epsilon x_a}, \quad (4.61)$$

$$G^{(2)}|_{X=\epsilon x_b} = D_R^{(2)} S^{(2)}|_{X=\epsilon x_b}, \quad S^{(3)}|_{X=\epsilon x_b} = D_T^{(2)} S^{(2)}|_{X=\epsilon x_b}, \quad (4.62)$$

where

$$\begin{aligned} D_R^{(1)} &= \frac{c-1}{c+1}, & D_T^{(1)} &= \frac{2}{c(1+c)}, \\ D_R^{(2)} &= 0, & D_T^{(2)} &= 1. \end{aligned}$$

These coefficients agree with previous work for a perfectly bonded waveguide [30, 42] and are intuitive as we would expect a wave to be, to leading order, wholly transmitted when travelling along a layer of the same material. If the value of  $c$  varies between sections of the bar i.e. the material in a single layer varies across the bar, then the coefficients should be calculated using the respective values of  $c$ .

## 4.4 Numerical Modelling

In our first case study we compare the results of the semi-analytical numerical modelling, based on the leading order terms of the weakly nonlinear solution of Section 4.3, with the results of direct numerical simulations for the problem (4.4) - (4.10). We also compare numerical results with theoretical predictions for the amplitude of the lead soliton in the delaminated region, made using the IST. We solve the original Boussinesq equations using the direct numerical method described in Appendix A.3, and the weakly nonlinear solution derived in Section 4.3 using the pseudospectral method described in Appendix C.

For the direct numerical method we use step sizes of  $\Delta x = \Delta t = 0.01$  and, for the pseudospectral method, we use  $\Delta \xi = 0.3$  (the same step size is used for all characteristic variables) and  $\Delta X = 0.001$ . In all cases, we assume  $\alpha = 1.05$ ,  $\beta = 1.05$ ,  $c = 1 + \epsilon/2$  and  $\epsilon = 0.05$ .

We note that, in a similar way to the single Ostrovsky equation, the coupled Ostrovsky equations (4.33) - (4.34) and (4.35) - (4.36) imply zero mean constraints

$$\int_{-\infty}^{\infty} (T^{(2)} - S^{(2)}) \, d\xi = 0 \quad \text{and} \quad \int_{-\infty}^{\infty} (R^{(2)} - G^{(2)}) \, d\eta = 0.$$

Therefore we first use initial conditions for the incident strain solitary wave which include a pedestal term [46], to guarantee zero mean, and then show that for this class of problems, one can also work with initial conditions in the form of pure strain solitary waves, without the pedestal terms. Indeed, in the latter case the zero mean constraints are still approximately satisfied, by the nature of the solutions of the problem, which we established in the direct numerical simulations using the finite-difference method. If the domain is given by  $[-L, L]$ , the average  $\frac{1}{2L} \int_{-L}^L (u - w) \, d\xi$  is  $O(10^{-5})$ , showing that the

zero mean constraint is approximately satisfied. A more accurate approach is required for general initial conditions with non-zero mean value [46].

Thus we use the following initial condition for the displacement in (4.4) (corresponding to localised initial condition for the strain in (4.11), integrated with respect to  $x$ ):

$$u(x, 0) = A \left[ \tanh\left(\frac{x}{\Lambda}\right) - 1 \right] - \Gamma \left[ \tanh\left(\frac{x+x_0}{\Lambda S}\right) + \tanh\left(\frac{x-x_0}{\Lambda S}\right) - 2 \right], \quad (4.63)$$

where we have

$$A = -\frac{v_1 \sqrt{v_1^2 - 1}}{\sqrt{2\epsilon}}, \quad \Lambda = \frac{2\sqrt{2\epsilon}v_1}{\sqrt{v_1^2 - 1}}, \quad \Gamma = \frac{\sigma A \tanh\left(\frac{L}{\Lambda}\right)}{\tanh\left(\frac{L+x_0}{\Lambda S}\right) + \tanh\left(\frac{L-x_0}{\Lambda S}\right)},$$

$\sigma$  can be zero or one,  $2L$  is the length of the domain,  $x_0$  is an arbitrary phase shift and the corresponding strain has zero mean (for  $\sigma = 1$ ). The constant of integration is chosen so that the waves propagate into an unperturbed medium. As we have a second order time derivative, we require two initial conditions for this equation. We have taken the exact travelling wave solution of the equation and therefore the second initial condition takes the form

$$u_t(x, 0) = -v_1 u_x(x, 0), \quad (4.64)$$

where  $u_x(x, 0)$  takes the form

$$u_x(x, 0) = \frac{A}{\Lambda} \operatorname{sech}^2\left(\frac{x}{\Lambda}\right) - \frac{\Gamma}{\Lambda S} \left[ \operatorname{sech}^2\left(\frac{x+x_0}{\Lambda S}\right) + \operatorname{sech}^2\left(\frac{x-x_0}{\Lambda S}\right) \right]. \quad (4.65)$$

Taking a forward difference approximation in time allows us to formulate the solution at  $u(x, \Delta t)$ , as required by the numerical scheme outlined in Appendix A.3.

The amplitude of the pedestal for the corresponding strains can be reduced by increasing the value of  $S$ . In all cases discussed here,  $S = 10$  and we set  $x_0 = 0$ . For  $w(x, 0)$  and  $w(x, \Delta t)$  we use the same expressions as we take the same initial condition in both layers. If the initial condition was given by an explicit analytic function, then we could deduce the second initial condition for the scheme directly. As with the previous case for a perfectly bonded bar, simulations have shown that either case is sufficiently accurate.

For the semi-analytical method we take the exact solitary wave solution of (4.24) governing the incident wave, with the same pedestal term (differentiated with respect to  $x$ ) as used in (4.63),

$$I(\xi, 0) = \tilde{A} \operatorname{sech}^2\left(\frac{\xi}{\tilde{\Lambda}}\right) - \frac{\tilde{\Gamma}}{\tilde{S}} \left[ \operatorname{sech}^2\left(\frac{\xi+x_0}{\tilde{\Lambda}\tilde{S}}\right) + \operatorname{sech}^2\left(\frac{\xi-x_0}{\tilde{\Lambda}\tilde{S}}\right) \right], \quad (4.66)$$

where

$$\tilde{A} = -\frac{v}{2}, \quad \tilde{\Lambda} = \frac{2}{\sqrt{v}}, \quad \tilde{\Gamma} = \frac{\sigma \tilde{A} \tanh\left(\frac{L}{\tilde{\Lambda}}\right)}{\tanh\left(\frac{L+x_0}{\tilde{\Lambda}S}\right) + \tanh\left(\frac{L-x_0}{\tilde{\Lambda}S}\right)},$$

where  $v$  is related to  $v_1$  by the approximate relation  $v_1 = 1 + \epsilon v + O(\epsilon^2)$ . For the initial conditions in other sections of the bi-layer, we make use of the relations in Section 4.3.4 to obtain the initial conditions in terms of (4.66).

#### 4.4.1 Solitons in the Delaminated Section

To obtain quantitative predictions for parameters of solitons in the delaminated section we use the IST applied to the KdV equations (4.42) and (4.43) derived in Section 4.3.3. Recall from the previous chapter that the solution of an initial-value problem for the KdV equation

$$U_\tau - 6UU_\chi + U_{\chi\chi\chi} = 0, \quad U|_{\tau=0} = U_0(\chi), \quad (4.67)$$

on the infinite line, for a sufficiently rapidly decaying initial condition  $U_0(\chi)$ , is related to the spectral problem for the Schrödinger equation

$$\Psi_{\chi\chi} + [\lambda - U_0(\chi)] \Psi = 0, \quad (4.68)$$

where  $\lambda$  is the spectral parameter [20]. In particular, parameters of solitons are defined by the discrete spectrum of the equation (4.68). In our previous studies of the scattering of an incident solitary wave in the delaminated area of the perfectly bonded waveguide, the discrete spectrum could be found analytically. However, in the present study, we are dealing with the scattering of radiating solitary waves generated in a two-layered bar with soft bonding, and scattered in the delaminated region of the bar. As we do not have an analytical expression for the radiating solitary wave, we have to find the spectrum of the Schrödinger equation numerically.

To achieve this we implement a shooting method [109]. We consider the potential  $U_0(\chi)$  for the Schrödinger equation, which is the initial condition in the KdV problem (4.67). It is well known that the discrete spectrum is bounded by the minimum of the initial condition (negative value) and zero [92]. Since the potential  $U_0(\chi)$  is localised, the eigenfunctions have the asymptotic behaviour

$$\Psi(\chi) = \begin{cases} e^{r\chi}, & \chi \rightarrow -\infty, \\ e^{-r\chi}, & \chi \rightarrow \infty, \end{cases} \quad (4.69)$$

where  $\lambda = -r^2$ . We rewrite the Schrödinger equation (4.68) in the form

$$\Psi_\chi = \Phi, \quad \Phi_\chi = [U_0(\chi) - \lambda] \Psi, \quad (4.70)$$

and solve this system from the boundary  $\chi = a$  to  $\chi = b$ . We normalise the solution by setting  $\Psi(a) = 1$  and  $\Phi(a) = r$ . The system is then solved using the standard Runge-Kutta 4<sup>th</sup> order method. The ratio of the values of these two functions is tested at the right boundary against the relation  $\Phi(b)/\Psi(b) = -r$  to determine if  $r$  is an eigenvalue.

We start with the least possible value for an eigenvalue (the minimum of the initial condition) and iterate to zero in sufficiently small steps in order to determine the eigenvalues to the desired accuracy. In our present study we consider the cases when in each layer there is only one soliton in the delaminated region. We use the method described here to determine the parameters of this soliton (in each layer), and compare with the solitons emerging in our modelling. In other settings, multiple solitons can be generated by a single incident soliton, such as those seen in a bar with perfect bonding in our previous study.

#### 4.4.2 Delamination of Semi-Infinite Length

We first consider the bi-layer shown in Figure 4.3 and use the initial conditions (4.63) and (4.66) with zero mean i.e. with  $\sigma = 1$ . The comparison between the two numerical approaches in this case can be seen in Figure 4.4. A radiating solitary wave is formed in the bonded section of the bar, shown at  $t = 600$ . When this radiating solitary wave enters the delaminated section of the bar, the soliton separates from the tail and becomes a classical soliton with dispersive radiation following behind.

The agreement between the semi-analytical method and the direct numerical method is good for the solitons and reasonable for the tail, with a small phase shift introduced. The agreement is improved by reducing  $\epsilon$ , and this has been tested for a number of values, but are omitted for brevity.

If we take the same initial conditions with non-zero mean, i.e.  $\sigma = 0$ , we obtain a similar result to the previously discussed case, as can be seen in Figure 4.5. The radiating solitary waves generated in the two layers are close to each other, and therefore the zero mean constraints for the difference of the two solutions are approximately satisfied (see discussion at start of Section 4.4).

We now apply the IST framework to the waves entering the delaminated section of the bar, as the behaviour of the transmitted waves in the two layers in this section is governed by two separate KdV equations. Since there is only one discrete eigenvalue for

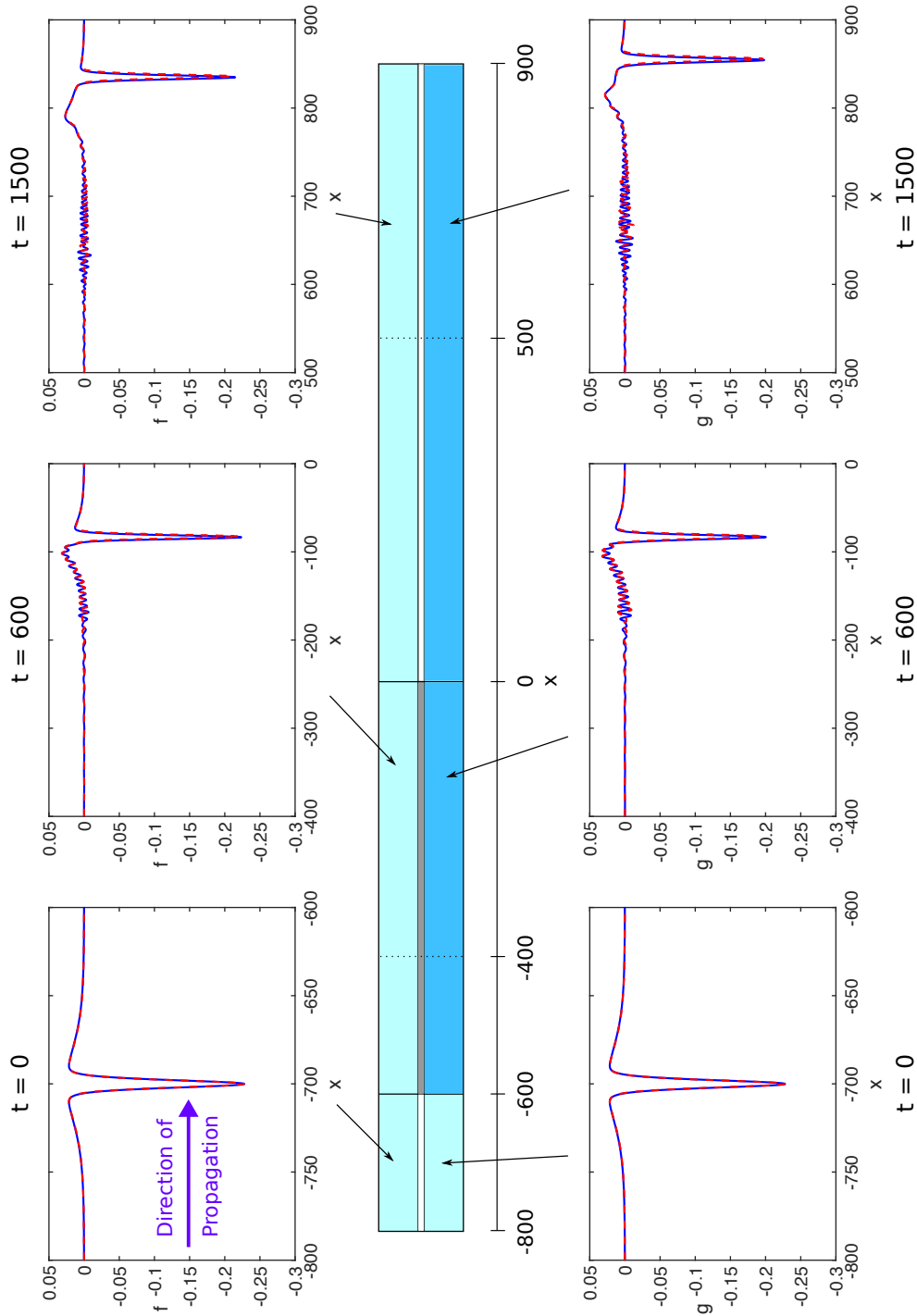


FIGURE 4.4: The waves  $f$  (upper layer) and  $g$  (lower layer) in the various sections of the bi-layer, for  $\alpha = \beta = 1.05$ ,  $c = 1.025$ ,  $\delta = \gamma = 1$ ,  $v_1 = 1.025$ ,  $\sigma = 1$  and  $\epsilon = 0.05$ : direct numerical simulations (blue, solid line) and semi-analytical method (red, dashed line). For the direct numerical method, the full computational domain is  $[-1000, 1000]$ . In the pseudospectral method,  $N = 16384$ .

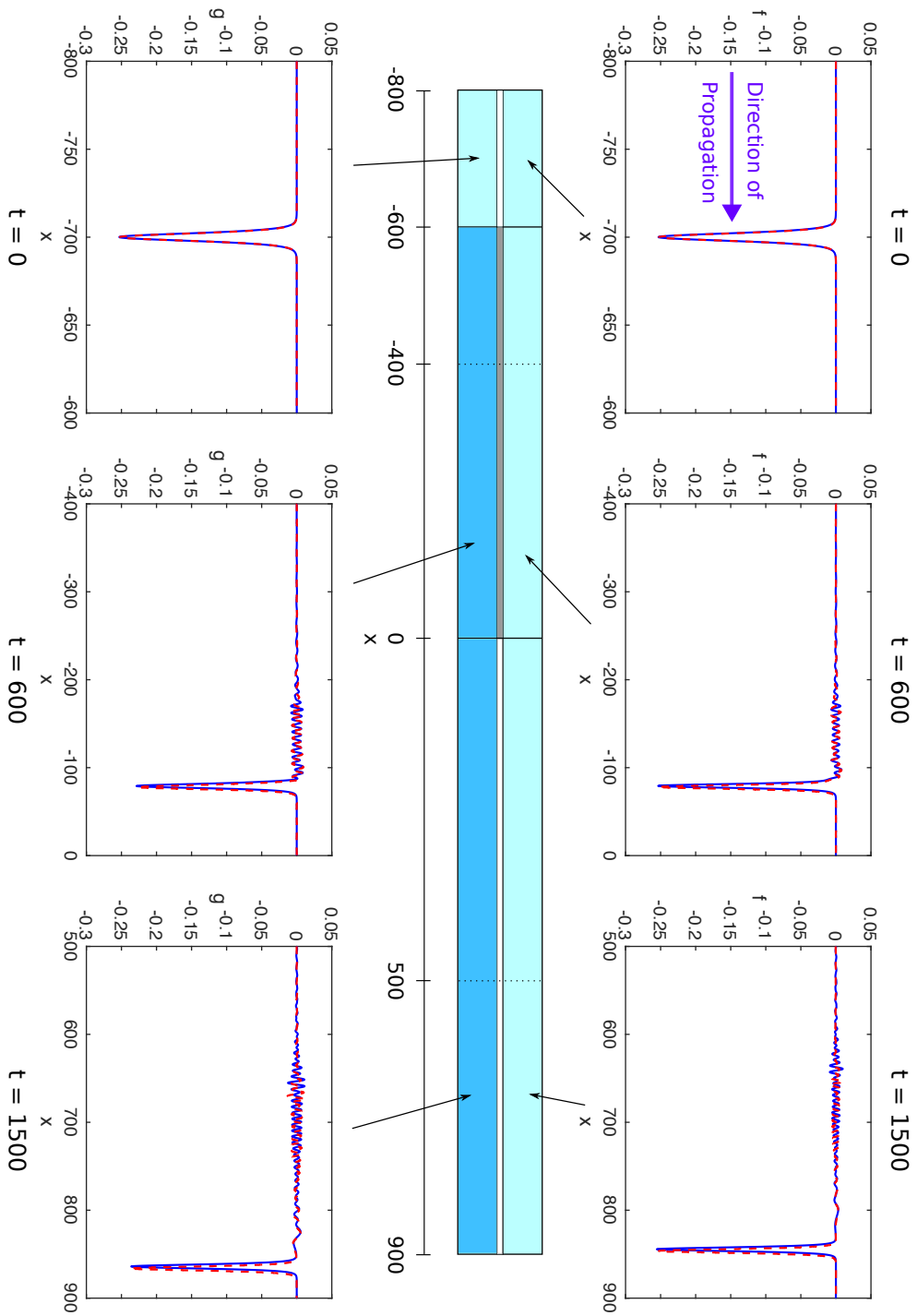


FIGURE 4.5: The waves  $f$  (upper layer) and  $g$  (lower layer) in the various sections of the bi-layer, for  $\alpha = \beta = 1.05$ ,  $c = 1.025$ ,  $\delta = \gamma = 1$ ,  $v = 1.025$ ,  $\sigma = 0$  and  $\epsilon = 0.05$ : direct numerical simulations (blue, solid line) and semi-analytical method (red, dashed line). For the direct numerical method, the full computational domain is  $[-1000, 1000]$ . In the pseudospectral method,  $N = 16384$ .

each layer of the waveguide, the long time asymptotic behaviour of the solution of the appropriate KdV equation consists of one soliton and dispersive radiation, which in the canonical form (4.67) is given by

$$U \sim -2r^2 \operatorname{sech}^2 [r (\chi - 4r^2 t - \chi_0)] + \text{radiation},$$

where  $r$  is defined by the eigenvalue  $\lambda = -r^2$ , and  $\chi_0$  is the phase shift.

We use the theoretical predictions to justify the numerical schemes used in this chapter. In each layer, the height of the soliton found using these schemes has been compared with the theoretical prediction using the IST, to confirm that the numerical schemes resolve the behaviour of the system correctly. The theoretical (IST) predictions and the numerical results for the height of the soliton are compared in Table 4.1.

Regime	Layer	Numerical	Theoretical
$\sigma = 1$	1	-0.2545	-0.2473
$\sigma = 1$	2	-0.2301	-0.2192
$\sigma = 0$	1	-0.2979	-0.2979
$\sigma = 0$	2	-0.2680	-0.2680

TABLE 4.1: Comparison of numerically calculated soliton amplitudes in the delaminated area for both layers with the predicted value using the IST, for zero mean ( $\sigma = 1$ ) and non-zero mean ( $\sigma = 0$ ) initial conditions.

In the case with zero mean initial condition, the prediction of the heights using the IST underestimates the numerical solution, as the solitons have not yet fully separated from the negative pedestal. These solitons take a very long time to separate - the pedestal still does not separate when the maximum time is increased by a factor of ten. In the case with initial condition having non-zero mean, the agreement between the theoretical predictions and the numerical results is excellent.

#### 4.4.3 Delamination of Finite Length

We now consider the same question posed in Section 3.6: is it possible to determine if there is a delamination in some part of the bar, between two bonded regions? In the previous case we had a perfect bond between the layers and therefore the waves entering the delaminated region were solitary waves. In our case, we have radiating solitary waves entering the delaminated region. A graphical representation of this structure is shown in Figure 4.6, and all considerations of Section 4.3 are extended to this situation. We introduce a fourth region in our modelling, with identical coefficients and structure to the second region of the bar. The weakly nonlinear solution in this fourth region is the

same as the second region, and we have full transmission as we did between regions two and three.

We know that transmitted waves will propagate in the delaminated area with speeds close to the characteristic speeds of the linear waves, and therefore the time it will take for the wave to travel through a delaminated region, of length  $l$ , can be estimated as  $T_i \approx l/c_i$ , where  $i$  represents the layers in the bar. Indeed, when the radiating solitary waves enter the delaminated region, as seen in Figure 4.7, the solitons propagate with speeds close to their respective characteristic speeds. When these solitons enter the second bonded region they again generate radiating solitary waves. If the separation between the two solitons is reasonably large when they enter the second bonded region, we see a distinctive double-humped wave of significantly reduced amplitude - a clear sign of delamination. If this delaminated region is even larger, so that the waves in both layers are distinctly separated, then we would obtain two well separated radiating solitary waves of smaller amplitude.

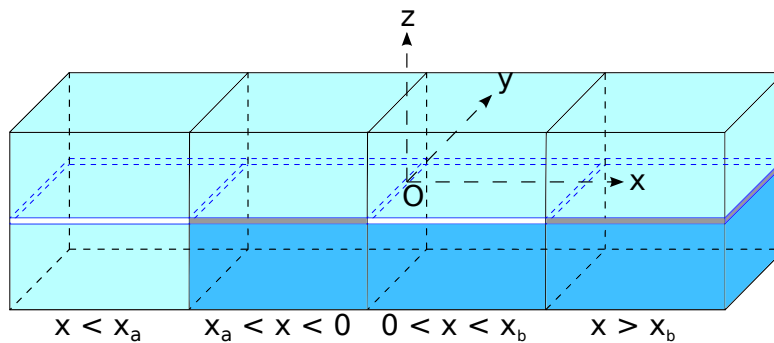


FIGURE 4.6: Bi-layer with two homogeneous layers for  $x < x_a$ , a bonded two-layered section for  $x_a < x < 0$ , a delaminated section for  $0 < x < x_b$  and another bonded two-layered section for  $x > x_b$ .

However if the delamination area is shorter, then the solitons in the delaminated section will not be fully separated. In this case, the radiating waves in the second bonded region overlap and generate a new single-humped radiating solitary wave. Irrespective of the separation, this process of creating a new radiating solitary wave is accompanied by some additional radiation, and therefore the amplitude of the new radiating solitary wave is reduced in both layers when compared to the radiating solitary wave propagating in a fully bonded waveguide, with no delamination. Indeed we can see this from the conservation laws of the KdV equation and coupled Ostrovsky equations. Furthermore, as the radiating solitary wave is not supported by the KdV equation, in the delaminated region the radiation separates from the soliton and the periodicity observed in the tail disappears as the tail transforms into a wave packet. This feature gives another indication that delamination is present.

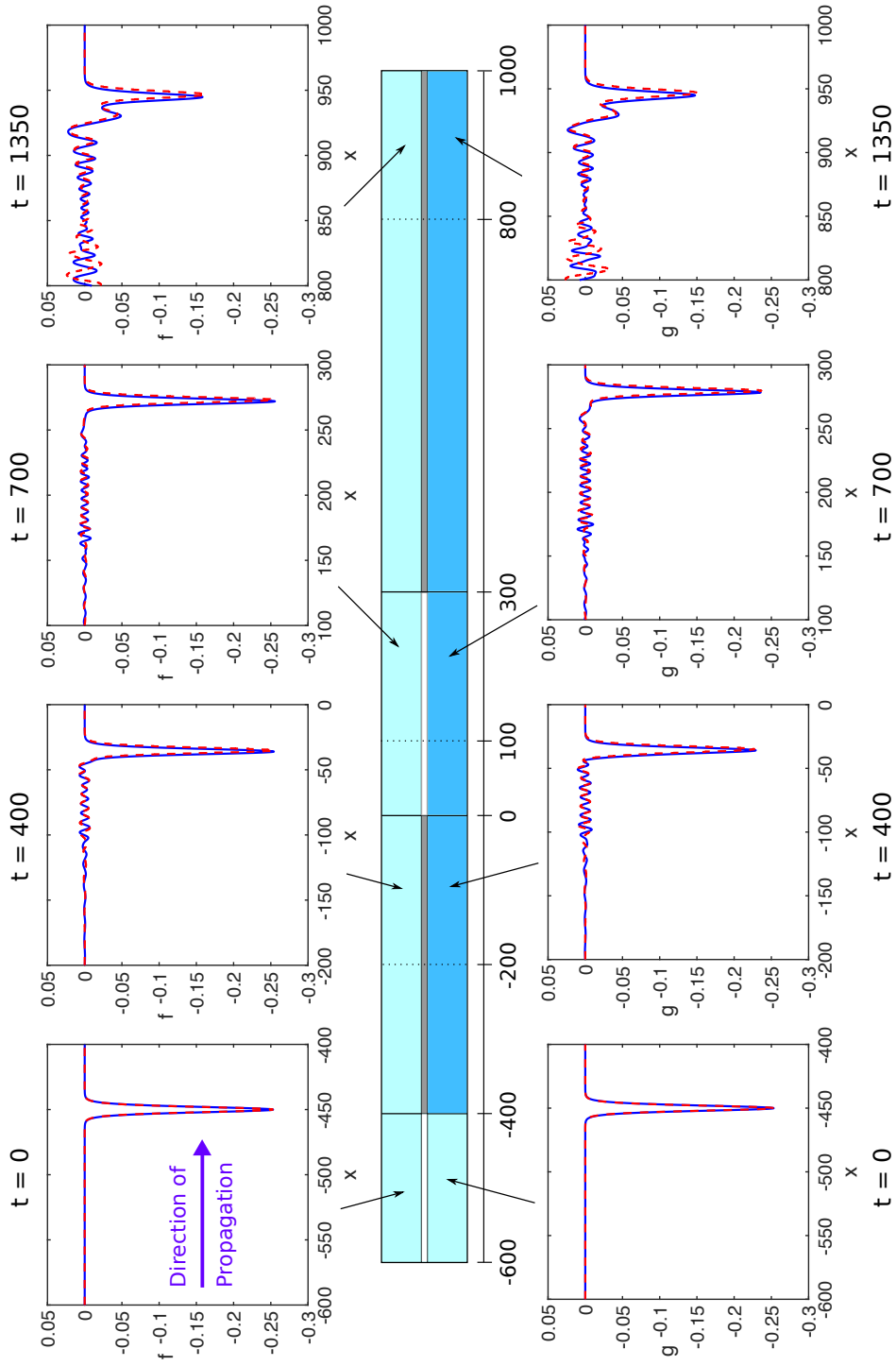


FIGURE 4.7: The waves  $f$  (upper layer) and  $g$  (lower layer) in the various sections of the bi-layer, for  $\alpha = \beta = 1.05$ ,  $c = 1.025$ ,  $\delta = \gamma = 1$ ,  $v = 1.025$ ,  $\sigma = 0$  and  $\epsilon = 0.05$ : direct numerical simulations (solid line) and weakly nonlinear solution (dashed line). Two homogeneous layers, of the same material as the upper layer, are on the left, and the waves propagate to the right. For the direct numerical method, the full computational domain is  $[-600, 1000]$ . In the semi-analytical method,  $N = 8192$ .

In order to investigate this behaviour more fully, we consider several cases with different delamination lengths, as measured in Full Width at Half Magnitude (FWHM) of the incident solitary wave in the same way as the previous section. In this case, the FWHM of the incident soliton measures approximately 5 units. We present results for delamination of length 10, 20, 40 and 60 FWHM, against the case where there is no delamination. Note that Figure 4.7 is for a delamination length of approximately 60 FWHM.

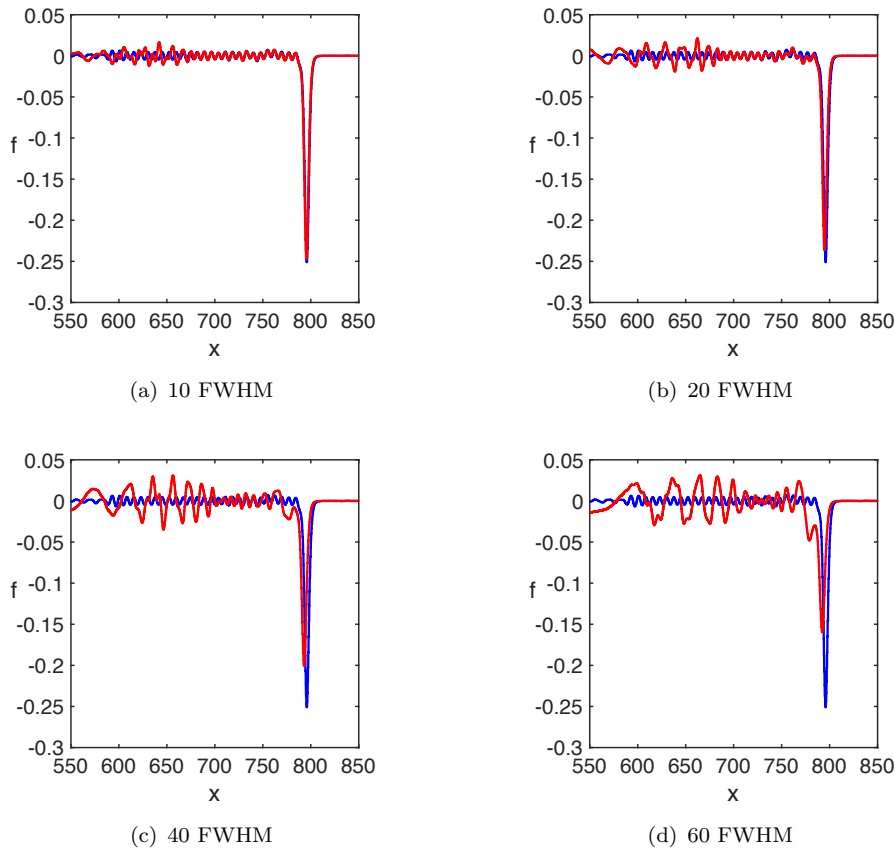


FIGURE 4.8: A comparison between the case without delamination (blue) and with delamination (red) of differing lengths, measured in FWHM of the incident soliton. The model is the same as that used in Figure 4.7 with the same parameters, and all images are for  $t = 1200$ .

To obtain the results in Figure 4.8, we use the semi-analytical method instead of the direct numerical method. We noted in Chapter 3 that the direct numerical method presented in Appendix A.2 solves for two sections of the bar at a time and therefore we must wait until the wave and its tail are fully contained in the region before moving the calculation domain. However, for a shorter delamination i.e. 20 FWHM or less, the leading wave front will reach the boundary of the calculation domain before the tail has fully entered this region. Therefore, the wave will either reflect and interfere with our solution, or we will lose part of the tail when we move the calculation domain. This is

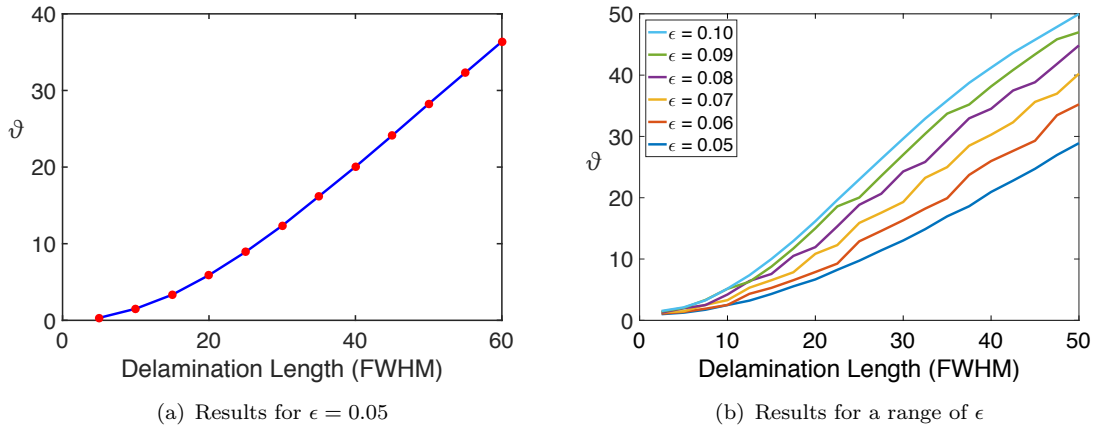


FIGURE 4.9: The percentage decrease in amplitude for various delamination lengths, measured in FWHM, at (a)  $\epsilon = 0.05$ , and (b) various values of  $\epsilon$ .

a natural limitation for the use of the finite-difference method in the form presented in Section A.2.

This could be remedied by solving for all sections of the bar simultaneously, and such a method is demonstrated in Appendix A.3. Testing for this method showed the same results as found with the semi-analytical method, however the theoretical estimates are based upon the KdV equation in the delaminated section and therefore they will be the most instructive. A comparison with the direct numerical method shows that the results are consistent.

We see from Figure 4.8 that there are some key differences between the model without delamination and the model with delamination. We only show the waves in the upper layer as the waves in the lower layer are similar.

Firstly, as the length of delamination increases, the amplitude of the radiating solitary wave created in the second bonded region is reduced. This can be explained by the fact that the waves in the delaminated section of the bar travel at different speeds in each layer and will be incident on the second bonded region at different times, so the energy exchange between the layers results in the generation of a radiating solitary wave of reduced amplitude. To measure this change, let us introduce the following measure:

$$\vartheta = \frac{|A_{\text{Final}} - A_{\text{RSW}}|}{A_{\text{RSW}}} \times 100. \quad (4.71)$$

A graph of the amplitudes against the delamination length, in FWHM, is presented in Figure 4.9(a). We can clearly see that after an initial growth period (up to 20 FWHM), the dependence is close to linear.

The presence of the double-humped solution, as seen in the image for 60 FWHM, clearly identifies a delamination. Further numerical experiments have shown that this double-humped structure emerges around 45-50 FWHM. The small hump behind the lead soliton in the 40 FWHM image is the start of a double-humped solution, but the second ‘hump’ has a similar amplitude to the radiation and therefore is not distinct. The speed of the waves in the delaminated region is different to the bonded region, and therefore when the new radiating solitary wave is formed in the second bonded region, it will have a phase shift with respect to the case of no delamination. Measuring from the minima of the waves, we calculate a phase shift of 0.2, 0.8, 2.7 and 3.6 for 10, 20, 40 and 60 FWHM respectively, growing with the delamination length as expected.

The radiating solitary wave is not a solution of the KdV equation and therefore, in the delaminated region, the radiating tail forms a wave packet, breaking the regularity of the tail region. This feature is again more pronounced for a larger delamination area, however it can already be clearly identified for a short delamination, such as in the case of 10 FWHM as seen in Figure 4.8. Further experiments have identified this behaviour for 5 FWHM, however the amplitude is similar to the rest of the tail and therefore this is difficult to identify visually.

We summarise these observations as follows. For very short delamination areas i.e. 5 FWHM, these differences are negligible and suggests that the soliton does not take care of delaminations shorter than a threshold value. For delamination areas that are greater than 5 FWHM, we can use our observations above for the amplitude reduction, phase shift and breaking the regularity of the tail to identify the presence of delamination. Modifying the FWHM value of the incident soliton can help identify shorter delaminations. A further example is presented in Figure 4.9(b) for various values of  $\epsilon$ . We see the same result that was observed for the perfectly bonded bar i.e. as the value of  $\epsilon$  is decreased, the FWHM value increases by the same factor, for a fixed value of amplitude decrease. Therefore we see a similar level of consistency between the two models.

#### 4.4.4 Further experiments

From a physical standpoint, we would like to test a given structure in as many ways as possible to obtain all possible information. Let us assume that we have a structure such as that in Figure 4.6 but with the two homogeneous layers removed. Given this structure, there are four natural tests that we can conduct: with two homogeneous layers of either the same material as the upper or lower layers, and attaching the homogeneous layers to either the left-hand side or right-hand side of the structure, with the waves propagating to the right or to the left, respectively. Examples using the same material

as the top layer are shown in Figure 4.7 and Figure 4.10 for the homogeneous layers being attached on the left-hand side and right-hand side respectively. We discuss all results here but omit the other cases for brevity.

Firstly we note that the double-humped structure is present in the second bonded region in all cases, confirming that each test identifies the presence of a sufficiently long delamination area, from our observations in Section 4.4.3. There is a small phase shift between the results for the different materials in the homogeneous layers, arising from the higher characteristic speed of the material of the lower layer.

We also note that, for the homogeneous layers being present on the right, the first bonded region is longer and this leads to a longer radiating tail. This tail becomes a wave packet in the delaminated region and we observe that the larger amplitude wave packet is closer to the double-humped structure for the case where the tail is longer, i.e. when the homogeneous section is on the right-hand side. Indeed, the length of the bonded region after the delamination is shorter in this case and therefore we would expect the wave packet to be closer to the leading wave. This gives us an indication of where the delamination is present in the bi-layer, i.e. if the radiation wave packet is closer to the leading wave when sending the waves from the right, then the delamination is closer to the left-hand side of the structure, and vice versa.

It is worth noting that the generated wave is of a larger amplitude in the case when the homogeneous layers are of the same material as the bottom layer (with a larger characteristic speed), and therefore the FWHM measure is smaller. However, as the difference in the characteristic speeds is  $O(\epsilon)$ , the difference in FWHM will be  $O(\epsilon)$  as well. Therefore, these images are omitted as they do not provide significantly new information.

## 4.5 Concluding Remarks

Here we have discussed the scattering of a long radiating bulk strain solitary wave in a delaminated bi-layer with a soft bonding between the layers. The modelling was performed within the framework of the non-dimensional coupled regularised Boussinesq equations (4.1), which were derived to describe long nonlinear longitudinal waves in a two-layered waveguide with a soft bonding layer ('imperfect interface') from a layered lattice model [38].

The developed direct numerical scheme and the semi-analytical scheme show good agreement in all regions of the bi-layer, with a small difference in the amplitude and minor phase shift between the results. This could be remedied by the inclusion of higher-order

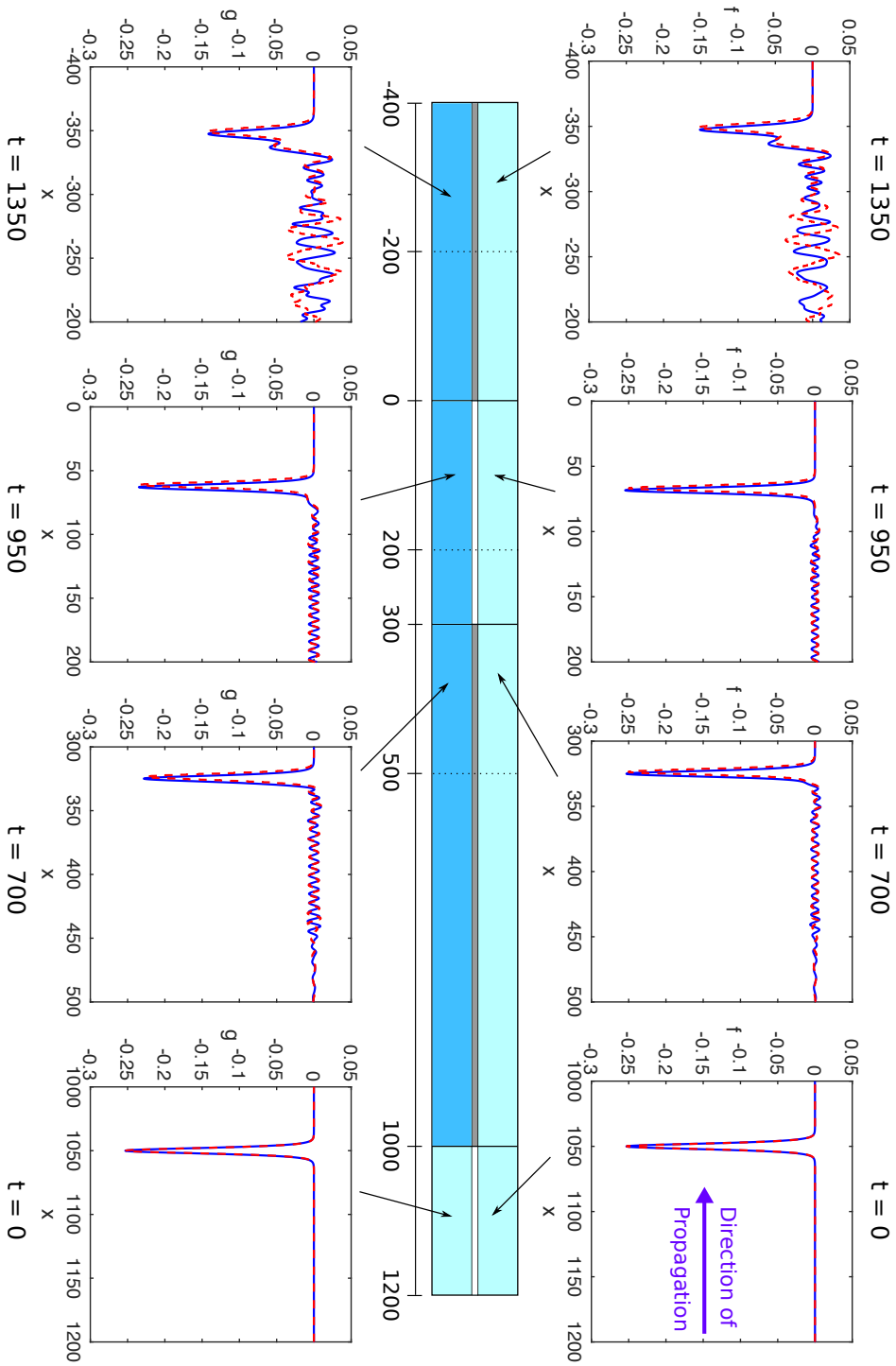


FIGURE 4.10: The waves  $f$  (upper layer) and  $g$  (lower layer) in the various sections of the bi-layer, for  $\alpha = \beta = 1.05$ ,  $c = 1.025$ ,  $\delta = \gamma = 1$ ,  $v_1 = 1.025$ ,  $\sigma = 0$  and  $\epsilon = 0.05$ : direct numerical simulations (blue, solid line) and semi-analytical method (red, dashed line). Two homogeneous layers, of the same material as the upper layer, are on the right, and the waves propagate to the left. For the direct numerical method, the full computational domain is  $[-400, 1200]$ . In the semi-analytical method,  $N = 8192$ .

corrections in the weakly nonlinear scheme, similarly to initial-value problems [39, 46]. We also note that the direct numerical method is expensive in comparison to the weakly nonlinear scheme.

Our study has revealed key features of the behaviour of radiating solitary waves in such delaminated bi-layers, for different lengths of the delaminated area compared to the wavelength (FWHM) of the incident soliton. If the delaminated area is sufficiently long ( $\geq 25$  FWHM), then there is a significant reduction in the amplitude of the transmitted radiating solitary wave ( $\geq 10$  %). In fact, the incident radiating solitary wave undergoes a complicated process of shedding a tail and propagating with slightly different speeds along the two layers in the delaminated region, followed by generation of a new radiating wave in the second bonded region. For shorter delamination regions ( $< 25$  FWHM), the key dynamical effect manifesting the presence of a delaminated region in the structure is the appearance of a wave packet in the regular tail of the radiating solitary wave. The waves are not sensitive to very short delamination regions, comparable to the wavelength of the incident soliton. In practice, using an admissible incident soliton with smaller wavelength (and higher amplitude), would increase the sensitivity to shorter delamination regions. If the delaminated region is longer ( $\geq 45$  FWHM) the separation of solitons, propagating in two layers in the delaminated region, leads to the emergence of a double-humped radiating wave in the second bonded region. We did not show the cases with delamination areas greater than 60 FWHM. The dynamical behaviour in these cases is simpler, leading to the emergence of two distinct radiating solitary waves in each layer of the second bonded region - a very clear sign of delamination. However, such cases are likely to be uncommon in real-world applications because of the dissipation processes which have not been accounted for in our modelling.

The generation of a radiating bulk strain solitary wave and subsequent disappearance of the ‘ripples’ in the delaminated area of a two-layered PMMA bar with PCP (polychloroprene-rubber-based) adhesive has been observed in experiments [36]. Our numerical modelling motivates further laboratory experimentation with a wide range of materials used in practical applications. It also paves the way for similar studies in other physical settings supporting radiating solitary waves and radiating dispersive shock waves, for example, in nonlinear optics [96, 97].



## Chapter 5

# Initial Value Problem for the Boussinesq-Ostrovsky Equation

### 5.1 Introduction

In this chapter we consider the initial value problem for a Boussinesq-type equation with the Ostrovsky term, which we will call the Boussinesq-Ostrovsky equation, for brevity. This equation arises as an extension to the regularised Boussinesq equation, as was derived in Chapter 2, for example in the case of a coupled FPU chain where the mass of the particles in one layer of the chain is chosen to be significantly larger than the other layer. In this case the displacement of particles in the chain with larger mass are significantly less and therefore, in the limit, can be assumed to be zero. The equation governing displacement in the other chain takes the form of the regularised Boussinesq-Ostrovsky equation,

$$u_{tt} - c^2 u_{xx} = \epsilon \left( \frac{\alpha}{2} (u^2)_{xx} + \beta u_{ttxx} - \gamma u \right), \quad (5.1)$$

where  $\gamma > 0$ ,  $\alpha$  and  $\beta$  are constant and  $\epsilon$  is a small parameter. In [46], a systematic approach to the construction of the weakly nonlinear solution of the initial value problem and rigorous estimates for the error terms of the Boussinesq-Ostrovsky equation (5.1) were found, and the convergence rates predicted by this derivation were confirmed by numerical experimentation. These results were obtained for a periodic domain, where the initial condition had non-zero mean value. However the formulae obtained were in terms of Fourier series and the constructed solution did not show an easy way of improving the accuracy of the leading order approximation (which was reduced compared to the case when  $\gamma = 0$ ).

In order to obtain a solution in a more explicit form, we aim to construct a weakly nonlinear solution of “d’Alambert’s type” in increasing powers of  $\sqrt{\epsilon}$ , in contrast to the previous works which used Fourier series and powers of  $\epsilon$  [46]. This allows us to find explicitly the terms at each order and the inclusion of terms at increasing orders will result in a more accurate solution.

This chapter is structured as follows. We consider the regularised Boussinesq-Ostrovsky equation with a non-zero mean initial condition. The mean value is subtracted from the function and we construct a weakly nonlinear solution in increasing powers of  $\sqrt{\epsilon}$ , up to  $O(\epsilon)$ , using two slow-scale variables. The direct solution of the Boussinesq-Ostrovsky equation is compared to the weakly nonlinear solution with an increasing number of terms included from the weakly nonlinear solution, in increasing powers of  $\sqrt{\epsilon}$ . Results are plotted for specific values of  $\gamma$  and we also plot the error against  $\epsilon$ , again with an increasing number of terms from the weakly nonlinear expansion. These results are repeated for a range of values of  $\gamma$  and several choices for the mean value of the initial condition. A further case is considered where the value of  $c$  is varied. Finally we conclude our results and make some further observations about the behaviour of the solution.

## 5.2 Weakly Nonlinear Solution

Let us consider the Boussinesq-Ostrovsky equation

$$u_{tt} - c^2 u_{xx} = \epsilon \left[ \frac{\alpha}{2} (u^2)_{xx} + \beta u_{ttxx} - \gamma u \right], \quad (5.2)$$

where  $\alpha$ ,  $\beta$ ,  $\gamma$  and  $\epsilon$  are constants and  $u(x, t)$  is the  $(2L)$ -periodic function to be found. Let us consider the equation defined on the domain  $\Omega = [-L, L] \times [0, T]$  and we take initial data

$$u|_{t=0} = F(x), \quad u_t|_{t=0} = V(x), \quad (5.3)$$

where  $F$  and  $V$  are assumed to be  $(2L)$ -periodic functions. Following [46] and integrating (5.2) in  $x$  over the period  $2L$  we obtain an evolution equation for the mean value of the form

$$\frac{d^2}{dt^2} \int_{-L}^L u(x, t) dx = -\epsilon\gamma \int_{-L}^L u(x, t) dx. \quad (5.4)$$

Solving this equation we have the mean value

$$\langle u \rangle(t) := \frac{1}{2L} \int_{-L}^L u(x, t) dx = A \cos(\sqrt{\epsilon\gamma}t) + B \sin(\sqrt{\epsilon\gamma}t). \quad (5.5)$$

Taking the mean value of the initial conditions and comparing these with (5.5) we see that

$$\langle u \rangle(t) := \frac{1}{2L} \int_{-L}^L u(x, t) \, dx = F_0 \cos(\sqrt{\epsilon\gamma}t) + V_0 \frac{\sin(\sqrt{\epsilon\gamma}t)}{\sqrt{\epsilon\gamma}}, \quad (5.6)$$

where we have

$$F_0 = \frac{1}{2L} \int_{-L}^L F(x) \, dx \quad \text{and} \quad V_0 = \frac{1}{2L} \int_{-L}^L V(x) \, dx. \quad (5.7)$$

To eliminate linear growth in the mean value  $\langle u \rangle$  in  $t$ , we require that

$$V_0 = \frac{1}{2L} \int_{-L}^L V(x) \, dx = 0, \quad (5.8)$$

as seen from the second term in (5.6). This condition appears naturally in many physical applications and indeed, in all cases that we consider in this chapter, this condition is satisfied.

The mean value is subtracted from the original solution to obtain an equation for a function with zero mean value. We take  $\tilde{u} = u - c_0 \cos(\omega t)$ , where  $\omega = \sqrt{\epsilon\gamma}$  and  $c_0 = F_0$ , so we obtain (omitting tildes)

$$u_{tt} - c^2 u_{xx} = \epsilon \left[ \alpha c_0 \cos(\omega t) u_{xx} + \frac{\alpha}{2} (u^2)_{xx} + \beta u_{ttxx} - \gamma u \right]. \quad (5.9)$$

We look for a weakly nonlinear solution of the form

$$\begin{aligned} u(x, t) = & f^\pm(\xi_\pm, \tau, T) + \sqrt{\epsilon} P(\xi_-, \xi_+, \tau, T) + \epsilon Q(\xi_-, \xi_+, \tau, T) + \epsilon^{3/2} R(\xi_-, \xi_+, \tau, T) \\ & + \epsilon^2 S(\xi_-, \xi_+, \tau, T) + O(\epsilon^{5/2}), \end{aligned} \quad (5.10)$$

where we introduce the following fast and slow variables:

$$\xi_\pm = x \pm ct, \quad \tau = \sqrt{\epsilon}t, \quad T = \epsilon t.$$

Note that, unlike [46], we introduce two slow time scales. We now substitute (5.10) into (5.9) and compare at various orders of  $\sqrt{\epsilon}$  to find expressions for all functions in the expansion. We noted earlier that the function  $u$  is  $2L$ -periodic in  $x$ , therefore we require that  $f^-$  and  $f^+$  are also  $2L$ -periodic in  $\xi_-$  and  $\xi_+$ , respectively. Moreover, it is natural to assume that all terms in the asymptotic expansion for  $u$  are products of the functions  $f^-$ ,  $f^+$ , and their derivatives. This assumption then implies that all terms are periodic in  $\xi_-/\xi_+$ , at fixed  $\xi_+/\xi_-$ . Furthermore, as the functions  $f^-$  and  $f^+$  have zero mean i.e.

$$\int_{-L}^L f^- \, d\xi_- = 0 \quad \text{and} \quad \int_{-L}^L f^+ \, d\xi_+ = 0, \quad (5.11)$$

then all terms in (5.10) will have zero mean in  $\xi_-/\xi_+$ , at fixed  $\xi_+/\xi_-$ .

The solution is satisfied at leading order, therefore we move to the next order immediately. At each stage we will also satisfy the initial condition for the previous order, as the functions at a given order are introduced by comparing terms at the previous order of  $\sqrt{\epsilon}$ .

### 5.2.1 Terms at $O(\sqrt{\epsilon})$

At this order the right-hand side of (5.9) does not contribute to the expansion, so we have

$$-4c^2 P_{\xi_- \xi_+} - 2cf_{\xi_- \tau}^- + 2cf_{\xi_+ \tau}^+ = 0. \quad (5.12)$$

We average (5.12) at constant  $\xi_-$  or  $\xi_+$  i.e. in the reference frame moving with the linear speed of the right- or left-propagating waves, respectively. Therefore, at constant  $\xi_-$  for example, we have

$$\frac{1}{2L} \int_{-L}^L P_{\xi_- \xi_+} dx = \frac{1}{4L} \int_{-2L-\xi_-}^{2L-\xi_-} P_{\xi_- \xi_+} d\xi_+ = \frac{1}{4L} [P_{\xi_-}]_{-2L-\xi_-}^{2L-\xi_-} = 0. \quad (5.13)$$

A similar result can be obtained for  $\xi_+$  and we see that under the averaging  $P_{\xi_- \xi_+} = 0$ . Averaging (5.12) at constant  $\xi_-$  and  $\xi_+$  therefore gives

$$f_{\xi_- \tau}^- = 0 \quad \text{and} \quad f_{\xi_+ \tau}^+ = 0. \quad (5.14)$$

Integrating with respect to the characteristic variables we obtain

$$f^- = \tilde{f}^-(\xi_-, T) + B^-(\tau, T) \quad \text{and} \quad f^+ = \tilde{f}^+(\xi_+, T) + B^+(\tau, T). \quad (5.15)$$

Noting that we have zero mean of all functions in the expansion, we require that  $B^\pm = 0$ . We will apply this rule at all orders to eliminate any functions of only  $\tau$  and  $T$ . Substituting (5.15) into (5.12) gives

$$P_{\xi_- \xi_+} = 0 \quad \Rightarrow \quad P = g^-(\xi_-, \tau, T) + g^+(\xi_+, \tau, T). \quad (5.16)$$

We rewrite our weakly nonlinear solution to accommodate these changes, so we have (omitting tildes for  $f^\pm$ )

$$\begin{aligned} u(x, t) = & f^\pm(\xi_\pm, T) + \sqrt{\epsilon} g^\pm(\xi_\pm, \tau, T) + \epsilon Q(\xi_-, \xi_+, \tau, T) + \epsilon^{3/2} R(\xi_-, \xi_+, \tau, T) \\ & + \epsilon^2 S(\xi_-, \xi_+, \tau, T) + O(\epsilon^{5/2}). \end{aligned} \quad (5.17)$$

## Initial Condition

Substituting (5.17) into (5.3) and comparing terms at  $O(1)$  we obtain the initial condition for  $f^\pm$  in the form of d'Alembert's solution, where we have

$$\begin{cases} f^- + f^+|_{t=0} = F(x) \\ -cf_{\xi_-}^- + cf_{\xi_+}^+|_{t=0} = V(x) \end{cases} \Rightarrow f^\pm|_{t=0} = \frac{1}{2c} \left( cF(x \pm ct) \pm \int_{-L}^{x \pm ct} V(x) dx \right). \quad (5.18)$$

### 5.2.2 Terms at $O(\epsilon)$

We now consider the terms at  $O(\epsilon)$ , using the results from the previous order. Substituting (5.17) into (5.9) and keeping terms of  $O(\epsilon)$  we obtain

$$\begin{aligned} -4c^2 Q_{\xi_- \xi_+} &= 2cg_{\xi_- \tau}^- - 2cg_{\xi_+ \tau}^+ + \left( 2cf_T^- + \alpha f^- f_{\xi_-}^- + \beta c^2 f_{\xi_- \xi_- \xi_-}^- \right)_{\xi_-} - \gamma f^- \\ &\quad + c_0 \alpha \cos(\omega t) \left( f_{\xi_- \xi_-}^- + f_{\xi_+ \xi_+}^+ \right) + \alpha \left[ f_{\xi_- \xi_-}^- f^+ + 2f_{\xi_-}^- f_{\xi_+}^+ + f^- f_{\xi_+ \xi_+}^+ \right] \\ &\quad + \left( -2cf_T^+ + \alpha f^+ f_{\xi_+}^+ + \beta c^2 f_{\xi_+ \xi_+ \xi_+}^+ \right)_{\xi_+} - \gamma f^+. \end{aligned} \quad (5.19)$$

Averaging (5.19) at constant  $\xi_-$  or constant  $\xi_+$  yields

$$\left( \mp 2cf_T^\pm + \alpha f^\pm f_{\xi_\pm}^\pm + \beta c^2 f_{\xi_\pm \xi_\pm \xi_\pm}^\pm \right)_{\xi_\pm} = \gamma f^\pm \pm 2cg_{\xi_\pm \tau}^\pm - c_0 \alpha \cos(\sqrt{\gamma}\tau) f_{\xi_\pm \xi_\pm}^\pm. \quad (5.20)$$

We rearrange this to obtain

$$\mp 2cg_{\xi_\pm \tau}^\pm = c_0 \alpha \cos(\sqrt{\gamma}\tau) f_{\xi_\pm \xi_\pm}^\pm + A(\xi_\pm, T), \quad (5.21)$$

and to avoid secular terms we require  $A = 0$ . Therefore we have equations for  $f^\pm$  and  $g^\pm$  of the form

$$\left( \mp 2cf_T^\pm + \alpha f^\pm f_{\xi_\pm}^\pm + \beta c^2 f_{\xi_\pm \xi_\pm \xi_\pm}^\pm \right)_{\xi_\pm} = \gamma f^\pm, \quad (5.22)$$

and

$$g^\pm = \pm \frac{c_0 \alpha}{2c\sqrt{\gamma}} \sin(\sqrt{\gamma}\tau) f_{\xi_\pm}^\pm + G^\pm(\xi_\pm, T) = \pm \theta f_{\xi_\pm}^\pm + G^\pm(\xi_\pm, T), \quad (5.23)$$

where we have introduced the coefficient

$$\theta = \frac{\alpha c_0}{2\sqrt{\gamma}} \sin(\sqrt{\gamma}\tau), \quad (5.24)$$

and the function  $G^\pm$  is to be found at the next order. Substituting (5.22) and (5.23) into (5.19) and integrating with respect to the characteristic variables we obtain

$$Q(\xi_-, \xi_+, \tau, T) = h^-(\xi_-, \tau, T) + h^+(\xi_+, \tau, T) + h_c(\xi_-, \xi_+, T), \quad (5.25)$$

where

$$h_c = -\frac{\alpha}{4c^2} \left( f_{\xi_-}^- \int f^+ d\xi_+ + 2f^- f^+ + f_{\xi_+}^+ \int f^- d\xi_- \right). \quad (5.26)$$

We rewrite the weakly nonlinear solution to reflect the new results for  $Q$ , derived in (5.25), so we have

$$\begin{aligned} u(x, t) &= f^\pm(\xi_\pm, T) + \sqrt{\epsilon}(g^\pm(\xi_\pm, \tau, T)) + \epsilon(h^\pm(\xi_\pm, \tau, T) + h_c(\xi_-, \xi_+, T)) \\ &\quad + \epsilon^{3/2}R(\xi_-, \xi_+, \tau, T) + \epsilon^2S(\xi_-, \xi_+, \tau, T) + O(\epsilon^{5/2}). \end{aligned} \quad (5.27)$$

### Initial Condition

Substituting (5.27) into (5.3) and now comparing terms at  $O(\sqrt{\epsilon})$  we obtain

$$\begin{cases} g^- + g^+|_{t=0} = 0 \\ -cg_{\xi_-}^- + cg_{\xi_+}^+|_{t=0} = 0 \end{cases} \Rightarrow \begin{cases} -\theta f_{\xi_-}^- + G^- + \theta f_{\xi_+}^+ + G^+|_{t=0} = 0, \\ -c\theta f_{\xi_- \xi_-}^- - cG_{\xi_-}^- + c\theta f_{\xi_+ \xi_+}^+ + cG_{\xi_+}^+|_{t=0} = 0. \end{cases}$$

From (5.24) we see that, at  $t = 0$ ,  $\theta = 0$  and therefore using the same method as (5.18) we have

$$\begin{cases} G^- + G^+|_{t=0} = 0 \\ -cG_{\xi_-}^- + cG_{\xi_+}^+|_{t=0} = 0 \end{cases} \Rightarrow G^\pm|_{t=0} = 0. \quad (5.28)$$

### 5.2.3 Terms at $O(\epsilon^{3/2})$

We follow the same steps as before, substituting (5.27) into (5.9) and keeping terms of  $O(\epsilon^{3/2})$  to obtain

$$\begin{aligned} -4c^2 R_{\xi_- \xi_+} &= 2ch_{\xi_- \tau}^- - 2ch_{\xi_+ \tau}^+ + \left( 2cg_T^- + \alpha(f^- g^-)_{\xi_-} + \beta c^2 g_{\xi_- \xi_- \xi_-}^- \right)_{\xi_-} - \gamma g^- \\ &\quad - g_{\tau\tau}^- - g_{\tau\tau}^+ + \left( -2cg_T^+ + \alpha(f^+ g^+)_{\xi_+} + \beta c^2 g_{\xi_+ \xi_+ \xi_+}^+ \right)_{\xi_+} - \gamma g^+ \\ &\quad + \alpha \left[ f_{\xi_- \xi_-}^- g^+ + 2f_{\xi_-}^- g_{\xi_+}^+ + f^- g_{\xi_+ \xi_+}^+ + g_{\xi_- \xi_-}^- f^+ + 2g_{\xi_-}^- f_{\xi_+}^+ + g^- f_{\xi_+ \xi_+}^+ \right] \\ &\quad + c_0 \alpha \cos(\omega t) \left( g_{\xi_- \xi_-}^- + g_{\xi_+ \xi_+}^+ \right). \end{aligned} \quad (5.29)$$

Averaging (5.29) at constant  $\xi_-$  or constant  $\xi_+$  yields

$$\begin{aligned} \pm 2ch_{\xi_{\pm}\tau}^{\pm} &= \theta \left( \mp 2cf_T^{\pm} + \alpha f_{\xi_{\pm}}^{\pm} + \beta c^2 f_{\xi_{\pm}\xi_{\pm}}^{\pm} \right)_{\xi_{\pm}} - \theta \gamma f_{\xi_{\pm}}^{\pm} \\ &\quad \left( \mp 2cG_T^{\pm} + \alpha (f^{\pm} G^{\pm})_{\xi_{\pm}} + \beta c^2 G_{\xi_{\pm}\xi_{\pm}}^{\pm} \right)_{\xi_{\pm}} - \gamma G^{\pm} \\ &\quad \pm \theta \gamma f_{\xi_{\pm}}^{\pm} \pm \theta c_0 \alpha \cos(\sqrt{\gamma}\tau) f_{\xi_{\pm}\xi_{\pm}}^{\pm}. \end{aligned} \quad (5.30)$$

Differentiating (5.22) with respect to the appropriate characteristic variable, we can eliminate the first line from (5.30) and therefore we have an expression for  $h_{\xi_{\pm}\tau}^{\pm}$  of the form

$$h_{\xi_{\pm}\tau}^{\pm} = \frac{\theta \gamma}{2c} f_{\xi}^{\pm} + \frac{\theta c_0 \alpha}{2c} \cos(\sqrt{\gamma}\tau) f_{\xi_{\pm}\xi_{\pm}}^{\pm} + \tilde{G}^{\pm}(\xi_{\pm}, T). \quad (5.31)$$

To avoid secular terms we require that  $\tilde{G}^{\pm} = 0$ . Therefore we have an equation for  $G^{\pm}$  of the form

$$\left( \mp 2cG_T^{\pm} + \alpha (f^{\pm} G^{\pm})_{\xi_{\pm}} + \beta c^2 G_{\xi_{\pm}\xi_{\pm}}^{\pm} \right)_{\xi_{\pm}} = \gamma G^{\pm}. \quad (5.32)$$

At this stage we note that the initial condition for  $G^{\pm}$ , as derived in (5.28), is  $G^{\pm} = 0$  and  $G_t^{\pm} = 0$ , and therefore, taking note of the form (5.32), we see that  $G^{\pm} = 0$  for all times. Integrating (5.31) we obtain

$$h^{\pm} = \frac{\gamma}{2c} \frac{\partial_{\tau}^{-1} \theta}{f^{\pm}} - \frac{\gamma (\partial_{\tau}^{-1} \theta)^2}{2} f_{\xi_{\pm}\xi_{\pm}}^{\pm} + \phi^{\pm}(\xi_{\pm}, T). \quad (5.33)$$

Substituting (5.33) into (5.29) and integrating with respect to the characteristic variables we obtain

$$R(\xi_-, \xi_+, \tau, T) = \psi^-(\xi_-, \tau, T) + \psi^+(\xi_+, \tau, T) + \psi_c(\xi_-, \xi_+, \tau, T), \quad (5.34)$$

where

$$\psi_c = -\frac{\alpha}{4c^2} \left( f^- f_{\xi_+}^+ - f_{\xi_-}^- f^+ + f_{\xi_+\xi_+} \int f^- d\xi_- - f_{\xi_-\xi_-}^- \int f^+ d\xi_+ \right). \quad (5.35)$$

We rewrite the weakly nonlinear solution to reflect the new results derived here, so we have

$$\begin{aligned} u(x, t) &= f^{\pm}(\xi_{\pm}, T) + \sqrt{\epsilon} (g^{\pm}(\xi_{\pm}, \tau, T)) + \epsilon (h^{\pm}(\xi_{\pm}, \tau, T) + h_c(\xi_-, \xi_+, T)) \\ &\quad + \epsilon^{3/2} (\psi^{\pm}(\xi_{\pm}, \tau, T) + \psi_c(\xi_-, \xi_+, \tau, T)) + \epsilon^2 S(\xi_-, \xi_+, \tau, T) + O(\epsilon^{5/2}). \end{aligned} \quad (5.36)$$

## Initial Condition

Substituting (5.36) into (5.3) and now comparing terms at  $O(\epsilon)$  we obtain

$$\begin{cases} h^- + h^+ + h_c|_{t=0} = 0 \\ f_T^- + f_T^+ + g_\tau^- + g_\tau^+ - ch_{\xi_-}^- + ch_{\xi_+}^+ - ch_{c\xi_-} + ch_{c\xi_+}|_{t=0} = 0 \end{cases} \\ \Rightarrow \phi^\pm = \frac{1}{2c} \left( cJ(\xi_\pm, \tau, T) \mp \int_{-L}^{x^\pm t} K(x, \tau, T) dx \right),$$

where we define

$$\begin{aligned} J &= -h_c - \frac{\gamma}{2c} \frac{\partial_\tau^{-1} \theta}{2c} f^- + \frac{\gamma (\partial_\tau^{-1} \theta)^2}{2} f_{\xi_- \xi_-}^- - \frac{\gamma}{2c} \frac{\partial_\tau^{-1} \theta}{2c} f^+ + \frac{\gamma (\partial_\tau^{-1} \theta)^2}{2} f_{\xi_+ \xi_+}^+, \\ K &= f_T^- + f_T^+ + \frac{\gamma}{2c} \frac{\partial_\tau^{-1} \theta}{2c} f_{\xi_-}^- - \frac{\gamma}{2c} \frac{\partial_\tau^{-1} \theta}{2c} f_{\xi_+}^+ + \frac{\gamma (\partial_\tau^{-1} \theta)^2}{2} f_{\xi_- \xi_- \xi_-}^- \\ &\quad - \frac{\gamma (\partial_\tau^{-1} \theta)^2}{2} f_{\xi_+ \xi_+ \xi_+}^+ - h_{c\xi_-} + h_{c\xi_+}. \end{aligned} \quad (5.37)$$

### 5.2.4 Terms at $O(\epsilon^2)$

We now use the new form of the weakly nonlinear solution, (5.36), and keep terms at  $O(\epsilon^2)$  to obtain

$$\begin{aligned} -4c^2 S_{\xi_- \xi_+} &= -2g_{\tau T}^- - 2g_{\tau T}^+ - f_{TT}^- - f_{TT}^+ - h_{\tau\tau}^- - h_{\tau\tau}^+ + 2ch_{\xi_- \tau}^- - 2ch_{\xi_+ \tau}^+ + 2ch_{c\xi_- \tau}^- \\ &\quad - 2ch_{c\xi_+ \tau}^+ + 2c\psi_{\xi_- \tau}^- - 2c\psi_{\xi_+ \tau}^+ + \alpha (f^- h^-)_{\xi_- \xi_-} + \alpha (f^+ h^+)_{\xi_+ \xi_+} \\ &\quad + \frac{\alpha}{2} (g^{-2})_{\xi_- \xi_-} + \frac{\alpha}{2} (g^{+2})_{\xi_+ \xi_+} + \beta c^2 h_{\xi_- \xi_- \xi_- \xi_-}^- + h_{\xi_+ \xi_+ \xi_+ \xi_+}^+ - \gamma h^- - \gamma h^+ \\ &\quad + c_0 \alpha \cos(\omega t) (h_{\xi_- \xi_-}^- + h_{\xi_+ \xi_+}^+) - 2c\beta g_{\xi_- \xi_- \xi_- \tau}^- + 2c\beta g_{\xi_+ \xi_+ \xi_+ \tau}^+ \\ &\quad - 2c\beta f_{\xi_- \xi_- \xi_- T}^- + 2c\beta f_{\xi_+ \xi_+ \xi_+ T}^+ - 4c^2 \mu_c, \end{aligned} \quad (5.38)$$

where  $\mu_c$  contains all the coupling terms between  $f^\pm$ ,  $g^\pm$  and  $h^\pm$  and the coefficient is chosen for convenience. When averaging (5.38) at constant  $\xi_-$  or constant  $\xi_+$ , the coupling terms are averaged out and therefore the averaging yields

$$\pm 2\psi_{\xi_\pm \tau}^\pm = H_1^\pm(\xi_\pm, \tau, T) + H_2^\pm(\xi_\pm, T), \quad (5.39)$$

where the functions  $H_1^\pm$ ,  $H_2^\pm$  are found from (5.38). Integrating (5.39) with respect to the respective characteristic variables, we see that to avoid secular terms we require

$H_2^\pm = 0$ . This allows us to derive an equation for  $\phi^\pm$  of the form

$$\begin{aligned} \left( \mp 2c\phi_T^\pm + \alpha (f^\pm \phi^\pm)_{\xi_\pm} + \beta c^2 \phi_{\xi_\pm \xi_\pm \xi_\pm}^\pm \right)_{\xi_\pm} &= \gamma \phi^\pm + f_{TT}^\pm \mp 2c\beta f_{\xi_\pm \xi_\pm \xi_\pm T}^\pm \\ &+ \frac{\gamma \tilde{\theta}^2}{2} f_{\xi_\pm \xi_\pm}^\pm - \frac{\alpha \tilde{\theta}^2}{2} (f_{\xi_\pm}^{\pm 2})_{\xi_\pm \xi_\pm}, \end{aligned} \quad (5.40)$$

where

$$\tilde{\theta} = \frac{\theta}{\sin(\sqrt{\gamma}\tau)} = \frac{\alpha c_0}{2\sqrt{\gamma}}. \quad (5.41)$$

At this stage we have fully defined all functions at  $O(\epsilon)$  and have therefore completed our expansion. The weakly nonlinear expansion takes the form

$$u(x, t) = f^\pm(\xi_\pm, T) + \sqrt{\epsilon} (g^\pm(\xi_\pm, \tau, T)) + \epsilon (h^\pm(\xi_\pm, \tau, T) + h_c(\xi_-, \xi_+, T)) + O(\epsilon^{3/2}). \quad (5.42)$$

## 5.3 Results

To solve the Boussinesq-Ostrovsky equation we use a pseudospectral method with a 4th order Runge-Kutta method for time stepping, as was used in [46, 110]. This method is described in Appendix C.3. For the Ostrovsky equations we again use a pseudospectral method, based upon the method in [40, 43]. These are presented in Appendix C.2.1 and C.2.2.

### 5.3.1 Error Analysis

We compare the weakly nonlinear solution (5.42) to the solution of the Boussinesq-Ostrovsky equation (5.1), with an increasing number of terms included from the weakly nonlinear solution. Let us denote the solution to (5.1) as  $u_{\text{num}}$ , (5.42) with only the leading order terms included as  $u_1$ , with terms up to and including  $O(\sqrt{\epsilon})$  terms as  $u_2$  and with terms up to and including  $O(\epsilon)$  as  $u_3$ . We consider the maximum absolute error over  $x$ , defined as

$$e_i = \max_{-L \leq x \leq L} |u_{\text{num}}(x, t) - u_i(x, t)|, \quad i = 1, 2, 3, \quad (5.43)$$

and use a least-squares power fit to determine how the maximum absolute error varies with the small parameter  $\epsilon$ . Therefore we write the errors in the form

$$\exp[e_i] = C_i \epsilon^{\alpha_i}, \quad (5.44)$$

and take the logarithm of both sides to form the error plot (the exponential factor is included so that we have  $e_i$  as the plotting variable). The values of  $C_i$  and  $\alpha_i$  are found using the Matlab function *polyfit*.

### 5.3.2 Results for Unity Coefficients

In this section we use a solitary wave as the initial condition, with a constant pedestal term introduced to increase the mean value of the initial condition (and therefore the value of  $c_0$ ). Explicitly we take

$$u(x, 0) = A \operatorname{sech}^2\left(\frac{x}{\Lambda}\right) + d, \quad (5.45)$$

$$u_t(x, 0) = \frac{2cA}{\Lambda} \operatorname{sech}^2\left(\frac{x}{\Lambda}\right) \tanh\left(\frac{x}{\Lambda}\right), \quad (5.46)$$

where  $d$  is a constant and we take

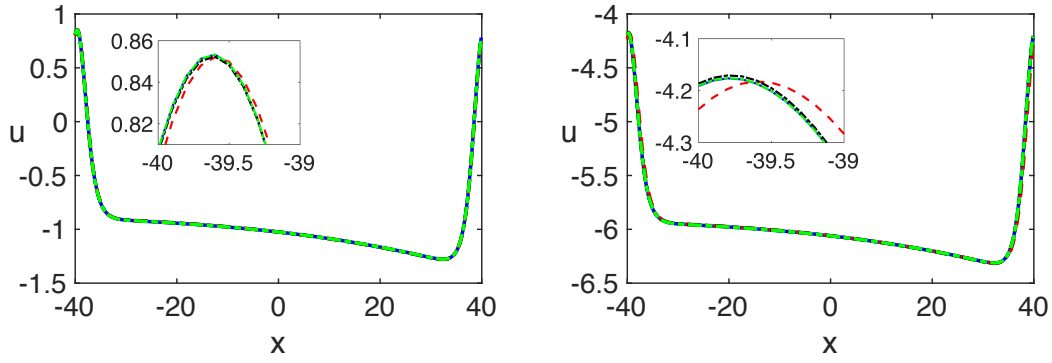
$$A = \frac{6ck^2}{\alpha}, \quad \Lambda = \frac{\sqrt{2c\beta}}{k}, \quad k = \sqrt{\frac{\alpha}{3c}}. \quad (5.47)$$

The mean value term  $c_0$  will therefore take the value

$$c_0 = d + \frac{A\Lambda}{2L} (\tanh(L) - \tanh(-L)) \approx d + \frac{A\Lambda}{L} \quad \text{for sufficiently large } L. \quad (5.48)$$

The initial condition for the higher order correction functions  $\phi^\pm$  are given in (5.37), using the initial condition for the leading order terms as defined in (5.18). In all results presented in this section we take  $c = \alpha = \beta = 1$ .

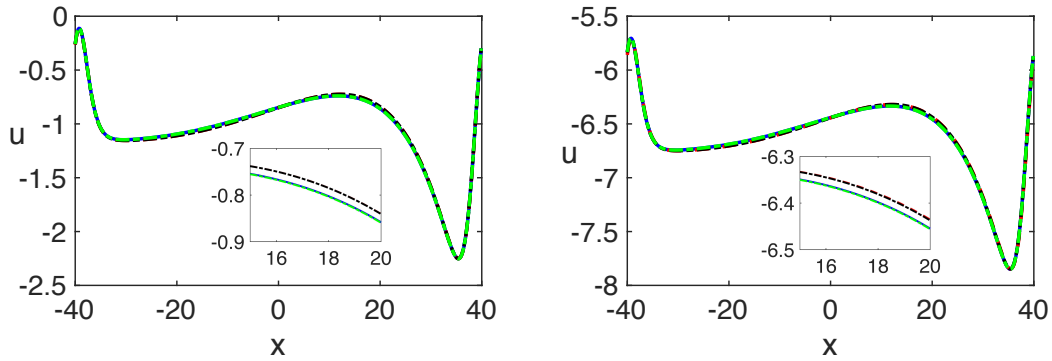
We compute the results for various values of  $\gamma$  and  $c_0$ . Here we plot a sample for small and large  $\gamma$ , and for small and large values of  $c_0$ . In Figure 5.1 we show that, for small  $\gamma$ , an increase in  $c_0$  increases the error in the solution (the weakly nonlinear solution is less accurate). The same behaviour occurs in Figure 5.2, and by comparison to Figure 5.1 we see that an increase in  $\gamma$  results in a corresponding increase in the error. To further understand the behaviour of the errors, we plot the corresponding error curves for the cases in Figures 5.1 and 5.2. These results are presented in Figure 5.3 and Figure 5.4 for  $\gamma = 0.1$  and  $\gamma = 0.5$  respectively. We see that the error curves in Figure 5.3 have slope 0.5, 1 and 1.5, corresponding to errors at  $O(\sqrt{\epsilon})$ ,  $O(\epsilon)$  and  $O(\epsilon^{3/2})$  respectively. This can be understood from (5.42), as the inclusion of terms at a given order of the expansion will result in errors at the next order. An interesting observation is that, as  $\gamma$  increases for a fixed value of  $c_0$ , the value of  $e_1$  tends to  $e_2$  and similarly  $e_3$  tends to the value expected with the inclusion of the next order of terms i.e. from 1.5 to 2. Analysing the form of equation (5.23) shows that, as  $\gamma$  increases, the magnitude of these terms



(a) The solution of the Boussinesq-Ostrovsky equation and the weakly nonlinear solutions for  $\gamma = 0.1$  and  $d = 1$ .

(b) The solution of the Boussinesq-Ostrovsky equation and the weakly nonlinear solutions for  $\gamma = 0.1$  and  $d = 7$ .

FIGURE 5.1: A comparison of the original Boussinesq-Ostrovsky equation (5.1) (solid, blue) at  $t = 1/\epsilon$ , for the weakly nonlinear solution including leading order (dashed, red),  $O(\sqrt{\epsilon})$  (dash-dot, black) and  $O(\epsilon)$  (dotted, green) corrections, for (a)  $d = 1$  and (b)  $d = 7$ . Parameters are  $L = 40$ ,  $N = 800$ ,  $k = 1/\sqrt{3}$ ,  $\alpha = \beta = c = 1$ ,  $\gamma = 0.1$ ,  $\epsilon = 0.001$ ,  $\Delta t = 0.01$  and  $\Delta T = \epsilon \Delta t$ . We see that the solution agrees well to leading order and this agreement is improved with the addition of higher order corrections.



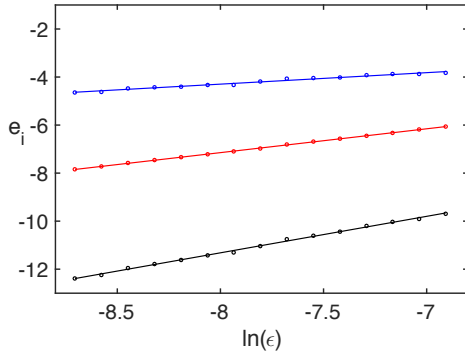
(a) The solution of the Boussinesq-Ostrovsky equation and the weakly nonlinear solutions for  $\gamma = 0.5$  and  $d = 1$ .

(b) The solution of the Boussinesq-Ostrovsky equation and the weakly nonlinear solutions for  $\gamma = 0.5$  and  $d = 7$ .

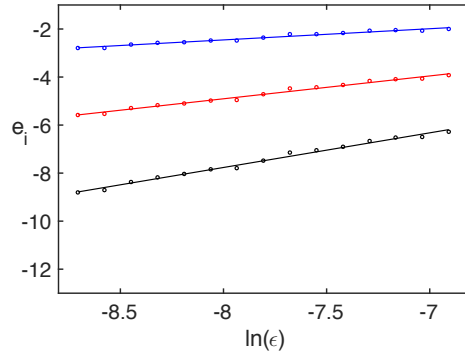
FIGURE 5.2: A comparison of the original Boussinesq-Ostrovsky equation (5.1) (solid, blue) at  $t = 1/\epsilon$ , for the weakly nonlinear solution including leading order (dashed, red),  $O(\sqrt{\epsilon})$  (dash-dot, black) and  $O(\epsilon)$  (dotted, green) corrections, for (a)  $d = 1$  and (b)  $d = 7$ . Parameters are  $L = 40$ ,  $N = 800$ ,  $k = 1/\sqrt{3}$ ,  $\alpha = \beta = c = 1$ ,  $\gamma = 0.5$ ,  $\epsilon = 0.001$ ,  $\Delta t = 0.01$  and  $\Delta T = \epsilon \Delta t$ . We see that the solution agrees well to leading order and this agreement is improved with the addition of higher order corrections.

decreases. However, from the initial condition for  $\phi$  as given in (5.37), the magnitude of  $\phi$  will increase as  $\gamma$  increases. Therefore the gradient of the error curves will tend to integer powers of epsilon, so the fractional powers will tend to the next largest integer power.

A further observation is that the increase of  $c_0$  will result in an increase in the errors, as we saw in Figure 5.1 and Figure 5.2. This can be seen by comparing the two images in

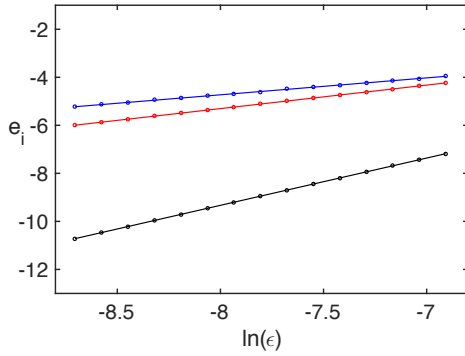


(a) Error curves for  $\gamma = 0.1$  and  $d = 1$ , for all values of  $e_i$ .

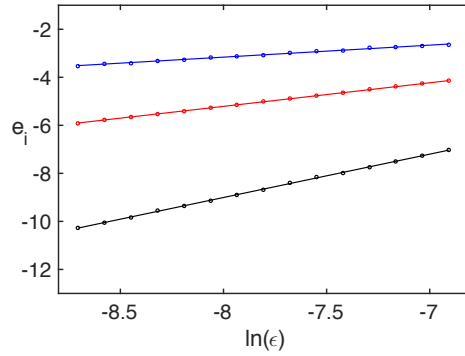


(b) Error curves for  $\gamma = 0.1$  and  $d = 7$ , for all values of  $e_i$ .

FIGURE 5.3: A comparison of error curves for varying values of  $\epsilon$ , at  $t = 1/\epsilon$ , for the weakly nonlinear solution including leading order (upper, blue),  $O(\sqrt{\epsilon})$  (middle, red) and  $O(\epsilon)$  (lower, black) corrections, for (a)  $d = 1$  and (b)  $d = 7$ . Parameters are  $L = 40$ ,  $N = 800$ ,  $k = 1/\sqrt{3}$ ,  $\alpha = \beta = c = 1$ ,  $\gamma = 0.1$ ,  $\Delta t = 0.01$  and  $\Delta T = \epsilon \Delta t$ . We see that the inclusion of more terms in the expansion increases the accuracy, and that the errors increase for larger values of  $d$ .



(a) Error curves for  $\gamma = 0.5$  and  $d = 1$ , for all values of  $e_i$ .



(b) Error curves for  $\gamma = 0.5$  and  $d = 7$ , for all values of  $e_i$ .

FIGURE 5.4: A comparison of error curves for varying values of  $\epsilon$ , at  $t = 1/\epsilon$ , for the weakly nonlinear solution including leading order (upper, blue),  $O(\sqrt{\epsilon})$  (middle, red) and  $O(\epsilon)$  (lower, black) corrections, for (a)  $d = 1$  and (b)  $d = 7$ . Parameters are  $L = 40$ ,  $N = 800$ ,  $k = 1/\sqrt{3}$ ,  $\alpha = \beta = c = 1$ ,  $\gamma = 0.5$ ,  $\Delta t = 0.01$  and  $\Delta T = \epsilon \Delta t$ . We see that the inclusion of more terms in the expansion increases the accuracy, and that the errors increase for larger values of  $d$ . The upper and lower curves are steeper for smaller values of  $d$ , and tend to their theoretical values as  $d$  increases.

Figure 5.3 and again for Figure 5.4. Furthermore, the gradient of the error curves tends towards the expected theoretical values as the value of  $c_0$  increases. This is expected as the magnitude of the terms in (5.23) increase as  $c_0$  increases.

To identify this behaviour more clearly, we tabulate the values of  $e_i$  for a range of values of  $c_0$  and  $\gamma$ . These results are shown in Tables 5.1, 5.2 and 5.3 for the inclusion of leading order terms,  $O(\sqrt{\epsilon})$  and  $O(\epsilon)$  i.e.  $e_1$ ,  $e_2$  and  $e_3$ . From these tables we clearly see

Value of $\gamma$	$d = 1$		$d = 4$		$d = 7$	
	$\alpha_1$	$C_1$	$\alpha_1$	$C_1$	$\alpha_1$	$C_1$
$\gamma = 0.1$	0.478	-0.471	0.468	0.742	0.466	1.274
$\gamma = 0.3$	0.559	-0.260	0.504	0.552	0.500	1.070
$\gamma = 0.5$	0.704	0.904	0.519	0.457	0.500	0.838

TABLE 5.1: Maximum absolute error scaling parameters for the leading order weakly nonlinear solution for the initial condition in (5.46). The domain lengths and parameters are  $\alpha = \beta = c = 1$ ,  $L = 40$  and  $k = 1/\sqrt{3}$ .

Value of $\gamma$	$d = 1$		$d = 4$		$d = 7$	
	$\alpha_2$	$C_2$	$\alpha_2$	$C_2$	$\alpha_2$	$C_2$
$\gamma = 0.1$	0.993	0.795	0.962	1.848	0.952	2.707
$\gamma = 0.3$	0.988	1.819	0.989	1.947	0.991	2.268
$\gamma = 0.5$	0.979	2.529	0.980	2.565	0.982	2.645

TABLE 5.2: Maximum absolute error scaling parameters for the weakly nonlinear solution up to  $O(\sqrt{\epsilon})$  for the initial condition in (5.46). The domain lengths and parameters are  $\alpha = \beta = c = 1$ ,  $L = 40$  and  $k = 1/\sqrt{3}$ .

Value of $\gamma$	$d = 1$		$d = 4$		$d = 7$	
	$\alpha_3$	$C_3$	$\alpha_3$	$C_3$	$\alpha_3$	$C_3$
$\gamma = 0.1$	1.519	0.835	1.455	2.505	1.443	3.776
$\gamma = 0.3$	1.920	4.755	1.643	3.290	1.528	3.310
$\gamma = 0.5$	1.969	6.418	1.913	6.071	1.805	5.434

TABLE 5.3: Maximum absolute error scaling parameters for the weakly nonlinear solution up to  $O(\epsilon)$  for the initial condition in (5.46). The domain lengths and parameters are  $\alpha = \beta = c = 1$ ,  $L = 40$  and  $k = 1/\sqrt{3}$ .

that the error values are close to the theoretical values for  $\gamma = 0.1$  and for large values of  $c_0$  with  $\gamma = 0.5$ . We also confirm that, as  $\gamma$  increases, the values of  $e_1$  and  $e_3$  tend to the next largest integer value. It is also clear from the values at  $\gamma = 0.5$  that, as  $c_0$  increases, the values of  $e_i$  tend towards their theoretical values.

A further interesting point arises from Figures 5.3 and 5.4. There will be a value of  $\epsilon$  where the error curves intercept, suggesting that the inclusion of higher order terms only improves the solution when  $\epsilon$  is below a theoretical limit, as expected for an asymptotic series. We introduce the following notation:

$$\epsilon_1 = \text{Intercept of } e_1 \text{ and } e_2 \text{ curves,} \quad \epsilon_2 = \text{Intercept of } e_2 \text{ and } e_3 \text{ curves.} \quad (5.49)$$

More precisely,  $\epsilon_1$  is the intercept of the leading order and  $O(\sqrt{\epsilon})$  curves, and  $\epsilon_2$  is the intercept of the  $O(\sqrt{\epsilon})$  and  $O(\epsilon)$  curves. We can calculate this using the values from Tables 5.1 - 5.3 and the results are shown in Table 5.4. We can see that, in general, an increase in  $\gamma$  results in a smaller value of  $\epsilon_1$  or  $\epsilon_2$  i.e. as  $\gamma$  increases we require a

Value of $\gamma$	Intercept of $O(1)$ and $O(\sqrt{\epsilon})$			Intercept of $O(\sqrt{\epsilon})$ and $O(\epsilon)$		
	$d = 1$	$d = 4$	$d = 7$	$d = 1$	$d = 4$	$d = 7$
$\gamma = 0.1$	0.0856	0.1066	0.0524	0.9268	0.2638	0.1134
$\gamma = 0.3$	0.0079	0.0563	0.0872	0.0428	0.1283	0.1436
$\gamma = 0.5$	0.0027	0.0103	0.0235	0.0197	0.0233	0.0337

TABLE 5.4: Intercept point of error curves, in terms of  $\epsilon$ , representing the maximum value of  $\epsilon$  at which the inclusion of  $O(\sqrt{\epsilon})$  or  $O(\epsilon)$  terms will decrease the error.

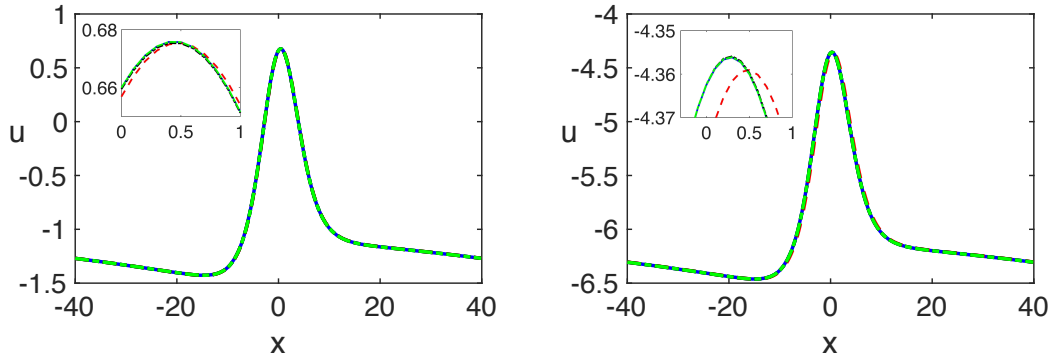
smaller value of  $\epsilon$  to improve the accuracy of the solution with the inclusion of higher order terms.

Another observation is that, for  $\gamma > 0.1$ , as  $d$  increases we see a corresponding increase in  $\epsilon_1$  or  $\epsilon_2$ . This suggests that for large  $\gamma$ , when a small value of  $\epsilon_1$  and  $\epsilon_2$  is required for the inclusion of multiple terms from the weakly nonlinear expansion, the threshold is increased with an increase in  $d$ . More importantly, in all cases here we have  $\epsilon_1 < \epsilon_2$  and therefore, if the inclusion of  $O(\sqrt{\epsilon})$  terms improves the accuracy of the solution for the choice of  $\epsilon$ , then the inclusion of  $O(\epsilon)$  terms will also improve the accuracy of the solution, without further restriction on  $\epsilon$ .

### 5.3.3 Results for Non-Unity Coefficients

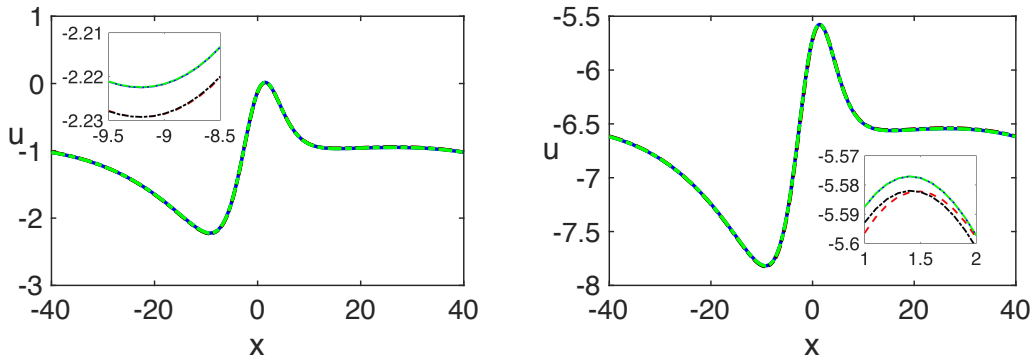
We now consider the system with a higher characteristic speed, namely  $c = 2$  and we also vary the values of  $\alpha$  and  $\beta$ , so we take  $\alpha = \beta = 2$ . As was done in Section 5.3.2, we compare the solution to the Boussinesq-Ostrovsky equation to the weakly nonlinear solution with an increasing number of terms included in the expansion. We plot the results for  $\gamma = 0.1$  and  $\gamma = 0.5$ , with a pedestal term of  $d = 1$  and  $d = 7$ , for direct comparison with the results for  $c = 1$ , in Figures 5.5 and 5.6. We can see that there is a larger phase shift in these cases; comparing directly between the cases for  $\gamma = 0.5$  when  $c = 1$  and  $c = 2$ , we see that the phase shift of the leading order solution (red line) is distinctly larger in the latter case than the former. Furthermore, the difference between the cases including terms up to  $O(\sqrt{\epsilon})$  and terms up to  $O(\epsilon)$  are more clearly highlighted in this case than the previous results for  $c = 1$ , as can again be seen clearly from Figure 5.5 and 5.6 for the enhanced inserts in each image.

As before we plot the corresponding error curves for the cases in Figures 5.5 and 5.6. These results are presented in Figure 5.7 and Figure 5.8 for  $\gamma = 0.1$  and  $\gamma = 0.5$  respectively. We again see that the error curves in Figure 5.7 have slope 0.5, 1 and 1.5 as expected. It is worth noting that the errors are similar to their previous cases by visual inspection of Figures 5.7 and 5.8 for  $c = 1$ . However, we see that as  $\gamma$  increases, while the curves for the leading order and the inclusion of  $O(\sqrt{\epsilon})$  terms do tend towards



(a) The solution of the Boussinesq-Ostrovsky equation and the weakly nonlinear solutions for  $\gamma = 0.1$  and  $d = 1$ . (b) The solution of the Boussinesq-Ostrovsky equation and the weakly nonlinear solutions for  $\gamma = 0.1$  and  $d = 7$ .

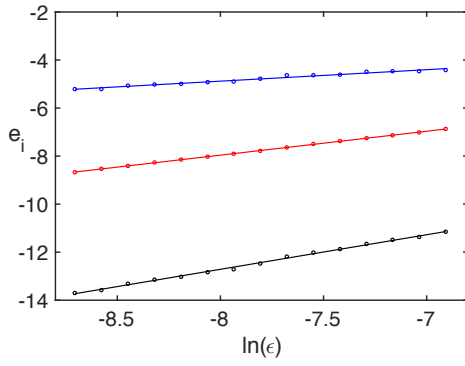
FIGURE 5.5: A comparison of the original Boussinesq-Ostrovsky equation (5.1) (solid, blue) at  $t = 1/\epsilon$ , for the weakly nonlinear solution including leading order (dashed, red),  $O(\sqrt{\epsilon})$  (dash-dot, black) and  $O(\epsilon)$  (dotted, green) corrections, for (a)  $d = 1$  and (b)  $d = 7$ . Parameters are  $L = 40$ ,  $N = 800$ ,  $k = 1/\sqrt{3}$ ,  $\alpha = \beta = c = 2$ ,  $\gamma = 0.1$ ,  $\epsilon = 0.001$ ,  $\Delta t = 0.01$  and  $\Delta T = \epsilon \Delta t$ . We see that the solution agrees well to leading order and this agreement is improved with the addition of higher order corrections.



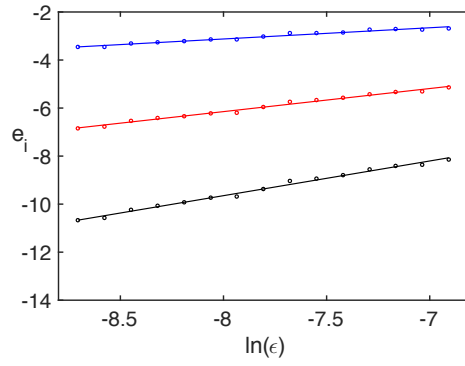
(a) The solution of the Boussinesq-Ostrovsky equation and the weakly nonlinear solutions for  $\gamma = 0.5$  and  $d = 1$ . (b) The solution of the Boussinesq-Ostrovsky equation and the weakly nonlinear solutions for  $\gamma = 0.5$  and  $d = 7$ .

FIGURE 5.6: A comparison of the original Boussinesq-Ostrovsky equation (5.1) (solid, blue) at  $t = 1/\epsilon$ , for the weakly nonlinear solution including leading order (dashed, red),  $O(\sqrt{\epsilon})$  (dash-dot, black) and  $O(\epsilon)$  (dotted, green) corrections, for (a)  $d = 1$  and (b)  $d = 7$ . Parameters are  $L = 40$ ,  $N = 800$ ,  $k = 1/\sqrt{3}$ ,  $\alpha = \beta = c = 2$ ,  $\gamma = 0.5$ ,  $\epsilon = 0.001$ ,  $\Delta t = 0.01$  and  $\Delta T = \epsilon \Delta t$ . We see that the solution agrees well to leading order and this agreement is improved with the addition of higher order corrections.

each other as in the case for  $c = 1$ , the rate at which this occurs is slower to the previous case when  $c = 1$ . To inspect this behaviour further, we again tabulate the errors in Tables 5.5, 5.6 and 5.7 for the inclusion of leading order terms,  $O(\sqrt{\epsilon})$  and  $O(\epsilon)$  i.e.  $e_1$ ,  $e_2$  and  $e_3$ . The errors are close to the theoretical values as before, however we can see from these tables that the theoretical slope values are obtained for a wider range of  $\gamma$  and  $c_0$  values in contrast to the previous case for  $c = 1$ . If we analyse the form of the

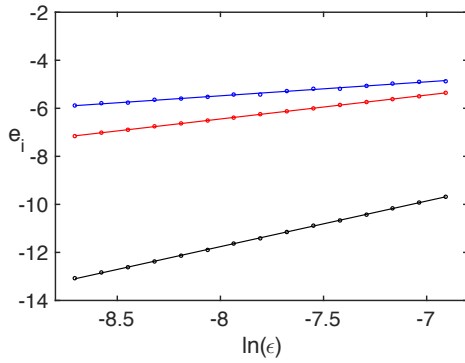


(a) Error curves for  $\gamma = 0.1$  and  $d = 1$ , for all values of  $e_i$ .

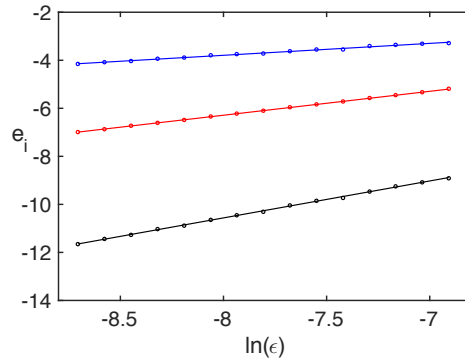


(b) Error curves for  $\gamma = 0.1$  and  $d = 7$ , for all values of  $e_i$ .

FIGURE 5.7: A comparison of error curves for varying values of  $\epsilon$ , at  $t = 1/\epsilon$ , for the weakly nonlinear solution including leading order (upper, blue),  $O(\sqrt{\epsilon})$  (middle, red) and  $O(\epsilon)$  (lower, black) corrections, for (a)  $d = 1$  and (b)  $d = 7$ . Parameters are  $L = 40$ ,  $N = 800$ ,  $k = 1/\sqrt{3}$ ,  $\alpha = \beta = c = 2$ ,  $\gamma = 0.1$ ,  $\Delta t = 0.01$  and  $\Delta T = \epsilon \Delta t$ . We see that the inclusion of more terms in the expansion increases the accuracy, and that the errors increase for larger values of  $d$ .



(a) Error curves for  $\gamma = 0.5$  and  $d = 1$ , for all values of  $e_i$ .



(b) Error curves for  $\gamma = 0.5$  and  $d = 7$ , for all values of  $e_i$ .

FIGURE 5.8: A comparison of error curves for varying values of  $\epsilon$ , at  $t = 1/\epsilon$ , for the weakly nonlinear solution including leading order (upper, blue),  $O(\sqrt{\epsilon})$  (middle, red) and  $O(\epsilon)$  (lower, black) corrections, for (a)  $d = 1$  and (b)  $d = 7$ . Parameters are  $L = 40$ ,  $N = 800$ ,  $k = 1/\sqrt{3}$ ,  $\alpha = \beta = c = 2$ ,  $\gamma = 0.5$ ,  $\Delta t = 0.01$  and  $\Delta T = \epsilon \Delta t$ . We see that the inclusion of more terms in the expansion increases the accuracy, and that the errors increase for larger values of  $d$ . The upper and lower curves are steeper for smaller values of  $d$ , and tend to their theoretical values as  $d$  increases.

expressions in (5.42) we can see that, for  $O(\sqrt{\epsilon})$ , the term is identical to the previous case if  $c = \alpha$ , as we have here. However, for  $O(\epsilon)$  (as can be seen from (5.33)) the first term in this expression is smaller due to the divisor of  $2c$ . This is further reflected in the initial condition for  $\phi$ , as the terms from (5.33) are present here as well. Therefore, the values present at  $O(\epsilon)$  are likely to be smaller and therefore more distinct from the previous value at  $O(\sqrt{\epsilon})$ , resulting in the estimates being obtained more distinctly for

Value of $\gamma$	$d = 1$		$d = 4$		$d = 7$	
	$\alpha_1$	$C_1$	$\alpha_1$	$C_1$	$\alpha_1$	$C_1$
$\gamma = 0.1$	0.477	-1.061	0.469	0.091	0.467	0.615
$\gamma = 0.3$	0.522	-1.154	0.498	-0.136	0.497	0.389
$\gamma = 0.5$	0.581	-0.828	0.501	-0.314	0.496	0.178

TABLE 5.5: Maximum absolute error scaling parameters for the leading order weakly nonlinear solution for the initial condition in (5.46). The domain lengths and parameters are  $\alpha = \beta = c = 2$ ,  $L = 40$  and  $k = 1/\sqrt{3}$ .

Value of $\gamma$	$d = 1$		$d = 4$		$d = 7$	
	$\alpha_2$	$C_2$	$\alpha_2$	$C_2$	$\alpha_2$	$C_2$
$\gamma = 0.1$	0.996	0.007	0.974	0.825	0.961	1.540
$\gamma = 0.3$	0.996	0.893	0.996	1.063	0.996	1.348
$\gamma = 0.5$	0.995	1.514	0.995	1.576	0.996	1.679

TABLE 5.6: Maximum absolute error scaling parameters for the weakly nonlinear solution up to  $O(\sqrt{\epsilon})$  for the initial condition in (5.46). The domain lengths and parameters are  $\alpha = \beta = c = 2$ ,  $L = 40$  and  $k = 1/\sqrt{3}$ .

Value of $\gamma$	$d = 1$		$d = 4$		$d = 7$	
	$\alpha_3$	$C_3$	$\alpha_3$	$C_3$	$\alpha_3$	$C_3$
$\gamma = 0.1$	1.440	-1.197	1.449	0.978	1.444	3.433
$\gamma = 0.3$	1.684	0.723	1.515	0.808	1.498	2.003
$\gamma = 0.5$	1.899	1.907	1.646	1.507	1.538	1.738

TABLE 5.7: Maximum absolute error scaling parameters for the weakly nonlinear solution up to  $O(\epsilon)$  for the initial condition in (5.46). The domain lengths and parameters are  $\alpha = \beta = c = 2$ ,  $L = 40$  and  $k = 1/\sqrt{3}$ .

the same set of  $\epsilon$  values as before. This behaviour is replicated for several values of  $\gamma$  and  $c_0$ , and indeed while for large  $\gamma$  we see the slope values differing from their theoretical estimates, the magnitude of the divergence is less than the previous case.

As was seen in the case for  $c = 1$ , from Figures 5.7 and 5.8 we notice that there will be a value of  $\epsilon$  where the error curves intercept, suggesting that the inclusion of higher order terms only improves the solution when  $\epsilon$  is below a theoretical limit, as expected for an asymptotic series. We again calculate this limit using the values from Tables 5.5 - 5.7 for each of the cases considered in Figures 5.7 and 5.8. The results are shown in Table 5.8.

Let us analyse the conclusions we drew for the previous case, referring to the notation in (5.49). As  $\gamma$  increases, we see that  $\epsilon_1$  decreases for all values of  $d$  whereas for  $\epsilon_2$ , in contrast to the previous case, as  $d$  increases this behaviour is reversed i.e. for  $d = 1$  we have that  $\epsilon_2$  decreases as  $\gamma$  increases, but for  $d = 7$  we have that  $\epsilon_2$  increases as  $\gamma$  increases. This suggests that the behaviour observed before is dependent upon the coefficients in the equation.

Value of $\gamma$	Intercept value $\epsilon_1$			Intercept value $\epsilon_2$		
	$d = 1$	$d = 4$	$d = 7$	$d = 1$	$d = 4$	$d = 7$
$\gamma = 0.1$	0.1277	0.2338	0.1537	15.0550	0.7246	0.0199
$\gamma = 0.3$	0.0133	0.0900	0.1463	1.2803	1.6345	0.2712
$\gamma = 0.5$	0.0035	0.0218	0.0497	0.6474	1.1118	0.8969

TABLE 5.8: Intercept point of error curves in Figures 5.7 and 5.8, in terms of  $\epsilon$ , representing the maximum value of  $\epsilon$  at which the inclusion of  $O(\sqrt{\epsilon})$  or  $O(\epsilon)$  terms will decrease the error.

The behaviour observed for increasing  $d$  is also different to before. For  $\gamma > 0.1$  we see that  $\epsilon_1$  increases as  $d$  increases, but for  $\epsilon_2$  there is no clear relation. This behaviour would need to be investigated further. As with the previous scenario, in almost all cases we see that  $\epsilon_1 < \epsilon_2$  and therefore, if the inclusion of  $O(\sqrt{\epsilon})$  terms improves the accuracy of the solution for the choice of  $\epsilon$ , then the inclusion of  $O(\epsilon)$  terms will also improve the accuracy of the solution, without further restriction on  $\epsilon$ .

There is one further conclusion that can be drawn by comparing the values obtained when we have unity coefficients. In almost every case (the only exception being  $\gamma = 0.1$  and  $d = 7$ ) we have that  $\epsilon_i$  is smaller for the unity coefficient case than for the case when  $c = \alpha = \beta = 2$ . This suggests that the threshold value of  $\epsilon$  increases when the coefficients increase and therefore a weakly nonlinear solution can be formed for larger values of  $\epsilon$ .

## 5.4 Conclusions

The discussion in this chapter has been dedicated to the initial-value problem for the Boussinesq-Ostrovsky equation where the initial condition has non-zero mean. We calculated the mean value of the solution and subtracted this from the function to obtain a modified Boussinesq-Ostrovsky equation where the solution has zero mean value. A weakly nonlinear solution was constructed in terms of the leading order left- and right-propagating waves in powers of  $\sqrt{\epsilon}$  so that all functions up to and including  $O(\epsilon)$  were fully defined. This weakly nonlinear solution was then substituted back into the initial condition to obtain initial conditions for the derived functions in the weakly nonlinear expansion.

We then compared the constructed weakly nonlinear solution to the numerically calculated solution to the Boussinesq-Ostrovsky equation, with an increasing number of terms included from the expansion. This showed that the accuracy improved as more terms from the weakly nonlinear expansion were included, with the  $O(\sqrt{\epsilon})$  correction compensating for a phase shift while the  $O(\epsilon)$  correction adjusted the amplitude of the

solution and captured higher-order left-propagating waves not captured by the leading order solution. The errors were plotted against  $\epsilon$  and we showed that the absolute error scales with the order of the next term in the weakly nonlinear expansion. We also showed that, as  $\gamma$  increases, the terms at non-integer powers of  $\epsilon$  become small and therefore the absolute error scales with the next integer power. Increasing the mean value of the initial condition reduced this effect as the terms at non-integer powers of  $\epsilon$  increase with the mean value, and this behaviour was seen in the tabulated values for the error curves.

A final study was performed for the case when the linear speed of waves was increased i.e. for  $c = 2$ . In this case we showed that the same conclusions can be drawn from the error curves as the previous case, and indeed the errors increase for larger values of the mean value as before. Furthermore, we again see that as  $\gamma$  increases the size of the terms in the weakly nonlinear expansion at fractional powers of  $\epsilon$  tend to the next largest integer value of  $\epsilon$  as before, but at a slower rate to before. This confirms that the estimates hold for non-unity values of the coefficients.

The work in this chapter lays the groundwork for an extension of the scattering problem considered in Chapter 4, as we could consider a layered bar with significantly different properties between the layers. Indeed, if the lower layer has a sufficiently large characteristic speed then the model gives a Boussinesq-Ostrovsky equation in the bonded section and a Boussinesq equation in the delaminated and homogeneous regions. These equations would have to be considered as having zero mean value and therefore the model is significantly more complicated than the previous case. We discuss this further in the conclusions of the thesis.



## Chapter 6

# Conclusions and Future Work

In this thesis, we have considered the scattering of longitudinal bulk strain waves of various types in layered waveguides with different types of bonds between the layers. In each case, we aimed to describe the behaviour of such waves in the delaminated region of the waveguide and, if possible, when they re-enter a bonded section of the bar. We developed numerical techniques in each case to aid our understanding of the problem.

In the first case we considered a perfectly bonded elastic bar with multiple layers, such as the one considered in [30]. Our numerical modelling has confirmed that, in this case, an incident solitary wave scatters in the delaminated region of the bar, generating multiple solitons and dispersive radiation. The number of solitons generated is dependent upon the number of layers and the geometry of the waveguide. We developed a semi-analytical technique (see [42]) based upon the weakly nonlinear solution to the problem (see [30]), which reduced the problem from the solution of multiple Boussinesq equations with matching at the boundaries (describing the longitudinal displacements in the bar) to the solving of at most two KdV equations in each section, describing reflected and transmitted strain waves. This method was shown to be highly efficient and can compute the solution to the problem many times faster than the direct method.

We continued this modelling to consider the case when the delamination region is finite, so the solitons generated in the delaminated region of the bar must re-enter a bonded section. In this case, we showed that the amplitudes of the generated solitons changed as they became solitary waves in the bonded section, rather than the delaminated section. Using the IST, we predicted the amplitudes of the lead soliton in this region (and indeed other solitons, but this was not relevant to the study) and compared this to the numerically calculated solution. As the length of the delamination region was increased, the value of the amplitude tended from the incident wave's amplitude to the theoretical

value. This allowed us to predict the length of the delamination region using the parameters of the equation and therefore provides a method for using this work in a physical setting for introscopy.

The next section of the work was dedicated to the case when we have a soft bond between the layers rather than a perfect bond. In this case, the material in the layers can be different. The propagation of longitudinal displacements is described by coupled Boussinesq equations [38], in contrast to the uncoupled equations we saw in the previous case. Following [39], there are two cases: one when the materials in the layers have sufficiently close properties, and the second when the materials in the layers are significantly different. We considered the first case in this thesis, when the difference is such that the characteristic speeds differ by approximately  $O(\epsilon)$ , and we observed the generation of radiating solitary waves in the bonded region of the bar, that is a solitary wave with a one-sided co-propagating oscillatory tail. When these waves entered a delaminated region, we observed that the solitary wave separated from its tail, while the tail evolves into a wave packet [111]. When this solitary wave re-entered a bonded region, the solitary wave formed another radiating solitary wave in this region, but due to an energy exchange between the layers, the new radiating solitary wave has a smaller amplitude. If the delamination region is of a shorter length, then the formed wave packet is not a single radiating solitary wave but rather a double-humped structure. However, due to the energy exchange, the change in amplitude is still consistent. Therefore, we have shown that the change in amplitude can be used as a measure of the delamination length. In addition, a phase shift between the case without delamination and the case with delamination also gives a measure of the length of the delamination. The length of the radiating solitary wave's tail and the position of the radiating tail behind the double-humped structure in the second bonded region provided another measure for the position of the delaminated region.

Finally we considered the so-called Boussinesq-Ostrovsky equation on the periodic domain, with the aim of constructing a weakly nonlinear solution to the initial value problem for the equation, extending the work in [45, 46]. In contrast to the previous cases where we considered the Boussinesq equation, the equations derived in the weakly nonlinear expansion necessarily require zero mean, while the initial condition may not necessarily have zero mean. In [46] it was shown that the mean value of the Boussinesq-Ostrovsky equation oscillated in time with period proportional to  $\sqrt{\epsilon}$ ; this mean value was subtracted from the original solution to obtain an equation for a function with zero mean value and therefore an expansion in zero mean functions. However the solution was obtained in terms of Fourier series, and was difficult to use. As instructed by this mean value term, we developed a new asymptotic expansion in terms of  $\sqrt{\epsilon}$  rather than  $\epsilon$ , and using two slow scales, in contrast to the case of a Boussinesq equation. Numerical

studies showed that the weakly nonlinear solution agrees reasonably well at leading order and the solution is improved with the addition of more terms from the expansion. In each case, the error scaled at the rate of the next term in the expansion and we showed that these estimates hold for non-unity coefficients in the equation. Furthermore, we found that there is a calculable value of  $\epsilon$  above which the inclusion of extra terms in the expansion does not improve the solution and would actually give a larger error. This point can be found for any order in the expansion and gives a measure to how “weakly nonlinear” the solution is, and indeed suggests that we require a certain value of  $\epsilon$  for improvements in the accuracy.

The work in the final chapter of the thesis for the Boussinesq-Ostrovsky equation is of critical importance to the scattering problem discussed in the earlier chapters of the thesis, as the derived solution for the coupled Boussinesq equations also has a restriction on the mean value of the solution. In the aforementioned case the mean value was small and therefore any errors introduced would be small. An extension of the work in this thesis would be to consider the case described in Chapter 4 for a two-layered bar with a soft bond between the layers. However, we allow the lower layer to have significantly different properties to the upper layer. For example, if we consider the lower layer to be a much higher density material, then if we take the limit we can assume that the displacements from the equilibrium position in this layer are negligible; in this case, we would find that the displacements in the upper layer would be described by a Boussinesq-Ostrovsky equation. This case could then be considered using the expansion developed in Chapter 5 for a non-zero mean initial condition and a weakly nonlinear solution to the scattering problem could be derived, taking account of the mean value of the initial condition. This would lead to an improvement in the solution and the methodology could be extended to the coupled Boussinesq equations, such as those described in Chapter 4, either for materials with close properties or indeed significantly different properties i.e.  $c - 1 = O(1)$ .



## Appendix A

# Finite-difference Techniques for the Boussinesq and Boussinesq-type Equations

Finite-difference techniques are commonly used to solve simple ODEs and PDEs and can also be extended to more complicated systems. The simplest case involves replacing the continuous equation by a discrete equation i.e. discretising the domain and replacing all derivatives by a discretised form. Many books have been written on these techniques and their applications to various equations [112, 113]. These methods can easily be extended to more complicated equations, such as the KdV equation [3, 93], one-dimensional Burgers equation [114], the Kadomtsev-Petviashvili equation [115], to name a few.

In our case, we will consider the application of finite-difference techniques to a Boussinesq equation. This method is generalised to the case of coupled regularised Boussinesq (cRB) equations and we show that the system can be solved using the same technique. We extend these methods to the system described in Chapter 3, where we have several Boussinesq equations with different coefficients, combined with continuity conditions on the interface. Finally, we show that these methods can be applied to the case in Chapter 4, where we have cRB equations with continuity conditions on the interface between sections.

## A.1 Finite-Difference Method for the Boussinesq Equation

Let us consider the initial value problem for the Boussinesq equation on the infinite line, taking the form

$$f_{tt} - c^2 f_{xx} = \epsilon \left( \frac{\alpha}{2} (f^2)_{xx} + \beta f_{ttxx} \right), \quad (\text{A.1})$$

$$f|_{t=0} = F(x, 0), \quad (\text{A.2})$$

$$f_t|_{t=0} = G(x, 0). \quad (\text{A.3})$$

We solve this method using a finite-difference method, as was done in [116]. As we are solving these equations numerically, we restrict ourselves to a finite domain  $x \in [-L, L]$  and discretise the  $(x, t)$  domain into a grid with spacings  $h = \Delta x$  and  $\kappa = \Delta t$ . The analytical solution  $f(x, t)$  is approximated by the exact solution of the difference scheme  $f(ih, j\kappa) = f_{i,j}$ , where we have  $i = 0, 1, \dots, N$  and  $j = 0, 1, \dots$ . We approximate the derivatives in (A.1) using central difference approximations (derived from the Taylor series) of the form

$$f_{xx} = \frac{f_{i+1,j} - 2f_{i,j} + f_{i-1,j}}{h^2}, \quad f_{tt} = \frac{f_{i,j+1} - 2f_{i,j} + f_{i,j-1}}{\kappa^2}. \quad (\text{A.4})$$

For the fourth-order derivative in (A.1) we apply the operators in (A.4) to each other to obtain

$$f_{ttxx} = \frac{f_{i+1,j+1} - 2f_{i+1,j} + f_{i+1,j-1} - 2f_{i,j+1} + 4f_{i,j} - 2f_{i,j-1} + f_{i-1,j+1} - 2f_{i-1,j} + f_{i-1,j-1}}{\kappa^2 h^2}. \quad (\text{A.5})$$

The approximations in (A.4) and (A.5) are applied to (A.1) to obtain a discretised equation. We introduce the notation

$$D_{xx}(f_{i,j}) = f_{i+1,j} - 2f_{i,j} + f_{i-1,j},$$

and therefore we have

$$\begin{aligned} & -\epsilon\beta f_{i+1,j+1} + (2\epsilon\beta + h^2) f_{i,j+1} - \epsilon\beta f_{i-1,j+1} = (\kappa^2 c^2 - 2\epsilon\beta) D_{xx}(f_{i,j}) + 2h^2 f_{i,j} \\ & - \frac{\epsilon\alpha\kappa^2}{2} \left[ (f_{i+1,j})^2 - 2(f_{i,j})^2 + (f_{i-1,j})^2 \right] + \epsilon\beta f_{i+1,j-1} - (2\epsilon\beta + h^2) f_{i,j-1} + \epsilon\beta f_{i-1,j-1}. \end{aligned} \quad (\text{A.6})$$

We can see from this that we require two initial conditions (as we have three time levels in the scheme) and boundary conditions. We impose zero first derivative on the boundaries i.e.  $f_x = 0$  at  $x = -L$  and  $x = L$ , and applying a central difference approximation we

obtain

$$f_{-1,j} = f_{1,j} \quad \text{and} \quad f_{N-1,j} = f_{N+1,j}, \quad \forall j. \quad (\text{A.7})$$

For a given analytical initial condition, we can take the initial condition for the difference equations of the form

$$f_{i,0} = F(ih, 0) \quad \text{and} \quad f_{i,1} = F(ih, \kappa), \quad \forall i. \quad (\text{A.8})$$

If the initial condition is not given analytically then we can use a forward-difference approximation to obtain the second initial condition for the scheme i.e

$$f_{i,0} = F(ih, 0), \quad \text{and} \quad f_{i,1} = F(ih, 0) + \kappa G(ih, 0), \quad \forall i. \quad (\text{A.9})$$

It can be seen that this system has tridiagonal form and therefore is amenable to solution via optimised algorithms such as the Thomas algorithm (e.g. [117]). This can be seen clearly by writing the system in matrix form for  $i = 0, 1, \dots, N$ , where it takes the form

$$\begin{pmatrix} 2\epsilon\beta + h^2 & -2\epsilon\beta & & & \\ -\epsilon\beta & 2\epsilon\beta + h^2 & -\epsilon\beta & & \\ & \ddots & \ddots & & \\ & & -\epsilon\beta & 2\epsilon\beta + h^2 & -\epsilon\beta \\ & & & -2\epsilon\beta & 2\epsilon\beta + h^2 \end{pmatrix} \begin{pmatrix} f_{0,j+1} \\ f_{1,j+1} \\ \vdots \\ f_{N-1,j+1} \\ f_{N,j+1} \end{pmatrix} = \begin{pmatrix} \tilde{f}_0 \\ \tilde{f}_1 \\ \vdots \\ \tilde{f}_{N-1} \\ \tilde{f}_N \end{pmatrix}, \quad (\text{A.10})$$

where  $\tilde{f}_i$  represents the right-hand side of (A.6) at index  $i$ . The Thomas algorithm is an optimised form of Gaussian elimination that makes use of the tridiagonal structure of the matrix to simplify the method of solution. A condition for stability of the algorithm is that the matrix (A.10) is diagonally dominant; we can clearly see that this condition is satisfied for (A.10).

The stability of this scheme can be shown via a von Neumann linear stability analysis [118]. In the subsequent sections, where we have a system of Boussinesq equations, each Boussinesq equation should be stable via the same analysis, and the modification at the interface between the equations should not have an adverse effect on this stability. The step sizes chosen in each case adhere to the restriction imposed by this stability analysis.

## A.2 Direct Numerical Method for a System of Two Boussinesq-type Equations

### A.2.1 Derivation for Boussinesq Equation

Let us recall equation system (3.1) from Chapter 3. Denoting the coefficients for  $x < 0$  with a subscript of 1 and for  $x > 0$  with subscript 2, we can express the system for  $x < 0$  and  $x > 0$  as

$$\begin{aligned} u_{tt}^- - c_1^2 u_{xx}^- &= 2\epsilon [-6\alpha_1 u_x^- u_{xx}^- + \beta_1 u_{ttxx}^-], & x < 0, \\ u_{tt}^+ - c_2^2 u_{xx}^+ &= 2\epsilon [-6\alpha_2 u_x^+ u_{xx}^+ + \beta_2 u_{ttxx}^+], & x > 0, \end{aligned} \quad (\text{A.11})$$

with appropriate initial conditions

$$u^\pm(x, 0) = F^\pm(x), \quad (\text{A.12})$$

and associated continuity conditions

$$u^-|_{x=0} = u^+|_{x=0}, \quad (\text{A.13})$$

$$c_1^2 u_x^- + 2\epsilon [-3\alpha_1 (u_x^-)^2 + \beta_1 u_{ttx}^-] \Big|_{x=0} = c_2^2 u_x^+ + 2\epsilon [-3\alpha_2 (u_x^+)^2 + \beta_2 u_{ttx}^+] \Big|_{x=0}. \quad (\text{A.14})$$

We aim to solve this system by extending the method described in Section A.1. An overview of the method is as follows. We discretise the Boussinesq equation in each section, introducing “ghost points” at the interface between the boundary. The Thomas algorithm is applied to solve the Boussinesq equation implicitly in terms of these “ghost points” and the continuity conditions are then discretised to obtain a system of equations relating the “ghost points” at the boundary. This system is solved to obtain values for the “ghost points” and this can then be substituted into the implicit solution for the Boussinesq equation to obtain an explicit solution at a given time step.

This method is described in [42], however the time derivative term in the second continuity condition is calculated incorrectly therefore the statement that the scheme is second order made in this paper is invalid. We have recalculated the derivative term to obtain a scheme that is second order, and this is applied in all subsequent work including [43, 111].

To simplify the notation, we assume that the interface between the two methods is located at  $x = 0$ . Therefore, we can discretise the domain  $([-L_1, 0] \cup [0, L_2]) \times [0, T]$  into a grid with equal spacings  $h = \Delta x$  and  $\kappa = \Delta t$ . Denoting the solution for  $x < 0$

as  $u^-$  and for  $x > 0$  as  $u^+$ , the analytical solution  $u^\pm(x, t)$  is approximated by the exact solution of the finite-difference scheme  $u^\pm(ih, j\kappa)$ , denoted  $u_{i,j}^\pm$ , where we have  $i = 0, 1, \dots, N_1$  for  $x < 0$  and  $i = 0, 1, \dots, N_2$  for  $x > 0$ . The discretised form of the Boussinesq equation is shown in (A.15) and (A.16) for generic coefficients. To simplify the obtained expressions, we introduce the notation

$$D_{xx} \left( u_{i,j}^- \right) = u_{i+1,j}^- - 2u_{i,j}^- + u_{i-1,j}^-.$$

Substituting these approximations into system (A.11) gives a tridiagonal system of equations, of the form

$$\begin{aligned} & -2\epsilon\beta_1 u_{i+1,j+1}^- + (4\epsilon\beta_1 + h^2) u_{i,j+1}^- - 2\epsilon\beta_1 u_{i-1,j+1}^- = (c_1^2 \kappa^2 - 4\epsilon\beta_1) D_{xx} \left( u_{i,j}^- \right) \\ & + 2h^2 u_{i,j}^- - \frac{6\epsilon\alpha_1 \kappa^2}{h} \left[ \left( u_{i+1,j}^- \right)^2 - \left( u_{i-1,j}^- \right)^2 - 2u_{i+1,j}^- u_{i,j}^- + 2u_{i,j}^- u_{i-1,j}^- \right] \\ & + 2\epsilon\beta_1 u_{i+1,j-1}^- - (4\epsilon\beta_1 + h^2) u_{i,j-1}^- + 2\epsilon\beta_1 u_{i-1,j-1}^-, \end{aligned} \quad (\text{A.15})$$

and

$$\begin{aligned} & -2\epsilon\beta_2 u_{i+1,j+1}^+ + (4\epsilon\beta_2 + h^2) u_{i,j+1}^+ - 2\epsilon\beta_2 u_{i-1,j+1}^+ = (c_2^2 \kappa^2 - 4\epsilon\beta_2) D_{xx} \left( u_{i,j}^+ \right) \\ & + 2h^2 u_{i,j}^+ - \frac{6\epsilon\alpha_2 \kappa^2}{h} \left[ \left( u_{i+1,j}^+ \right)^2 - \left( u_{i-1,j}^+ \right)^2 - 2u_{i+1,j}^+ u_{i,j}^+ + 2u_{i,j}^+ u_{i-1,j}^+ \right] \\ & + 2\epsilon\beta_2 u_{i+1,j-1}^+ - (4\epsilon\beta_2 + h^2) u_{i,j-1}^+ + 2\epsilon\beta_2 u_{i-1,j-1}^+. \end{aligned} \quad (\text{A.16})$$

Discretising the first continuity condition, (A.13), we obtain

$$u_{N_1,j+1}^- = u_{0,j+1}^+. \quad (\text{A.17})$$

In the continuity condition (A.14) we make use of central difference approximations and introduce the aforementioned ‘‘ghost points’’ of the form  $u_{N_1+1,j+1}^-$  and  $u_{-1,j+1}^+$ . Making these substitutions (A.14) becomes

$$\begin{aligned} & h\kappa^2 c_1^2 \left( u_{N_1+1,j+1}^- - u_{N_1-1,j+1}^- \right) - 3\kappa^2 \epsilon \alpha_1 \left[ \left( u_{N_1+1,j+1}^- \right)^2 + \left( u_{N_1-1,j+1}^- \right)^2 \right. \\ & \left. - 2u_{N_1+1,j+1}^- u_{N_1-1,j+1}^- \right] + 2h\epsilon\beta_1 \left( 2u_{N_1+1,j+1}^- - 2u_{N_1-1,j+1}^- - 5u_{N_1+1,j}^- + 5u_{N_1-1,j}^- \right. \\ & \left. + 4u_{N_1+1,j-1}^- - 4u_{N_1-1,j-1}^- - u_{N_1+1,j-2}^- + u_{N_1-1,j-2}^- \right) = h\kappa^2 c_2^2 \left( u_{1,j+1}^+ - u_{-1,j+1}^+ \right) \\ & + 2h\epsilon\beta_2 \left( 2u_{1,j+1}^+ - 2u_{-1,j+1}^+ - 5u_{1,j}^+ + 5u_{-1,j}^+ + 4u_{1,j-1}^+ - 4u_{-1,j-1}^+ - u_{1,j-2}^+ + u_{-1,j-2}^+ \right) \\ & - 3\kappa^2 \epsilon \alpha_2 \left[ \left( u_{1,j+1}^+ \right)^2 + \left( u_{-1,j+1}^+ \right)^2 - 2u_{1,j+1}^+ u_{-1,j+1}^+ \right]. \end{aligned} \quad (\text{A.18})$$

As we are considering localised initial data for strains, if we take  $L$  large enough then we can enforce zero boundary conditions for the strain i.e.  $u_x = 0$ . Therefore, applying a central difference approximation to this condition, we have

$$\frac{u_{1,j+1}^- - u_{-1,j+1}^-}{2h} = 0 \quad \Rightarrow \quad u_{1,j+1}^- = u_{-1,j+1}^- \quad \text{and similarly} \quad u_{N_1+1,j+1}^+ = u_{N_1-1,j+1}^+. \quad (\text{A.19})$$

Here we note that, as we have used central difference approximations everywhere, we have a second-order scheme. The systems (A.15) and (A.16) are tridiagonal for the values  $i = 0, \dots, N_1$  and  $i = 0, \dots, N_2$ . We denote the right-hand side of (A.15) as  $f_i$  and the right-hand side of (A.16) as  $g_i$ , for the appropriate values of  $i$ . At the central boundary we can rearrange to obtain

$$\tilde{f}_{N_1} = f_{N_1} + 2\epsilon\beta_1 u_{N_1+1,j+1}^-, \quad \tilde{g}_0 = g_0 + 2\epsilon\beta_2 u_{-1,j+1}^+. \quad (\text{A.20})$$

Therefore we can write (A.15) for  $i = 0, \dots, N_1$  in matrix form as

$$\begin{pmatrix} 4\epsilon\beta_1 + h^2 & -4\epsilon\beta_1 & & & \\ -2\epsilon\beta_1 & 4\epsilon\beta_1 + h^2 & -2\epsilon\beta_1 & & \\ & \ddots & \ddots & & \\ & & -2\epsilon\beta_1 & 4\epsilon\beta_1 + h^2 & -2\epsilon\beta_1 \\ & & & -2\epsilon\beta_1 & 4\epsilon\beta_1 + h^2 \end{pmatrix} \begin{pmatrix} u_{0,j+1}^- \\ u_{1,j+1}^- \\ \vdots \\ u_{N_1-1,j+1}^- \\ u_{N_1,j+1}^- \end{pmatrix} = \begin{pmatrix} f_0 \\ f_1 \\ \vdots \\ f_{N_1-1} \\ \tilde{f}_{N_1} \end{pmatrix}. \quad (\text{A.21})$$

Similarly we can write (A.16) in matrix form, for  $i = 0, \dots, N_2$ , as

$$\begin{pmatrix} 4\epsilon\beta_2 + h^2 & -2\epsilon\beta_2 & & & \\ -2\epsilon\beta_2 & 4\epsilon\beta_2 + h^2 & -2\epsilon\beta_2 & & \\ & \ddots & \ddots & & \\ & & -2\epsilon\beta_2 & 4\epsilon\beta_2 + h^2 & -2\epsilon\beta_2 \\ & & & -4\epsilon\beta_2 & 4\epsilon\beta_2 + h^2 \end{pmatrix} \begin{pmatrix} u_{0,j+1}^+ \\ u_{1,j+1}^+ \\ \vdots \\ u_{N_2-1,j+1}^+ \\ u_{N_2,j+1}^+ \end{pmatrix} = \begin{pmatrix} \tilde{g}_0 \\ g_1 \\ \vdots \\ g_{N_2-1} \\ g_{N_2} \end{pmatrix}. \quad (\text{A.22})$$

As both (A.21) and (A.22) are tridiagonal we can use the Thomas algorithm (e.g. [117]) to solve these systems implicitly, in terms of  $u_{N_1+1,j+1}^-$  and  $u_{-1,j+1}^+$  respectively. This intermediary solution is then substituted into (A.18) to obtain a nonlinear equation in terms of these ghost points. Noting that the Boussinesq solution is solved implicitly, we can express each point in the domain as an explicit component and a multiplier of the ghost point. Therefore we write each point in (A.18) in terms of an implicit and explicit component, so we have

$$u_{N_1,j+1}^- = \phi_1^- + \psi_1^- u_{N_1+1,j+1}^-, \quad u_{0,j+1}^+ = \phi_1^+ + \psi_1^+ u_{-1,j+1}^+,$$

$$u_{N_1-1,j+1}^- = \phi_2^- + \psi_2^- u_{N_1+1,j+1}^-, \quad u_{1,j+1}^+ = \phi_2^+ + \psi_2^+ u_{-1,j+1}^+, \quad (\text{A.23})$$

where we calculate the coefficients  $\phi_1^\pm, \psi_1^\pm, \phi_2^\pm, \psi_2^\pm$  from (A.21) and (A.22). The resulting equation will be a single equation in terms of both ghost points. Therefore we use (A.17) to express  $u_{-1,j+1}^+$  in terms of  $u_{N_1+1,j+1}^-$ , and also use (A.23) to express  $u_{N_1-1,j+1}^+$  and  $u_{1,j+1}^+$  in terms of the ghost points. Denoting  $u = u_{N_1+1,j+1}^-$  for brevity, we make use of (A.17) and (A.23) to obtain

$$u_{-1,j+1}^+ = \frac{\phi_1^- - \phi_1^+ + \psi_1^- u}{\psi_1^+} \quad \text{and} \quad u_{1,j+1}^+ = \phi_2^+ + \frac{\psi_2^+}{\psi_1^+} (\phi_1^- - \phi_1^+ + \psi_1^- u). \quad (\text{A.24})$$

Substituting (A.23) and (A.24) into (A.18) we can find a quadratic equation for  $u$  of the form

$$h_0 u^2 + h_1 u + h_2 = 0, \quad (\text{A.25})$$

where we have

$$\begin{aligned} h_0 &= -3\kappa^2 \epsilon \alpha_1 (\psi_2^- - 1)^2 + 3\kappa^2 \epsilon \alpha_2 \left( \frac{\psi_1^-}{\psi_1^+} \right)^2 (\psi_2^+ - 1)^2, \\ h_1 &= (1 - \psi_2^-) (h\kappa^2 c_1^2 + 2h\epsilon\beta_1 + 6\kappa^2 \epsilon \alpha_1 \phi_2^-) + 6\kappa^2 \epsilon \alpha_2 \frac{\psi_1^- (\phi_1^- - \phi_1^+)}{(\psi_1^+)^2} \left[ (\psi_2^+)^2 - 2\psi_2^+ + 1 \right] \\ &\quad + (1 - \psi_2^+) \left( \frac{\psi_1^-}{\psi_1^+} \right) (h\kappa^2 c_2^2 + 2h\epsilon\beta_2 - 6\kappa^2 \epsilon \alpha_2 \phi_2^+), \\ h_2 &= -\phi_2^- (h\kappa^2 c_1^2 + 2h\epsilon\beta_1) - 3\kappa^2 \epsilon \alpha_1 (\phi_2^-)^2 + 2h\epsilon\beta_1 \left( -5u_{N_1+1,j}^- + 5u_{N_1-1,j}^- \right. \\ &\quad \left. + 4u_{N_1+1,j-1}^- - 4u_{N_1-1,j-1}^- - u_{N_1+1,j-2}^- + u_{N_1-1,j-2}^- \right) \\ &\quad + 3\kappa^2 \epsilon \alpha_2 \left[ (\phi_2^+)^2 + \left( \frac{\phi_1^- - \phi_1^+}{\psi_1^+} \right)^2 (\psi_2^+ - 1)^2 + 2(\psi_2^+ - 1) \left( \frac{\phi_2^+ (\phi_1^- - \phi_1^+)}{\psi_1^+} \right) \right] \\ &\quad - (h\kappa^2 c_2^2 + 2h\epsilon\beta_2) \left[ \phi_2^+ + \frac{\phi_1^- - \phi_1^+}{\psi_1^+} (\psi_2^+ - 1) \right] \\ &\quad - 2h\epsilon\beta_2 \left( -5u_{1,j}^+ + 5u_{-1,j}^+ + 4u_{1,j-1}^+ - 4u_{-1,j-1}^+ - u_{1,j-2}^+ + u_{-1,j-2}^+ \right). \end{aligned} \quad (\text{A.26})$$

In order to simplify equations (A.26), we consider the intermediary steps in the Thomas algorithm. We can deduce that, for  $N_1, N_2$  large enough, we can set  $\psi_1^- = \psi_1^+$  and  $\psi_2^- = \psi_2^+$  (this has been confirmed by numerical calculation, and is covered in more detail in Section A.3 for the expanded scheme) and therefore  $h_0 \equiv 0$  if  $\alpha_1 = \alpha_2$ . In all cases where this scheme is implemented this condition is satisfied. This leads to the result

$$u = -\frac{h_2}{h_1}, \quad (\text{A.27})$$

and therefore we can determine  $u_{N_1, j+1}^-$ ,  $u_{0, j+1}^+$  and similarly  $u_{N_1-1, j+1}^-$  and  $u_{1, j+1}^+$ . These values are then substituted into the implicit solution of the tridiagonal system to determine the solution at each time step. If we did not have  $\alpha_1 = \alpha_2$  then the quadratic equation (A.25) would have to be solved and the appropriate solution chosen based upon the physical setting of the problem.

## A.2.2 Extension to Coupled Regularised Boussinesq Equations

The method outlined in Section A.2.1 is derived for the standard Boussinesq equation, however the work in Chapter 4 is for the coupled regularised Boussinesq (cRB) equations. We note that the continuity conditions are identical to those for the Boussinesq equation. Therefore the previous method can be extended to the case of the cRB equations by computing the implicit solution to the cRB equations using a similar method to those for the regular Boussinesq equation. This implicit solution takes the same form and therefore we can apply the rest of the method in the same way as before.

Let us consider a system of two cRB equations, one for  $x < 0$  and one for  $x > 0$ , where the variable for the upper layer is  $u(x, t)$  and  $w(x, t)$  for the lower layer. We denote coefficients for the upper layer by a subscript of 1, and for the lower layer with a subscript of 2. Similarly, for the equation system at  $x < 0$  we denote the coefficients with a superscript of (1) and for  $x > 0$  we denote coefficients with a superscript of (2). A similar notation is used for the variables in each section, so in the first section for the upper layer we have  $u^{(1)}$ , in the second section  $u^{(2)}$ , and similarly for  $w$ . Therefore we have the equation system

$$\begin{aligned} u_{tt}^{(1)} - \left(c_1^{(1)}\right)^2 u_{xx}^{(1)} &= 2\epsilon \left[ -6\alpha_1^{(1)} u_x^{(1)} u_{xx}^{(1)} + \beta_1^{(1)} u_{ttxx}^{(1)} - \delta_1^{(1)} \left( u^{(1)} - w^{(1)} \right) \right], \\ w_{tt}^{(1)} - \left(c_2^{(1)}\right)^2 w_{xx}^{(1)} &= 2\epsilon \left[ -6\alpha_2^{(1)} w_x^{(1)} w_{xx}^{(1)} + \beta_2^{(1)} w_{ttxx}^{(1)} + \delta_2^{(1)} \left( u^{(1)} - w^{(1)} \right) \right], \end{aligned} \quad (\text{A.28})$$

for  $x < 0$ , and for  $x > 0$  we have the same system but with upper indices of (2). We take appropriate initial conditions

$$u^{(1,2)}(x, 0) = F^{(1,2)}(x), \quad w^{(1,2)}(x, 0) = G^{(1,2)}(x), \quad (\text{A.29})$$

and associated continuity conditions

$$u^{(1)}|_{x=0} = u^{(2)}|_{x=0}, \quad (\text{A.30})$$

$$\begin{aligned} & \left. \left( c_1^{(1)} \right)^2 u_x^{(1)} + 2\epsilon \left[ -3\alpha_1^{(1)} \left( u_x^{(1)} \right)^2 + \beta_1^{(1)} u_{ttx}^{(1)} \right] \right|_{x=0} = \\ & \left. \left( c_1^{(2)} \right)^2 u_x^{(2)} + 2\epsilon \left[ -3\alpha_1^{(2)} \left( u_x^{(2)} \right)^2 + \beta_1^{(2)} u_{ttx}^{(2)} \right] \right|_{x=0}. \end{aligned} \quad (\text{A.31})$$

We can write the same system for  $w$  by replacing  $u$  with  $w$  and replacing subscript 1 coefficients with subscript 2 coefficients.

We can discretise the domain  $([-L_1, 0] \cup [0, L_2]) \times [0, T]$  into a grid with equal spacings  $h = \Delta x$  and  $\kappa = \Delta t$  as we did before. Denoting the solution for  $x < 0$  as  $u^{(1)}$  and  $w^{(1)}$ , and for  $x > 0$  as  $u^{(2)}$  and  $w^{(2)}$ , the analytical solution  $u^{(1,2)}(x, t)$  is approximated by the exact solution of the finite-difference scheme  $u^{(1,2)}(ih, j\kappa)$ , denoted  $u_{i,j}^{(1,2)}$ , where we have  $i = 0, 1, \dots, N_1$  for  $x < 0$  and  $i = 0, 1, \dots, N_2$  for  $x > 0$ . The same notation is used for  $w$ . Following the same idea as before we use central difference approximations to obtain a discretised form of (A.28). As before, to simplify the obtained expressions, we introduce the notation

$$D_{xx} \left( u_{i,j}^{(1)} \right) = u_{i+1,j}^{(1)} - 2u_{i,j}^{(1)} + u_{i-1,j}^{(1)}.$$

For  $x < 0$  we have

$$\begin{aligned} & -2\epsilon\beta_1^{(1)} u_{i+1,j+1}^{(1)} + \left( 4\epsilon\beta_1^{(1)} + h^2 \right) u_{i,j+1}^{(1)} - 2\epsilon\beta_1^{(1)} u_{i-1,j+1}^{(1)} = \left( c_1^2 \kappa^2 - 4\epsilon\beta_1^{(1)} \right) D_{xx} \left( u_{i,j}^{(1)} \right) \\ & + 2h^2 u_{i,j}^{(1)} - \frac{6\epsilon\alpha_1^{(1)} \kappa^2}{h} \left[ \left( u_{i+1,j}^{(1)} \right)^2 - \left( u_{i-1,j}^{(1)} \right)^2 - 2u_{i+1,j}^{(1)} u_{i,j}^{(1)} + 2u_{i,j}^{(1)} u_{i-1,j}^{(1)} \right] \\ & + 2\epsilon\beta_1^{(1)} u_{i+1,j-1}^{(1)} - \left( 4\epsilon\beta_1^{(1)} + h^2 \right) u_{i,j-1}^{(1)} + 2\epsilon\beta_1^{(1)} u_{i-1,j-1}^{(1)} - 2\epsilon\delta_1^{(1)} \left( u_{i,j}^{(1)} - w_{i,j}^{(1)} \right), \end{aligned} \quad (\text{A.32})$$

and

$$\begin{aligned} & -2\epsilon\beta_2^{(1)} w_{i+1,j+1}^{(1)} + \left( 4\epsilon\beta_2^{(1)} + h^2 \right) w_{i,j+1}^{(1)} - 2\epsilon\beta_2^{(1)} w_{i-1,j+1}^{(1)} = \left( c_2^2 \kappa^2 - 4\epsilon\beta_2^{(1)} \right) D_{xx} \left( w_{i,j}^{(1)} \right) \\ & + 2h^2 w_{i,j}^{(1)} - \frac{6\epsilon\alpha_2^{(1)} \kappa^2}{h} \left[ \left( w_{i+1,j}^{(1)} \right)^2 - \left( w_{i-1,j}^{(1)} \right)^2 - 2w_{i+1,j}^{(1)} w_{i,j}^{(1)} + 2w_{i,j}^{(1)} w_{i-1,j}^{(1)} \right] \\ & + 2\epsilon\beta_2^{(1)} w_{i+1,j-1}^{(1)} - \left( 4\epsilon\beta_2^{(1)} + h^2 \right) w_{i,j-1}^{(1)} + 2\epsilon\beta_2^{(1)} w_{i-1,j-1}^{(1)} + 2\epsilon\delta_2^{(1)} \left( u_{i,j}^{(1)} - w_{i,j}^{(1)} \right). \end{aligned} \quad (\text{A.33})$$

We can derive the same for the second section by replacing the upper index of (1) with (2). The continuity conditions can be found in the same way as before, and are omitted here for brevity as they take the same form but with different indices.

As before we note that the systems (A.32), (A.33) and their equivalents for  $x > 0$ , are

tridiagonal for the values  $i = 0, \dots, N_1$  and  $i = 0, \dots, N_2$ . Following the same idea as for Section A.2.1, we denote the right-hand side of (A.32) as  $f_i$  and the right-hand side of (A.33) as  $g_i$ , for the appropriate values of  $i$ . At the central boundary we can rearrange to obtain

$$\tilde{f}_{N_1} = f_{N_1} + 2\epsilon\beta_1^{(1)}u_{N_1+1,j+1}^{(1)}, \quad \tilde{g}_{N_1} = g_{N_1} + 2\epsilon\beta_2^{(1)}w_{N_1+1,j+1}^{(1)}. \quad (\text{A.34})$$

The same rearrangement can be made for the system describing  $x > 0$ , at the boundary  $x = 0$ . We can write (A.32) for  $i = 0, \dots, N_1$  in matrix form as

$$\begin{pmatrix} 4\epsilon\beta_1^{(1)} + h^2 & -4\epsilon\beta_1^{(1)} & & & \\ -2\epsilon\beta_1^{(1)} & 4\epsilon\beta_1^{(1)} + h^2 & -2\epsilon\beta_1^{(1)} & & \\ & \ddots & \ddots & & \\ & & -2\epsilon\beta_1^{(1)} & 4\epsilon\beta_1^{(1)} + h^2 & -2\epsilon\beta_1^{(1)} \\ & & & -2\epsilon\beta_1^{(1)} & 4\epsilon\beta_1^{(1)} + h^2 \end{pmatrix} \begin{pmatrix} u_{0,j+1}^{(1)} \\ u_{1,j+1}^{(1)} \\ \vdots \\ u_{N_1-1,j+1}^{(1)} \\ u_{N_1,j+1}^{(1)} \end{pmatrix} = \begin{pmatrix} f_0 \\ f_1 \\ \vdots \\ f_{N_1-1} \\ \tilde{f}_{N_1} \end{pmatrix}. \quad (\text{A.35})$$

Similarly we can write (A.33) in matrix form, for  $i = 0, \dots, N_2$ , as

$$\begin{pmatrix} 4\epsilon\beta_2^{(1)} + h^2 & -2\epsilon\beta_2^{(1)} & & & \\ -2\epsilon\beta_2^{(1)} & 4\epsilon\beta_2^{(1)} + h^2 & -2\epsilon\beta_2^{(1)} & & \\ & \ddots & \ddots & & \\ & & -2\epsilon\beta_2^{(1)} & 4\epsilon\beta_2^{(1)} + h^2 & -2\epsilon\beta_2^{(1)} \\ & & & -4\epsilon\beta_2^{(1)} & 4\epsilon\beta_2^{(1)} + h^2 \end{pmatrix} \begin{pmatrix} w_{0,j+1}^{(1)} \\ w_{1,j+1}^{(1)} \\ \vdots \\ w_{N_1-1,j+1}^{(1)} \\ w_{N_1,j+1}^{(1)} \end{pmatrix} = \begin{pmatrix} g_0 \\ g_1 \\ \vdots \\ g_{N_1-1} \\ \tilde{g}_{N_1} \end{pmatrix}. \quad (\text{A.36})$$

Similar matrices can be derived for the system describing  $x > 0$ . At this stage we note that we can express the solution to the discretised cRB equations in the same way as was done for the single Boussinesq equation: we can write each point in the domain as the sum of an explicit part and an implicit part multiplied by a coefficient. Therefore, when substituting into the discretised form of the continuity conditions (A.30) and (A.31), we obtain a similar quadratic equation for the ‘‘ghost points’’ as was obtained in (A.25), with the coefficients taking a similar form to those defined in (A.26). As before we omit these expressions for brevity, however they can be easily obtained following the same approach as before or indeed by modifying (A.26) and replacing  $u^-$  with  $u^{(1)}$ ,  $u^+$  with  $u^{(2)}$ , and replacing the indices on the coefficients so that  $\alpha_1$  become  $\alpha_1^{(1)}$  and  $\alpha_2$  becomes  $\alpha_1^{(2)}$ . Similarly, we can derive the system for  $w$  by replacing all instances of  $u$  with  $w$  and changing the subscript on coefficients from 1 to 2.

Once the solution for the ‘‘ghost points’’ is obtained at the boundary for both  $u$  and  $w$ , this solution can be substituted into the implicit solution that was found for the cRB

equations to obtain an explicit solution to this system at a given time step. As we have used central difference approximations to the derivatives at each stage, this scheme is also second order.

### A.3 Direct Numerical Method for a System of $M$ Boussinesq Equations

The scheme derived in Section A.2.1 and A.2.2 is applicable to two sections of a layered structure. However we can use this scheme to find the solution for a bar of 3 or more sections, with some conditions. We illustrate this with an example. Let us consider a bar with three sections, such as the one in Figure 3.6, where the domains are  $\Omega_1 = [-L_1, 0]$ ,  $\Omega_2 = [0, x_a]$  and  $\Omega_3 = [x_a, L_2]$ . We initially compute the solution in  $\Omega_1$  and  $\Omega_2$  with two constraints: that the generated solitary wave has not reached the boundary between the second and third sections at  $x_a$ , and that the waves reflected at  $x = 0$  have not reflected back from  $L_1$  and entered the second domain at  $x = 0$ . The speed of the incident solitary wave and the generated solitary waves in the subsequent regions will be close to the characteristic speed in each section of the bar, and therefore both constraints can be satisfied by choosing an appropriate time interval for the calculation. A similar approach is then followed for the solution in  $\Omega_2$  and  $\Omega_3$ , where we choose an appropriate time so that the waves in  $\Omega_2$  have not reflected from the boundary  $x = x_a$  and back again from the boundary  $x = 0$ .

The outlined method has a clear problem; if the solution is not localised, then we cannot compute the solution for all three sections without losing some information from the solution. Furthermore if one of the sections is of limited length, for example a short finite delamination, the solution is unlikely to be fully contained in this section at any time and therefore some information will be lost when the calculation window is moved.

Therefore, we extend the method described in Section A.2.1 and A.2.2 to a structure with  $M$  sections. Let us consider the system of cRB equations defined in Chapter 4. In this case we have either coupled Boussinesq equations (cRB) or uncoupled Boussinesq equations in each section. In what follows, we will assume that we have cRB equations in each section, and the coefficient of the coupling term can be set to zero as necessary. We note that the matching at the interfaces is the same in either case and therefore this generalisation is valid. This allows us to write the equations in each section in the

following convenient form:

$$\begin{aligned} u_{tt}^{(l)} - u_{xx}^{(l)} &= 2\epsilon \left[ -6u_x^{(l)}u_{xx}^{(l)} + u_{ttxx}^{(l)} - \delta_l \left( u^{(l)} - w^{(l)} \right) \right], \\ w_{tt}^{(l)} - c_l^2 w_{xx}^{(l)} &= 2\epsilon \left[ -6\alpha_l w_x^{(l)}w_{xx}^{(l)} + \beta_l w_{ttxx}^{(l)} + \gamma_l \left( u^{(l)} - w^{(l)} \right) \right], \quad x_{l-1} < x < x_l, \end{aligned} \quad (\text{A.37})$$

where  $x_l$  is the position of the interface between the equations, and we have  $l = 1, \dots, M$  sections. Here we have assumed that the only unknown constant in the upper layer is the coupling term  $\delta_l$ , which can be achieved through a rescaling of parameters. The scheme could be written for general coefficients in each layer however this would result in a more complicated notation being required for the coefficients, similar to the one applied in Section A.2.2. Therefore we introduce the subscript notation for coefficients representing the section in which the coefficient is applied. We have continuity of longitudinal displacement and continuity of normal stress at the interface between the equations, described by

$$u^{(l)}|_{x=x_l} = u^{(l+1)}|_{x=x_l}, \quad w^{(l)}|_{x=x_l} = w^{(l+1)}|_{x=x_l}, \quad l = 1, \dots, M-1, \quad (\text{A.38})$$

and

$$\begin{aligned} u_x^{(l)} + 2\epsilon \left[ -3 \left( u_x^{(l)} \right)^2 + u_{ttx}^{(l)} \right] \Big|_{x=x_l} &= u_x^{(l+1)} + 2\epsilon \left[ -3 \left( u_x^{(l+1)} \right)^2 + u_{ttx}^{(l+1)} \right] \Big|_{x=x_l}, \\ c_l^2 w_x^{(l)} + 2\epsilon \left[ -3\alpha_l \left( w_x^{(l)} \right)^2 + \beta_l w_{ttx}^{(l)} \right] \Big|_{x=x_l} &= \\ c_{l+1}^2 w_x^{(l+1)} + 2\epsilon \left[ -3\alpha_{l+1} \left( w_x^{(l+1)} \right)^2 + \beta_{l+1} w_{ttx}^{(l+1)} \right] \Big|_{x=x_l}, \end{aligned} \quad (\text{A.39})$$

respectively, for  $l = 1, \dots, M-1$ .

To solve the equation system (A.37) - (A.39), we again make use of central difference approximations. Let us first discretise each domain  $[x_{l-1}, x_l] \times [0, T]$  into a grid with equal spacings  $h_l = \Delta x$  and  $\kappa = \Delta t$ . Then the analytical solution  $u^{(l)}(x, t)$  is approximated by the exact solution of the finite-difference scheme  $u^{(l)}(jh_l, j\kappa)$ , denoted  $u_{i,j}^{(l)}$ . Note here that we have assumed the discretisation in  $x$  can be different in each section, allowing for a complex wave in one section to be computed with a finer mesh and a sparse mesh can be used when the solution is simple, which will improve the speed of the computation. The condition on  $\Delta t$  will be calculated from the smallest value of the discretisation in  $x$  i.e.  $h_{\min} = \min_{l=1, \dots, M} h_l$ .

We make use of first order and second order central difference approximations in the main equations, as was done in Section A.2. To simplify the obtained expressions, we

introduce the notation

$$D_{xx} \left( u_{i,j}^{(l)} \right) = u_{i+1,j}^{(l)} - 2u_{i,j}^{(l)} + u_{i-1,j}^{(l)}.$$

Substituting these approximations into system (A.37) gives a coupled system of tridiagonal equations, of the form

$$\begin{aligned} & -2\epsilon u_{i+1,j+1}^{(l)} + (4\epsilon + h_l^2) u_{i,j+1}^{(l)} - 2\epsilon u_{i-1,j+1}^{(l)} = (\kappa^2 - 4\epsilon) D_{xx} \left( u_{i,j}^{(l)} \right) \\ & + 2h_l^2 u_{i,j}^{(l)} - \frac{6\epsilon\kappa^2}{h_l} \left[ \left( u_{i+1,j}^{(l)} \right)^2 - \left( u_{i-1,j}^{(l)} \right)^2 - 2u_{i+1,j}^{(l)} u_{i,j}^{(l)} + 2u_{i,j}^{(l)} u_{i-1,j}^{(l)} \right] \\ & + 2\epsilon u_{i+1,j-1}^{(l)} - (4\epsilon + h_l^2) u_{i,j-1}^{(l)} + 2\epsilon u_{i-1,j-1}^{(l)} \\ & - 2\epsilon\delta_l h_l^2 \kappa^2 \left( u_{i,j}^{(l)} - w_{i,j}^{(l)} \right), \quad l = 1, \dots, M, \end{aligned} \quad (\text{A.40})$$

and

$$\begin{aligned} & -2\epsilon\beta_l w_{i+1,j+1}^{(l)} + (4\epsilon\beta_l + h_l^2) w_{i,j+1}^{(l)} - 2\epsilon\beta_l w_{i-1,j+1}^{(l)} = (\kappa^2 c_l^2 - 4\epsilon\beta_l) D_{xx} \left( w_{i,j}^{(l)} \right) \\ & + 2h_l^2 w_{i,j}^{(l)} - \frac{6\epsilon\alpha_l \kappa^2}{h_l} \left[ \left( w_{i+1,j}^{(l)} \right)^2 - \left( w_{i-1,j}^{(l)} \right)^2 - 2w_{i+1,j}^{(l)} w_{i,j}^{(l)} + 2w_{i,j}^{(l)} w_{i-1,j}^{(l)} \right] \\ & + 2\epsilon\beta_l w_{i+1,j-1}^{(l)} - (4\epsilon\beta_l + h_l^2) w_{i,j-1}^{(l)} + 2\epsilon\beta_l w_{i-1,j-1}^{(l)} \\ & + 2\epsilon\gamma_l h_l^2 \kappa^2 \left( u_{i,j}^{(l)} - w_{i,j}^{(l)} \right), \quad l = 1, \dots, M. \end{aligned} \quad (\text{A.41})$$

Assuming the domain can be discretised, we calculate the number of points in the domain as  $N_l = (x_l - x_{l-1})/h_l$  and we have  $i = 0, 1, \dots, N_l$  in each section. Therefore continuity condition (A.38) becomes

$$u_{N_l,j+1}^{(l)} = u_{0,j+1}^{(l+1)}, \quad l = 1, \dots, M-1, \quad (\text{A.42})$$

and

$$w_{N_l,j+1}^{(l)} = w_{0,j+1}^{(l+1)}, \quad l = 1, \dots, M-1. \quad (\text{A.43})$$

In the continuity condition (A.39) we make use of the central difference approximations and introduce ‘‘ghost points’’ of the form  $u_{N_l+1,j+1}^{(l)}$ ,  $u_{-1,j+1}^{(l+1)}$ ,  $w_{N_l+1,j+1}^{(l)}$  and  $w_{-1,j+1}^{(l+1)}$ . Therefore, (A.39) becomes

$$\begin{aligned} & h_l \kappa^2 \left( u_{N_l+1,j+1}^{(l)} - u_{N_l-1,j+1}^{(l)} \right) + 2h_l \epsilon \left( 2u_{N_l+1,j+1}^{(l)} - 2u_{N_l-1,j+1}^{(l)} \right. \\ & \quad \left. - 5u_{N_l+1,j}^{(l)} + 5u_{N_l-1,j}^{(l)} + 4u_{N_l+1,j-1}^{(l)} - 4u_{N_l-1,j-1}^{(l)} - u_{N_l+1,j-2}^{(l)} + u_{N_l-1,j-2}^{(l)} \right) \\ & \quad - 3\kappa^2 \epsilon \left[ \left( u_{N_l+1,j+1}^{(l)} \right)^2 + \left( u_{N_l-1,j+1}^{(l)} \right)^2 - 2u_{N_l+1,j+1}^{(l)} u_{N_l-1,j+1}^{(l)} \right] = \end{aligned}$$

$$\begin{aligned}
& \frac{h_l^2}{h_{l+1}} \kappa^2 \left( u_{1,j+1}^{(l+1)} - u_{-1,j+1}^{(l+1)} \right) + 2 \frac{h_l^2}{h_{l+1}} \epsilon \left( 2u_{1,j+1}^{(l+1)} - 2u_{-1,j+1}^{(l+1)} \right. \\
& \quad \left. - 5u_{1,j}^{(l+1)} + 5u_{-1,j}^{(l+1)} + 4u_{1,j-1}^{(l+1)} - 4u_{-1,j-1}^{(l+1)} - u_{1,j-2}^{(l+1)} + u_{-1,j-2}^{(l+1)} \right) \\
& - 3 \frac{h_l^2}{h_{l+1}^2} \kappa^2 \epsilon \left[ \left( u_{1,j+1}^{(l+1)} \right)^2 + \left( u_{-1,j+1}^{(l+1)} \right)^2 - 2u_{1,j+1}^{(l+1)} u_{-1,j+1}^{(l+1)} \right], \tag{A.44}
\end{aligned}$$

for  $l = 1, \dots, M - 1$ , and

$$\begin{aligned}
& h_l \kappa^2 c_l^2 \left( w_{N_l+1,j+1}^{(l)} - w_{N_l-1,j+1}^{(l)} \right) + 2h_l \epsilon \beta_l \left( 2w_{N_l+1,j+1}^{(l)} - 2w_{N_l-1,j+1}^{(l)} \right. \\
& \quad \left. - 5w_{N_l+1,j}^{(l)} + 5w_{N_l-1,j}^{(l)} + 4w_{N_l+1,j-1}^{(l)} - 4w_{N_l-1,j-1}^{(l)} - w_{N_l+1,j-2}^{(l)} + w_{N_l-1,j-2}^{(l)} \right) \\
& - 3\kappa^2 \epsilon \alpha_l \left[ \left( w_{N_l+1,j+1}^{(l)} \right)^2 + \left( w_{N_l-1,j+1}^{(l)} \right)^2 - 2w_{N_l+1,j+1}^{(l)} w_{N_l-1,j+1}^{(l)} \right] = \\
& \frac{h_l^2}{h_{l+1}} \kappa^2 c_{l+1}^2 \left( w_{1,j+1}^{(l+1)} - w_{-1,j+1}^{(l+1)} \right) + 2 \frac{h_l^2}{h_{l+1}} \epsilon \beta_{l+1} \left( 2w_{1,j+1}^{(l+1)} - 2w_{-1,j+1}^{(l+1)} \right. \\
& \quad \left. - 5w_{1,j}^{(l+1)} + 5w_{-1,j}^{(l+1)} + 4w_{1,j-1}^{(l+1)} - 4w_{-1,j-1}^{(l+1)} - w_{1,j-2}^{(l+1)} + w_{-1,j-2}^{(l+1)} \right) \\
& - 3 \frac{h_l^2}{h_{l+1}^2} \kappa^2 \epsilon \alpha_{l+1} \left[ \left( w_{1,j+1}^{(l+1)} \right)^2 + \left( w_{-1,j+1}^{(l+1)} \right)^2 - 2w_{1,j+1}^{(l+1)} w_{-1,j+1}^{(l+1)} \right], \tag{A.45}
\end{aligned}$$

for  $u$  and  $w$  respectively. As we are again considering localised initial data for strains, if we take  $L$  large enough then we can enforce zero boundary conditions for the strain i.e.  $u_x = 0$ . Therefore, applying a central difference approximation to this condition, we have

$$u_{1,j+1}^{(1)} = u_{-1,j+1}^{(1)} \quad \text{and similarly} \quad u_{N_M+1,j+1}^{(M)} = u_{N_M-1,j+1}^{(M)}, \tag{A.46}$$

and equivalent relations for  $w$ . Therefore, as we have used central difference approximations everywhere, we have a second-order scheme (which is consistent with the approach used before). The systems (A.40) and (A.41) are tridiagonal for the values  $i = 0, \dots, N_l$ . As before, we denote the right-hand side of (A.40) as  $f_i^{(l)}$  and the right-hand side of (A.41) as  $g_i^{(l)}$ , for the appropriate values of  $i$ .

At this point we diverge from the method presented in Section A.2. In each domain, defined by  $l$ , we have two ghost points – one at the left-hand side boundary and one at the right-hand side boundary. The exceptions are the first and  $M$ -th domain, where we do not have a ghost point on the left-hand side of the first domain and the right-hand side of the  $M$ -th domain. We apply the relations defined in (A.46) in these special domains to obtain a tridiagonal system. Before we write these matrices for each section, we make a rearrangement at the boundaries to accommodate these ghost points. We

have

$$\begin{aligned} \tilde{f}_0^{(l)} &= f_0^{(l)} + 2\epsilon u_{-1,j+1}^{(l)}, & \tilde{f}_{N_l}^{(l)} &= f_{N_l}^{(l)} + 2\epsilon u_{N_l+1,j+1}^{(l)}, \\ \tilde{g}_0^{(l)} &= g_0^{(l)} + 2\epsilon \beta_l w_{-1,j+1}^{(l)}, & \tilde{g}_{N_l}^{(l)} &= g_{N_l}^{(l)} + 2\epsilon \beta_l w_{N_l+1,j+1}^{(l)}. \end{aligned} \quad (\text{A.47})$$

We can write (A.40) in matrix form for each  $l$ , with two exceptional cases at the boundary. A similar system can be formed for (A.41) but we omit this expression for brevity, as it takes the same form. Therefore, in the first section, we have for  $i = 0, \dots, N_1$ ,

$$\begin{pmatrix} 4\epsilon + h^2 & -4\epsilon & & & \\ -2\epsilon & 4\epsilon + h^2 & -2\epsilon & & \\ & \ddots & \ddots & & \\ & & -2\epsilon & 4\epsilon + h^2 & -2\epsilon \\ & & & -2\epsilon & 4\epsilon + h^2 \end{pmatrix} \begin{pmatrix} u_{0,j+1}^{(1)} \\ u_{1,j+1}^{(1)} \\ \vdots \\ u_{N_1-1,j+1}^{(1)} \\ u_{N_1,j+1}^{(1)} \end{pmatrix} = \begin{pmatrix} f_0^{(1)} \\ f_1^{(1)} \\ \vdots \\ f_{N_1-1}^{(1)} \\ \tilde{f}_{N_1}^{(1)} \end{pmatrix}. \quad (\text{A.48})$$

Similarly for the final section we have

$$\begin{pmatrix} 4\epsilon + h^2 & -2\epsilon & & & \\ -2\epsilon & 4\epsilon + h^2 & -2\epsilon & & \\ & \ddots & \ddots & & \\ & & -2\epsilon & 4\epsilon + h^2 & -2\epsilon \\ & & & -4\epsilon & 4\epsilon + h^2 \end{pmatrix} \begin{pmatrix} u_{0,j+1}^{(M)} \\ u_{1,j+1}^{(M)} \\ \vdots \\ u_{N_M-1,j+1}^{(M)} \\ u_{N_M,j+1}^{(M)} \end{pmatrix} = \begin{pmatrix} \tilde{f}_0^{(M)} \\ f_1^{(M)} \\ \vdots \\ f_{N_M-1}^{(M)} \\ f_{N_M}^{(M)} \end{pmatrix}. \quad (\text{A.49})$$

Finally we have the generic matrix for all other regions, for  $1 < l < M$ , which takes the form

$$\begin{pmatrix} 4\epsilon + h^2 & -2\epsilon & & & \\ -2\epsilon & 4\epsilon + h^2 & -2\epsilon & & \\ & \ddots & \ddots & & \\ & & -2\epsilon & 4\epsilon + h^2 & -2\epsilon \\ & & & -2\epsilon & 4\epsilon + h^2 \end{pmatrix} \begin{pmatrix} u_{0,j+1}^{(l)} \\ u_{1,j+1}^{(l)} \\ \vdots \\ u_{N_l-1,j+1}^{(l)} \\ u_{N_l,j+1}^{(l)} \end{pmatrix} = \begin{pmatrix} \tilde{f}_0^{(l)} \\ f_1^{(l)} \\ \vdots \\ f_{N_l-1}^{(l)} \\ \tilde{f}_{N_l}^{(l)} \end{pmatrix}. \quad (\text{A.50})$$

We have now formed tridiagonal systems for the functions  $u$  and  $w$  and this system can be solved using the Thomas algorithm (e.g. [117]) to solve these systems implicitly, in terms of the ghost points on the left-hand boundary and right-hand boundary. Therefore we can express the solution at each point in terms of the explicit solution (if no ghost

points exist) and a multiplicative factor of the ghost points. We denote this as

$$u_{i,j+1}^{(l)} = \phi_i^{(l)} + \psi_i^{(l)} u_{-1,j+1}^{(l)} + \omega_i^{(l)} u_{N_l+1,j+1}^{(l)}, \quad (\text{A.51})$$

and we have a similar relationship for  $w$ . We note that  $\psi_i^{(1)} = 0$  and  $\omega_i^{(M)} = 0$  as there are no ghost points on these far boundaries. This implicit solution (A.51) is then substituted into (A.42) and (A.44) to obtain a nonlinear system of equations. This is a complicated system and therefore we aim to simplify the expressions if possible.

Analysing the form of the matrices (A.48) - (A.50) we can estimate the values of the coefficients  $\psi$  and  $\omega$ . Following the steps of the Thomas algorithm, we find that the coefficients are dependent upon  $h_l$  in a complicated way, leading to a continued fraction in terms of  $h_l$ . As  $h_l$  is the step size, we are taking it to be reasonably small and therefore we can make an estimate of these coefficients by assuming  $h_l = 0$ . In this case we find that, for  $i = 0, \dots, N_l$ , we have

$$\psi_i^{(l)} = \frac{N_l + 1 - i}{N_l + 2}, \quad \omega_i^{(l)} = \frac{1 + i}{N_l + 2}. \quad (\text{A.52})$$

Here  $N_l$  is the number of points in a given domain and therefore, for a sufficiently large domain (or a sufficiently small value of  $h_l$  to increase the number of points to the necessary level) we have that the coefficient of the left ghost point in a given domain is approximately zero at the right-hand boundary, and vice versa for the right ghost point at the left-hand boundary. These have been calculated numerically for  $N = 50000$  and the value at the boundary was essentially zero ( $O(10^{-300})$ ). Furthermore, it was found that the value falls below machine precision ( $O(10^{-16})$ ) when  $N = 500$ . This suggests that a value of  $h$  and the corresponding value of  $N$  can be found for most domain sizes. This allows us to simplify the problem so that we only require the solution of two equations at each interface, in terms of two ghost points.

In order to obtain this nonlinear equation, we use (A.42) to express  $u_{-1,j+1}^{(l+1)}$  in terms of  $u_{N_l+1,j+1}^{(l)}$ , making use of (A.52) to express  $u_{N_l-1,j+1}^{(l)}$  and  $u_{1,j+1}^{(l+1)}$  in terms of the ghost points. Substituting (A.52) into (A.42) gives

$$\phi_{N_l}^{(l)} + \omega_{N_l}^{(l)} u_{N_l+1,j+1}^{(l)} = \phi_0^{(l+1)} + \psi_0^{(l+1)} u_{-1,j+1}^{(l+1)}, \quad (\text{A.53})$$

and therefore we have

$$u_{-1,j+1}^{(l+1)} = \frac{\phi_{N_l}^{(l)} - \phi_0^{(l+1)} + \omega_{N_l}^{(l)} u_{N_l+1,j+1}^{(l)}}{\psi_0^{(l+1)}},$$

$$u_{1,j+1}^{(l+1)} = \phi_1^{(l+1)} + \frac{\psi_1^{(l+1)}}{\psi_0^{(l+1)}} \left( \phi_{N_l}^{(l)} - \phi_0^{(l+1)} + \omega_{N_l}^{(l)} u_{N_l+1,j+1}^{(l)} \right), \quad (\text{A.54})$$

and a similar equation for  $w$ . Substituting (A.52) and (A.54) into (A.44) we obtain a quadratic equation in  $u_{N_l+1,j+1}^{(l)}$  and therefore we need to solve a quadratic equation for each boundary. Explicitly we have

$$h_0 \left( u_{N_l+1,j+1}^{(l)} \right)^2 + h_1 u_{N_l+1,j+1}^{(l)} + h_2 = 0, \quad (\text{A.55})$$

where we have

$$\begin{aligned} h_0 &= -3\kappa^2\epsilon \left( \omega_{N_l-1}^{(l)} - 1 \right)^2 + 3\frac{h_l^2}{h_{l+1}^2}\kappa^2\epsilon \left( \frac{\omega_{N_l}^{(l)}}{\psi_0^{(l+1)}} \right)^2 \left( \psi_1^{(l+1)} - 1 \right)^2, \\ h_1 &= \left( 1 - \omega_{N_l-1}^{(l)} \right) \left( h_l\kappa^2 + 4h_l\epsilon + 6\kappa^2\epsilon\phi_{N_l-1}^{(l)} \right) \\ &\quad + \left( 1 - \psi_1^{(l+1)} \right) \left( \frac{\omega_{N_l}^{(l)}}{\psi_0^{(l+1)}} \right) \left( \frac{h_l^2}{h_{l+1}}\kappa^2 + 4\frac{h_l^2}{h_{l+1}}\epsilon - 6\frac{h_l^2}{h_{l+1}^2}\kappa^2\epsilon\phi_1^{(l+1)} \right) \\ &\quad + 6\frac{h_l^2}{h_{l+1}^2}\kappa^2\epsilon \frac{\omega_{N_l}^{(l)} \left( \phi_{N_l}^{(l)} - \phi_0^{(l+1)} \right)}{\left( \psi_0^{(l+1)} \right)^2} \left[ \left( \psi_1^{(l+1)} \right)^2 - 2\psi_1^{(l+1)} + 1 \right], \\ h_2 &= -\phi_{N_l-1}^{(l)} \left( h_l\kappa^2 + 4h_l\epsilon \right) - 3\kappa^2\epsilon \left( \phi_{N_l-1}^{(l)} \right)^2 + 2h_l\epsilon \left( -5u_{N_l+1,j}^{(l)} + 5u_{N_l-1,j}^{(l)} \right. \\ &\quad \left. + 4u_{N_l+1,j-1}^{(l)} - 4u_{N_l-1,j-1}^{(l)} - u_{N_l+1,j-2}^{(l)} + u_{N_l-1,j-2}^{(l)} \right) \\ &\quad + 3\frac{h_l^2}{h_{l+1}^2}\kappa^2\epsilon \left[ \left( \phi_1^{(l+1)} \right)^2 + \left( \frac{\phi_{N_l}^{(l)} - \phi_0^{(l+1)}}{\psi_0^{(l+1)}} \left( \psi_1^{(l+1)} - 1 \right) \right)^2 \right. \\ &\quad \left. + 2 \left( \psi_1^{(l+1)} - 1 \right) \left( \frac{\phi_1^{(l+1)} \left( \phi_{N_l}^{(l)} - \phi_0^{(l+1)} \right)}{\psi_0^{(l+1)}} \right) \right] \\ &\quad - \left( \frac{h_l^2}{h_{l+1}}\kappa^2 + 4\frac{h_l^2}{h_{l+1}}\epsilon \right) \left[ \phi_1^{(l+1)} + \frac{\phi_{N_l}^{(l)} - \phi_0^{(l+1)}}{\psi_0^{(l+1)}} \left( \psi_1^{(l+1)} - 1 \right) \right] \\ &\quad - 2\frac{h_l^2}{h_{l+1}^2}\epsilon \left( -5u_{1,j}^{(l+1)} + 5u_{-1,j}^{(l+1)} + 4u_{1,j-1}^{(l+1)} - 4u_{-1,j-1}^{(l+1)} - u_{1,j-2}^{(l+1)} + u_{-1,j-2}^{(l+1)} \right). \quad (\text{A.56}) \end{aligned}$$

In the special case that  $h_0 \equiv 0$  then we can solve a linear equation on the boundary (in the same way as when  $\alpha_2 = \alpha_1$  in Section A.2) and numerical experiments have shown that, if the nonlinearity coefficient is the same in both sections of the bar, this condition is again satisfied. However, in the general case when the nonlinearity coefficient can change between section, we must choose the appropriate sign in the quadratic expression, and this is chosen to be consistent with the solution in the surrounding region.

The results in Chapter 4 computed via this method, in contrast to the previous method where the calculation was performed for two sections at a time (as was done in [43]),

---

showed little change when the domain sizes were sufficiently large. This is the expected behaviour in this case, as the large domain sizes allow the wave to be fully captured within a section before the calculation window is moved. However, this method allowed for the reflected waves to be traced throughout the calculation, whereas they would be lost after the calculation window is moved via the first method. The study of these reflected waves was beyond the scope of this thesis, however their presence shows that this method could be used to study their behaviour. Furthermore, this method can be used to compute the solution for short domain lengths, such as a finite delamination of length 5 Full Width at Half Magnitude (FWHM) of the incident soliton. In Chapter 4 this analysis was performed using the weakly nonlinear solution but this could now be performed in more detail with the direct numerical method. This is again an extension that goes beyond the work in this thesis.

## Appendix B

# SSPRK(5,4) Scheme for KdV Equations

In Chapter 3 we sought a weakly nonlinear solution to the system of equations. This derivation produced a series of KdV equations. There are several methods for solving such an equation: a finite-difference approach as developed by Zabusky and Kruskal [3, 19], a numerical Inverse Scattering Transform method for solving the KdV or mKdV [26], a pseudospectral method [119, 120] (which is discussed in more detail in Appendix C), a hybrid Runge-Kutta method using finite-difference operators for the spacial derivatives [93], for example.

We develop a numerical technique based upon the Strong Stability Preserving Runge-Kutta (SSPRK(5,4)) scheme as described in [94] (see [121] for an example of this method). This time-stepping method captures the nonlinear effects of a governing equation better than the standard Runge-Kutta method, and therefore increases the overall accuracy of a numerical scheme implementing this form of time-stepping. We compared these results to a hybrid Runge-Kutta scheme (e.g. [93]) and found the SSPRK(5,4) scheme had a higher accuracy, due to its stability preserving properties, and the computational time was similar for both schemes.

We implement the scheme for a KdV equation, where we assume generic coefficients. This is to simplify the presentation of the scheme, as it will be applied for multiple KdV equations with different characteristic variables and there will be a significant amount of redundancy. Therefore, we will assume a KdV equation of the form

$$u_X + \alpha uu_\xi + \beta u_{\xi\xi\xi} = 0, \tag{B.1}$$

where  $\alpha$  and  $\beta$  are constants,  $X = \epsilon x$  and  $\xi = x - t$ . This scheme can easily be adapted for the characteristic variable  $\eta = x - t$  via a quick transform from  $\xi$  to  $\eta$ . We will proceed with this form of the equation, with generic coefficients.

The scheme is as follows. We discretise the domain  $[-L, L] \times [x_a, x_b]$  into a grid with equal spacings  $h = \Delta\xi$ ,  $\kappa = \Delta X$ , and the analytical solution  $u(\xi, X)$  is approximated by the exact solution of the numerical scheme,  $u(ih, j\kappa)$  (denoted  $u_{i,j}$ ). Here we have  $N = 2L/h$  and therefore  $i = 0, \dots, N$ . Given that the solution at time  $X_j = x_a + j\kappa$  is given by

$$u_{i,j} = u(ih, j\kappa), \quad i = 0, \dots, N, \quad (\text{B.2})$$

then the solution at  $X_{j+1} = x_a + (j+1)\kappa$  is given by

$$\begin{aligned} u^{(1)} &= u_{i,j} + 0.391752226571890\kappa F(u_{i,j}), \\ u^{(2)} &= 0.444370493651235u_{i,j} + 0.555629506348765u^{(1)} + 0.368410593050371\kappa F(u^{(1)}), \\ u^{(3)} &= 0.620101851488403u_{i,j} + 0.379898148511597u^{(2)} + 0.251891774271694\kappa F(u^{(2)}), \\ u^{(4)} &= 0.178079954393132u_{i,j} + 0.821920045606868u^{(3)} + 0.544974750228521\kappa F(u^{(3)}), \\ u_{i,j+1} &= 0.517231671970585u^{(2)} + 0.096059710526147u^{(3)} + 0.063692468666290\kappa F(u^{(3)}) \\ &\quad + 0.386708617503269u^{(4)} + 0.226007483236906\kappa F(u^{(4)}), \end{aligned} \quad (\text{B.3})$$

where the function  $F$  is the finite-differenced form of all the terms in the KdV equation involving spatial derivatives. Note that the coefficients here are chosen in such a way to optimise the time step at each point and, due to the complexity of each coefficient, are presented to 15 decimal places. The formulae for the coefficients can be found in [94].

To obtain the discretised form of the spatial derivatives, and hence the function  $F$ , central difference approximations are applied for the first and third derivatives and an average is taken for the nonlinear term (as was performed by Zabusky and Kruskal, see [3, 19]). We also assume boundary conditions of the form

$$u(\pm L, t) = 0, \quad u_x(\pm L, t) = 0 \quad \Rightarrow \quad u_{0,j} = u_{1,j} = u_{N-1,j} = u_{N,j} = 0, \quad (\text{B.4})$$

which is justified for a localised initial condition and is equivalent to the derivatives at the boundary being equal to zero. Using this scheme for equation (B.1) we obtain

$$\begin{aligned} F(u_{i,j}) &= \frac{1}{6h} (u_{i+1,j} + u_{i,j} + u_{i-1,j}) (u_{i+1,j} - u_{i-1,j}) \\ &\quad - \frac{1}{2h^3} (u_{i+2,j} - 2u_{i+1,j} + 2u_{i-1,j} - u_{i-2,j}). \end{aligned} \quad (\text{B.5})$$

If we wanted to improve the accuracy of the scheme, the discretisation of the spatial derivatives could be replaced with compact finite-difference operators. These implicit finite-difference schemes provide higher spatial resolution than the well-known explicit schemes (almost spectral-like resolution) [121, 122].



## Appendix C

# Pseudospectral Methods

As described in Appendices A and B, finite-difference techniques can be used to solve PDEs with a simple approach, and this approach can be extended to more complicated systems. There are many other techniques that can be applied to the solution of PDEs. Another method that can be used is finite element techniques (e.g. [123]) and these have been applied to many problems, such as interfacial dynamics of non-Newtonian fluids [124], for the KdV equation [125] and the Boussinesq equation [126], amongst others.

Another approach that has come to the forefront in recent years is spectral methods [127]. In the case where we have smooth data on a periodic domain, spectral methods will usually offer the best accuracy and computational efficiency. The principle of spectral methods is to write the solution to a given differential equation in terms of a sum of basis functions, then by implementing the Fast Fourier Transform (FFT) algorithm, one can determine the coefficients of the sum to yield the best approximation of the solution to the differential equation. The FFT is an algorithm developed in 1965 by Cooley and Tukey [128]. This algorithm is an efficient method for computing the discrete Fourier transform (DFT), and similarly the inverse fast Fourier transform (IFFT) is used for calculating the inverse discrete Fourier transform (IDFT). In essence, the FFT and IFFT are analogous to the Fourier and inverse Fourier transforms for continuous functions.

Here we define the Fourier and inverse Fourier transforms, before defining their discrete equivalents. Let us consider a function  $u(x, t)$  defined on the infinite line i.e.  $x \in \mathbb{R}$ . We denote the Fourier transform of the function  $u(x, t)$  by  $\mathcal{F}\{u(x, t)\} = \hat{u}(k, t)$ , as

$$\hat{u}(k, t) = \int_{-\infty}^{\infty} e^{-ikx} u(x, t) dx, \quad (\text{C.1})$$

where  $k \in \mathbb{R}$  is known as the transform variable. We can also consider this as a discretised and scaled wave number. For the inverse Fourier transform, we use the notation

$\mathcal{F}^{-1}\{\hat{u}(k, t)\} = u(x, t)$  and define the transform as

$$u(x, t) = \frac{1}{2\pi} \int_{-\infty}^{\infty} e^{ikx} \hat{u}(k, t) dk. \quad (\text{C.2})$$

When we consider the application to KdV and Ostrovsky equations, we need to calculate the Fourier transform of derivatives with respect to  $x$ . Differentiating (C.1) with respect to  $x$  we obtain

$$\mathcal{F} \left\{ \frac{\partial u}{\partial x} \right\} = \int_{-\infty}^{\infty} e^{-ikx} \frac{\partial u}{\partial x} dx. \quad (\text{C.3})$$

Integrating this expression by parts and assuming that  $u(x, t) \rightarrow 0$  as  $|x| \rightarrow \infty$  (in our later work, we only require that the derivative is periodic in  $x$  which yields the same result) we obtain

$$\mathcal{F} \left\{ \frac{\partial u}{\partial x} \right\} = \left[ e^{-ikx} u \right]_{-\infty}^{\infty} + ik \int_{-\infty}^{\infty} e^{-ikx} u(x, t) dx = ik \hat{u}(k, t). \quad (\text{C.4})$$

This can be extended for higher derivatives and therefore, if the function  $u$  is  $n$  times differentiable and all derivatives tend to zero at infinities, then we have

$$\mathcal{F} \left\{ \frac{\partial^n u}{\partial x^n} \right\} = (ik)^n \hat{u}(k, t). \quad (\text{C.5})$$

Therefore we have described the method to be applied for a function on an infinite domain. However, in the numerical methods applied, we only consider finite domains as the discretised techniques can only be applied to a finite interval. This is where the FFT and IFFT come into play. Let us consider a function  $u(x, t)$  on a finite domain  $x \in [-L, L]$  and we discretise the domain into  $N$  equally spaced points, so we have the spacing  $\Delta x = 2L/N$ . In all calculations we consider in this appendix, we scale the domain from  $x \in [-L, L]$  to  $\tilde{x} \in [0, 2\pi]$ , which can be achieved by applying the transform  $\tilde{x} = sx + \pi$ , where  $s = \pi/L$ . Denoting  $x_j = -L + j\Delta x$  for  $j = 0, \dots, N$ , we define the DFT for the function  $u(x, t)$  as

$$\hat{u}(k, t) = \frac{1}{\sqrt{N}} \sum_{j=1}^N u(x_j, t) e^{-ikx_j}, \quad -\frac{N}{2} \leq k \leq \frac{N}{2} - 1, \quad (\text{C.6})$$

and similarly the IDFT is defined as

$$u(x, t) = \frac{1}{\sqrt{N}} \sum_{k=-N/2}^{N/2-1} \hat{u}(k, t) e^{ikx_j}, \quad j = 1, 2, \dots, N, \quad (\text{C.7})$$

where the discretised and scaled wavenumber is now  $k \in \mathbb{Z}$ .

To perform these transforms we implement the FFTW3 algorithm in C [129]. This

is the same algorithm used in *Matlab* when invoking the in-built functions *fft* and *ifft* for Fourier transforms. In our work we have used even values of  $N$  however any value of  $N$  can be chosen. The FFT algorithm optimises the computation of the DFT; the number of steps required to compute the DFT is normally  $O(N^2)$ , while with the FFT algorithm this can be reduced to  $O(N \log N)$ . In order to achieve the best reduction in computational time,  $N$  must be highly composite and therefore the most common form used is  $N = 2^m$  for some integer  $m$ .

In the remainder of this appendix we will apply the transforms described above and apply them to the KdV, Ostrovsky and Boussinesq-type equations. The domain will be transformed from  $x \in [-L, L]$  to  $x \in [0, 2\pi]$  and therefore derivatives in  $x$  will be transformed as  $u_x \rightarrow su_{\tilde{x}}$ . This will be shown in each subsection for the relevant equation.

We implement a pseudospectral method for solving the relevant equation and use the 4<sup>th</sup>-order Runge-Kutta method for time stepping in the Fourier space. The nonlinear terms are calculated in the real domain and transformed back to the Fourier space for use in the calculation, rather than calculating the convolution of two functions. This appears to be the standard approach used in modern calculations, however in an earlier paper [130] the derivatives were calculated in the Fourier space and the time evolution was performed in the real space. We have tested both methods and found that there is no discernible difference between them, with the benefits arising from the structure of the equation. If an equation has few nonlinear terms and high order derivatives, it is faster to compute the nonlinear terms in the real space and evolve time in the Fourier space. Similarly, if an equation has only low order derivatives and many nonlinear terms, then it is faster to compute the derivatives in the Fourier space and evolve time in the real space. In our case, the difference in time is negligible.

To remove aliasing effects, we use the truncation 2/3-rule by Orszag in Boyd [120]. This effect is due to the pollution of the numerically calculated Fourier transform by higher frequencies due to the series being truncated. Other methods have been proposed for removing aliasing effects, such as those by Hou and Li in [131]. In our work we saw no discernible difference between the two methods and used the 2/3 rule due to its simplicity. In a more complicated equation the method by Hou and Li may result in more accurate results.

## C.1 Pseudospectral Scheme for the KdV Equation

We previously (in Appendix B) presented a finite-difference method for solving the KdV equation, using the SSPRK(5,4) scheme with finite-difference operators applied for the spatial derivatives. To improve the accuracy at which the spatial derivatives are calculated, we compute the derivatives using the DFT as outlined above. In theory we could implement the SSPRK(5,4) method for time-stepping to further improve the accuracy, however we found that the results computed with a standard 4<sup>th</sup>-order Runge-Kutta method for time stepping provide sufficient accuracy for our purposes. If the results do not provide the required accuracy, the SSPRK(5,4) algorithm could be used to further improve the results.

Let us consider the KdV equation

$$u_t + \alpha uu_x + \beta u_{xxx} = 0, \quad (\text{C.8})$$

where  $\alpha$  and  $\beta$  are constants, defined on the intervals  $t \in [0, T]$  and  $x \in [-L, L]$ . Firstly we transform the spatial domain  $[-L, L]$  to  $[0, 2\pi]$  via the transform  $\tilde{x} = sx + \pi$ , where  $s = \pi/L$ . Applying this transform and omitting tildes we obtain

$$u_t + s\alpha uu_x + s^3\beta u_{xxx} = 0. \quad (\text{C.9})$$

The nonlinear term is calculated in the real domain, then transformed to the Fourier space. We can rewrite the nonlinear term by introducing the notation

$$uu_x = z_x, \quad z = \frac{u^2}{2}.$$

As outlined in the introduction to this appendix, we discretise the spatial domain using  $N$  equidistant points with the spacing  $\Delta x = 2\pi/N$ , where  $N$  is chosen to be highly composite and we denote the discretised variable  $x_j = -L + j\Delta x$ . As we have a discretised equation, we can apply the DFT and IDFT as outlined in (C.6) and (C.7) above. The discrete Fourier transform of equation (C.9) with respect to  $x$  gives

$$\hat{u}_t + iks\alpha\hat{z} - ik^3s^3\beta\hat{u} = 0. \quad (\text{C.10})$$

This is an ODE in  $\hat{u}$  and  $k$  that can be solved numerically using the 4<sup>th</sup>-order Runge-Kutta method for time evolution. Assume that the solution at  $t$  is given by  $\hat{u}_j = u(k, j\kappa)$ , where  $\kappa = \Delta t$ . Then the solution at  $t = (j+1)\Delta t$  is given by

$$\hat{u}_{k,(j+1)\kappa} = \hat{u}_{k,j\kappa} + \frac{1}{6}(a + 2b + 2c + d), \quad (\text{C.11})$$

where  $a, b, c, d$  are functions of  $k$  at a given moment in time,  $t$ , and are defined as

$$\begin{aligned} a &= \kappa F(\hat{u}_j), & b &= \kappa F\left(\hat{u}_j + \frac{a}{2}\right), \\ c &= \kappa F\left(\hat{u}_j + \frac{b}{2}\right), & d &= \kappa F(\hat{u}_j + c). \end{aligned}$$

The function  $F$  is found as a rearrangement of (C.10) to contain all non-time derivatives. Explicitly we have

$$F(\hat{u}_j) = -iks\alpha\hat{z} + ik^3s^3\beta\hat{u}_j. \quad (\text{C.12})$$

To remove aliasing effects, we use the truncation 2/3-rule by Orszag in Boyd [120] as outlined in the introduction to this appendix.

## C.2 Pseudospectral Scheme for the Ostrovsky and Coupled Ostrovsky Equations

In previous studies, the uncoupled Ostrovsky equation [132] and coupled Ostrovsky equations [40] have been solved using finite-difference and pseudospectral techniques respectively. We previously (in Appendix B) presented a finite-difference method for solving the KdV equation, using the SSPRK(5,4) scheme. However this scheme becomes more difficult to implement for the Ostrovsky equations, as the equation has to be rearranged to obtain all non-time derivatives, and this leads to the introduction of an integral operator [121]. While this has been shown to provide accurate results (and indeed we have tested this method and found that the results are consistent with the method presented in this appendix) it is more difficult to implement due to the integral operator. Therefore, we consider a pseudospectral scheme for the KdV and (coupled/uncoupled) Ostrovsky equations and will present the method for each equation separately.

We will consider three cases. Firstly we implement a pseudospectral method for a single Ostrovsky equation. The same method is applied for a linearised Ostrovsky equation on a non-zero background, where we apply a more efficient form of the Runge-Kutta algorithm. Finally we solve a system of coupled Ostrovsky equations using an extension of the method for the single Ostrovsky equation.

### C.2.1 Ostrovsky Equation

Let us consider a single Ostrovsky equation

$$(u_t + \alpha uu_x + \beta u_{xxx})_x = \delta u, \quad (\text{C.13})$$

where  $\alpha$ ,  $\beta$ ,  $\delta$  are constants, and we consider the equation on domains  $t \in [0, T]$  and  $x \in [-L, L]$  as we did for the case in Section C.1. We again transform the interval from  $[-L, L]$  to  $[0, 2\pi]$  via the transform  $\tilde{x} = sx + \pi$  and  $s = \pi/L$  to obtain (omitting tildes)

$$(u_t + s\alpha uu_x + s^3\beta u_{xxx})_x = \frac{\delta}{s}u. \quad (\text{C.14})$$

As was done for the KdV equation, the nonlinear term is calculated in the real domain then transformed to the Fourier space. We can rewrite the nonlinear term by introducing the notation

$$uu_x = z_x, \quad z = \frac{u^2}{2}.$$

The spatial domain is discretised by  $N$  equidistant points with spacing  $\Delta x = 2\pi/N$ , where as before  $N$  is highly composite. We use the Discrete Fourier Transform as defined in (C.6) and the inverse transform is as defined in (C.7), and make use of the Fast Fourier Transform (FFT) algorithm to implement these transforms efficiently. The discrete Fourier transform of equation (C.14) with respect to  $x$  gives

$$\hat{u}_t + iks\alpha\hat{z} - ik^3s^3\beta\hat{u} = -\frac{i\delta}{ks}\hat{u}. \quad (\text{C.15})$$

This system is solved numerically using the 4<sup>th</sup>-order Runge-Kutta method for time stepping, as was done for the KdV equation. Assuming that the solution at  $t$  is given by  $\hat{u}_j = u(k, j\kappa)$ , where  $\kappa = \Delta t$ , the method as defined in (C.11) can be applied to our equations, where we modify the function  $F$  to be a rearrangement of the terms in (C.15) rather than (C.10). So we have the function given as

$$F(\hat{u}_j) = -iks\alpha\hat{z} + ik^3s^3\beta\hat{u}_j - \frac{i\delta}{ks}\hat{u}_j. \quad (\text{C.16})$$

If the initial condition has zero mean value then we can exclude the zero mode from the calculation of function  $F$ , as this cannot be evaluated due to the final term in (C.16). We note that, if  $k = 0$ , then (C.15) is satisfied if both sides are multiplied by  $k$ . However, if the initial condition does not have zero mean value then the zero mode will be non-zero. In this case, we can calculate the initial value for the zero mode and then assume that it does not evolve during the calculation. For a sufficiently small value of the zero mode, this will result in (C.15) being approximately satisfied and therefore the error introduced by this method should be small. The alternative method would be to modify the equation to solve for a solution that has zero mean value and then convert back to the original solution, as was done in [46]. A discussion of this approach is contained in Chapter 5 for the Boussinesq-Ostrovsky equation.

For some of the cases considered we find that the radiating waves generated by the equation can re-enter the periodic domain and therefore we need to introduce a linear

damping region ('sponge layer') and add this at each end of the domain to prevent radiated waves re-entering the region of interest and interfering with the main wave structure [40]. The sponge layer is defined as

$$r(x) = \frac{\nu}{2} \left[ 2 + \tanh K \left( x - \frac{3L}{4} \right) - \tanh K \left( x + \frac{3L}{4} \right) \right], \quad (\text{C.17})$$

for some constants  $\nu, K$ . We choose  $K$  so that  $KL = 12$  and  $\nu$  is chosen so that damping occurs quickly. This sponge layer is incorporated into (C.13) as

$$(u_t + \alpha uu_x + \beta u_{xxx} + r(x)u)_x = \delta u. \quad (\text{C.18})$$

We treat the sponge layer term in the same way as the nonlinear term i.e. we calculate the product  $r(x)u$  in the real domain and then transform it to the Fourier space for use in the 4<sup>th</sup>-order Runge-Kutta method.

## C.2.2 Linearised Ostrovsky Equation on Non-Zero Background

We now present a method for the linearised Ostrovsky equation on non-zero background, with the potential for a non-zero forcing term. This is the type of equation that appears in Chapter 5 and in [46]. We write it in the most general form here, but it can easily be adjusted to suit the form presented in Chapter 5.

We take the equation for  $u$ , on a background of  $f$ , of the form

$$(u_t + \alpha (fu)_x + \beta u_{xxx})_x = \gamma u + H(f, x, t), \quad (\text{C.19})$$

where  $\alpha, \beta$  and  $\gamma$  are constants and  $H$  can take any form. In Chapter 5  $H$  was given in the form

$$H = f_{tt} + 2f_{xxx} + af_{xx} + b(f_x^2)_{xx}, \quad (\text{C.20})$$

where  $a$  and  $b$  are known. For the purposes of presenting the method here, we will solve the equation in terms of a generic  $H$  and then separately consider how to calculate the terms in (C.20). We note that the background  $f$  is the solution of a single Ostrovsky equation, for example replacing  $u$  with  $f$  in (C.13).

As before we consider the equation on the domain  $t \in [0, T]$  and  $x \in [-L, L]$ . We again transform the interval from  $[-L, L]$  to  $[0, 2\pi]$  via the transform  $\tilde{x} = sx + \pi$  and  $s = \pi/L$  to obtain (omitting tildes)

$$(su_t + \alpha s^2 (fu)_x + \beta s^4 u_{xxx})_x = \gamma u + H(f, x, t). \quad (\text{C.21})$$

The nonlinear terms are calculated in the real domain then transformed to the Fourier space. In many cases the terms contained in  $H$  may also be nonlinear and therefore require the same treatment. The spatial domain is discretised by  $N$  equidistant points with spacing  $\Delta x = 2\pi/N$ , and we apply the DFT and IDFT as defined in (C.6) and (C.7) respectively. The discrete Fourier transform of equation (C.14) with respect to  $x$  gives

$$u_t = i \left( s^3 k^3 \beta - \frac{\gamma}{sk} \right) \hat{u} - isk\alpha \widehat{fu} - \frac{i}{sk} \hat{H}. \quad (\text{C.22})$$

At this stage we would normally apply the 4<sup>th</sup>-order Runge-Kutta method. Before this is applied, we consider using the approach presented in [133] to remove the stiff term from this equation. This modified method allows for a larger time discretisation step to be used without loss of accuracy. Therefore we multiply through by the multiplicative factor  $M$  and introduce a new function  $U$ , where  $M$  and  $U$  take the form

$$M = e^{-i(s^3 k^3 \beta - \frac{\gamma}{sk})t}, \quad \hat{U} = e^{-i(s^3 k^3 \beta - \frac{\gamma}{sk})t} \hat{u}, \quad (\text{C.23})$$

which yields an ODE for  $U$  of the form

$$\hat{U}_t = -iks\alpha M \mathcal{F} \left\{ f \mathcal{F}^{-1} \left[ \frac{\hat{U}}{M} \right] \right\} - \frac{i}{sk} M \hat{H}. \quad (\text{C.24})$$

This yields an optimised 4<sup>th</sup>-order Runge-Kutta algorithm. Discretising the time domain as  $t_i = i\Delta t$  and discretising the functions  $\hat{U}_i = \hat{U}(k, t_i)$ ,  $\hat{u}_i = \hat{u}(k, t_i)$  and  $\hat{f}_i = \hat{f}(k, t_i)$ , we introduce the function

$$E = e^{\frac{i}{2}(s^3 k^3 \beta - \frac{\gamma}{sk})\Delta T}, \quad (\text{C.25})$$

and therefore we can use the optimised Runge-Kutta algorithm (written in the original variable  $u$ )

$$\hat{u}_{i+1} = E^2 \hat{u}_i + \frac{1}{6} [E^2 k_1 + 2E(k_2 + k_3) + k_4],$$

$$\begin{aligned} \text{where } k_1 &= -iks\Delta t \mathcal{F} \left\{ \hat{f}_i \mathcal{F}^{-1} [\hat{u}_i] \right\} - \frac{i\Delta t}{sk} \hat{H}, \\ k_2 &= -isk\Delta t \mathcal{F} \left\{ \hat{f}_i \mathcal{F}^{-1} \left[ E \left( \hat{u}_i + \frac{k_1}{2} \right) \right] \right\} - \frac{i\Delta t}{sk} \hat{H}, \\ k_3 &= -isk\Delta t \mathcal{F} \left\{ \hat{f}_i \mathcal{F}^{-1} \left[ E \hat{u}_i + \frac{k_2}{2} \right] \right\} - \frac{i\Delta t}{sk} \hat{H}, \\ k_4 &= -isk\Delta t \mathcal{F} \left\{ \hat{f}_i \mathcal{F}^{-1} [E^2 \hat{u}_i + E k_3] \right\} - \frac{i\Delta t}{sk} \hat{H}. \end{aligned} \quad (\text{C.26})$$

We can apply this algorithm to the case of a homogeneous Ostrovsky equation by setting  $\hat{H} = 0$  and replacing the term  $fu$  with  $u^2/2$ .

In the case of  $H$  as presented in (C.20), the Fourier transform of the term  $af_{xx}$  can be calculated directly. For the term  $b(f_x^2)_{xx}$ , we calculate  $f_x$  in the Fourier space by multiplying  $f$  by  $isk$ . We can then calculate the remainder of the term by taking

$$b \widehat{(f_x^2)_{xx}} = -bs^2k^2 \mathcal{F} \left\{ \mathcal{F}^{-1} \left\{ isk\hat{f} \right\}^2 \right\}. \quad (\text{C.27})$$

For the terms  $f_{tt}$  and  $f_{xxx}$ , we make use of (C.15) (replacing  $u$  with  $f$ ) and calculate  $f_t$ . Therefore we have

$$\hat{f}_{xxx} = -is^3k^3\hat{f}_t = (s^6k^6\beta - s^2k^2\gamma)\hat{f} + \frac{s^4k^4\alpha}{2}\widehat{f^2}. \quad (\text{C.28})$$

For  $f_{tt}$  we differentiate (C.15) with respect to  $t$  and we obtain

$$\hat{f}_{tt} = i \left( s^3k^3\beta - \frac{\gamma}{sk} \right) \hat{f}_t - isk\alpha f\hat{f}_t. \quad (\text{C.29})$$

If other terms were present in  $H$  they could be calculated in a similar way.

### C.2.3 Pseudospectral Scheme for the Coupled Ostrovsky Equations

Previously we have considered only a single equation in each case. Pseudospectral methods can be extended to a system of equations, as was done in [40] for a system of coupled Ostrovsky equations. We present a pseudospectral method here based upon that method, a direct extension of the method used for a single Ostrovsky equation in Section C.2.1. Let us consider the system of coupled Ostrovsky equations defined as

$$\begin{aligned} (u_t + \alpha_1 uu_x + \beta_1 u_{xxx})_x &= \delta(u - w), \\ (w_t + \omega w_x + \alpha_2 ww_x + \beta_2 w_{xxx})_x &= \gamma(w - u), \end{aligned} \quad (\text{C.30})$$

where  $\alpha_1, \alpha_2, \beta_1, \beta_2, \omega, \delta$  and  $\gamma$  are constants, and we consider the equation on domains  $t \in [0, t]$  and  $x \in [-L, L]$  as we did for the cases in Section C.1 and C.2.1. As with the previous two sections, we transform the solution interval from  $[-L, L]$  to  $[0, 2\pi]$  via the transform  $\tilde{x} = sx + \pi$  and  $s = \pi/L$  to obtain (omitting tildes)

$$\begin{aligned} (u_t + s\alpha_1 uu_x + s^3\beta_1 u_{xxx})_x &= \frac{\delta}{s}(u - w), \\ (w_t + s\omega w_x + s\alpha_2 ww_x + s^3\beta_2 w_{xxx})_x &= \frac{\gamma}{s}(w - u). \end{aligned} \quad (\text{C.31})$$

As before, the nonlinear terms are calculated in the real domain then transformed to the Fourier space. We can rewrite the nonlinear terms by introducing the notation

$$uu_x = z_{ax}, \quad z_a = \frac{u^2}{2}, \quad ww_x = z_{bx}, \quad z_b = \frac{w^2}{2}.$$

The spatial domain is discretised by  $N$  equidistant points with spacing  $\Delta x = 2\pi/N$ , and we have the DFT and IDFT as defined in (C.6) and (C.7) respectively, with an appropriately similar transform for  $w$ . The discrete Fourier transform of equations (C.31) with respect to  $x$  gives

$$\begin{aligned} \hat{u}_t + ik_s \alpha_1 \hat{z}_a - ik^3 s^3 \beta_1 \hat{u} &= -\frac{i\delta}{ks} (\hat{u} - \hat{w}), \\ \hat{w}_t + ik_s \omega \hat{w} + ik_s \alpha_2 \hat{z}_b - ik^3 s^3 \beta_2 \hat{w} &= -\frac{i\gamma}{ks} (\hat{w} - \hat{u}). \end{aligned} \quad (\text{C.32})$$

This system is solved numerically using the 4th-order Runge-Kutta method for time stepping. In this case we have a coupled system of equations and therefore, while we use the same algorithm as in Section C.1, we reproduce the equations here as they are modified for a coupled system. Assume that the solution at  $t$  is given by  $\hat{u}_j = \hat{u}(k, j\kappa)$  and  $\hat{w}_j = \hat{w}(k, j\kappa)$ , where  $\kappa = \Delta t$ . Then the solution at  $t = (j+1)\Delta t$  is given by

$$\begin{aligned} \hat{u}_{k,(j+1)\kappa} &= \hat{u}_{k,j\kappa} + \frac{1}{6} (a_1 + 2b_1 + 2c_1 + d_1), \\ \hat{w}_{k,(j+1)\kappa} &= \hat{w}_{k,j\kappa} + \frac{1}{6} (a_2 + 2b_2 + 2c_2 + d_2), \end{aligned} \quad (\text{C.33})$$

where  $a_i, b_i, c_i, d_i$  are functions of  $k$  at a given moment in time,  $t$ , and are defined as

$$\begin{aligned} a_i &= \kappa F_i(\hat{u}_j, \hat{w}_j), & b_i &= \kappa F_i\left(\hat{u}_j + \frac{a_1}{2}, \hat{w}_j + \frac{a_2}{2}\right), \\ c_i &= \kappa F_i\left(\hat{u}_j + \frac{b_1}{2}, \hat{w}_j + \frac{b_2}{2}\right), & d_i &= \kappa F_i(\hat{u}_j + c_1, \hat{w}_j + c_2), \end{aligned}$$

for  $i = 1, 2$ . The functions  $F_i$  are found as a rearrangement of (C.32) to contain all non-time derivatives. Explicitly we have

$$\begin{aligned} F_1(\hat{u}_j, \hat{w}_j) &= -ik_s \alpha_1 \hat{z}_a + ik^3 s^3 \beta_1 \hat{u}_j - \frac{i\delta}{ks} (\hat{u}_j - \hat{w}_j), \\ F_2(\hat{u}_j, \hat{w}_j) &= -iks (\alpha_2 \hat{z}_b + \omega \hat{w}_j) + ik^3 s^3 \beta_2 \hat{w}_j - \frac{i\gamma}{ks} (\hat{w}_j - \hat{u}_j). \end{aligned}$$

To obtain a solution at the next step, the functions  $a_i, b_i, c_i, d_i$ , for  $i = 1, 2$ , must be calculated in pairs, that is we calculate  $a_1$  followed by  $a_2$ , then  $b_1$  followed by  $b_2$ , and so on.

In what follows we first exclude the zero mode, i.e. we let  $k \neq 0$ , assuming zero mean

value initial conditions for  $u$  and  $w$ . In some of the cases considered in Chapter 4 the initial condition does not satisfy the zero mean value constraint of the coupled Ostrovsky equation. In this case, we calculate the zero mode in the usual way (the integral of the function across the spatial domain in the real space) and obtain a small constant, approximately  $O(10^{-2})$ . The maximum of the zero mode of  $u - w$  is  $O(10^{-3})$  for the cases considered, and therefore this approximation introduces only a small error, approximately satisfying the equations (C.32) (multiplied by  $k$ ) for zero modes. In the real space, the average  $\frac{1}{2L} \int_{-L}^L (u - w) dx$  is  $O(10^{-5})$ , showing that the zero mean value constraint is approximately satisfied.

A different approach is required for a general initial conditions with non-zero mean value [46]. The initial value problem for the Boussinesq-Ostrovsky equation is considered in Chapter 5 for non-zero mean initial condition. This approach could be extended to the scattering problem discussed in Chapter 4, however this extension is non-trivial. There are some comments about this method in the conclusions of this thesis but the extension is future work to be completed.

As was mentioned in Section C.2.1, for some of the cases considered in Chapter 4 Section 4.4.3, where the waves re-enter a coupled region after a delamination, we need to introduce a linear damping region ('sponge layer') and add this at each end of the domain to prevent radiated waves re-entering the region of interest and interfering with the main wave structure [40]. The sponge layer is defined in the same way as Section C.2.1 (namely in (C.17)) and incorporated into (C.30) as

$$\begin{aligned} (u_t + \alpha_1 uu_x + \beta_1 u_{xxx} + r(x)u)_x &= \delta(u - w), \\ (w_t + \omega w_x + \alpha_2 ww_x + \beta_2 w_{xxx} + r(x)w)_x &= \gamma(w - u). \end{aligned} \quad (\text{C.34})$$

We treat the sponge layer term in the same way as the nonlinear term i.e. we calculate the product  $r(x)u$  or  $r(x)w$  in the real domain and then transform it to the Fourier space for use in the 4<sup>th</sup>-order Runge-Kutta method.

### C.3 Pseudospectral Scheme for the Boussinesq-Ostrovsky Equation

In Chapters 3 and 4 we considered the solution to the Boussinesq equation using finite-difference techniques. Another possible technique for solving the Boussinesq equation is to apply a pseudospectral method. This method is an extension to the approach

outlined in [110] which solves the regularised Boussinesq equation in the context of microstructured solids.

Let us consider the Boussinesq-Ostrovsky equation defined as

$$\begin{aligned} u_{tt} - c^2 u_{xx} &= \epsilon \left( \frac{\alpha}{2} (u^2)_{xx} + \beta u_{ttxx} - \gamma u \right), \\ u|_{t=0} &= F(x), \\ u_t|_{t=0} &= V(x), \end{aligned} \quad (\text{C.35})$$

on the periodic domain  $-L \leq x \leq L$ . We introduce the change of variable

$$w = u - \epsilon \beta u_{xx}, \quad (\text{C.36})$$

so that we have

$$w_{tt} = c^2 u_{xx} + \epsilon \left( \frac{\alpha}{2} (u^2)_{xx} - \gamma u \right). \quad (\text{C.37})$$

Taking the Fourier transform of (C.36) we obtain

$$\hat{w} = (1 + \epsilon \beta k^2) \hat{u} \quad \Rightarrow \quad \hat{u} = \frac{\hat{w}}{1 + \epsilon \beta k^2}. \quad (\text{C.38})$$

We take the Fourier transform of (C.37) and substitute (C.38) into this expression to obtain an ODE in  $\hat{w}$ , taking the form

$$\hat{w}_{tt} = -\frac{\epsilon \gamma + c^2 k^2}{1 + \epsilon \beta k^2} \hat{w} - \frac{\epsilon \alpha k^2}{2} \mathcal{F} \left\{ \mathcal{F}^{-1} \left[ \frac{\hat{w}}{1 + \epsilon \beta k^2} \right]^2 \right\} = \hat{S}(\hat{w}). \quad (\text{C.39})$$

We solve this ODE using a 4<sup>th</sup>-order Runge-Kutta method for time stepping, such as the one used in [40, 43]. Let us define the following:

$$\hat{w}_t = \hat{G}, \quad \hat{G}_t = \hat{S}(\hat{w}), \quad (\text{C.40})$$

where we defined  $\hat{S}$  as the right-hand side of (C.39). We discretise the time domain and functions as  $t = t_n$ ,  $\hat{w}(k, t_n) = \hat{w}_n$ ,  $\hat{G}(k, t_n) = \hat{G}_n$  for  $n = 0, 1, 2, \dots$ , where  $t_n = n\Delta t$ . Here  $k$  discretises the Fourier space. Taking the Fourier transform of the initial conditions as defined in (C.35) and making use of (C.38) we obtain initial conditions  $\hat{w}_0$  and  $\hat{G}_0$  of the form

$$\begin{aligned} \hat{w}_0 &= (1 + \epsilon \beta k^2) \mathcal{F} \{F(x)\}, \\ \hat{G}_0 &= (1 + \epsilon \beta k^2) \mathcal{F} \{V(x)\}. \end{aligned} \quad (\text{C.41})$$

Now we have initial conditions, we implement the following 4<sup>th</sup>-order Runge-Kutta method:

$$\hat{w}_{n+1} = \hat{w}_n + \frac{1}{6} [k_1 + 2k_2 + 2k_3 + k_4], \quad \hat{G}_{n+1} = \hat{G}_n + \frac{1}{6} [l_1 + 2l_2 + 2l_3 + l_4],$$

where

$$\begin{aligned} k_1 &= \Delta t \hat{G}_n, & l_1 &= \Delta t \hat{S}(\hat{W}_n), \\ k_2 &= \Delta t \left( \hat{G}_n + \frac{l_1}{2} \right), & l_2 &= \Delta t \hat{S} \left( \hat{W}_n + \frac{k_1}{2} \right), \\ k_3 &= \Delta t \left( \hat{G}_n + \frac{l_2}{2} \right), & l_3 &= \Delta t \hat{S} \left( \hat{W}_n + \frac{k_2}{2} \right), \\ k_4 &= \Delta t \left( \hat{G}_n + l_3 \right), & l_4 &= \Delta t \hat{S} \left( \hat{W}_n + k_3 \right). \end{aligned} \quad (\text{C.42})$$

As was done for the scheme in Section C.2.3, the system has to be solved in pairs i.e. we calculate  $k_1$ , then  $l_1$ , followed by  $k_2$  and  $l_2$ , and so on. To obtain the solution in the real domain, we transform  $\hat{w}$  back to  $u$  through relation (C.38). Explicitly we have

$$u(x, t) = \mathcal{F}^{-1} \left\{ \frac{\hat{w}}{1 + \epsilon \beta k^2} \right\}. \quad (\text{C.43})$$



# Bibliography

- [1] M. J. Ablowitz and H. Segur, *Solitons and the Inverse Scattering Transform*, SIAM (1981).
- [2] M. J. Ablowitz, *Nonlinear dispersive waves: asymptotic analysis and solitons*, Cambridge University Press (2011).
- [3] P. G. Drazin and R. S. Johnson, *Solitons: An Introduction*, Cambridge University Press (1989).
- [4] A. C. Newell, *Solitons in Mathematics and Physics*, Philadelphia, SIAM (1985).
- [5] R. H. J. Grimshaw, *Solitary Waves in Fluids*, Southampton, WIT Press (2007).
- [6] R. S. Johnson, *A Modern Introduction to the Mathematical Theory of Water Waves*, Cambridge University Press (1997).
- [7] J. Yang, *Nonlinear Waves in Integrable and Nonintegrable Systems*, SIAM (2010).
- [8] G. B. Whitham, *Linear and Nonlinear Waves*, New York, Wiley (1974).
- [9] L. A. Ostrovsky, *Nonlinear internal waves in a rotating ocean*, *Oceanology* **18**, 119–125 (1978).
- [10] R. Grimshaw and K. R. Helfrich, *Long-time solutions of the Ostrovsky equation*, *Stud. Appl. Math.* **121**, 71–88 (2008).
- [11] R. Grimshaw and K. R. Helfrich, *The effect of rotation on internal solitary waves*, *IMA J. Appl. Math.* **77**, 326–339 (2012).
- [12] R. H. J. Grimshaw, K. R. Helfrich and E. R. Johnson, *Experimental study of the effect of rotation on nonlinear internal waves*, *Phys. Fluids* **25**, 056602 (2013).
- [13] J. S. Russell, *Report of the fourteenth meeting of the British Association for the Advancement of Science*, London (1844).

- [14] J. V. Boussinesq, *Théorie des ondes et des remous qui se propagent le long d'un canal rectangulaire horizontal, en communiquant au liquide contenu dans ce canal des vitesses sensiblement pareilles de la surface au fond*, J. Math. Pures Appl., ser. (2) **17**, 55–108 (1872).
- [15] J. V. Boussinesq, *Essai sur la théorie des eaux courantes. Mémoires présentés par divers savants à l'Académie des Sciences*, Inst. NAT. France **XXIII**, 1–660 (1877).
- [16] Lord J. W. S. Rayleigh, *On Waves*, Phil. Mag. **1**, 257–279 (1876).
- [17] D. J. Korteweg and G. De Vries, *On the change of form of long waves advancing in a rectangular canal, and on a new type of long stationary waves*, Phil. Mag. (5) **39**, 422–443 (1895).
- [18] E. Fermi, J. Pasta and S. Ulam, *Studies on nonlinear problems*, I. Los Alamos Scientific Laboratory **Report No. LA-1940** (1955).
- [19] N. J. Zabusky and M. D. Kruskal, *Interaction of “Solitons” in a Collisionless Plasma and the Recurrence of Initial States*, Phys. Rev. Lett. **15**, 240–243 (1965).
- [20] C. S. Gardner, J. M. Greene, M. D. Kruskal and R. M. Miura, *Method for solving the Korteweg-de Vries equation*, Phys. Rev. Lett. **19**, 1095–1097 (1967).
- [21] C. S. Gardner, J. M. Greene, M. D. Kruskal and R. M. Miura, *Korteweg-de Vries Equation and Generalizations. VI. Methods for Exact Solution*, Commun. Pur. Appl. Math. **27**, 97–133 (1974).
- [22] G. I. Stegeman and M. Segev, *Optical Spatial Solitons and Their Interactions: Universality and Diversity*, Science **286**, 1518–1523 (1999).
- [23] J. D. Nash and J. N. Moum, *River plumes as a source of large-amplitude internal waves in the coastal ocean*, Nature **437**, 400–403 (2005).
- [24] M. A. Hoefer, M. J. Ablowitz, I. Coddington, E. A. Cornell, P. Engels and V. Schweikhard, *Dispersive and classical shock waves in Bose-Einstein condensates and gas dynamics*, Phys. Rev. A **74**, 023623 (2006).
- [25] G. V. Dreiden, A. M. Samsonov, I. V. Semenova and A. G. Shvartz, *Strain solitary waves in a thin-walled waveguide*, Appl. Phys. Lett. **105**, 211906 (2014).
- [26] T. Trogdon, S. Olver and B. Deconinck, *Numerical inverse scattering for the Korteweg-de Vries and modified Korteweg-de Vries equations*, Physica D **241**, 1003–1025 (2012).

- [27] V. E. Zakharov and A. B. Shabat, *Exact theory of two-dimensional self-focusing and one-dimensional self-modulation of waves in nonlinear media*, Sov. Phys. JETP **34**, 62–69 (1972).
- [28] A. R. Osborne, *Nonlinear Ocean Waves*, New York, Academic Press (2009).
- [29] J. M. Soto-Crespo, N. Devine and N. Akhmediev, *Integrable turbulence and rogue waves: Breathers or solitons?*, Phys. Rev. Lett. **116**, 103901 (2016).
- [30] K. R. Khusnutdinova and A. M. Samsonov, *Fission of a longitudinal strain solitary wave in a delaminated bar*, Phys. Rev. E **77**, 066603 (2008).
- [31] A. M. Samsonov, *Strain Solitons in Solids and How to Construct Them*, CRC Press (2001).
- [32] A. V. Porubov, *Amplification of Nonlinear Strain Waves in Solids*, World Scientific (2003).
- [33] G. V. Dreiden, K. R. Khusnutdinova, A. M. Samsonov and I. V. Semenova, *Splitting induced generation of soliton trains in layered waveguides*, J. Appl. Phys. **107**, 034909 (2010).
- [34] A. M. Samsonov, G. V. Dreiden and I. V. Semenova, *Do the bulk strain solitary waves decay?*, P. I. Mech. Eng. C-J. Mec. **222**, 1975–1980 (2008).
- [35] A. M. Samsonov, I. V. Semenova and A. V. Belashov, *Direct determination of bulk strain soliton parameters in solid polymeric waveguides*, Wave Motion **71**, 120–126 (2017).
- [36] G. V. Dreiden, K. R. Khusnutdinova, A. M. Samsonov and I. V. Semenova, *Bulk strain solitary waves in bonded layered polymeric bars with delamination*, J. Appl. Phys. **112**, 063516 (2012).
- [37] I. V. Semenova, A. V. Belashov, G. V. Dreiden, N. V. Petrov and A. M. Samsonov, *Rapid detection of delamination areas in laminated structural elements by means of optically monitored strain solitons*, Proc SPIE **9525**, 95253V (2015).
- [38] K. R. Khusnutdinova, A. M. Samsonov and A. S. Zakharov, *Nonlinear layered lattice model and generalized solitary waves in imperfectly bonded structures*, Phys. Rev. E **79**, 056606 (2009).
- [39] K. R. Khusnutdinova and K. R. Moore, *Initial-value problem for coupled Boussinesq equations and a hierarchy of Ostrovsky equations*, Wave Motion **48**, 738–752 (2011).

- [40] A. Alias, R. H. J. Grimshaw and K. R. Khusnutdinova, *On strongly interacting internal waves in a rotating ocean and coupled Ostrovsky equations*, *Chaos* **23**(2), 023121 (2013).
- [41] A. Alias, R. H. J. Grimshaw and K. R. Khusnutdinova, *Coupled Ostrovsky equations for internal waves in a shear flow*, *Phys. Fluids* **26**(12), 126603 (2014).
- [42] K. R. Khusnutdinova and M. R. Tranter, *Modelling of nonlinear wave scattering in a delaminated elastic bar*, *P. Roy. Soc. A* **471**(2183), 20150584 (2015).
- [43] K. R. Khusnutdinova and M. R. Tranter, *On radiating solitary waves in bi-layers with delamination and coupled Ostrovsky equations*, *Chaos* **27**, 013112 (2017).
- [44] G. V. Dreiden, A. M. Samsonov, I. V. Semenova and K. R. Khusnutdinova, *Observation of a radiating bulk strain soliton in a solid-state waveguide*, *Tech. Phys.* **56**, 889–892 (2011).
- [45] K. R. Khusnutdinova and K. R. Moore, *Weakly nonlinear extension of d’Alembert’s formula*, *IMA J. Appl. Math.* **77**, 361–381 (2012).
- [46] K. R. Khusnutdinova, K. R. Moore and D. E. Pelinovsky, *Validity of the weakly nonlinear solution of the Cauchy problem for the Boussinesq-type equation*, *Stud. Appl. Math.* **133**, 52–83 (2014).
- [47] K. R. Moore, *Coupled Boussinesq equations and nonlinear waves in layered waveguides*, PhD Thesis, Loughborough University, 2013.
- [48] R. H. J. Grimshaw, *Adjustment processes and radiating solitary waves in a regularised Ostrovsky equation*, *Eur. J. Mech. B-Fluid* **18**, 535–543 (1999).
- [49] G. Deng, G. Biondini and S. Trillo, *Small dispersion limit of the Korteweg-de Vries equation with periodic initial conditions and analytical description of the Zabuskyy-Kruskal experiment*, *Physica D* **333**, 137–147 (2016).
- [50] S. Trillo, G. Deng, G. Biondini, M. Klein, G. F. Clauss, A. Chabchoub et al., *Experimental Observation and Theoretical Description of Multisoliton Fission in Shallow Water*, *Phys. Rev. Lett.* **117**, 144102 (2016).
- [51] E. Volterra, *The equations of motions for curved and twisted elastic bar deduced by the use of the “method of internal constraints”*, *Ing. Arch.* **24**, 392–400 (1956).
- [52] E. Volterra and E. C. Zachmanoglou, *Dynamics of Vibrations*, Columbus, Merrill (1965).
- [53] A. E. H. Love, *Nonlinear Ocean Waves*, New York, Dover (1944).

- [54] H. N. Abramson, H. J. Plass and E. A. Ripperger, *Stress wave propagation in rods and beams*, Adv. Appl. Mech. **5**, 111–194 (1958).
- [55] E. I. Grigolyuk and I. T. Selezov, *Non-Classical Theories of Vibrations of Rods, Plates and Shells*, Moscow, VINITI (1973).
- [56] T. B. Benjamin, J. L. Bona and J. J. Mahony, *Model equations for long waves in nonlinear dispersive systems*, Philos. Trans. R. Soc. Lond. A **272**, 47–48 (1972).
- [57] J. L. Bona, M. Chen and J. C. Saut, *Boussinesq equations and other systems for small-amplitude long waves in nonlinear dispersive media. I: derivation and linear theory*, J. Nonlinear Sci. **12**, 283–318 (2002).
- [58] J. L. Bona, M. Chen and J. C. Saut, *Boussinesq equations and other systems for small-amplitude long waves in nonlinear dispersive media. I: the nonlinear theory*, Nonlinearity **17**, 925–952 (2004).
- [59] J. L. Bona, T. Colin and D. Lannes, *Long wave approximations for water waves*, Arch. Ration. Mech. **178**, 373–410 (2005).
- [60] J. Gear and R. Grimshaw, *Weak and strong interactions between internal solitary waves*, Stud. Appl. Math. **70**, 235–258 (1984).
- [61] W. Craig, *An existence theory for water waves and the Boussinesq and Korteweg-de Vries scaling limits*, Comm. Partial Differential Equations **10**, 787–1003 (1985).
- [62] T. Kano and T. Nishida, *A mathematical justification for Korteweg-de Vries equation and Boussinesq equation of water surface waves*, Osaka J. Math. **23**, 389–413 (1986).
- [63] L. A. Kalyakin, *Long wave asymptotics. Integrable equations as the asymptotic limit of non-linear systems*, Russ. Math. Surv. **44**, 5–34 (1989).
- [64] G. Schneider, *The long wave limit for a Boussinesq equation*, SIAM J. Appl. Math. **58**, 1237–1245 (1998).
- [65] W. Ben Youssef and T. Colin, *Rigorous derivation of Korteweg-de Vries-type systems from a general class of nonlinear hyperbolic systems*, ESAIM: M2AN **34**, 873–911 (2000).
- [66] G. Schneider and C. E. Wayne, *The long-wave limit for the water wave problem. I. The case of zero surface tension*, Comm. Pure Appl. Math. **53**, 1475–1535 (2000).
- [67] C. E. Wayne and J. D. Wright, *Higher order modulation equations for a Boussinesq equation*, SIAM J. Appl. Dyn. Syst. **1**, 271–302 (2002).

- [68] M. A. Christou and C. I. Christov, *Interacting localized waves for the regularized long wave equation via a Galerkin spectral method*, Math. Comp. Sim **69**, 257–268 (2005).
- [69] V. E. Zakharov, *On stochastisation of one-dimensional chains of nonlinear oscillators*, Sov. Phys. JETP **38**, 108–110 (1974).
- [70] A. I. Leonov, *The effect of the earth's rotation on the propagation of weak nonlinear surface and internal long oceanic waves*, Ann. NY Acad. Sci. **373**, 150–159 (1981).
- [71] R. H. J. Grimshaw, J. M. He and L. A. Ostrovsky, *Terminal damping of a solitary wave due to radiation in rotational systems*, Stud. Appl. Math. **101**, 197–210 (1998).
- [72] K. R. Helfrich, *Decay and return of internal solitary waves with rotation*, Phys. Fluids **19**, 026601 (2007).
- [73] R. Grimshaw and K. Helfrich, *Long-time solutions of the Ostrovsky equation*, Stud. Appl. Math. **121**, 71–88 (2008).
- [74] T. Gerkema, *A unified model for the generation and fission of internal tides in a rotating ocean*, J. Marine Res. **54**, 421–450 (1996).
- [75] G. A. Nariboli and A. Sedov, *Burgers's-Korteweg-De Vries equation for viscoelastic rods and plates*, J. Math. Anal. Appl. **32**, 661–677 (1970).
- [76] L. A. Ostrovskii and A. M. Sutin, *Nonlinear elastic waves in rods*, J. Appl. Math. Mech. **41**, 543–549 (1977).
- [77] J. Engelbrecht, *Nonlinear Wave Processes of Deformation in Solids*, London, Pitman (1983).
- [78] A. M. Samsonov, *Soliton evolution in a rod with variable cross section*, Sov. Phys. Dokl. **29**, 586–588 (1984).
- [79] G. V. Dreiden, Y. I. Ostrovsky, A. M. Samsonov, I. V. Semenova and E. V. Sokurinskaya, *Formation and propagation of deformation solitons in a nonlinearly elastic solid*, Zh. Tekh. Fiz. **58**, 2040–2047 (1988).
- [80] A. M. Samsonov, G. V. Dreiden, A. V. Porubov and I. V. Semenova, *Longitudinal-strain soliton focusing in a narrowing nonlinearly elastic rod*, Phys. Rev. B **57**, 5778 (1998).
- [81] I. V. Semenova, G. V. Dreiden and A. M. Samsonov, *On nonlinear wave dissipation in polymers*, Proc. SPIE, Optical Diagnostics **5880**, 588006 (2005).

- [82] G. V. Dreiden, K. R. Khusnutdinova, A. M. Samsonov and I. V. Semenova, *Comparison of the effect of cyanoacrylate- and polyurethane-based adhesives on a longitudinal strain solitary wave in layered polymethylmethacrylate waveguides*, J. Appl. Phys. **104**, 086106 (2008).
- [83] G. V. Dreiden, A. M. Samsonov and I. V. Semenova, *Observation of bulk strain solitons in layered bars of different materials*, Tech. Phys. Lett. **40**, 1140–1141 (2014).
- [84] V. A. Shutilov, *Basics of Ultrasound Physics*, Leningrad, Leningrad University Press (1980).
- [85] E. Maeva, I. Severina, S. Bondarenko, G. Chapman, B. O’Neill, F. Severin et al., *Acoustical methods for the investigation of adhesively bonded structures: A review*, Can. J. Phys. **82**, 981–1025 (2004).
- [86] E. N. Pelinovsky, *On the Soliton Evolution in Inhomogeneous Media*, Prikl. Mekh. Tekh. Fiz. **6**, 80–85 (1971).
- [87] F. D. Tappert and N. J. Zabusky, *Gradient-Induced Fission of Solitons*, Phys. Rev. Lett. **27**, 1774 (1971).
- [88] R. S. Johnson, *On the development of a solitary wave moving over an uneven bottom*, Proc. Camb. Philos. Soc. **73**, 183–203 (1973).
- [89] V. D. Djordjević and L. G. Redekopp, *Fission and Disintegration of Internal Solitary Waves Moving over Two-Dimensional Topography*, J. Phys. Oceanogr. **8**, 1016–1024 (1978).
- [90] R. Grimshaw, E. Pelinovsky and T. Talipova, *Fission of a weakly nonlinear interfacial solitary wave at a step*, Geophys. Astrophys. Fluid Dyn. **102**, 179–194 (2008).
- [91] V. Maderich, T. Talipova, R. Grimshaw, K. Terletska, I. Brovchenko, E. Pelinovsky et al., *Interaction of Large Amplitude Interfacial Solitary Wave of Depression with Bottom Step*, Phys. Fluids **22**, 076602 (2010).
- [92] L. D. Landau and E. M. Lifshitz, *Quantum Mechanics: Non-Relativistic Theory*, Elsevier Science (2013).
- [93] T. R. Marchant and N. F. Smyth, *The initial boundary value problem for the KdV equation on the negative quarter-plane*, Proc. R. Soc. Lond. A **458**, 857–871 (2002).

- [94] S. Gottlieb, D. I. Ketcheson and C. W. Shu, *High Order Strong Stability Preserving Time Discretizations*, J. Sci. Comput. **38**, 251–289 (2009).
- [95] R. H. J. Grimshaw, K. R. Khusnutdinova and K. R. Moore, *Radiating solitary waves in coupled Boussinesq equations*, IMA J. Appl. Math. **82**, 802–820 (2017).
- [96] D. V. Skryabin and A. V. Gorbach, *Looking at a soliton through the prism of optical supercontinuum*, Rev. Mod. Phys. **82**, 1287–1299 (2010).
- [97] M. Conforti, S. Trillo, A. Mussat and A. Kudlinski, *Parametric excitation of multiple resonant radiations from localized wavepackets*, Sci. Rep. **5**, 9433 (2015).
- [98] E. S. Benilov, R. Grimshaw and E. P. Kuznetsova, *The generation of radiating waves in a singularly perturbed Korteweg-de Vries equation*, Physica D **69**, 270–278 (1993).
- [99] V. V. Voronovich, I. A. Sazonov and V. I. Shrira, *On radiating solitons in a model of the internal wave-shear flow resonance*, J. Fluid Mech **568**, 273–302 (2006).
- [100] J. L. Bona, V. A. Dougalis and D. E. Mitsotakis, *Numerical solution of Boussinesq systems of KdV-KdV type: II. Evolution of radiating solitary waves*, Nonlinearity **21**, 2825 (2008).
- [101] J. P. Boyd, *Weakly Nonlinear Solitary Waves and Beyond-All-Orders Asymptotics*, Boston, Kluwer (1998).
- [102] C. Fochesato, F. Dias and R. H. J. Grimshaw, *Generalized solitary waves and fronts*, Physica D **210**, 96–117 (2005).
- [103] R. H. J. Grimshaw and G. Iooss, *Solitary waves of a coupled Korteweg-de Vries system*, Math. Comput. Simulat. **62**, 31–40 (2003).
- [104] R. Grimshaw and N. Joshi, *Weakly Nonlocal Solitary Waves in a Singularly Perturbed Korteweg-de Vries Equation*, SIAM J. Appl. Math. **55**, 124–135 (1995).
- [105] V. I. Karpman, *Radiation by solitons due to higher-order dispersion*, Phys. Rev. E **47**, 2073–2082 (1993).
- [106] E. Lombardi, *Oscillatory Integrals and Phenomena Beyond all Algebraic Orders*, Berlin, Springer (2000).
- [107] J. M. Vanden-Broeck, *Elevation solitary waves with surface tension*, Phys. Fluids **A3**, 2659–2663 (1991).
- [108] R. H. J. Grimshaw, L. A. Ostrovsky, V. I. Shrira and Yu. A. Stepanyants, *Long nonlinear surface and internal gravity waves in a rotating ocean*, Surv. Geophys. **19**, 289–338 (1998).

- [109] J. Stoer and R. Bulirsch, *Introduction to Numerical Analysis*, New York, Springer-Verlag (1980).
- [110] J. Engelbrecht, A. Salupere and K. Tamm, *Waves in microstructured solids and the Boussinesq paradigm*, *Wave Motion* **48**, 717–726 (2011).
- [111] K. R. Khusnutdinova and M. R. Tranter, *Scattering of bulk strain solitary waves in bi-layers with delamination*, *Procedia Eng.* **199**, 1533–1538 (2017).
- [112] C. F. Gerald and P. O. Wheatley, *Applied Numerical Analysis*, World Student Series, Addison-Wesley (1984).
- [113] G. D. Smith, *Numerical Solution of Partial Differential Equations: Finite Difference Methods*, Oxford Applied Mathematics, Clarendon Press (1985).
- [114] S. Kutluay, A. R. Bahadir and A. Özdeş, *Numerical solution of one-dimensional Burgers equation: explicit and exact-explicit finite difference methods*, *J. Comput. Appl. Math.* **103**, 251–261 (1999).
- [115] A. G. Bratsos and E. H. Twizell, *An explicit finite-difference scheme for the solution of the Kadomtsev-Petviashvili equation*, *Int. J. Comput. Math.* **68**, 175–187 (1998).
- [116] M. P. Sørensen, P. L. Christiansen and P. S. Lomdahl, *Solitary waves on nonlinear elastic rods*, *J. Acoust. Soc. Am.* **76**, 871–879 (1984).
- [117] W. F. Ames, *Numerical Methods for Partial Differential Equations*, 2nd ed., Academic Press, Inc. (1977).
- [118] E. Isaacson and H. B. Keller, *Analysis of Numerical Methods*, Dover Books on Mathematics, Dover (1994).
- [119] F. Z. Nouri and D. M. Sloan, *A comparison of Fourier pseudo-spectral methods for the solution of the Korteweg-de Vries equation*, *J. Comput. Phys.* **83**, 324–344 (1989).
- [120] J. P. Boyd, *Chebyshev and Fourier Spectral Methods*, Dover, Springer (2001).
- [121] M. A. Obregon, E. Sanmiguel-Rojas and R. Fernandez-Feria, *High accuracy numerical methods for the Gardner-Ostrovsky equation*, *Appl. Math. Comput.* **240**, 140–148 (2014).
- [122] S. K. Lele, *Compact Finite Difference Schemes with Spectral-like Resolution*, *J. Comput. Phys.* **103**, 16–42 (1992).
- [123] J. Donea and A. Huerta, *Finite Element Methods for Flow Problems*, Wiley (2003).

- 
- [124] P. Yue, C. Zhou, J. J. Feng, C. F. Ollivier-Gooch and H. H. Hu, *Phase-field simulations of interfacial dynamics in viscoelastic fluids using finite elements with adaptive meshing*, J. Comput. Phys. **219**, 47–67 (2006).
- [125] A. Canivar, M. Sari and I. Dag, *A Taylor-Galerkin finite element method for the KdV equation using cubic B-splines*, Physica B **405**, 3376–3383 (2010).
- [126] Y. S. Li, S. X. Liu, Y. X. Yu and G. Z. Lai, *Numerical modeling of Boussinesq equations by finite element method*, Coast. Eng. **37**, 97–122 (1999).
- [127] B. Fornberg, *A Practical Guide to Pseudospectral Methods*, 1st ed., Cambridge, Cambridge University Press (1996).
- [128] J. W. Cooley and J. W. Tukey, *An algorithm for the machine calculation of complex Fourier series*, Math. Comput. **19**, 297–301 (1965).
- [129] M. Frigo and S. G. Johnson, *The Design and Implementation of FFTW3*, Proc. IEEE **93**(2), 216–231 Special issue on “Program Generation, Optimization, and Platform Adaptation” (2005).
- [130] B. Fornberg and G. B. Whitham, *A numerical and theoretical study of certain nonlinear wave phenomena*, Phil. Trans. R. Soc. A **289**, 373–404 (1978).
- [131] T. Y. Hou and R. Li, *Computing nearly singular solutions using pseudo-spectral methods*, J. Comp. Phys. **226**, 379–397 (2007).
- [132] M. A. Obregon and Y. A. Stepanyants, *On Numerical Solution of the Gardner-Ostrovsky Equation*, Math. Model. Nat. Phenom. **7**(2), 113–130 (2012).
- [133] L. N. Trefethen, *Spectral Methods in MATLAB*, Philadelphia, PA, SIAM (2000).